

IN-02
98084

NASA Technical Memorandum 107310

Experimental Investigation of the Flow Field in a Transonic, Axial Flow Compressor With Respect to the Development of Blockage and Loss

Kenneth L. Suder
Lewis Research Center
Cleveland, Ohio

October 1996



National Aeronautics and
Space Administration

Experimental Investigation of the Flow
Field in a Transonic, Axial Flow Compressor with
Respect to the Development of Blockage and Loss

by

Kenneth L. Suder

Submitted in partial fulfillment of the requirements
for the degree of Doctor of Philosophy

Thesis Adviser: Professor Eli Reshotko

Department of Mechanical and Aerospace Engineering

CASE WESTERN RESERVE UNIVERSITY

Experimental Investigation of the Flow Field in a Transonic, Axial Flow Compressor with Respect to the Development of Blockage and Loss

Abstract

by

Kenneth L. Suder

A detailed experimental investigation to understand and quantify the development of loss and blockage in the flow field of a transonic, axial flow compressor rotor has been undertaken. Detailed laser anemometer measurements were acquired upstream, within, and downstream of a transonic, axial compressor rotor operating at design and off-design conditions. The rotor was operated at 100%, 85%, 80%, and 60% of design speed which provided inlet relative Mach numbers at the blade tip of 1.48, 1.26, 1.18, and 0.89 respectively.

At design speed the blockage is evaluated ahead of the rotor passage shock, downstream of the rotor passage shock, and near the trailing edge of the blade

row. The blockage is evaluated in the core flow area as well as in the casing endwall region. Similarly at part speed conditions for the cases of 1) where the rotor passage shock is much weaker than that at design speed and 2) where there is no rotor passage shock, the blockage and loss are evaluated and compared to the results at design speed. Specifically, the impact of the rotor passage shock on the blockage and loss development, pertaining to both the shock / boundary layer interactions and the shock / tip clearance flow interactions, is discussed. In addition, the blockage evaluated from the experimental data is compared to 1) an existing correlation of blockage development which was based on computational results, and 2) computational results on a limited basis.

The results indicate that for this rotor the blockage in the endwall region is 2–3 times that of the core flow region and the blockage in the core flow region more than doubles when the shock strength is sufficient to separate the suction surface boundary layer. The distribution of losses in the core flow region indicate that the total loss is primarily comprised of the shock loss when the shock strength is not sufficient to separate the suction surface boundary layer. However when the shock strength is sufficient to separate the suction surface boundary layer, the profile loss is comparable to the shock loss and can exceed the shock loss.

Acknowledgments

I would like to thank my colleagues at NASA Lewis Research Center for their assistance throughout this project. I am especially thankful to Dr. Anthony Strazisar, and Mr. Jerry Wood for their constructive criticisms, guidance and encouragement throughout this research program. In addition, I wish to thank Dr. John Adamczyk, Dr. M. Hathaway, Dr. R. Chriss, and Mr. Dale Van Zante for their many helpful suggestions. Special thanks also go to Glenn Christman for keeping the computers and data acquisition electronics talking to each other and to Bob McCluskey, Mike McGhee, Mike Goin, Bob Gronski, and Rick Brokopp for keeping everything else working in the facility.

I would like to thank Professor Eli Reshotko for his patience, encouragement, and advice throughout the course of this research program.

Finally, I wish to acknowledge the National Aeronautics and Space Administration's Lewis Research Center for their support of this research program.

Contents

Abstract	ii
Dedication	iv
Acknowledgments	v
List of Figures	x
List of Tables	xvi
Symbols and Notation	xvii
Chapter 1 Introduction	1
Chapter 2 Research Equipment	21
2.1 Facility	21
2.2 Research Compressor	22
2.3 Conventional Instrumentation	24
2.3.1 Tip Clearance Measurements	24
2.3.2 Aerodynamic Probe Measurements	26
2.4 Laser Anemometer System	29
2.4.1 Overall Characteristics	29
2.4.2 LFA System Components	30
2.5 Computational Tool	40
Chapter 3 Experimental Procedure	43
3.1 Data Acquisition	43
3.1.1 Survey Locations	43
3.1.2 Operating Conditions	47
3.2 Data Reduction	49
3.2.1 Aerodynamic Probe Data	49
3.2.2 Laser Anemometer Data	51

Chapter 4 Results and Discussion of Flow Field Physics	56
4.1 Overall Performance Characteristics Based on Aerodynamic Probe Surveys and Their Comparison with Design and CFD Results	56
4.1.1 Performance Map	57
4.1.2 Radial Distributions	60
4.1.3 Comparisons with CFD	69
4.2 General Flow Field Description	78
4.2.1 Description of Cross-Channel Flow Field Upstream and Downstream of the Rotor	78
4.2.2 Description of Blade-to-Blade Flow Field	85
4.2.3 Comparison of the Axisymmetric Average Flow Field Versus the Flow Field at Mid-pitch.	88
4.3 Data Integrity	93
4.4 Sensitivity of Loss and Blockage Development in the 'Core Flow Region' to Changes in the Rotor Back Pressure at Design Speed.	96
4.4.1 Impact on Measured Blade-to-Blade Flow Field	97
4.4.2 Impact on Measured Blade Loading Distribution	104
4.4.3 Comparison to CFD Blade-to-Blade Flow Field	111
4.4.4 Summary of 'Core ' Flow Field Results at Design Speed	114
4.5 Sensitivity of Loss and Blockage Development in the Outer 'Endwall' Flow Region' to Changes in the Rotor Back Pressure at Design Speed.	115
4.5.1 Impact on Measured Blade-to-Blade Flow Field	116
4.5.2 Comparison to CFD Blade-to-Blade Flow Field	125
4.5.3 Summary of Endwall Flow Field Results at Design Speed	128

4.6 Loss and Blockage Development in the Rotor at Part Speed Conditions	129
4.6.1 Core Flow Field Results Measured at 80% Speed	129
4.6.2 Core Flow Field Results Measured at 80% and 60% Speed	135
4.6.3 Endwall Flow Field Results Measured at 60% and 80% Speed.	139
4.7 Summary of Flow Physics Regarding Blockage and Loss Development	148
Chapter 5 Quantification of Blockage and Loss Estimates . . .	152
5.1 Quantification of Blockage	153
5.1.1 Quantification of Blockage Downstream of the Rotor Blade Row	156
5.1.2 Quantification of Blockage within the Rotor . .	161
5.2 Calculation of Blockage	168
5.2.1 Downstream Blockage Calculations	168
5.2.2 Blockage Development within the Rotor Passage	184
5.3 Quantification and Estimation of Losses	193
5.3.1 Comparison of Profile Loss to Lieblein's Correlation	198
Chapter 6 Concluding Remarks & Recommendations for Future Work	203
6.1 Concluding Remarks	203
6.2 Recommendations for Future Work.	209

Bibliography	212
Appendix A Data Integrity	218
A.1 Repeatability of the Data	218
A.2 Evaluation of Particle Lag	220
A.3 LFA Passage-to-Passage Flow Field Variations	225
A.4 Comparison of LFA and Aerodynamic Probe Measurements	230
A.5 Geometry Considerations	239

List of Figures

Figure 1	Estimation of Blockage Related Losses.	14
Figure 2	Impact of Blockage on Compressor Pressure Rise.	16
Figure 3	Facility Schematic.	22
Figure 4	Photographs of Rotor Wheel Geometry.	23
Figure 5	Aerodynamic Probe Geometry.	27
Figure 6	Aerodynamic Probe Survey Locations.	28
Figure 7	In-Situ Photograph of Laser Anemometer System.	31
Figure 8	Schematic of Optical Components Layout in the Laser Anemometer System.	34
Figure 9	Photograph of Laser Anemometer System and its Traversing Mechanism.	36
Figure 10	SEM Photograph of Seed Particles.	39
Figure 11	LFA and Aerodynamic Probe Survey Locations.	44
Figure 12	Overall Performance Characteristics.	58
Figure 13	Radial distributions of the overall performance characteristics at a) 100% speed, b) 80% speed, and c) 60% speed for the rotor operating along a throttle line.	62
Figure 14	Overall performance characteristics at 100% design speed indicating repeatability of rotor performance over the entire test period.	66
Figure 15	Radial distributions of the overall performance characteristics at 100% design speed indicating sensitivity of performance with downstream throttle resistance.	68
Figure 16	CFD blind testcase results: Overall Performance Characteristics.	73
Figure 17	CFD blind testcase results: Radial distributions of total pressure and total temperature ratio.	75
Figure 18	Contours of relative Mach number in a cross-channel plane, a) upstream (-5% chord at station #1a) and b) downstream (station #3) of the rotor operating at design speed and low flow condition.	81

Figure 19	Contours of Absolute Flow Angle in a cross-channel plane, a) downstream (station #3) and b) downstream (station #4a) of the rotor operating at design speed and low flow condition. .	83
Figure 20	Contours of relative Mach number along the 70% streamsurface for the rotor operating at design speed and low flow condition.	85
Figure 21	Zoom of Figure 20 depicting blade leading edge and shock boundary layer interaction region.	87
Figure 22	Axisymmetric average and mid-pitchline relative Mach number and absolute flow angle distributions along the 70% streamsurface for the rotor operating at design speed and low flow condition.	90
Figure 23	Contours of the relative Mach number in a blade-to-blade view along the 70% streamsurface for design speed and the a) max flow condition, b) high flow condition, and c) low flow condition.	98
Figure 24	Pitchwise line plots of the relative Mach number at the 70% streamsurface for design speed and max flow, high flow, and low flow condition at 20% chord, 40% chord, 65% chord, 90% chord, and 104% chord.	101
Figure 25	Distributions of the relative Mach number near the blade surfaces along the 70% streamsurface for design speed and the a) max flow condition, b) high flow condition, and c) low flow condition.	107
Figure 26	Distributions of the isentropic static pressure coefficient along the 70% streamsurface for design speed and the a) max flow condition, b) high flow condition, and c) low flow condition.	108
Figure 27	Contours of the relative Mach number in a blade-to-blade view along the 70% streamsurface for design speed and the high flow condition — a) based on the CFD solution and b) based on the experimental measurements.	112

Figure 28	Comparison of the relative Mach number along the Midpitch line at 70% streamsurface for design speed and the high flow condition — a) based on the CFD solution and b) based on the experimental measurements.	113
Figure 29	Contours of the relative Mach number in a blade-to-blade view along the 95% streamsurface for design speed and the a) max flow condition, b) high flow condition, and c) low flow condition where - — — — indicates trajectory of tip leakage vortex. .	117
Figure 30	Relative Mach number distributions in the 95% streamsurface plotted along a line corresponding to the vortex trajectory at design speed and a) high flow condition, and b) low flow condition.	119
Figure 31	Pitchwise line plots of the relative Mach number at the 95% streamsurface for design speed and max flow, high flow, and low flow condition at 20% chord, 40% chord, 65% chord, 90% chord, and 104% chord.	121
Figure 32	CFD relative Mach number distributions on the a) 95% span and b) 98% span streamsurface for the rotor operating at 100% speed and high flow.	127
Figure 33	Relative Mach number distributions on the 70% span streamsurface for the rotor operating at 80% speed and near peak efficiency.	130
Figure 34	Pitchwise plots of relative Mach number distributions on the 70% span streamsurface at 20%, 40%, 65%, 90% and 104% chord for the rotor operating at 80% speed and 100% speed at high flow condition.	131
Figure 35	Blade surface relative Mach number distribution and static pressure coefficient on the 70% span streamsurface for the rotor operating at 80% speed and near peak efficiency. . .	134
Figure 36	Relative Mach number distributions on the 90% span streamsurface for the rotor operating at 80% & 60% speed near peak efficiency.	136

Figure 37	Pitchwise plots of relative Mach number distributions on the 90% span streamsurface at 20%, 40%, 65%, 90% and 104% chord for the rotor operating at 80% & 60% speed near peak efficiency.	140
Figure 38	Relative Mach number distributions on the 95% span streamsurface for the rotor operating at 80% & 60% speed near peak efficiency where - — — indicates trajectory of vortex.	142
Figure 39	Pitchwise plots of relative Mach number distributions on the 95% span streamsurface at 20%, 40%, 65%, 90% and 104% chord for the rotor operating at 60% & 80% speed near peak efficiency. (- — — indicates overlay of data at 90% span.)	145
Figure 40	Procedure to calculate blockage downstream of the blade row.	155
Figure 41	Impact of density on blockage calculation using CFD results.	160
Figure 42	Example indicating that data is not acquired near the blade surfaces.	162
Figure 43	Blockage calculation inside the blade row.	164
Figure 44	Sample calculation showing estimation of boundary layer parameters.	166
Figure 45	Development of the boundary layer thickness parameters, δ , δ^* , and θ for the low flow, design speed condition.	167
Figure 46	Wake profiles versus chord at 70% span for a) high flow and b) low flow operating condition at 100% speed.	169
Figure 47	Wake decay versus percent of rotor chord at 70% span for high flow and low flow operating condition at 100% speed.	170
Figure 48	Wake momentum thickness versus chord at 70% span for high flow operating condition at 100% speed.	171
Figure 49	Radial distribution of blockage at 115% and 130% rotor chord for the 100% speed high flow operating condition.	172
Figure 50	Radial distribution of Blockage at 60%, 80%, and 100% speed.	173

Figure 51	Radial distribution of Blockage at 130% chord and 100% speed for the low flow and high flow conditions.	176
Figure 52	Radial distribution of Blockage at 130% chord and 100% speed for the high flow conditions — Comparison between CFD and Data.	177
Figure 53	Khalid's correlation of loading versus endwall blockage. .	180
Figure 54	Comparison of NASA rotor 37 data to Khalid's correlation of loading versus endwall blockage.	181
Figure 55	Blockage Development inside the blade passage at 70% span for max flow, high flow, and low flow conditions at design speed.	185
Figure 56	Seddon's model depicting the boundary layer separation due to a normal two-dimensional shock wave.	186
Figure 57	Deviation from blade surface angles on the 70% span streamsurface at max flow, high flow and low flow conditions at design speed.	189
Figure 58	CFD results depicting the edge of the boundary layer on the 70% span streamsurface based on the entropy contour for the high flow design speed condition.	190
Figure 59	Deviation from blade surface angles on the 70% span streamsurface at 85% speed and 80% speed.	192
Figure 60	Distribution of Losses in the core flow region.	199
Figure 61	Comparison of measured wake profile loss at 70% span with Lieblein's correlation of loading parameter versus loss parameter.	201
Figure 62	Repeatability of Aerodynamic Probe Data.	219
Figure 63	Particle lag evaluated in the streamwise direction (along line A-A at 70% span and 90% pitch from blade suction surface) across a nearly normal shock at design speed high flow condition.	222
Figure 64	Particle lag evaluated in the pitchwise direction across a nearly normal shock.	224

Figure 65	Pitchwise distribution of relative Mach number for each of the 36 blade passages at 20%chord, 70% span for the rotor operating at design speed and high flow conditions.	226
Figure 66	Pitchwise distribution of relative Mach number comparing the ensemble average of the nearly identical 21 passages to the ensemble average of all 36 blade passages at 20% chord, 70% span for the rotor operating at design speed and high flow conditions.	229
Figure 67	Pitchwise distribution of relative Mach number for all 36 passages at station #3, 70% span for the rotor operating at design speed and high flow conditions.	230
Figure 68	A comparison of the probe measured flow angle at station #4 to the LFA measured flow angle at station #4a for the rotor operating at design speed and low flow conditions.	233
Figure 69	A comparison of the probe measured total temperature at station #4 to the LFA inferred total temperature at station #4a for the rotor operating at design speed and low flow conditions.	234
Figure 70	A comparison of the probe inferred absolute velocity at station #4 to the LFA inferred absolute velocity at station #4a for the rotor operating at design speed and low flow conditions. . .	236
Figure 71	A comparison of the CFD absolute velocity at station #1 to the LFA inferred absolute velocity at station #1 for the rotor operating at design speed and high flow conditions.	237
Figure 72	Design blade sections and location of inspection plane. . .	240
Figure 73	Comparison between the manufacturing coordinates and the inspected blade section near 70% span.	242
Figure 74	Comparison between the designed blade surface angles and the inspected blade surface angles for the blade section near 70% span.	243
Figure 75	Comparison of the tip geometry measured with the LFA to that predicted by NASTRAN at design speed and to the 'cold' geometry at base speed.	246

List of Tables

Table 1	Rotor 37 Design Parameters.	25
Table 2	Inlet Mach Numbers versus Rotor Wheel Speed	48
Table 3	Summary of LFA Streamsurface Survey Data	49
Table 4	Sampling of CFD Code Attributes.	71
Table 5	Desired CFD accuracy according to blade designers in industry.	72
Table 6	Summary of Integrated Blockage Results Downstream of the Rotor	183
Table 7	Estimation of Losses	195

Symbols and Notation

A	area, m ²
a	speed of sound, m/s
B	blockage, $1 - \frac{\text{effective flow area}}{\text{geometric flow area}}$
C _p	static pressure coefficient
c _p	specific heat at constant pressure, 1004 J/kg K
DF	diffusion factor
i _{inc}	mean incidence angle, angle between inlet air direction and line tangent to blade mean camber line at the leading edge, deg
H	boundary layer shape factor, $\frac{\delta^*}{\theta}$
h	enthalpy, J/kg
M	Mach number
N	rotation speed of rotor, rpm
NB	number of rotor blades, 36
P	total pressure, N/m ²
P _{ref}	reference pressure, 101325 N/m ²
p	static pressure, N/m ²
Q	heat energy added to the flow, J/kg
Re _c	Reynolds number based on chord
R _θ	Reynolds number based on momentum thickness

r	radius, cm
s	blade pitch, cm
T	total temperature, K
T_{ref}	reference temperature, 288.2 K
T_s	static temperature, K
U	wheel speed, m/s
u	local velocity, m/s
V	air velocity, m/s
W	mass flow, kg/s
W_{θ}	relative tangential velocity, m/s
y	distance normal from a surface, cm
z	axial distance referenced from rotor-blade-hub leading edge, cm
β	air flow angle (angle between air velocity and axial direction), deg
γ	ratio of specific heats
δ	boundary layer thickness, cm
δ^*	boundary layer displacement thickness, cm
η	adiabatic efficiency
θ	boundary layer momentum thickness, cm
κ	blade surface angle measured from axial direction, deg
ρ	density, kg/m ³

σ	solidity, chord/blade pitch
τ	shear stress or rotor tip clearance height
ω	loss coefficient

subscripts

abs	absolute or laboratory frame of reference
an	annulus
le	rotor leading edge
n	normal to the flow direction
ps	pressure surface
r	radial direction
rel	relative to the rotor frame of reference
s	streamwise direction
ss	suction surface
t	tangential to the flow direction
te	rotor trailing edge
z	axial direction
θ	tangential or circumferential direction
01	total conditions at inlet
02	total conditions at exit
1	inlet aerodynamic probe survey station

4 exit aerodynamic probe survey station

4a exit laser anemometer survey station

superscripts

* conditions at sonic conditions

— mass averaged

' relative to the rotor reference frame

1 Introduction

Aerodynamic blockage refers to an effective reduction in flow area, which affects the work output and the mass flow capacity in axial compressors. Sources of blockage in an axial compressor include the blockage generated by tip clearance flows, blade boundary layers, endwall boundary layers, secondary flows, mixing processes, and separations. The significance of understanding the development of and the level of the blockage in both compressor design and performance prediction is best depicted by the following quotes taken from Cumpsty [1]: “Small changes in the flow area have a very large effect on the stage performance both because it affects the mass flow at choke and because it affects the amount of work done by the rotor. The blockage needs to be accurately specified if the stage performance is to be correctly predicted. Unfortunately, there is no generally accurate method for predicting blockage and errors in its estimation are probably the greatest single cause of inaccuracy in predicting multistage performance.” Cumpsty also discusses the importance of blockage in the design of multistage machines: “.. relatively small errors in the estimate of blockage can have large effects on the matching of stages... The blockage is perhaps the most critical quantity in high speed compressor design, but as will be shown, its creation is not well understood nor its magnitude accurately predictable.”

In turbomachinery blade design codes [2] the evaluation of blockage is primarily based on the displacement thickness of the endwall boundary layers measured at the inlet and exit of the blade row. However, some design codes [3] do provide an input for the blockage distribution within the blade passage and this distribution of blockage is either estimated from experience and/or empirical correlations or it is neglected. For example, in multistage machines the rule of thumb for blockage development [1] is to add a blockage of 0.5% per blade row until the blockage reaches a value of 4% after which it is assumed to remain constant.

A methodology to quantify the blockage generated within the blade row by the tip clearance flow was made by Khalid [4]. His results were based on three-dimensional Navier Stokes computations of the flowfields in a low speed stator, low speed rotor, and a transonic fan with several values of tip clearance height. His results indicated that the loss in total pressure in the endwall region resulted from the interaction of the leakage flow and passage flows and that the vortical structure associated with the clearance vortex was not a major factor in generating the endwall blockage. Khalid developed a correlation between the endwall blockage and the aerodynamic loading on the blade which indicated there is a limiting value of the loading.

It is clear that there is a relationship between the blockage in a turbomachine and the losses, pressure rise, and flow range of that turbomachine [5, 6]. For example, Smith [7] correlated the casing boundary layer displacement thickness (normalized by the blade spacing) to the static pressure rise (normalized by the maximum pressure rise) and efficiency from a number of low speed multistage compressor tests. Furthermore, Smith demonstrated that for low speed axial compressors the endwall boundary layer thickness was directly related to 1) the blade-to-blade passage width, 2) the aerodynamic loading level, and 3) the tip clearance. Smith never used the term blockage, but his work clearly demonstrates the direct relationship of the blockage to the pressure rise and losses in the endwall region of low speed compressors.

McNally [8] has classified the losses in turbomachines as follows:

1. Viscous Friction Loss — due to the presence of boundary layers on the blade surfaces and the endwalls.
2. Trailing Edge Loss— due to formation of the rotor wake as the blade boundary layers from the pressure and suction surface meet at the trailing edge of the blade.
3. Mixing Loss — losses due to the dissipation of the wake in momentum exchange between low velocity wake fluid and the higher velocity freestream.

4. Shock Loss — due to the passage of flow through normal or oblique shocks located upstream and within the rotor passage.
5. Secondary Flow Loss — due to flows in a direction other than the throughflow direction.
6. Tip Clearance Loss — due to flow between blade tips and adjacent endwalls.
7. Disc Friction Loss — due to rotation of the rotor wheel within its housing.
8. Mechanical Loss — due to friction in the bearings and seals.

Howell [9] has subdivided the losses which occur in a subsonic axial compressor into the endwall loss, secondary flow loss, and profile loss. His results indicate that at design conditions 39% of the losses are attributed to profile loss, 41% to the secondary flow loss, and 20% of the losses result from the endwalls. The secondary flow losses actually included all other losses which were not attributed to the endwalls or the blade boundary layers. Howell's analysis was limited to low speed compressors where there were no shock losses. In more recent analysis which included shock losses, Jennions [10] showed a breakdown of the losses based on the generation of entropy from a numerical simulation of the flowfield of a transonic compressor rotor. His results indicated that the blade profile loss was 35% of the loss, the shock loss was 30% of the loss, the endwall losses were about 15% of the loss, and he did not specify the source of the remaining 20% of the loss. Denton [11] wrote an excellent summary paper

on the origins and effects of loss in turbomachines. He defines the loss in terms of entropy production and relates the entropy increase to the conventional loss coefficients. Denton's breakdown of the losses are similar to those of Howell and Jennions. For axial compressors he discusses the blade boundary layer loss and trailing edge loss, the tip leakage loss, the endwall loss, and the shock losses.

Based on the breakdown of loss regions described above, a discussion of the previous research which influenced the present investigation is divided into the following areas: 1) blade boundary layers and wake mixing, 2) shock / boundary layer interaction studies, 3) shock structure, and 4) the endwall region.

Blade Boundary Layers and Wake Mixing. Lieblein and Roudebush [12] correlated the profile loss in terms of the wake momentum thickness and form factor (ratio of wake displacement thickness to momentum thickness) from cascade data. Their correlation, which is suited for two-dimensional, incompressible flow and attached boundary layers, showed how the mixing loss varied with distance downstream of the blade trailing edge. For example, if the wake measurements were made at 10% chord downstream of the blade the additional loss due to mixing the wake to uniform flow would be 10% of the measured loss and at a distance of 20% chord downstream of the blade trailing edge the additional loss due to mixing would be about 5% of the measured loss. These results indicated that the total loss could be evaluated from measurements made 30% chord downstream

of the blade trailing edge and provided a means to estimate the total loss from measurements acquired closer to the trailing edge. Based on this correlation, Lieblein [13] derived an equation for the profile loss which was merely a function of the wake momentum thickness, blade chord, solidity and inlet and exit flow angles. This equation became the standard for incompressible wake loss. Stewart [14] extended the research of Lieblein [13] and Lieblein and Roudebush [12] to include the effects of compressibility on the loss characteristics downstream of two-dimensional blade sections. Lieblein et al. [15] developed a loading parameter which was based on the diffusion of the flow on the blade suction surface and was termed the diffusion factor. Lieblein correlated the wake momentum thickness and losses with diffusion factor and evaluated a blade-limiting diffusion factor above which the blade suction surface boundary layer would separate. These results were based on data from NACA 65-series compressor blade sections in a low-speed two dimensional cascade. These correlations of the diffusion factor with loss served as the basis for loss estimates used in turbomachinery design codes such as that developed by Crouse [2].

Lieblein's [15] notion of a limiting value for the diffusion capability on a two-dimensional blade section was extended to axial compressor stages by Koch [5] who related the blade geometry, blade chord Reynolds number, tip clearance, and axial spacing between the blade rows of a compressor stage to a stalling static

pressure rise coefficient. Koch's correlations for maximum static pressure rise coefficient and the development of the correlation parameters were consistent with the maximum pressure rise capability of two-dimensional diffusers. Similarly, Koch and Smith [6] extended Lieblein's and Roudebush's [12] analysis for blade profile loss to higher Reynolds number and Mach number ranges typical of core compressors. Based on compressible turbulent boundary layer theory Koch and Smith related the profile loss to the suction surface diffusion ratio, the streamtube contraction, the Reynolds number, and the Mach number. Their results indicate that as the Mach number is increased at constant Reynolds number and diffusion ratio the total pressure loss coefficient increases significantly. Their model was based on years of testing various blade geometries in a low speed compressor facility and has proven to be very effective for core compressor design. Unfortunately these models are suspect for transonic flows where the shock dramatically affects the blade loading distribution and may induce a boundary layer separation.

Denton [11] illustrated that the entropy production in the boundary layer is proportional to $\left(\frac{V}{V_{inlet}}\right)^3$, and since the velocities are much higher on the blade suction surface than the pressure surface, it is clear that the suction surface boundary layer dominates the blade boundary layer loss. Denton also indicates the entropy production at the trailing edge (due to the mixing of the blade suction and pressure surface boundary layers) is approximately 15% of the entropy production

in the blade surface boundary layers for attached boundary layers, but for separated boundary layers the trailing edge loss increases dramatically and the entropy production can exceed that in the blade surface boundary layers.

Shock / Boundary Layer Interaction Studies. Most of our understanding of the interaction between a shock and boundary layer is based on experiments and analysis performed in wind tunnels or cascades. The wind tunnel data provides insight into our understanding of the flow physics of the shock wave / boundary layer interaction. Many of the flow characteristics of the shock / boundary layer interaction observed in the wind tunnel tests are also prevalent in transonic compressor cascade studies. The following studies were used in this investigation to understand the shock / boundary layer interaction in a high speed compressor.

Nussdorfer [16], Atkin and Squire [17], Alber [18], Chriss [19], and others have studied the interaction between a normal shock and a turbulent boundary layer, while Seddon [20] developed a model for this type of interaction. These investigations supported Seddon's model and have shown that there is a critical pressure rise above which the boundary layer will separate and this pressure rise occurs across a normal shock when the Mach number exceeds 1.3 to 1.4. Nussdorfer [16] defined a static pressure ratio of 1.89 as the critical pressure rise (which corresponds to the static pressure rise across a normal shock of Mach

number equal to 1.33). Alber [18] observed that a deflection of the external flow by 6.6° is also a good indicator that the shock has separated the boundary layer.

Schreiber [21], and Schultz, Bolcs, and Dalbert [22] studied shock-wave turbulent boundary layer interactions in a transonic compressor cascade with inlet Mach numbers ranging from 1.3 to 1.59. For Mach numbers from 1.32 to 1.44 there were local separations and reattachments but beyond a Mach number of 1.45 there was complete boundary layer separation. Their results indicate that the details of the flowfield within the shock boundary layer interaction region are consistent with the classical model of Seddon [20]. In addition, their conclusions are consistent with those of Griepentrog [23] who concludes from the data of Ackeret et al. [24], Liepmann [25], and Percy [26], that the interaction region is mainly affected by 1) the displacement thickness of the boundary layer upstream of the shock, 2) the shock strength, and 3) the pressure gradient downstream of the shock.

Bell and Fottner [27] studied the shock-wave / boundary layer interaction and shock induced transition on laminar / transitional boundary layers on a highly loaded compressor cascade (NACA 65 series). Their results were: 1) the profile loss increased significantly with increasing Mach number which was attributed to the shock/boundary layer interaction, 2) at lower Reynolds numbers the shock induced boundary layer transition occurs above a separated flow region, and 3) at higher Reynolds numbers the shock induced boundary layer transition occurs

without separation. Bell concludes that the separation at the lower Reynolds number is attributed to the increased boundary layer thickness relative to the higher Reynolds number flow. For a laminar boundary layer nearing transition Bell observed shock induced separation for a case where the maximum suction surface Mach number was 1.15.

Shock Structure. The total pressure loss across a normal shock varies as $(M - 1)^3$ where M is the Mach number [1]. Miller, Lewis, and Hartmann [28] developed a model to estimate the shock loss in compressor blading by assuming the loss in total pressure was equivalent to the loss across a normal shock with a Mach number equivalent to the average of the inlet Mach number and the Mach number at the suction surface shock impingement point. Freeman & Cumpsty [29] developed a simple one dimensional model, based on conservation of stagnation enthalpy, mass flow and momentum in the inlet region, to predict the loss in the inlet region of supersonic compressor airfoils and validated it with measurements. Freeman and Cumpsty claim their model predicts the loss as well as the classical Miller-Lewis-Hartmann shock loss model [28] at design conditions and that it does a better job of predicting the shock loss at off-design conditions. Neither of these models consider the three-dimensional aspects of the rotor shock structure. Strazisar [30] investigated the unsteadiness and three dimensionality of the shock structure in a transonic fan using detailed laser anemometer measurements. He

concluded that for the fan he studied the shock oscillates about its mean location with an amplitude of 3–4 percent of rotor chord and the shock surface was nearly two-dimensional with loading levels above peak efficiency but becomes more complex at lower loading levels. Wood et al. [31] further investigated the measurements of Strazisar. They evaluated the shock loss in a transonic fan where the shock loss was evaluated on a point-by-point basis across the passage using the measured inlet Mach number and the geometry of the shock surface. The shock loss was evaluated using the typical two-dimensional shock geometry (i.e. in the blade-to-blade plane) and was compared to the shock loss which accounted for the three dimensionality (spanwise lean) of the shock surface. Wood evaluated the efficiency of the shock as a compression system by calculating the isentropic efficiency from the total pressure ratio and temperature ratio across the shock in the absolute frame of reference. The calculations accounting for the three-dimensional geometry of the shock surface indicated a reduction of the work done by the rotor and a reduction in the shock loss which resulted in an increase in the efficiency of 2 percentage points relative to the calculation considering only the two-dimensional shock structure. The analysis of Wood et. al. indicated that the three-dimensionality of the shock structure must be taken into account in the design of axial compressor blade rows where there is a considerable twist in the stacking of the blade sections from hub to tip.

Endwall Region. Wisler [32] reports that an increase in tip clearance from 1.4% to 2.8% of blade height in a low speed multistage compressor resulted in a 1.5 point efficiency penalty, an 11% reduction in flow range, and a 10% reduction in peak pressure rise. The accumulation of low momentum fluid near the blade tip and the vortical structure of the flow downstream of low speed compressors has been documented by the experimental measurements of Inoue et al. [33], Inoue and Kuroumari [34], McDougall [35], Stauter [36], and others. Inoue and Kuroumari [34] have also provided data concerning the endwall flow field within the compressor blade passage in a low speed compressor using hot wire measurements obtained in the tip clearance region. Although these investigations have shed light on the endwall flow in low speed machines, there is much less information concerning the endwall flow fields within the blade passage in high speed compressors. Measurements reported have been primarily limited to high-response static pressure data over the rotor tip, for example those of Copenhaver et al. [37].

Our understanding of the endwall flow has been enhanced by models of the tip clearance flow developed from detailed measurements in the endwall region of low speed compressors. For example, Storer and Cumpsty [38] have shown that the losses due to the tip leakage flow are primarily associated with the mixing process that takes place between the leakage flow and the throughflow, and that these

losses can be predicted from the angle formed between the clearance flow and the throughflow. In addition, Chen et al. [39] developed a model to describe the trajectory of the leakage vortex. These modelling efforts have yielded reasonable agreement with data available from low speed compressors.

Due to the limited availability of detailed measurements, our understanding of the endwall flow in high speed compressors has also been advanced through numerical simulations. In high speed compressors the endwall flow is further complicated by the interaction between the rotor passage shock and the tip leakage flow. Adamczyk et al. [40] and Copenhaver et al. [37] have used 3D Navier-Stokes solvers to study this shock / vortex interaction. Adamczyk studied the effect of variations in tip clearance on the performance of a transonic rotor, and showed that the shock / vortex interaction plays a major role in determining the compressor flow range. Although such efforts have improved our understanding of the endwall flow over the last 5-10 years, we continue to have difficulty in accurately predicting the blockage in the endwall region, especially in multistage compressors.

It is clear that there is a need for detailed experimental data within high speed compressors to assess numerical simulations and models and to enhance our understanding of the interaction between the shock and tip leakage flow and between the shock and blade boundary layers.

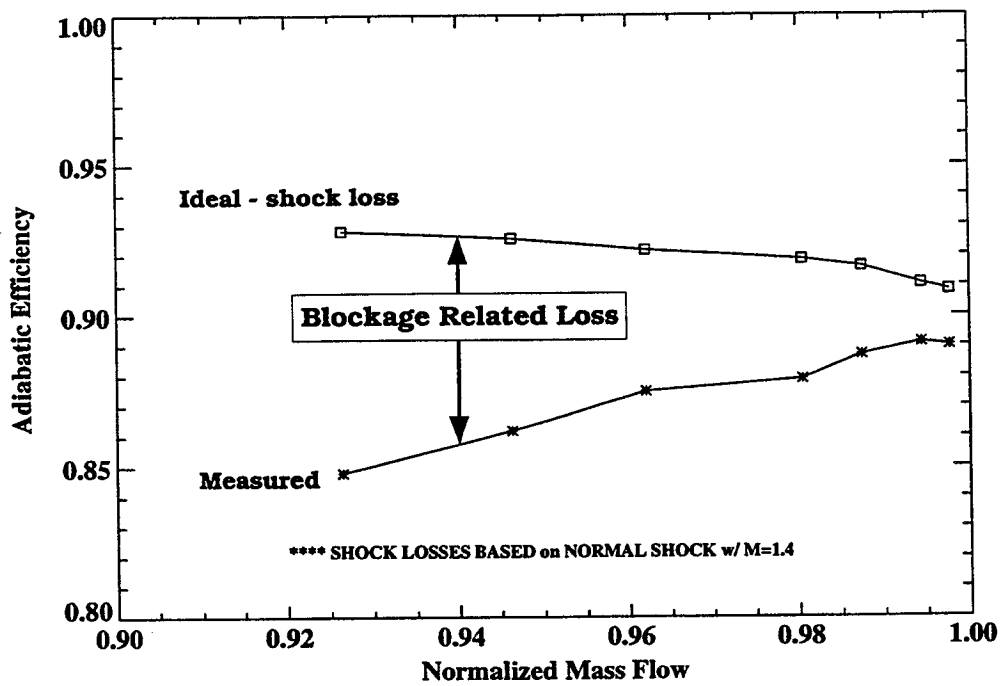
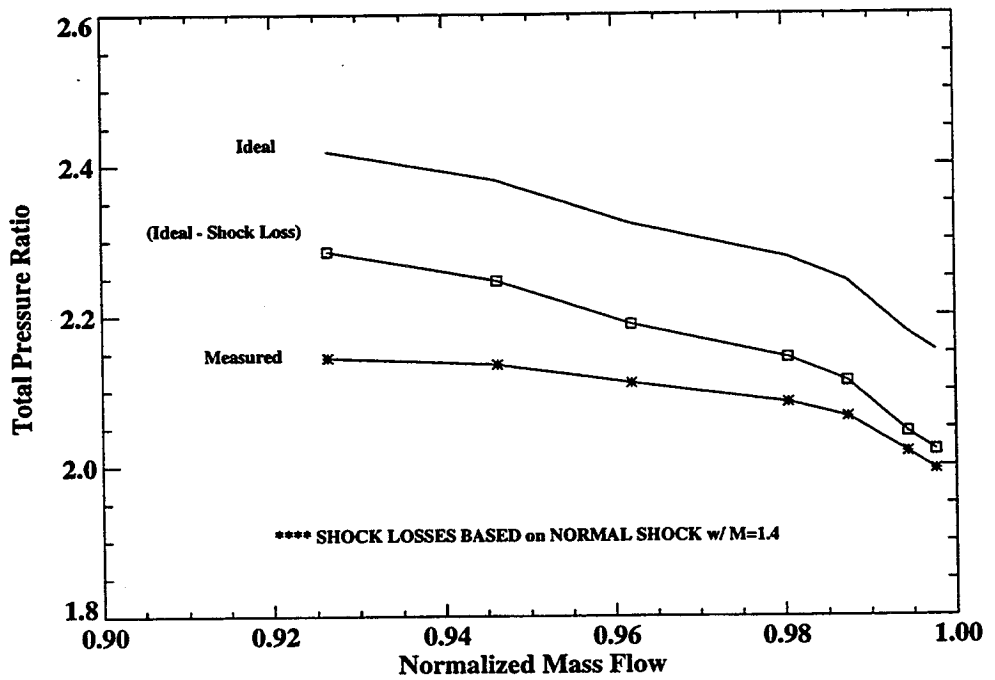


Figure 1 Estimation of Blockage Related Losses.

To illustrate the contribution of the shock losses to all remaining losses which are commonly lumped together as the 'profile losses' in the compressor used in this investigation, the measured and ideal pressure rise and adiabatic efficiency characteristics for this test compressor operating at design speed are plotted in Figure 1, where the mass flow has been normalized by the choking mass flow. The profile losses include the losses due to blade boundary layers, blade wakes, secondary flows, and tip clearance flows. Since all of these flow phenomena are indicative of a blockage to the flow, they will also be referred to as the blockage related losses. Each data point represents a different rotor operating condition resulting from increasing the rotor backpressure from the maximum flow to near stall operating condition. The ideal pressure ratio was calculated by assuming all of the work input, as determined from the measured total temperature, went into raising the pressure (adiabatic efficiency of one). In addition, the ideal pressure minus the loss in pressure due to the rotor shock is plotted as the curve with square symbols. The shock loss was calculated using a normal shock with an inlet Mach number of 1.4, which results in an overestimation of the shock loss as will be verified later in the discussion of the shock strength. The region between the curve representing the ideal pressure minus the shock loss, and the measured total pressure indicates the loss in total pressure due to tip clearance flows, secondary flows, and viscous related losses all of which are blockage related phenomena.

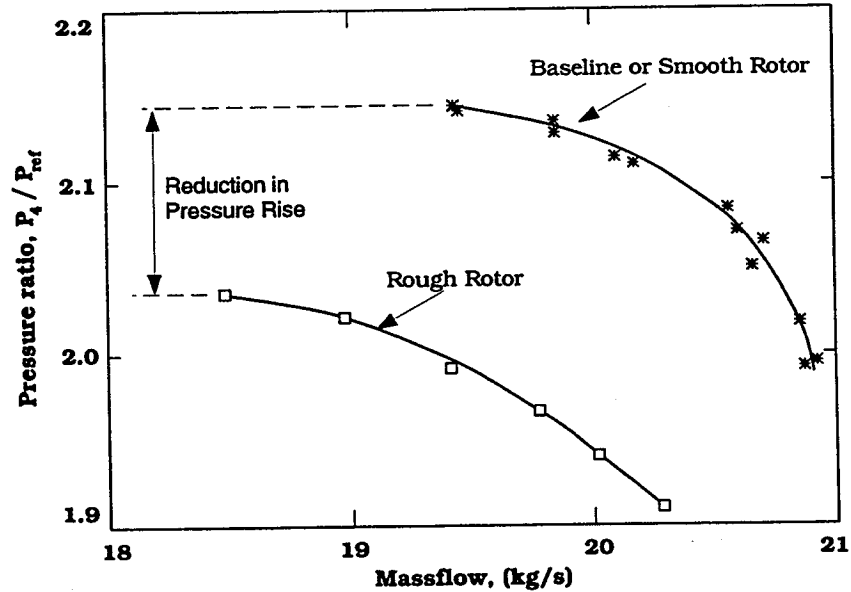


Figure 2 Impact of Blockage on Compressor Pressure Rise.

Comparing these two regions it is evident that there is much potential for gains in machine performance if we can understand the blockage development and optimize the design to minimize these blockage related losses.

To further illustrate the sensitivity of blockage to the pressure rise of the compressor rotor used in this investigation, see Figure 2 which resulted from a study of the effects of blade surface roughness on compressor performance [41]. In this figure the overall pressure rise characteristics of the rotor are presented for two cases: nominal and elevated blade surface roughness levels. (The nominal or 'baseline' case represents a hydraulically smooth surface with equivalent sand roughness Reynolds number of about 90 [6] and the 'rough' case corresponds to an equivalent sand roughness Reynolds of about 500.) This study concluded that the decreased pressure rise capability illustrated in Figure 2 for the case

of increased surface roughness resulted primarily from the increased blockage associated with the suction surface boundary layer and its interaction with the rotor shock. However, there was no attempt to quantify the blockage nor investigate the details of the shock / boundary layer interaction. These results are presented to point out 1) the performance of this rotor is sensitive to changes in blockage, and 2) blade surface roughness is an additional parameter to consider when evaluating loss and blockage. However, the present investigation of the blockage and loss development in a transonic compressor will only consider the case of a hydraulically smooth surface.

It is evident that the performance of the rotor used in this investigation is very sensitive to changes in blockage and that the blockage related losses account for a significant amount of the total loss. It is believed that this sensitivity results from the high loading levels, high Mach numbers and tight choke area margin (A/A^* of 1.03 to 1.05) associated with this rotor. The compressor blade loading levels and tip speeds of NASA rotor 37 are typical of modern axial compressor designs for the class of turbomachine for which pressure rise capability is a higher priority than the efficiency. Therefore, in order to optimize the design of compressors with high loading levels and tip speeds comparable to or in excess of the compressor rotor used in this investigation, it is paramount to understand the flow mechanisms

which lead to the development of blockage and loss and to be able to accurately predict and / or model the resulting flowfield and performance.

The intent of this work is to explain and verify with experimental evidence the flow mechanisms responsible for the development of blockage and loss in a transonic, axial compressor rotor operating at design and off-design conditions, and to assess the level and source of blockage in different regions of the compressor. Previous research in this area has either been performed using computational methods to calculate the flowfield or experimental measurements acquired downstream of the compressor—generally for low speed machines operating at design conditions. In this investigation detailed laser anemometer measurements acquired upstream, within, and downstream of a transonic, axial compressor rotor operating at design and off-design conditions are used to investigate blockage development due to:

1. blade boundary layers
2. shock / boundary layer interactions
3. wake mixing processes
4. tip clearance flows
5. shock / clearance flow interactions

At design speed where the rotor shock is present, data is presented and analysis performed to show the blockage development within and downstream of the rotor blade row. Inside the blade row the blockage is evaluated ahead of the rotor passage shock, downstream of the rotor passage shock, and near the trailing edge of the blade row. This analysis is performed in the core flow area as well as in the casing endwall region. Blockage is also evaluated for two part speed conditions for which 1) the rotor passage shock is much weaker than that at design speed and 2) there is no rotor passage shock.

The specific fluid dynamic questions to be addressed are:

1. How does the interaction between the rotor passage shock and the blade boundary layer impact blockage and loss development?
2. How does the interaction between the rotor passage shock and the tip clearance flow impact blockage and loss development?
3. What are the contributions to the blockage and loss in the endwall region relative to the coreflow region?
4. How does blockage and loss vary with blade loading?

In addition, the blockage evaluated from the experimental data will be compared to 1) an existing correlation of blockage development [4] which was based on computational results, and 2) computational results on a limited basis.

A brief description of the subsequent chapters follows. Chapter 2 discusses the research equipment used in this investigation including a description of the facility, the research compressor, and the instrumentation. Chapter 3 focuses on the data acquisition and reduction procedures, summarizes the location of the data that was acquired at each operating condition, and includes an assessment of the measurement uncertainties. The results of this investigation are provided in chapters 4 and 5. Chapter 4 elaborates on the flow mechanisms responsible for the loss and blockage development in this compressor. The loss and blockage development is discussed in the endwall region and in the core flow region at both design and off-design operating conditions. The techniques used to quantify the blockage and estimate the losses are discussed in chapter 5, after which the resulting blockage and loss estimates at design and off-design conditions are presented. Chapter 6 summarizes the significant results and includes recommendations for future research.

2 Research Equipment

2.1 Facility

The experiment was performed in the single stage transonic compressor facility at the NASA Lewis Research Center, shown in Figure 3. This is an open loop facility with atmospheric inlet and exit conditions. The compressor is driven by a 3000 hp DC drive motor in conjunction with a gearbox having a 5.55:1 gear increasing ratio, which provides a maximum shaft speed of 20000 rpm. The mass flow rate is measured by an orifice plate located far upstream of the compressor. The nozzles, which are used to inject seed material into the flow for the laser anemometer system, are located far upstream of the plenum. The plenum serves as a settling chamber for the seed to disperse throughout and adjust to the main throughflow prior to entering the test section. The size of the test section is limited to 50.8 cm (20 in.) in diameter and 91.4 cm (36 in.) in length. Downstream of the test section, the flow passes through a sleeve-type throttle valve which is used to vary the exit flow area, thereby providing a means of varying the rotor exit pressure and mass flow through the compressor. The flow dumps to a large collector and then exits the test facility. The exhaust air is then cooled and finally vented to the atmosphere. A more detailed mechanical description of the facility is

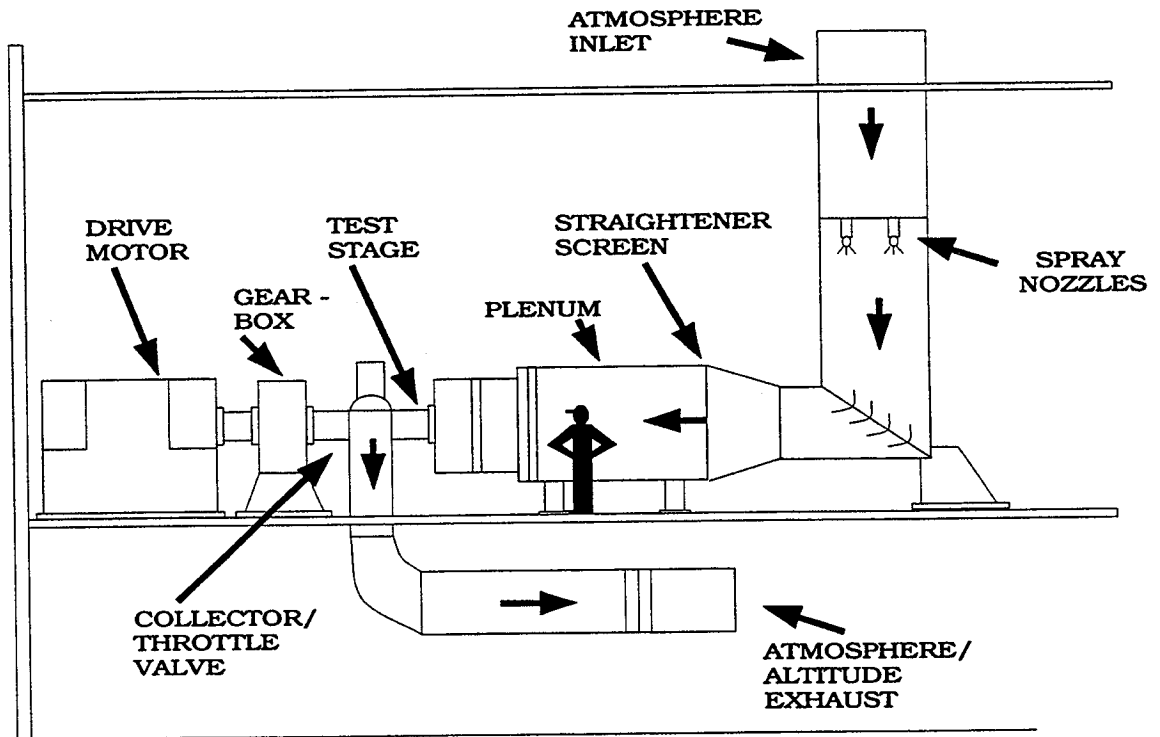
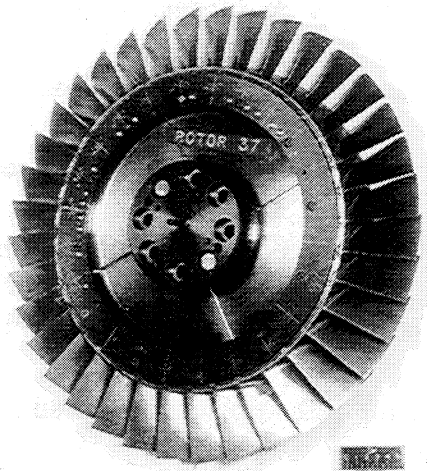


Figure 3 Facility Schematic.

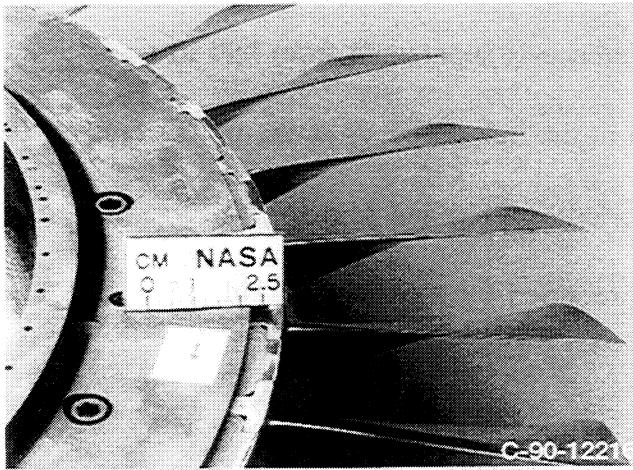
given by Urasek and Janetzke [42] and a description of the facility instrumentation and controls is provided by Bruckner et al. [43].

2.2 Research Compressor

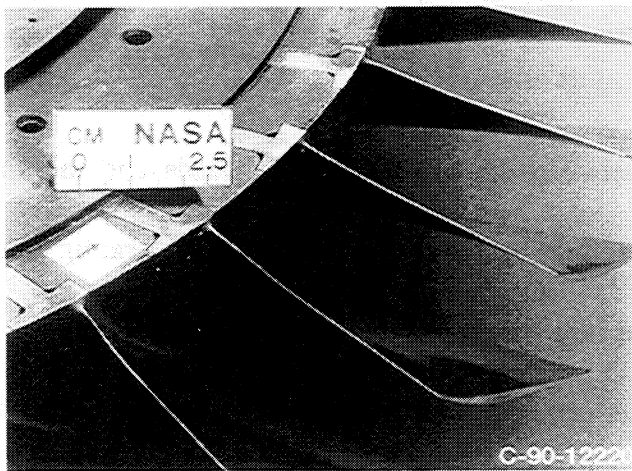
The test compressor was designed as an inlet stage for an eight-stage 20:1 pressure ratio advanced core compressor and is designated as NASA Stage 37. For this experiment the rotor was tested in isolation to avoid the interaction effects generated by the presence of an upstream inlet guide vane or downstream stator blade row. The rotor is a low aspect ratio and high solidity design employing multiple circular arc blading, and is representative of in-service flight hardware. Photographs of the rotor wheel assembly are given in Figure 4. Figure 4a shows



a) Wheel Assembly



b) Channel View
Looking Downstream



c) Channel View
Looking Upstream

Figure 4 Photographs of Rotor Wheel Geometry.

the 20" diameter wheel assembly consisting of 36 blades. Figure 4b shows a close-up view looking in the flow direction of the rotor blade leading edge, the flow channel between rotor blades, and the radial twist of the blade resulting from the radial stacking of two-dimensionally designed blade sections. Similarly Figure 4c is a close-up view, looking in the upstream direction, of the blade trailing edge, the exit-flow channel, and the profile of the rotor tip section. A summary of the design parameters are given in Table 1. At the design rotor wheel speed the inlet flow in the rotor frame of reference is supersonic from hub to tip with an inlet relative Mach number of 1.13 at the hub and 1.48 at the tip. Details of the rotor aerodynamic design were reported by Reid and Moore [44]. Overall aerodynamic performance of the stage was reported by Moore and Reid [45].

2.3 Conventional Instrumentation

2.3.1 Tip Clearance Measurements

The clearance distance between the tip of the rotor blade and the shroud plays a significant role in determining the performance and operating range of a compressor [40]. Therefore, the tip clearance height is considered part of the geometry and experimental set-up, and the results of these measurements will be presented in this section.

Table 1 Rotor 37 Design Parameters.

PARAMETER	DESIGN VALUE
Rotor Total Pressure Ratio	2.106
Rotor Total Temperature Ratio	1.270
Rotor Adiabatic Efficiency	0.877
Rotor Head Rise Coefficient	0.333
Flow Coefficient	0.453
Mass Flow, kg/s	20.188
Rotor Wheel Speed, rpm	17188.7
Rotor Tip Speed, m/s	454.14
Hub / Tip Radius Ratio	0.70
Rotor Aspect Ratio	1.19
Number of Rotor Blades	36
Blading Type	Multiple Circular Arc (MCA)

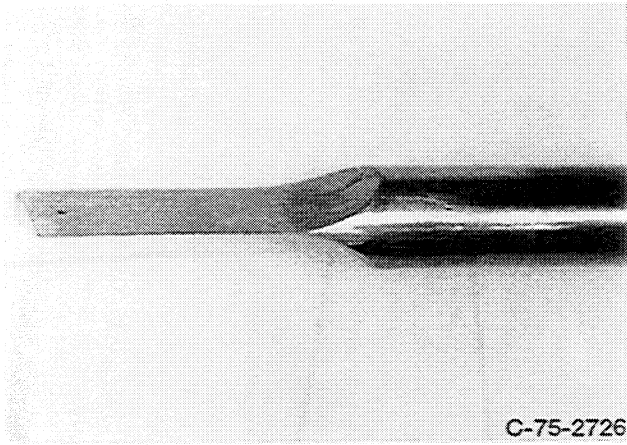
The rotor tip clearance was measured using both a Rotodata touch probe and rub probes. The uncertainty in the touch probe and rub probe clearance measurements is estimated to be 0.05 mm (0.002 in.). Touch probe measurements were obtained at 10, 50, and 90% of rotor chord at one circumferential location on the compressor casing and indicated a design speed tip clearance of 0.330 mm with a variance of 0.005 mm. The rub probes were located in three different regions around the circumference and indicated an average tip clearance of 0.320 mm with a variance of 0.120 mm. Both the touch probe and the rub probes measure the longest blade and therefore yield a conservative measure of the tip clearance. An inspection of the rotor wheel assembly at the conclusion of testing revealed that the variance in tip radius was ± 0.075 mm. Therefore, 0.075 mm

was added to the average clearance probe measurement of 0.325 mm to arrive at an estimated clearance of 0.400 mm (0.016 in.) which corresponds to 0.5% of blade span and 0.7% of rotor tip chord. Similarly at part speed conditions the average tip clearances were estimated to be 0.500 mm (0.020 in.) at 80% speed and 0.580 mm (0.023 in.) at 60% speed.

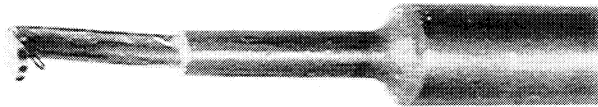
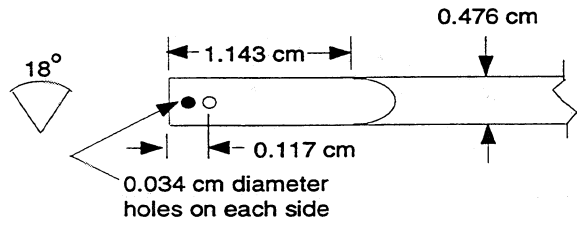
2.3.2 Aerodynamic Probe Measurements

The performance characteristics of the rotor are determined from aerodynamic probes which are surveyed radially upstream and downstream of the compressor rotor. Cobra probes are used to measure the radial distribution of the total pressure, total temperature, and flow angle upstream and downstream of the rotor. The static pressure and a redundant measure of the flow angle are measured using an 18 degree wedge probe. Photographs and dimensions of the wedge and cobra probes are shown in Figure 5. The pressures measured by the side ports on both the cobra and wedge probe are balanced in order to align the probe with the flow and thereby determine the flow angle.

These radial distributions of total and static pressure, total temperature, and flow angle are measured at stations 1 and 4 which are shown in Figure 6. Stage 37 is a close-coupled stage, and there is not sufficient space for a survey station between the rotor and stator. Since additional survey stations were not added in



a) Wedge Probe



b) Cobra Probe

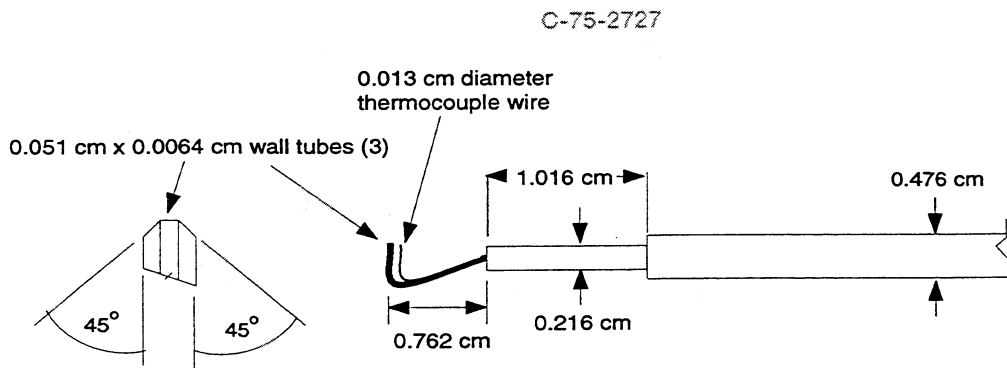


Figure 5 Aerodynamic Probe Geometry.

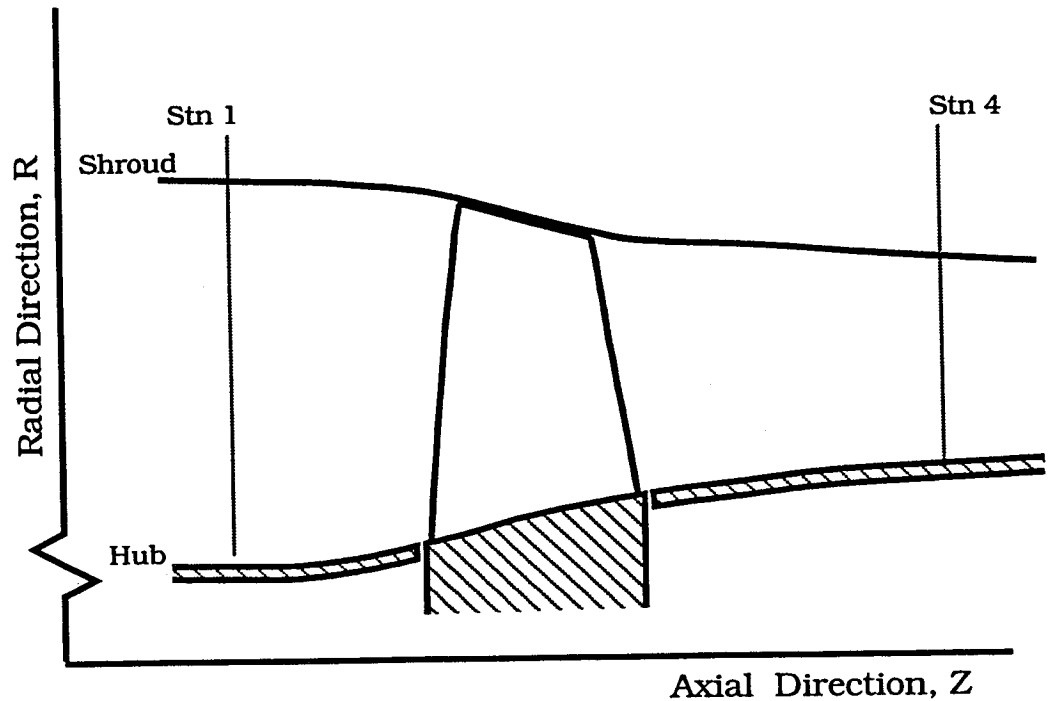


Figure 6 Aerodynamic Probe Survey Locations.

the present work, Station 4, which is normally used to survey the stator outlet flow, is the first available aerodynamic survey station downstream of the rotor.

The probe measurements are corrected for Mach number and streamline slope based on a calibration of each probe used and on the design streamline slope. All measurements are corrected to sea-level standard-day conditions at the rotor inlet. Radial distributions of total temperature are mass averaged across the annulus. Radial distributions of total pressure are energy averaged by converting them to their enthalpy equivalents and then mass averaging them across the annulus. The details of these calculations will be described in the 'Data Reduction' section of **Chapter 3: Experimental Procedure**. The measurement uncertainties are:

massflow, ± 0.3 kg/s; flow angle, ± 1.0 degrees; total pressure, ± 0.01 N/cm²; total temperature, ± 0.6 K.

2.4 Laser Anemometer System

2.4.1 Overall Characteristics

Detailed flow field measurements made upstream, within, and downstream of the transonic compressor are acquired with a two-color, fringe-type laser anemometer system employing on-axis backscatter collection optics. The two anemometer channels are configured to simultaneously acquire the tangential and axial velocity components. One of the laser beams in each of the two channels is frequency shifted to enable detection of flow reversals. The effective length of the measurement volume is reduced by using a short focal length f2 focussing lens and by using optical masks in the collection optics. The measurement volume (or probe volume) is $60 \mu\text{m}$ in diameter and has an effective length of 0.5 mm, which corresponds to less than 1% of the blade span. The uncertainties in the laser anemometer velocity and flow angle measurements are estimated as 1% and 0.5 degrees, respectively. For more details on the LFA techniques and its application to making measurements in turbomachinery see [46, 47].

Optical access to the compressor is provided by a 2.54 mm thick alumina silica window, which is contoured in both the axial and circumferential directions to conform to the rotor flowpath and preserve the proper tip clearance over the rotor.

The process used to form this window is described by Verhoff [48]. The window extends more than one rotor chord upstream and three rotor chords downstream, providing continuous access throughout the rotor flow field. Polystyrene latex particles are injected into the flow field far upstream of the test compressor to 'seed' the flow for the LFA system. In the following sections the details of the optics configuration, traversing mechanism, and seeding issues are addressed.

2.4.2 LFA System Components

Optical configuration. Due to the space limitations in the facility the traversing mechanism and optics layout were designed specifically for this application. For example, Figure 7 shows a photograph of the LFA system, sandwiched between the plenum and the collector (refer to Figure 3), with the probe volume located at a position in the rotor coordinate system to acquire data at mid-span and slightly upstream of the rotor. The LFA system components were chosen from various vendors using state-of-the-art optical components to maximize the signal-to-noise ratio of the optics system. Previous laser anemometer systems used at NASA Lewis in this research facility as reported by Strazisar, Wood, Pierzga, and Hathaway [49, 30, 31, 50, 51] used a single channel, dual beam, fringe-type anemometer and a fluorescent seeding material. The theory of operation of the previously used and current system is similar, but the application and hardware associated with

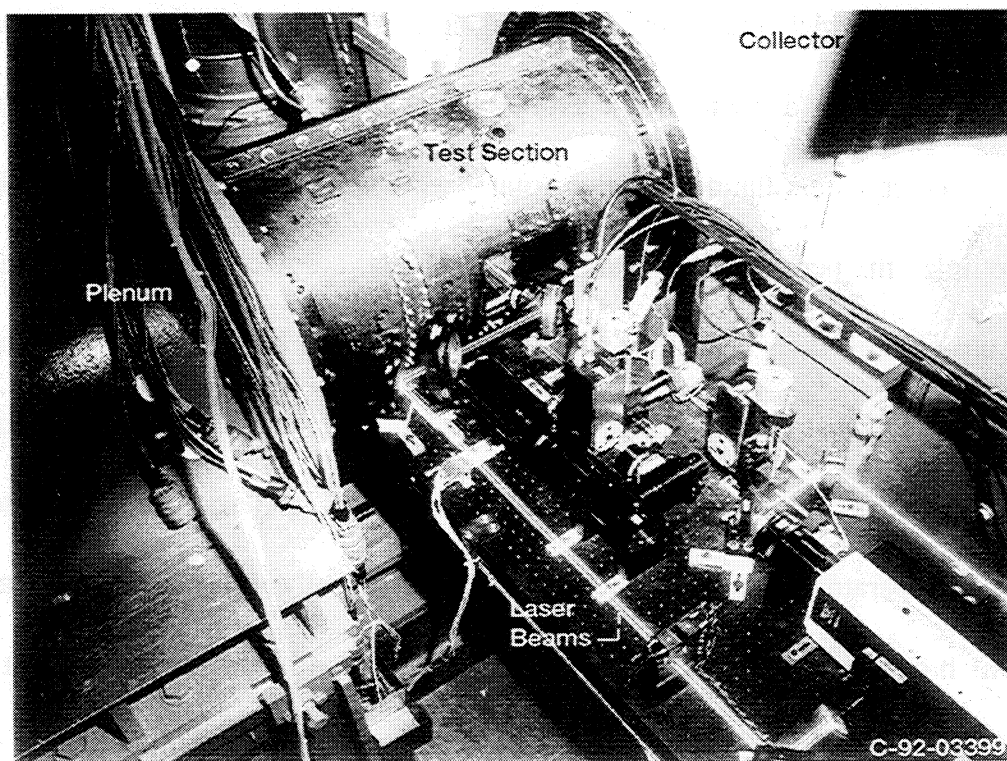


Figure 7 In-Situ Photograph of Laser Anemometer System.

each system are somewhat different. Therefore, a brief discussion of the optical configuration of this enhanced laser anemometer system is provided herein.

A schematic depicting the top view of the optical components of the laser anemometer system (shown in Figure 7) is provided in Figure 8. The optical components are screw-mounted on the optics breadboard, which is a table top consisting of a honeycomb filler sandwiched between two aluminum plates and provides a light-weight and stable surface. A single laser beam containing wavelengths within the visible spectrum exits the 6W Argon-ion laser, is turned by two mirrors which are coated for maximum reflectivity, and enters the beam

collimator, which minimizes the divergence of the laser beam and places the minimum waist diameter at the probe volume. Downstream of the collimator, the laser beam enters the polarization rotator which aligns the polarity of the beam to optimize the performance of the TSI Colorburst, a device used to split the single, multi-colored laser beam into two green beams, two blue beams, and two violet beams. Downstream of the polarization rotator are additional mirrors which are used to direct the output laser beam into the TSI Colorburst beam separator. The beam separator contains an acousto-optic cell (usually referred to as a Bragg cell) which generates two multicolor beams, one with a 40 Mhz frequency shift and the other not shifted. This frequency shift either adds to (if the direction of shift is against the flow direction) or subtracts from (if the direction of shift is with the flow direction) the measured doppler shift, thereby, allowing the presence or occurrence of flow reversals to be detected. Next the two beams pass through dispersion prisms which separate each multicolor beam into green (wavelength of 514.5 nm), blue (wavelength of 488 nm) and violet (wavelength of 476.5 nm) wavelengths. In this application only the green and blue beams (which both contain more power than the violet) are used to measure the tangential and axial velocity components in the rotor, respectively. The beam separator system was originally designed for fiber optic systems, therefore, a set of mirrors and displacement optics were used to space the beams at a separation of 22 mm to align the beams for the conventional

downstream optics used in this application. The beams then pass through a mirror assembly which flips the direction of frequency shift for the vertical beams but maintains the direction of frequency shift of the horizontal beams. (This change in the direction of frequency shift was required in order to make measurements in our rotating compressor where the velocity in the horizontal direction, corresponding to the axial flow direction, maintains a nearly constant value, but the velocity in the vertical direction, corresponding to the tangential flow direction, varies from a value of near zero at the rotor inlet to a velocity comparable to the throughflow velocity near the rotor exit.) The beams are turned by a mirror and pass through the center of a doughnut-shaped mirror which has been machined with a hole in its center just large enough to allow all four of the transmitting beams to pass through it. The final mirror turns the beams and directs them to a focussing lens which cause the four beams to converge at the focal point, thereby forming the probe measurement volume. The light scattered from the seed particles which cross the probe volume is collected by the same focussing lens and directed back along the same line as the transmitted beams to the doughnut mirror where the collected light is diverted from the path of the transmitted laser beams. Downstream of the doughnut mirror the collected light is sent through a field stop apparatus which consists of two focussing lenses and a pinhole assembly. The first focusing lens in the field stop apparatus focuses only the light originating at the probe volume

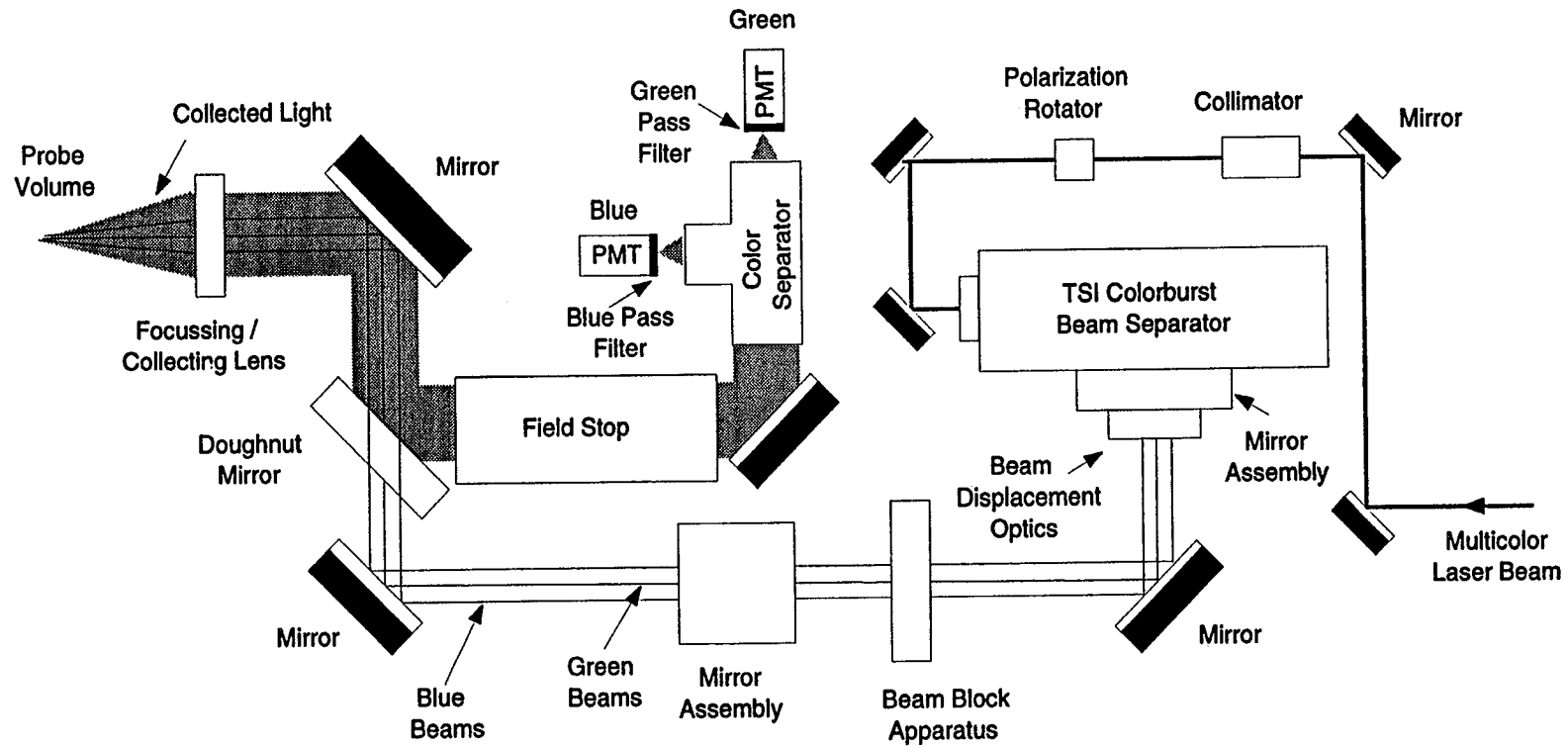


Figure 8 Schematic of Optical Components Layout in the Laser Anemometer System.

to a point. At this focal point a small disk with a pinhole of 100 μm diameter is placed so that all stray light which is not originating from the probe volume is blocked and only the light originating from the probe volume is permitted to pass through the pinhole. Downstream of the pinhole is another lens focused at the pinhole which collects the scattered light, collimates it, and directs the collected light into a commercially available set of color separation optics which separates the green scattered light from the blue scattered light. The blue separated light is then focused through a blue pass filter and second pinhole of 100 μm diameter and onto the photomultiplier tube (PMT) which converts the light energy to an electrical signal which is then sent to the counter processor and data acquisition system computer. Similarly, the green component is filtered and processed.

Traversing mechanism. The motorized positioning hardware used to move the LFA measurement volume throughout the rotor flow field is shown in Figure 9. The laser and optics breadboard are mounted to three positioning tables which provide positioning in the axial, radial, and vertical (hidden in Figure 9) directions to within an uncertainty of 0.02 mm (0.0008 in.). The focusing lens and final turning mirror (refer to Figure 8) are mounted on a goniometric cradle so that they move together as a unit. This goniometric stage provides a means for the transmitted beams to be directed into the compressor off of a radial line and also rotates the beams to various orientations. Therefore, by moving the three-axis positioning tables in

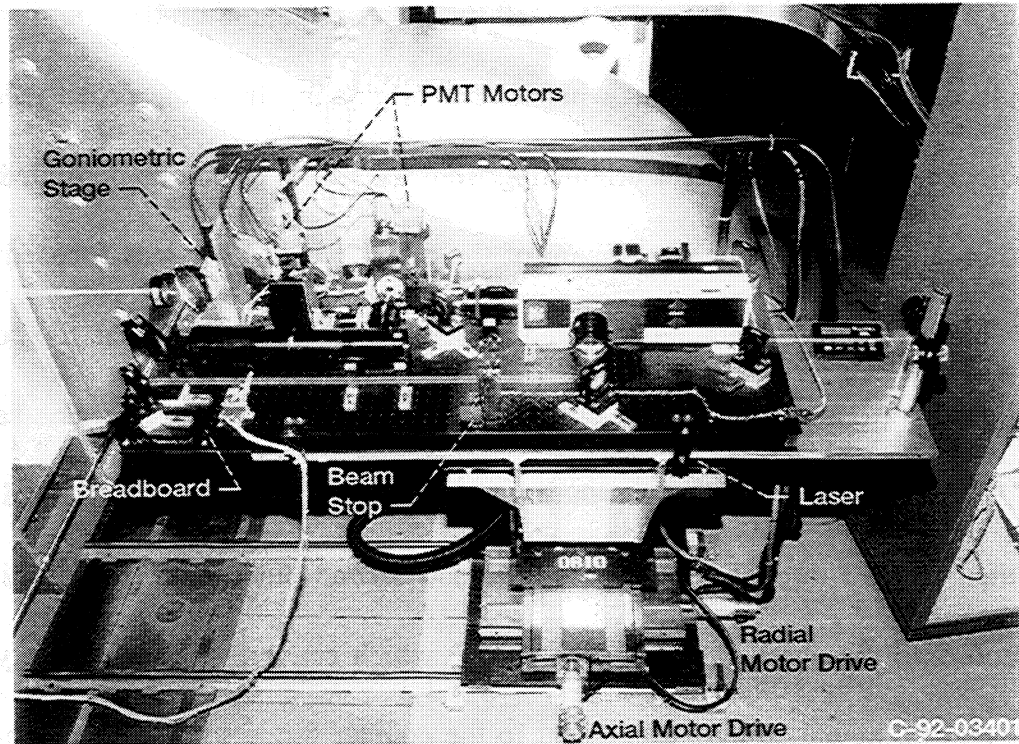


Figure 9 Photograph of Laser Anemometer System and its Traversing Mechanism.

conjunction with the goniometric cradle the laser probe volume could be moved in the axial, radial, and circumferential directions, independently. However, in this investigation the goniometric stage and vertical positioning stage were aligned so that the beams entered the compressor along a radial line, and the blue beams measured only the axial velocity and the green beams measured only the tangential velocity. The probe volume was moved in the radial and axial directions only. In order to transfer the position of the probe volume from the coordinate system of the traversing mechanism to the rotor coordinate system, the intersection of the leading edge of the rotor wheel assembly and the hub flowpath was used to

establish the axial and radial reference position within the rotor coordinate system. The uncertainty of positioning the probe volume in the rotor coordinate system is within 0.12 mm (0.005 in.).

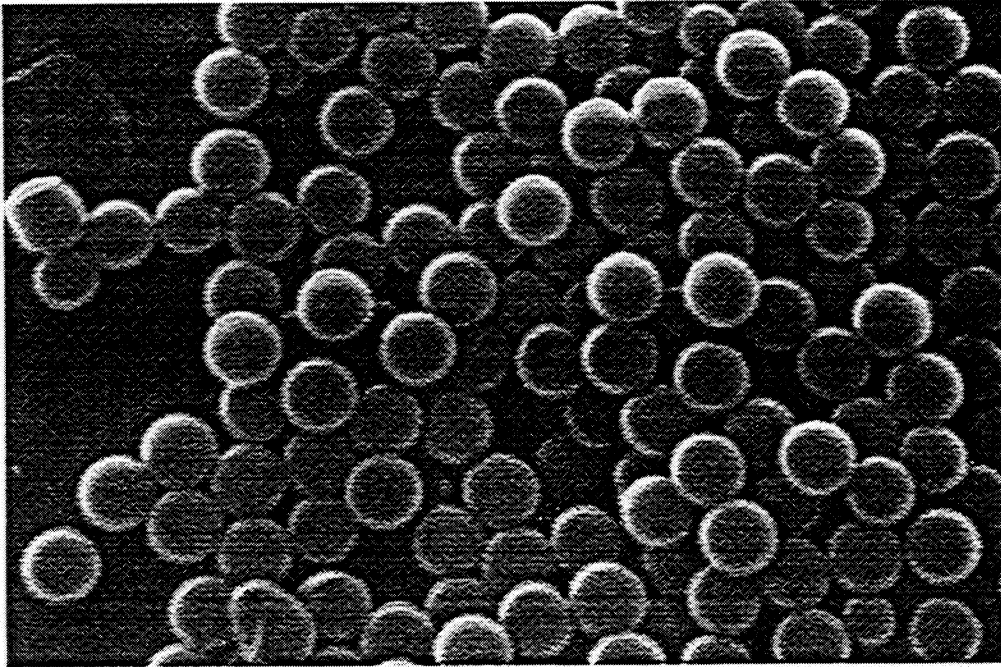
The circumferential variations in the flow field are generated by the rotation of the rotor. Therefore, in order to resolve the flow variations in the circumferential direction, the measurements are synchronized to the rotor circumferential position using a high frequency clock and supporting electronics as described in Hathaway et al. [52].

In addition to the motors used to position the laser probe volume, motor drives were connected to each of the photomultiplier tubes so that the system could be aligned from the control room during a test. Also, there is a motorized beam stop system which can independently block each of the four beams forming the laser probe volume (refer to Figure 8). By blocking selective beams the optics system can be checked from the control room during a research test to insure that the green beams do not contaminate the measurements made by the blue beams, and vice-versa.

Seeding. To obtain measurements with the laser anemometer system, the particles in the flow which pass through the LFA probe measurement volume must be large enough to scatter a sufficient amount of light to be detected by the LFA system. Since the inlet flow to the facility is filtered and therefore relatively clean,

polystyrene latex spheres are injected into the flow field far upstream of the test compressor to seed the flow and scatter a sufficient amount of light for the laser anemometer system to measure. These particles are manufactured using the process developed by Nichols [53] and their size is determined using scanning electron microscope (SEM) photographs. The range of particle sizes used in the present investigation is 0.7–0.9 μm . The SEM photographs indicate that although the particle size varies within this range between batches, the size within a given batch is uniform to within 0.1 μm — see Figure 10. Particle batches were not mixed during research runs. Laser anemometer measurements acquired under identical operating conditions with particles manufactured in different batches indicate that there are no differences in the measurements attributable to particle size variations within this range. Therefore, all LFA data were acquired with uniformly sized particles, although the mean particle size varied between 0.7–0.9 μm .

In addition, the particle size must be as small as possible to follow the gradients in the flow. Therefore, there is the compromise of making the particle large enough to be measured by the LFA system yet small enough to follow the gradients in the flow. By trying various sizes of particles it was concluded that it was quite difficult to measure particles smaller than 0.6 μm in diameter. The inability of the particles to follow the gradients in the flow, referred to as the particle lag, will be addressed in the 'Data Integrity' section of **Chapter 4: Results and Discussion of**



Scale: ——— 1 μm

Figure 10 SEM Photograph of Seed Particles.

Flow Field Physics. As will be shown in that section, the particle lag associated with particles of 0.7–0.9 μm in diameter does not compromise the results. Use of smaller seed particles would have reduced the particle lag distance. However, the difficulty of detecting a seed particle with the laser anemometer increases rapidly as the particle size is reduced. The particle size used in the present work is therefore a compromise between reasonable data rates and reasonable flow tracking ability.

In order to inject the seed material into the rotor flow, the seed material is suspended in alcohol and atomized through agricultural sprayers located in the inlet piping upstream of the plenum (refer to Figure 3). The agricultural sprayers

emit rather large droplets (on the order of 100–1000 μm). In order to make sure the alcohol was evaporated before reaching the test section, tests were run back-to-back with and without seed particles suspended in the alcohol. A particle sizing device was used to sample the flow and the results indicated that not only was the alcohol evaporated prior to entering the test section, but the particle size was in agreement with the electron microscope photographs.

2.5 Computational Tool

The LFA system measures only the axial velocity and tangential velocity component of the flow field and the radial velocities are assumed to be negligible in the determination of the total velocity vector. Therefore, to assess the effect of the radial velocity component on the flow field and to serve as an overall check on the LFA measurements and data reduction procedure, a Navier-Stokes solver was used on a limited basis. It is not the intent of this document to compare all of the LFA results to the computational results, but rather to use both the LFA and the computational fluid dynamics code (CFD) as tools to gain a better understanding of the flow field in NASA rotor 37.

The analysis code used in the present study solves the Reynolds-Averaged form of the Navier-Stokes equations [54]. The code employs a four-stage Runge-Kutta time marching scheme and uses Baldwin-Lomax turbulence modeling with wall functions. The flow in the clearance gap was simulated using a model suggested

by Kirtley et al. [55], which treats the clearance flow as an orifice flow with no loss in mass, momentum, or energy. The effect of the vena contracta which occurs in orifice flows is accounted for by using a discharge coefficient, which makes the effective tip clearance gap smaller than the actual clearance. A discharge coefficient of 0.5 is used for all results presented herein.

The grid used in the simulations had 51 cells in the radial direction, 41 cells in the circumferential direction, and 132 cells were placed between the inlet and exit boundaries, of which 41 were along the blade chord line. The clearance gap was spanned by two cells in the radial direction. The grid in the clearance gap region above the rotor tip is constructed by simply extending the grid below the tip to the shroud while maintaining the tangential distance across the blade passage fixed to its value at the rotor tip. The number of grid points spanning the gap in the radial direction would be too few if one were interested in resolving the details of the flow entering and exiting the gap, as done by Crook [56]. In the present study however, we are interested mainly in the clearance flow interaction with the primary throughflow in the blade passage. Several studies have shown that reasonable estimates of this interaction can be obtained without a detailed description of the flow exiting the gap if one has a good estimate of the gap mass flow. This can be accomplished in a numerical simulation with as few as one

grid cell spanning the radial direction if one accounts for the blockage introduced by the vena contracta.

3 Experimental Procedure

3.1 Data Acquisition

3.1.1 Survey Locations

The meridional view of the compressor flowpath and the locations for both the aerodynamic probe and LFA measurement planes are presented in Figure 11. There are three distinct types of data acquisition surveys: 1) aerodynamic probe surveys, 2) laser anemometer cross-channel plane or radial surveys, and 3) laser anemometer blade-to-blade streamsurface surveys.

Aerodynamic probe surveys. The aerodynamic survey probe data were acquired for eighteen radial locations (5%, 10%, 15%, 20%, 25%, 30%, 37%, 44%, 51%, 58%, 65%, 70%, 75%, 80%, 85%, 90%, 94%, and 97% span from the hub) at a constant axial location upstream (denoted survey station #1 in Figure 11) and downstream of the rotor (denoted survey station #4 in Figure 11). At each survey station there is a wedge probe measuring an average static pressure and flow angle, and a cobra probe measuring an average total pressure, total temperature, and flow angle for each radial survey location. Since the rotor blade passing frequency is 10 Khz at design speed, it is obvious that these pneumatic probes cannot respond to oscillations associated with the rotor blade passing. The probes are fixed in the laboratory reference frame and therefore are performing some

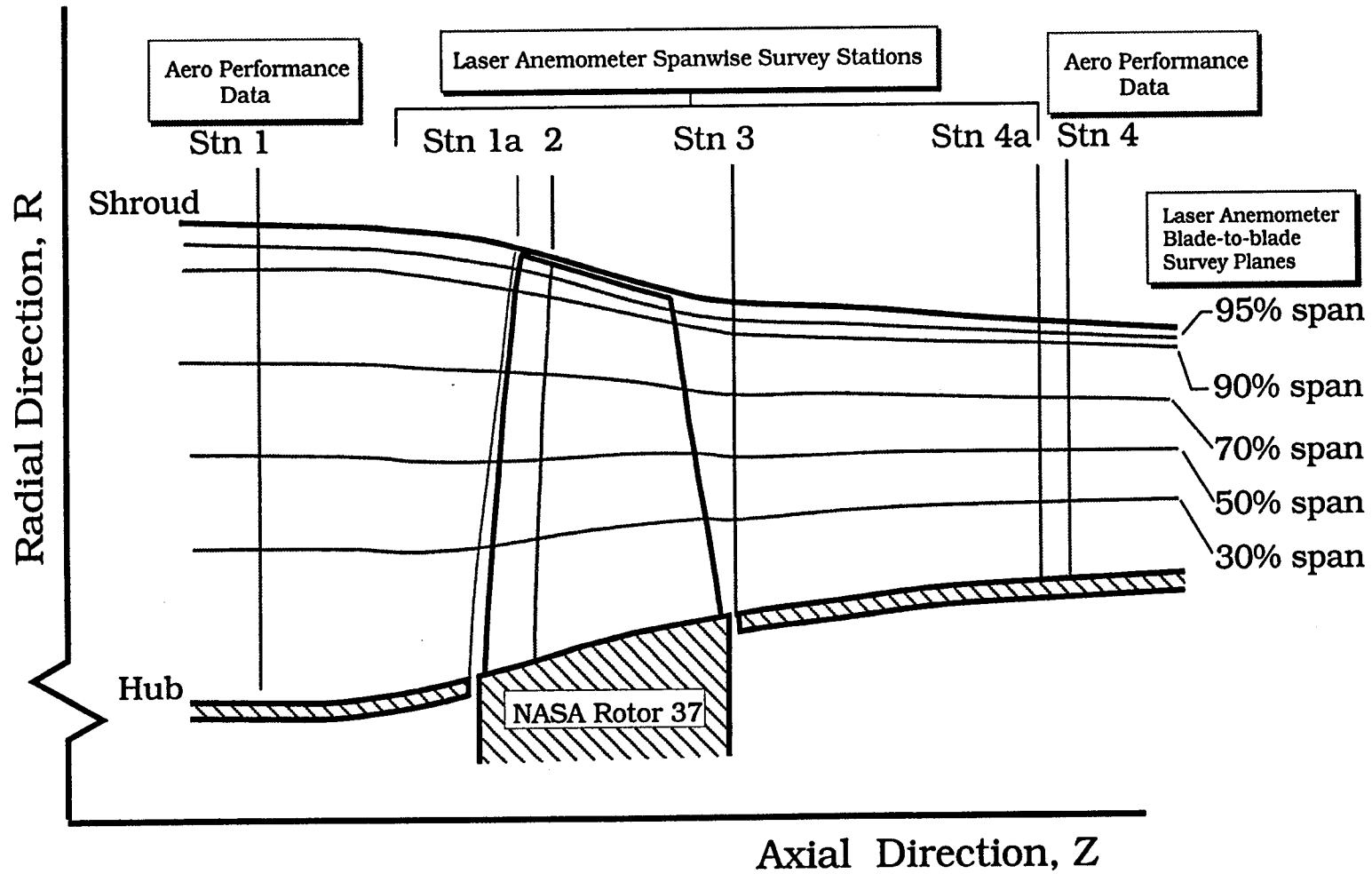


Figure 11 LFA and Aerodynamic Probe Survey Locations.

type of average to the 'true' flow features which are related to the rotor blade passing. How these probes average the flow field is a research topic unto itself and will not be addressed herein. However, the impact of this probe averaging has been minimized by placing the survey probes far upstream and far downstream of the rotor such that the unsteadiness generated by the blade passing frequency is essentially mixed out and the probes are in a region of relatively small amplitude fluctuations. These levels of the fluctuations in flow properties at the probe survey stations will be addressed in the 'Data Integrity' section of **Chapter 4: Results and Discussion of Flow Field Physics**, where comparisons between the survey probes and the LFA data are made.

Laser anemometer cross-channel survey. A cross-channel survey plane indicates the variation of flow features in the circumferential (analogous to pitchwise or tangential) direction and the radial direction at either a constant axial location (such as station 3 and 4a in Figure 11) or constant percent of rotor chord from the blade leading edge (such as station 1a and 2 in Figure 11). Note since the laser anemometer has access over the entire optical window it is not constrained to make measurements in the radial direction at a fixed axial location as is the case for the survey probes. At each axial/radial measurement location within a cross-channel survey plane data were acquired across all 36 blade passages at a circumferential resolution of 184 points across each blade pitch. There were

approximately 60000–100000 measurements acquired at each axial/radial location and they were randomly distributed around the circumference. The radial spacing of the data points in the cross-channel survey planes was approximately every 5% of local rotor span from 0–80% of span and was refined to every 2% of span from 80–100% span. In general, measurements were not acquired below 20% span and above 98% span. The measurement grid was refined in the outer 20% of rotor span because the gradients of the flow features increased in this region near the outer endwall. Measurements were made as close as 1 mm (0.040 in.) from the shroud, which corresponds to 2.5 times the clearance gap at design speed.

Laser anemometer streamsurface survey A streamsurface plane consists of data acquired at various axial and circumferential locations along a constant percent of span from the rotor hub, i.e., constant surfaces of revolution. For example, the streamsurface survey planes denoted as 30%, 50%, 70%, 90%, and 95% of span in Figure 11 contain data on blade-to-blade surfaces of revolution at 30, 50, 70, 90, and 95% of span from the rotor hub, respectively. Similar to the cross-channel survey, data were acquired across all 36 blade passages at a circumferential resolution of 184 points across each blade pitch, and there were approximately 60000–100000 measurements acquired at each axial/radial location. The axial spacing of the data points in the blade-to blade streamsurface surveys

was approximately 5% of rotor chord and generally started one chord upstream of the rotor, went through the rotor, and extended one chord downstream of the rotor.

In summary probe surveys provide the radial distribution of measured flow properties at axial locations far upstream and downstream of the rotor. Laser anemometer surveys provide either the radial and circumferential variation of flow properties (cross-channel surveys) or the circumferential and axial variation of the flow properties (blade-to-blade streamsurface surveys) throughout the rotor flow field.

3.1.2 Operating Conditions

The majority of the data were acquired for the rotor operating at design speed conditions. However, to evaluate the effect of the inlet Mach number on the rotor performance and flow field features, data were acquired (to a lesser extent) at part speed conditions. Aerodynamic probe survey data and LFA data were acquired at 60%, 80%, 85%, and 100% of rotor design wheel speed. At design speed (17188 rpm) the inlet relative flow is supersonic from hub to tip, which is typical of inlet rotors used for military applications. At 85% and 80% speed the relative flow is transonic (supersonic at the tip and subsonic at the hub), which is typical of low hub/tip radius ratio fans used in commercial aircraft flying today. At 60% of design speed the relative flow is subsonic from hub to tip, which is more characteristic of middle- and exit-stage core compressor blading. A very limited amount of data

Table 2 Inlet Mach Numbers versus Rotor Wheel Speed

% Design Speed	M_{rel} at Hub	M_{rel} at Tip
60	0.68	0.89
80	0.90	1.18
85	0.96	1.26
100	1.13	1.48

was acquired at 85% speed which provided more data in the transonic flow regime with slightly higher Mach numbers than the 80% speed case. The relative inlet Mach numbers at the rotor tip and hub for each speed are provided in Table 2.

With the exception of 85% speed, the overall performance of the rotor with mass flows varying from wide-open throttle or maximum flow to near stall conditions was measured with aerodynamic probe surveys. At 85% speed the aerodynamic probe surveys were performed only at the wide-open throttle operating condition.

Detailed laser anemometer surveys were performed at one setting of the throttle valve for the data acquired at 60%, 80%, and 85% of rotor design speed. However, at design speed the LFA data were acquired at three throttle valve positions corresponding to: 1) wide-open throttle valve position, hereafter, referred to as the max flow condition, 2) partially-closed throttle valve position, hereafter, referred to as the high flow condition, and 3) the partially-open throttle valve position which corresponded to a near stall operating condition, hereafter, referred to as the low flow condition. Note the terms max flow, high flow, and low flow

Table 3 Summary of LFA Streamsurface Survey Data

Operating Condition	Streamsurface Survey Locations
60% design speed	90% and 95% span
80% design speed	70%, 90%, and 95% span
85% design speed	70% span
100% design speed, max flow	70%, 90%, and 95% span
100% design speed, high flow	30%, 50%, 70%, 90%, and 95% span
100% design speed, low flow	30%, 50%, 70%, 90%, and 95% span

are in reference to the amount of mass flow through the rotor. Cross-channel surveys were performed at station #1a and station #3 in Figure 11 for all operating conditions except for the 85% speed operating condition. There are many partial cross-channel surveys that focused on the outer 20% span downstream of the rotor, but they are too numerous to mention herein. Streamsurface surveys provide the detailed development of the flow within the rotor passage and are used to describe the rotor shock structure. The summary of streamsurface surveys are given in Table 3. Not all of the data will be presented herein, but it is available if a need for this data develops.

3.2 Data Reduction

3.2.1 Aerodynamic Probe Data

The static pressure, total pressure, and total temperature measured with the aerodynamic survey probes at stations #1 and #4 of Figure 11 are first corrected for Mach number and streamline curvature. The corrections are based on a calibration

of each probe which was performed for a Mach number range of 0.3 to 0.9 and a pitch angle (angle between the axial flow direction and the streamline direction) range of -20° to $+20^\circ$. The streamline slope or pitch angle is not measured, but the pitch angle corrections were based on the pitch angle calculated from the Navier Stokes solver. All measurements are corrected to NACA standard-day sea-level conditions (temperature, $T_{ref} = 288.2 \text{ K}$ and pressure, $P_{ref} = 101325 \frac{\text{N}}{\text{m}^2}$) at the rotor inlet corresponding to station #1 in Figure 11. The orifice mass flow, W , and rotor wheel speed, N , are also corrected to their equivalent values at standard day conditions.

$$W_{corr} = \frac{W \sqrt{\frac{T_{inlet}}{T_{ref}}}}{\frac{P_{inlet}}{P_{ref}}} \quad \text{and} \quad N_{corr} = \frac{N}{\sqrt{\frac{T_{inlet}}{T_{ref}}}} \quad (1)$$

The local Mach number, static temperature, and absolute velocity at each measurement location are evaluated from the measured total temperature, total pressure, static pressure and the isentropic flow relations as follows:

$$M = \frac{V}{a} = \sqrt{\left[\left(\frac{P}{p} \right)^{\frac{\gamma-1}{\gamma}} - 1 \right] \frac{2}{(\gamma-1)}} \quad \text{and,} \quad (2)$$

$$a = \sqrt{\gamma R T_s}, \quad \text{where } T_s = T \left(\frac{p}{P} \right)^{\frac{\gamma-1}{\gamma}}$$

The rotor overall performance is based on orifice mass flow, rotor wheel speed, and the aerodynamic survey measurements acquired at stations #1 and #4 in Figure 11. The radial distributions of total temperature are mass averaged

across the annulus. The radial distributions of total pressure are energy averaged by converting them to their enthalpy equivalents and then mass averaging them across the annulus. The equations used are as follows:

$$\frac{\overline{P}_j}{P_{ref}} = \left[\frac{\sum_{i=1}^{nrp} \left(\frac{P_i}{P_{ref}} \right)^{\left(\frac{\gamma-1}{\gamma} \right)} \rho_{j,i} (V_z \Delta A_{an})_{j,i}}{\sum_{i=1}^{nrp} \rho_{j,i} (V_z \Delta A_{an})_{j,i}} \right]^{\frac{\gamma}{(\gamma-1)}} \quad (3)$$

$$\overline{T}_j = \frac{\sum_{i=1}^{nrp} T_{j,i} \rho_{j,i} (V_z \Delta A_{an})_{j,i}}{\sum_{i=1}^{nrp} \rho_{j,i} (V_z \Delta A_{an})_{j,i}}$$

The subscript j refers to the probe axial location (station #1 or station #4 in Figure 11) and subscript i refers to the radial measurement location, where i varies from one to the number of radial positions (nrp) across the annulus. The overall efficiency is calculated from the overall pressure ratio and temperature ratio calculated from the survey stations as follows:

$$\eta_{ad} = \frac{\left(\frac{\overline{P}_4}{\overline{P}_1} \right)^{\left(\frac{\gamma-1}{\gamma} \right)} - 1}{\frac{\overline{T}_4}{\overline{T}_1} - 1} \quad (4)$$

3.2.2 Laser Anemometer Data

Similar to the orifice mass flow and rotor wheel speed, the LFA measured velocities are also corrected to their equivalent values at standard day conditions. The difference in the standard day correction for the laser anemometer data as

compared to the aerodynamic probe data is that the plenum and not the survey station #1 conditions are used as the inlet conditions.

$$V_{corr} = V \sqrt{\frac{T_{ref}}{T_{plenum}}} \quad (5)$$

From this point forward, all values will be considered to be standard day corrected and the subscript 'corr' will be omitted. Recall that the LFA data were acquired across all 36 blade passages at a circumferential resolution of 184 points across each blade pitch resulting in a total of 6624 circumferential measurements around the circumference of the rotor wheel. In general, the laser anemometer results presented are based on the velocity distribution across an averaged blade passage, which is calculated by ensemble-averaging the measurements acquired in each of the 6624 circumferential measurement windows and then averaging the pitchwise distribution in each passage to form an average passage. The ensemble average is performed to arrive at the average velocity at each circumferential measurement window as follows:

$$\bar{V}_j = \frac{1}{nm_j} \sum_{i=1}^{nm_j} V_{i,j} \quad , \text{ where } j = 1, 6624 \quad (6)$$

Note, $V_{i,j}$ refers to each individual velocity measurement i at circumferential position j . The subscript j refers to each of the 6624 circumferential measurement windows and nm_j refers to the number of measurements at each measurement

window, j . The pitchwise distribution of the velocity in the averaged blade passage, V_k , is calculated as follows:

$$\bar{V}_k = \frac{1}{(np - nz)} \sum_{n=1}^{np} \overline{V_{(k+(n-1)*184)}} \quad \text{where } k = 1, 184 \quad (7)$$

Here np is the number of passages (36 in this case) and nz is the number of passages that had zero measurements in window k .

The passage averaged velocity distribution is calculated for each of the laser anemometer channels corresponding to the axial and tangential velocity components. In the 'Data Integrity' section of **Chapter 4: Results and Discussion of Flow Field Physics** the variation in the flow field from one blade passage to the next blade passage will be addressed. Otherwise, the discussions will deal with the passage averaged velocity distributions and the bar will be dropped in the notation. From the axial velocity, V_z , the tangential velocity, V_θ , and the wheel speed, $U=Nr$, the absolute velocity, V_{abs} , the relative velocity, V_{rel} , the relative tangential velocity, W_θ , can be calculated as follows:

$$\begin{aligned} V_{abs} &= \sqrt{(V_z^2 + V_\theta^2)} \\ W_\theta &= V_\theta - U \\ V_{rel} &= \sqrt{V_z^2 + W_\theta^2} \end{aligned} \quad (8)$$

In addition, the absolute and relative flow angles, β_{abs} and β_{rel} , respectively, are calculated as follows:

$$\begin{aligned}\beta_{abs} &= \text{COS}^{-1}\left(\frac{V_z}{V_{abs}}\right) = \text{TAN}^{-1}\left(\frac{V_z}{V_\theta}\right) \\ \beta_{rel} &= \text{COS}^{-1}\left(\frac{V_z}{V_{rel}}\right) = \text{TAN}^{-1}\left(\frac{V_z}{W_\theta}\right)\end{aligned}\quad (9)$$

The relative Mach number is calculated from the relative velocity and the local speed of sound at each point in the flow field. The static temperature required to compute the local speed of sound is calculated by using Euler's turbine equation, and the energy equation assuming adiabatic flow. Euler's equation for turbomachinery and the energy equation (where work into to the fluid is considered positive work) are:

$$\text{Work}|_1^2 = U_2V_{\theta,2} - U_1V_{\theta,1} \quad (10)$$

$$(Q + \text{Work})|_1^2 = h_{02} - h_{01} \quad (11)$$

Assuming adiabatic flow, $Q=0$, and using the standard day corrected plenum conditions as the inlet station, where $V_{\theta,1} = 0$, these two equations can be solved for the work input and put into the following form:

$$U_2V_{\theta,2} = c_pT_s + \frac{V_2^2}{2} - c_pT_{ref} \quad (12)$$

From this equation the static temperature, and therefore, the local speed of sound and Mach number can be calculated. Note that the evaluation of the static temperature essentially assumes the following: 1) the flow is steady in the rotating frame of the rotor, 2) no work is done on the flow in the rotating frame, and 3) there is no heat flow to or from the flow.

Note that the radial velocity component, which is not measured by the laser anemometer, is ignored in the calculation of the relative and absolute velocity which also impacts the calculation of the absolute and relative Mach number. Using the predicted flow fields generated by the 3D Navier-Stokes simulations described below, the Mach number distributions throughout the flow field were calculated with and without the radial velocity component. These calculations indicated that ignoring the radial velocity component resulted in a maximum error of less than 1% in the relative Mach number. All measured Mach number distributions presented below do not include the radial velocity component, while all predicted Mach number distributions do include the radial velocity component.

4 Results and Discussion of Flow Field Physics

The emphasis in this chapter is to discuss the flow field physics pertaining to the development of blockage and loss in a transonic axial compressor operating at design speed and part speed conditions. The data acquired within NASA rotor 37 will serve as the basis for this discussion and CFD code results will complement and/or supplement the discussion. This chapter is broken into six major sections: 1) a discussion of the measured overall performance characteristics and their comparison with the design intent and CFD results; 2) a general discussion of the flow field physics in NASA rotor 37; 3) a discussion of the integrity of the data; 4) a discussion of the sensitivity of the loss and blockage development to changes in the rotor back pressure at design speed; 5) a discussion of the loss and blockage development in the rotor at part speed conditions; and 6) a summary of the chapter. In the context of this chapter the terms 'blockage' and 'loss' will be used conceptually, however, in Chapter 5 blockage and loss will be quantified.

4.1 Overall Performance Characteristics Based on Aerodynamic Probe Surveys and Their Comparison with Design and CFD Results

The objectives of this section are: 1) to discuss the general operating characteristics of the rotor and 2) to compare the measured performance

characteristics with both the design intent and predictions by state-of-the-art CFD codes.

4.1.1 Performance Map

This section discusses the general performance characteristics that are extracted from conventional aerodynamic probe surveys. Recall that the probes were located far upstream and downstream of the rotor at stations #1 and #4 in Figure 6, respectively. The performance characteristics of this compressor operating at 60%, 80%, and 100% of design speed are plotted in terms of corrected mass flow versus the total pressure ratio and adiabatic efficiency in Figure 12. At a given wheel speed the mass flow is decreased by closing a downstream throttle valve which results in an increase in the resistance downstream of the compressor. Since the rotor was designed for an axial inlet flow, decreasing the mass flow and keeping the wheel speed constant results in an increase in the blade incidence. So in effect the operating map at a given wheel speed depicts the change in performance with incidence or blade loading from the maximum flow or choke condition to the mass flow at which the blade stalls. The data at 80% and 60% speed range from the choke flow condition to the near stall condition. However, at design speed the maximum flow (20.9 kg/s) corresponds to choking of the facility diffuser located between the rotor and the throttle valve, rather than the choking of the rotor itself. Diffuser choke occurred prior to rotor choke because the diffuser

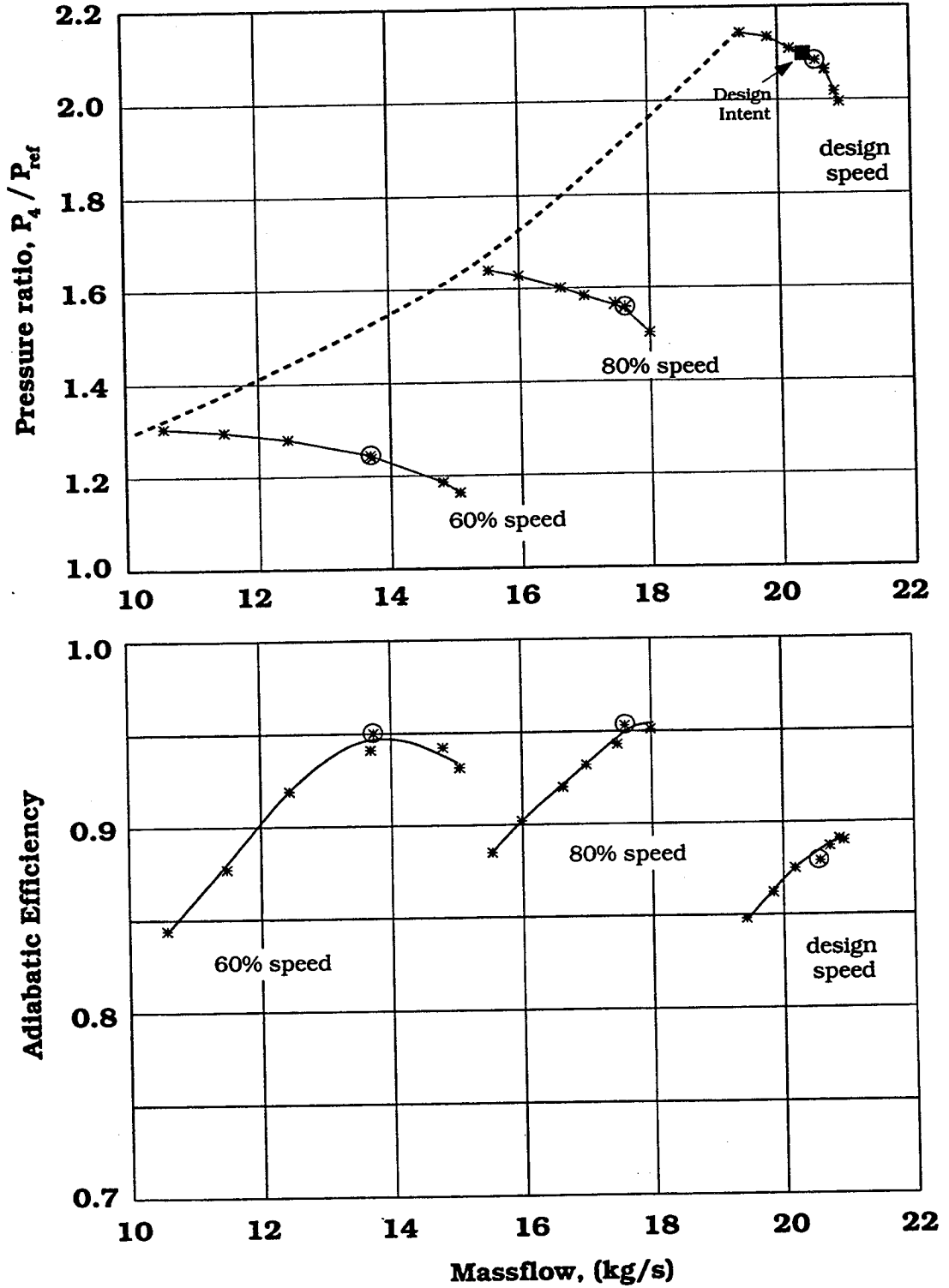


Figure 12 Overall Performance Characteristics.

was designed to accept the axial outflow of stage 37 rather than the swirling outflow of rotor 37. Subsequent testing with the stator in place, which removes the rotor outlet flow swirl before the flow enters the diffuser, has verified that the isolated rotor configuration was choked at 60% and 80% speed but not choked at design speed. Based on the CFD simulations of the rotor only configuration and experimental testing of the full stage configuration, the best estimate of the actual rotor choking mass flow is 20.93 kg/s. This discrepancy between the measured maximum flow rate of 20.90 kg/s and the inferred choking flow rate of 20.93 kg/s does not affect the conclusions drawn herein, but it does mean that the rotor is not choked at the highest mass flow rate in Figure 12. The circled data points in Figure 12 indicate the operating condition where the detailed laser anemometer surveys were acquired and represent a mass flow which maintains nearly the same flow incidence angle for 60%, 80%, and 100% of design speed. Note that the operable range of mass flow (stall margin) decreases with increasing rotor wheel speed largely due to compressibility effects — refer to Table 2. Also note that the highest value for the efficiency does not occur at design speed which is consistent with transonic compressors where the efficiency penalty is accepted for an increase in the pressure ratio. In conclusion, this overall operating map provides a one dimensional view of the compressor performance and was obtained from

averaging measurements made at several spanwise locations across the annulus both upstream and downstream of the rotor.

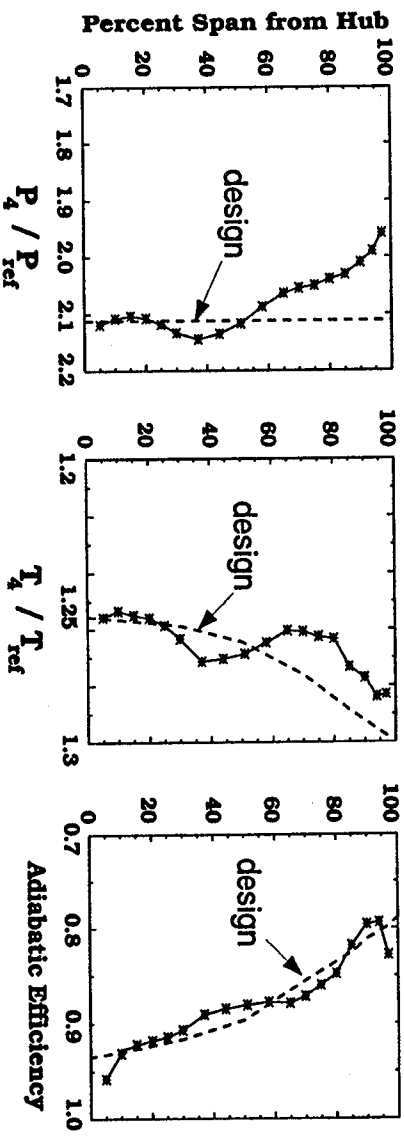
A comparison of the data acquired at 60%, 80%, and 100% speed at constant rotor incidence angle is an effective way of evaluating the effects of inlet Mach number on the rotor performance. In contrast, a comparison of the data along a speed line (line of constant rotor wheel speed) is an effective way of investigating the effects on the rotor flow field due to changes in incidence and blade loading. In the following sections the variation in the rotor performance and flow field due to 1) changes in incidence at design speed, and 2) changes in the inlet Mach number at a constant incidence angle near that of the design intent will be discussed.

4.1.2 Radial Distributions

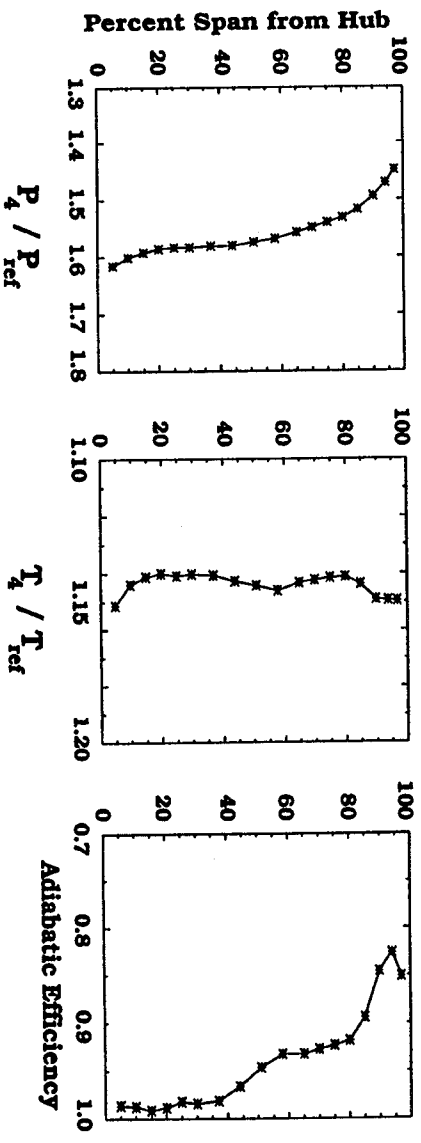
Effect of Inlet Mach Number The goal of the compressor is to produce a given pressure rise with the minimal amount of work put into the fluid. The temperature added to the flow is directly related to the work added to the flow, whereas, the total pressure indicates how much pressure rise was achieved for that amount of work added. The effectiveness of this process is expressed in terms of the adiabatic efficiency (see equation 4). The radial distribution of total pressure ratio, total temperature ratio, and adiabatic efficiency at survey station #4 for the rotor operating conditions corresponding to the circled data points in Figure 12 are presented in Figure 13. These operating conditions represent a variation in the

nominal relative inlet Mach number at mid-span from 0.8 to 1.3 with the rotor inlet incidence angle held nearly constant. Note that these plots are based on the measurements made at their respective spanwise location. They represent the average value as perceived by the measuring instrument and are not mass averaged quantities. Because the variation in performance values differed greatly with changes in the rotor wheel speed, the data were plotted on different scales but with the same sensitivity so comparisons could be made between operating conditions.

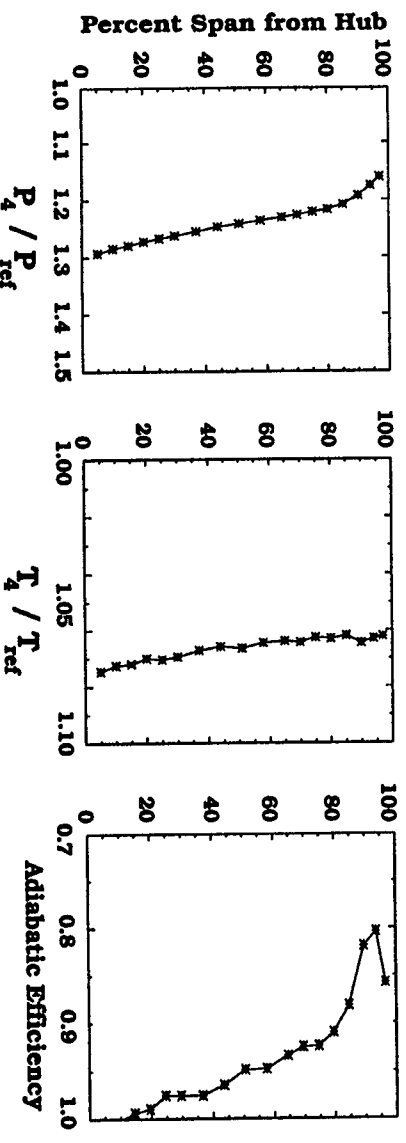
The shape of the radial distribution of total temperature ratio and total pressure ratio is similar at 60% and 80% speed and very much different from that at design speed. The shape of the radial distribution of the efficiency is very similar for all speed conditions. The values of the adiabatic efficiency are nearly identical across the span for the 60% and 80% speed data, but are significantly reduced at all radial locations for the design speed case. At part speed conditions the pressure ratio and temperature distribution from 20% to 80% span is more uniform as compared to the distribution at design speed. At 5% and 10% of span, the efficiency data at 60% speed is slightly greater than 1 (1.01 and 1.03 respectively), and is primarily due to the uncertainty in the total temperature measurement. For instance, note at 60% speed the temperature rise is about 40°R and therefore an uncertainty of 1°R results in an uncertainty in efficiency calculation of .03 or 3 points.



(A) 100% SPEED, NEAR PEAK EFFICIENCY, 20.31 KG/S



(B) 80% SPEED, NEAR PEAK EFFICIENCY, 17.44 KG/S



(C) 60% SPEED, NEAR PEAK EFFICIENCY, 13.71 KG/S

Figure 13 Radial distributions of the overall performance characteristics at a) 100% speed, b) 80% speed, and c) 60% speed for the rotor operating along a throttle line.

Comparison to Design Intent. The design intent (100% speed and peak efficiency) of the rotor was to produce a uniform rotor exit pressure ratio of 2.106 and a temperature ratio distribution as defined in Figure 13a at a mass flow rate of 20.19 kg/s. The curve representing the design intent for the adiabatic efficiency was calculated using the design values of the pressure and temperature for the energy-averaged pressure and mass-averaged temperature values in equation 4. It is obvious from the figure that the measured radial distribution of temperature and pressure rise is radically different from the design intent. Also for all speed conditions the efficiency is lowest in the outer endwall region, yet this is expected and consistent with the design intent. Note that at design speed where there is an increase in the pressure (for example at 40% span) there is a corresponding increase in temperature which is consistent with an increase in the work input producing more pressure rise and the efficiency remaining approximately the same.

In the outer spans (from 50% to 100% span) the pressure ratio is lower than the design intent and this could be attributed to the lower than design values for the temperature ratio or work input in the outer spans. A NASTRAN analysis of the blade geometry indicated 1–2° of untwist in the blade tip section under load at design speed conditions which was not accounted for in the mechanical blade design. (Refer to Appendix A: Data Integrity for more details on the NASTRAN analysis of the blade geometry.) This could explain why the measured

performance data indicates less work and less pressure rise in the tip section than anticipated from the design intent (Figure 13a). In the actual blade (as described by the NASTRAN predicted geometry) there is a larger throat area than in the designed blade (due to the additional 1–2 degrees of untwist) in the upper radii of the blade which essentially lowers the throttle resistance and therefore the rotor exit pressure. The lower rotor backpressure results in the shock being pulled further downstream into the passage and thereby providing a weaker shock. Since the shock is responsible for most of the static pressure rise and turning of the flow, a weaker shock in the actual geometry as compared to the design geometry would explain why the work input in the outer radii is lower for the actual blade geometry in comparison to the design geometry. This argument does not quantify the reduction in the work input and pressure rise for a weakening of the designed shock structure but clearly indicates the appropriate trend.

Although the measured radial distributions of pressure and temperature differ from the design intent, the overall mass averaged results for the measured values of pressure ratio, temperature ratio, and adiabatic efficiency of 2.084, 1.265, and 0.88, respectively are comparable to the design values of 2.106, 1.270, and 0.88, respectively. The discrepancy in the radial distributions of the pressure and temperature ratio between the measured and design values can be explained by a redistribution of the mass flow. For example, a comparison of the measured and

design radial distributions of the axial velocity (not shown herein) indicate that in the measured distribution there is more flow from 20% to 60% span where the pressure and temperature are high and less mass flow in the outer 20% of span where the pressure and temperature are low, as compared to the design intent, such that the mass averaged quantities of the actual and design performance parameters are comparable. Why is the actual radial distribution of mass flow different from the design intent? Does this difference in the radial distribution of the mass flow occur within the rotor or is it due to radial mixing of the flow that occurs between the rotor trailing edge and the measurement station which is approximately two rotor chords downstream of the rotor trailing edge? In order to answer these questions detailed laser anemometer measurements made throughout the rotor flow field were acquired and these issues will be addressed later.

In summary, there is a change in the shape of the radial distribution of the pressure and temperature rise that occurs at design speed as compared to both the part speed radial distributions and the design intent. There appears to be a redistribution of the flow which either occurs within or downstream of the rotor or possibly a little of each.

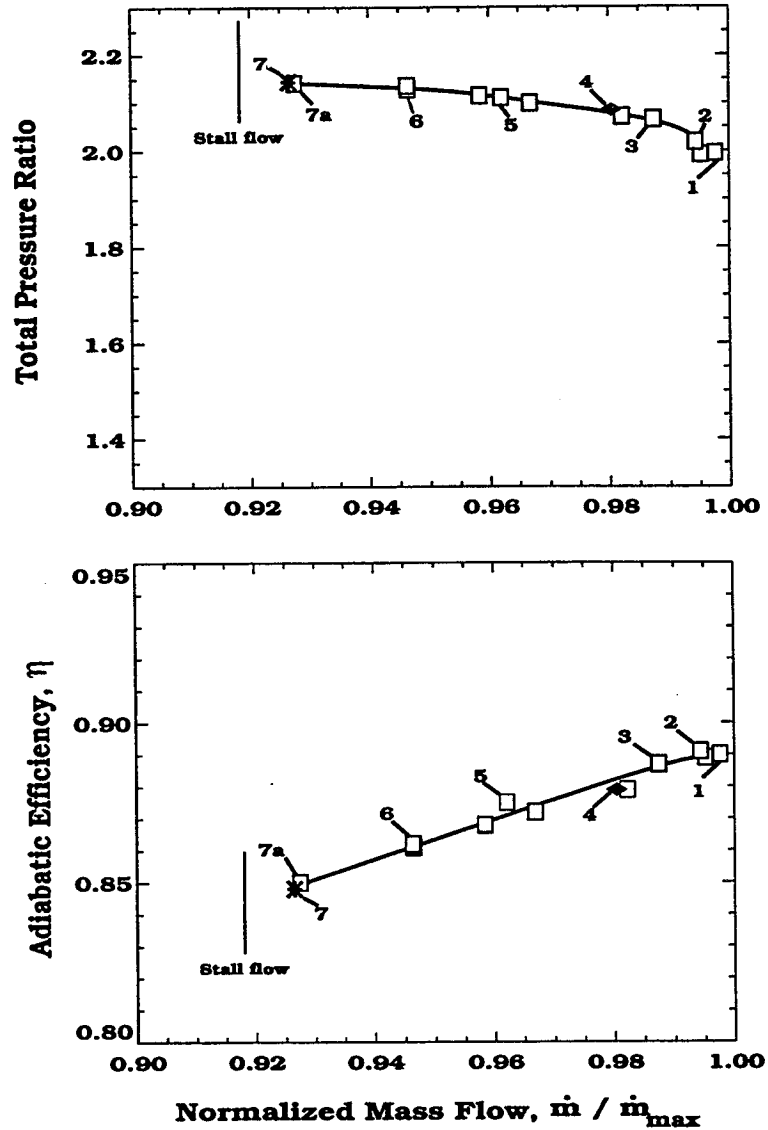


Figure 14 Overall performance characteristics at 100% design speed indicating repeatability of rotor performance over the entire test period.

Effect of Changes in Blade Incidence or Blade Loading. We will now compare the radial distributions of the pressure, temperature, and adiabatic efficiency for different blade loadings at design speed. The overall performance map at design speed is plotted in Figure 14. Throughout the test program which

spanned several years the overall operating characteristics were repeated and compared to the original performance as denoted by data points labelled 1–7 (these labelled points are identical to the seven points plotted in Figure 12). The unlabelled data points indicate random checks of the compressor performance throughout the test program. The data points labelled '7' and '7a' indicate the operating conditions at which the repeatability of the data is discussed in Appendix A : Data Integrity. Points 1, 4, and 7 represent the max flow, high flow, and low flow operating conditions, respectively, at which laser anemometer data were acquired.

The radial distribution of total pressure ratio, total temperature ratio, and adiabatic efficiency for the data points labelled 1–7 in Figure 14 are presented in Figure 15. For all curves in this figure data were acquired at the same radial locations as that indicated by the symbols of curve 4 and curve 7. The data symbols were eliminated on the remaining curves for clarity. In this rotor the flow in the rotor-relative frame is supersonic across the span at design speed with a nominal inlet Mach number of 1.48 at the tip and 1.10 at the hub. In the hub region the pressure rise occurs from both the shock and the subsonic turning in the rear of the blade. In the outer radii the rotor pressure rise occurs primarily across the shock system. Figure 15 indicates that the rotor shock structure in the outer radii is more sensitive than that near the hub to changes in the rotor back

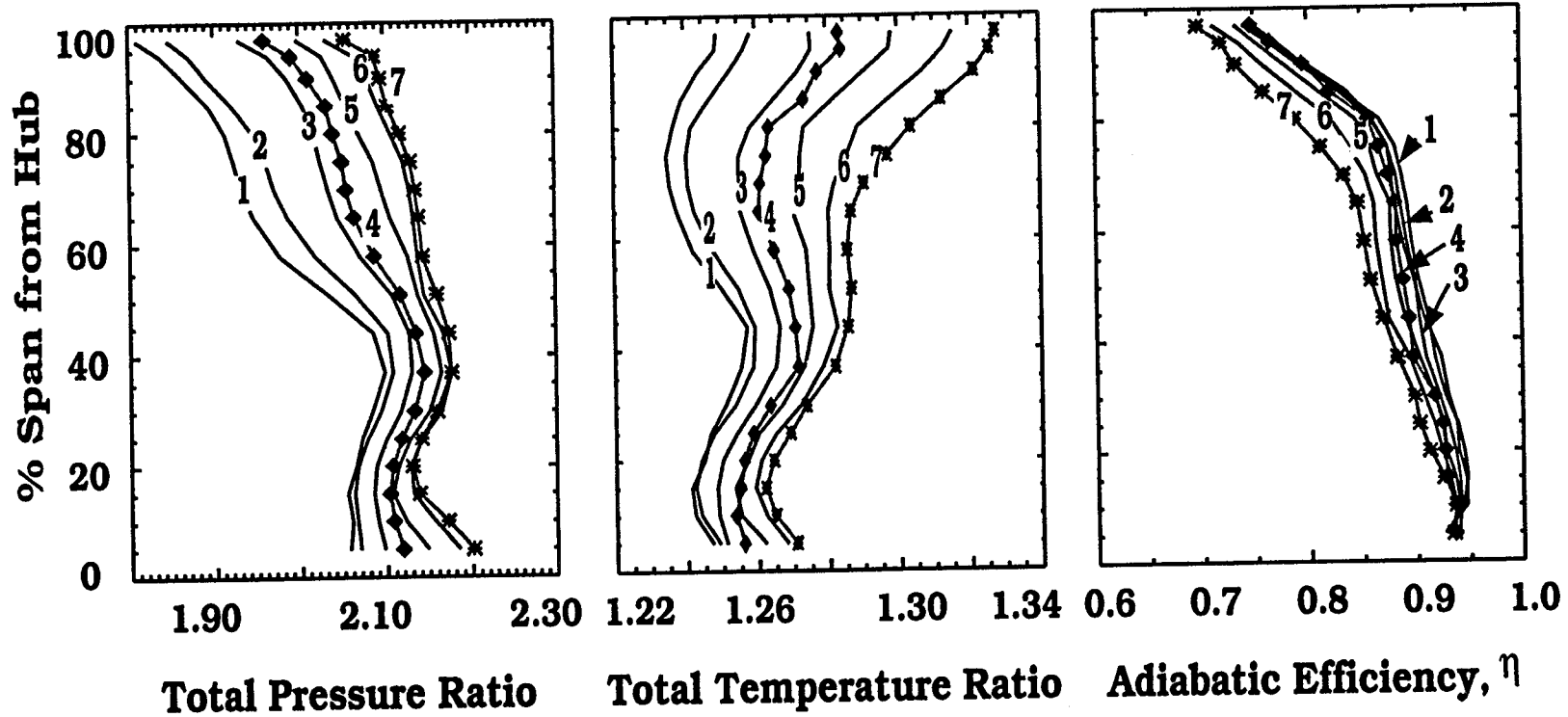


Figure 15 Radial distributions of the overall performance characteristics at 100% design speed indicating sensitivity of performance with downstream throttle resistance.

pressure. The characteristics of the rotor shock structure at design and part speed conditions will be discussed in subsequent sections.

Figure 15 indicates the sensitivity of the spanwise distributions of flow properties to changes in the compressor operating point. This information is useful when comparing CFD predictions to the data, especially when the CFD predictions are developed for operating conditions which do not exactly match those values at which the data were acquired.

4.1.3 Comparisons with CFD

This rotor is of interest because it exhibits aggressive performance in that it produces a high pressure rise at a respectable efficiency. In this subsection it will be shown that the CFD codes (3D Navier-Stokes solvers) have not accurately predicted the measured performance characteristics of NASA rotor 37. The intent of making these comparisons is to demonstrate the need to better understand the details of the flow field within the passages of this rotor and not to get into a comparison of CFD results to data.

This data set was selected to be the data set used in an ASME sponsored international CFD blind testcase. Participants of the CFD blind testcase were invited to solve the flow field for NASA rotor 37 operating at design speed at the high flow and low flow operating conditions. The CFD participants were provided the geometry (which accounted for the blade deflections when under

load at design speed) and inlet boundary conditions but did not have access to the data until all participants provided their solution to the ASME CFD testcase committee. The results of the testcase were presented at the 1994 ASME IGTI turbomachinery conference held in The Hague, The Netherlands and a written report is underway. The CFD codes used in this study represent a good sample of the state-of-the-art technology in computational algorithms, turbulence models, and grid topology. The code types include finite difference, finite volume, and pressure based solution procedures, and some codes are explicit and some are implicit. Table 4 summarizes some of the features for each of the CFD codes. The column entitled "Blocked Grid in Clearance Gap" refers to the treatment of the grid in the clearance region between the rotor tip and the casing shroud. A response of "modeled" in this column implies that the flow in the tip clearance gap is modeled, whereas a number of cells or nodes indicates the number of volumes or grid points placed in the tip clearance region. The column entitled, "Distribution of Grid Points", depicts the number of grid points in the radial (R), circumferential (θ), and axial (Z) directions used by each CFD code. The intent of this table is not to fully describe the code attributes, but rather to provide a flavor for the diversity of the features employed in the various CFD codes.

The purpose of the ASME sponsored CFD testcase was to assess the capability of the CFD codes to predict the flow field in a transonic / supersonic compressor.

Table 4 Sampling of CFD Code Attributes.

CFD Participant	Blocked Grid in Clearance Gap	Turbulence model	Grid Type	Distribution of Grid Points R, θ, Z	Total Number of Grid Points
1	7 cells	Baldwin / Lomax	H	26, 51, 71	101,000
2	modeled	Baldwin / Lomax	H	51, 41, 132	276,000
3	7 nodes	k - ϵ	I	51, 58, 151	447,000
4	7 cells	Baldwin / Lomax	C	41, 41, 225	378,000
5	modeled	Baldwin / Lomax	H	51, 41, 132	276,000
6	modeled	Baldwin / Lomax	H	33, 33, 99	108,000
7	modeled	k - ϵ	H	35, 30, 95	100,000
8	13 nodes	Baldwin / Lomax	C, H, O	63, 46, 319	1,050,000

This was especially important because it is recognized that the details of the flow field within the blade passages must be understood to make further technology improvements. The existing 2D design strategies, which are based on empirical correlations for blockage and loss in conjunction with large experimentally derived databases, are still used and are sufficient when designing within the same parameter base. But to extend beyond previously designed parameters, designers are beginning to incorporate 3D CFD simulations into the design system. The rising costs of building hardware and performance testing force the designers to rely more heavily on the computational tools available to them. Therefore, the evaluation, validation, and/or calibration of the CFD codes is essential for further technology advancement.

Table 5 Desired CFD accuracy according to blade designers in industry.

Performance Parameter	Desired CFD Accuracy
Total Pressure Ratio	$\pm 1.0 - 2.0\%$
Total Temperature Ratio	$\pm 1.0 - 2.0\%$
Adiabatic Efficiency	$\pm 0.5 - 1.0\%$
Absolute Flow Angle	$\pm 1.0 - 2.0$ degrees

Blade designers in the industry were asked how good do the CFD results have to be to serve as a useful tool to the designer. Their response was 1) *the shape of the radial distributions of flow field parameters must be correct, i.e., if the rotor hub is strong, the simulation must show it*, and 2) *the code must provide an accurate prediction of the differences in performance between two different configurations and this is just as important as an accurate prediction of the absolute levels*. Also the designers were asked how accurate in terms of absolute values the solution must be and their response is outlined in Table 5. Therefore, when the results are compared to the data, these bands of desired accuracy will be used as the criteria to judge the ability of the CFD solutions to predict the rotor flow field and performance characteristics.

Comparisons of Overall Performance. The computed results of the overall pressure ratio and adiabatic efficiency for the rotor from the participants in the test case study are presented in Figure 16. The numbered curves represent the various CFD solutions and the data are shown as symbols with error bars to denote the

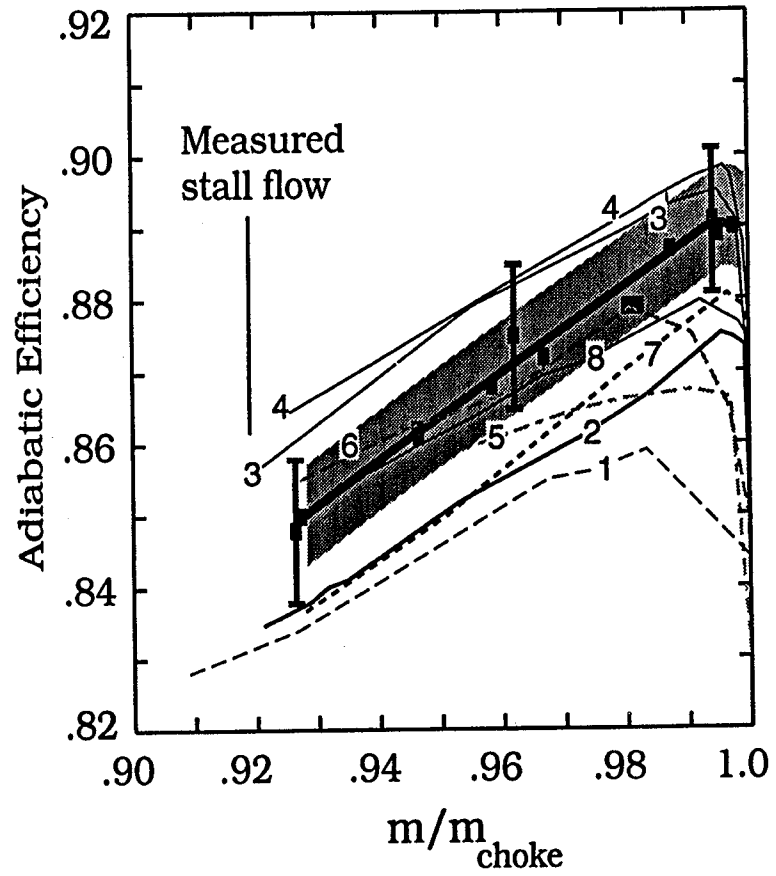
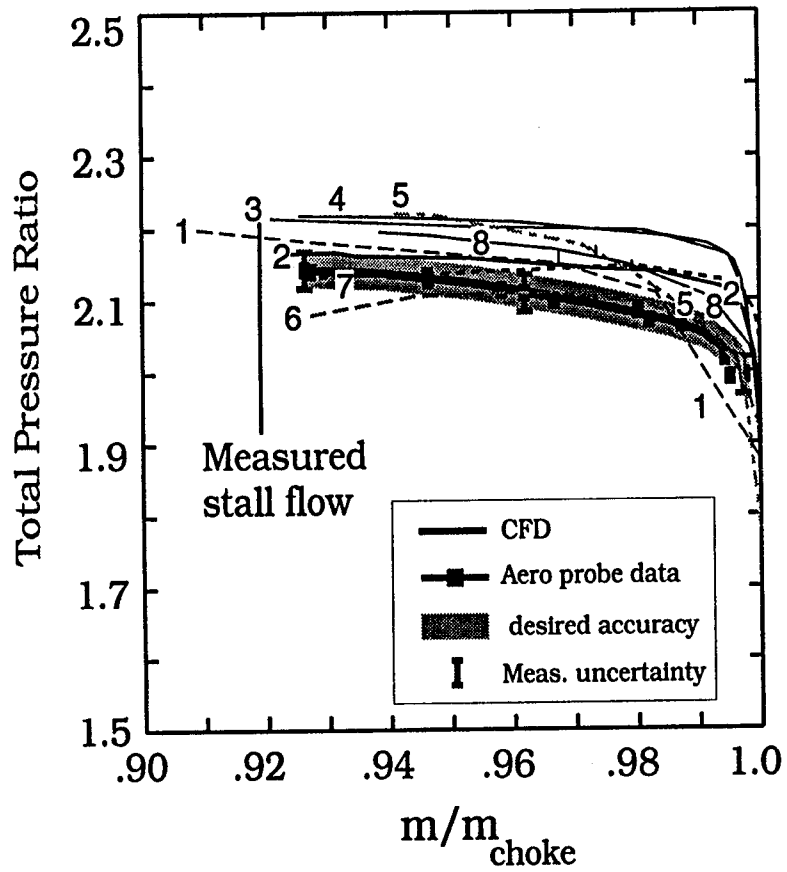


Figure 16 CFD blind testcase results: Overall Performance Characteristics.

measurement uncertainty. (The error bars represent the uncertainty band for a 95% confidence interval and were calculated using the propagation of uncertainty analysis outlined by Kline and McClintock [57].) The shaded area surrounding the data represents the blade designer's desired accuracy range from Table 5. In general the pressure and temperature (not shown) are overpredicted by the CFD and the solutions' adiabatic efficiency is sometimes higher and sometimes lower than the data. However, in most instances the CFD simulations are outside of the shaded region, and therefore outside of the accuracy range desired by blade designers.

Comparisons of the Radial Distributions of Pressure and Temperature. For the design speed high flow operating condition ($m/m_{\text{choke}}=0.98$) the experimental and computational radial distributions of total pressure and total temperature ratios are plotted in Figure 17. Note that not only was the overall performance characteristic not predicted accurately, but the spanwise variation of the flow parameters is quite different from the data, i.e. *the CFD is not predicting the shape of the radial distributions of flow field parameters*. This discrepancy between the data and CFD is much greater than could be explained by the sensitivity of rotor performance to differences in the inlet mass flow — refer to Figure 15. In addition, note that there is quite a large variation in the radial distributions among the CFD results themselves. This is especially important because blade designers today are using 3D CFD to analyze their design and

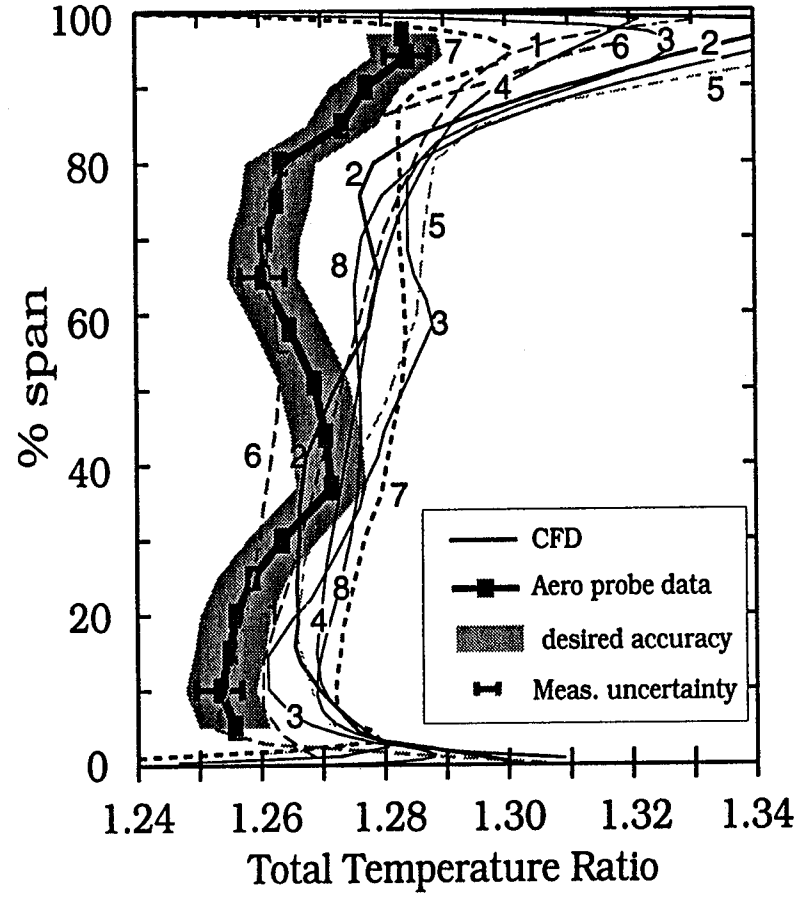
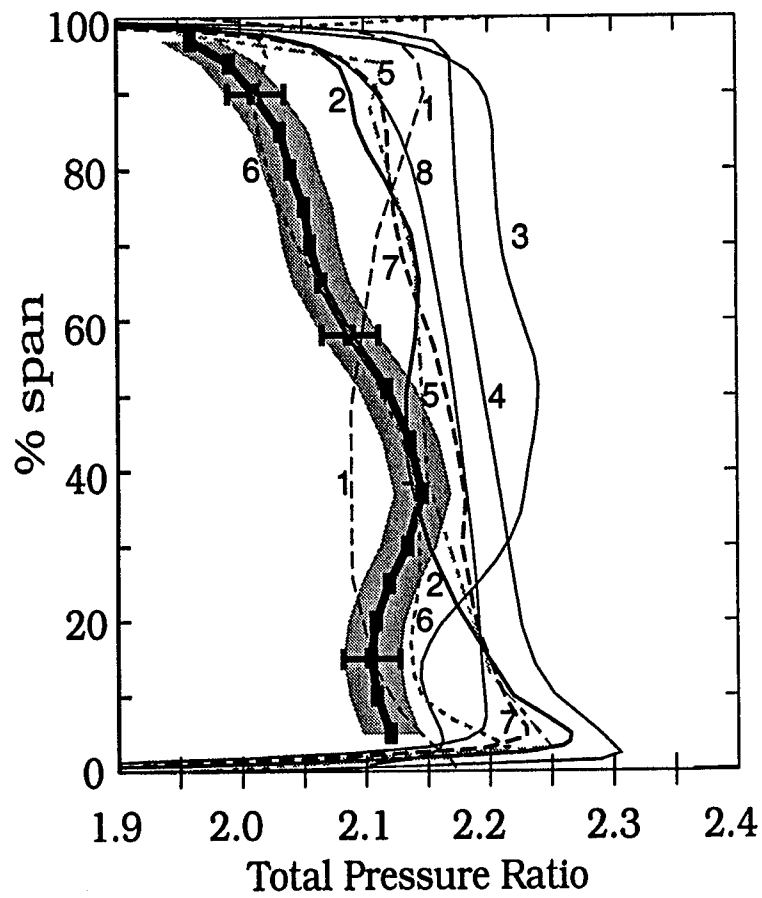


Figure 17 CFD blind testcase results: Radial distributions of total pressure and total temperature ratio.

optimize the radially-stacked blade sections accordingly. After the test results were released, the blind test case participants have done grid refinement studies, adjusted coefficients in their turbulence models, and have implemented different turbulence models. These efforts have enabled them to better match the overall performance levels. Yet they are still unable to match the radial distribution of pressure and temperature. Clearly, the CFD codes are not completely resolving the proper flow physics for this rotor. Why is this? What could be wrong? Possibilities include the following issues: 1) maybe the blade geometry is wrong, 2) maybe the data are wrong, 3) maybe the inaccuracies in the turbulence models are significant for this configuration, and 4) maybe the steady state CFD codes cannot be used for this configuration, i.e. a flow unsteadiness may be generated in the rotor which has a large impact on the flow field which is not being captured with the steady-state solutions. Geometry and data issues will be addressed in the 'Data Integrity' section of this chapter, and suffice it to say that they are not believed to be the problem. Issue 4 is being investigated using an unsteady CFD code but for an isolated rotor configuration it is difficult to believe that the flow unsteadiness is the problem. It is the author's belief that the problem lies within issue 3 in conjunction with the sensitivity of this rotor's performance to small changes in blockage. The sensitivity of this rotor's performance to small changes in blockage will be further discussed in **Chapter 5: Quantification of Blockage and Loss Estimates.**

It is somewhat surprising that the CFD simulations did not match the measured radial distributions of pressure and temperature for this rotor. However one must realize that rotor 37, in which the flow is supersonic from hub to tip with a pressure ratio greater than 2.1, is pushing the outer limits of the experience base where the CFD codes have been validated and calibrated. Fans generally have a pressure ratio of 1.4–1.6 and are subsonic in the lower half of the blade span, whereas core compressor stages are generally subsonic across the span. In addition, there is a very limited amount of detailed data on high speed rotors, and prior to this test virtually no detailed data within the blade passages existed on a rotor with supersonic inlet conditions across the span. Also, note that this machine was designed with a tight throat margin such that its performance is sensitive to small changes in blockage. In addition with such high inlet tip Mach numbers ($M_{rel}=1.48$) there is the potential for the shock to separate the boundary layer. Asking the CFD to accurately model the shock / boundary layer interaction is a true test of the CFD codes because they must accurately 1) simulate the characteristics of the boundary layer upstream of the shock / boundary layer interaction region, 2) predict the shock strength and location, 3) predict the interaction between the boundary layer and the shock, and 4) determine if the flow separates and if so how big is the separation. Calculating this phenomenon especially in a 3D situation is obviously a difficult task and is apparently beyond our current level of capability.

In conclusion, note that the reason for giving a brief synopsis of the ASME sponsored blind testcase results was to demonstrate the need to better understand the details of the flow field within the passages of this rotor. In the remainder of the report the emphasis will be to describe the flow physics within NASA rotor 37 using detailed experimental data which will enhance our understanding of this flow field and also serve as a benchmark for the CFD community.

4.2 General Flow Field Description

The objectives of this section are to 1) provide a general description of the circumferential variations that exist in the flow field, 2) show that the data acquired in both the radial-circumferential plane and the axial-circumferential plane are coherent, 3) define the endwall and core-flow regions of the flow field, 4) depict the circumferential variations that exist in the flow field at the downstream probe measurement location, and 5) provide experimental evidence depicting the generation of loss and blockage.

4.2.1 Description of Cross-Channel Flow Field Upstream and Downstream of the Rotor

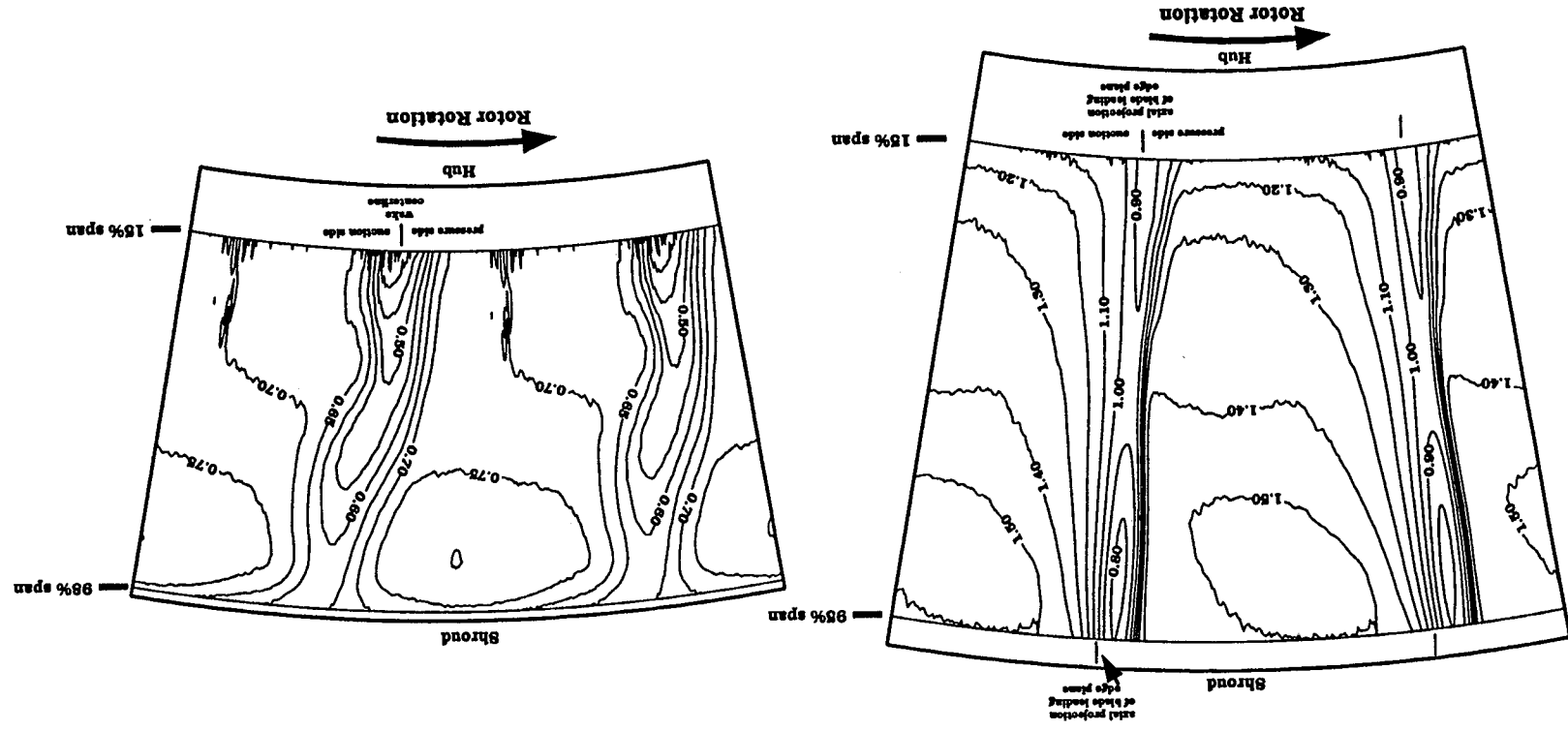
The axisymmetric rotor flow field was described in terms of the radial distribution of the total pressure ratio and total temperature ratio obtained across the rotor in the 'Overall Performance Characteristics' section above. These data were acquired with conventional low-response survey probes. In this section the

circumferential variations of the flow field as determined from laser anemometer measurements will be presented upstream and downstream of the rotor. The data will be presented in cross-channel plots of relative Mach number and absolute flow angle, which depict the flow field in the radial-circumferential plane. The inlet relative Mach number is primarily set by the radius and the wheel speed while the change in the relative Mach number across the rotor is directly related to the diffusion in the rotor blade passage. The absolute flow angle represents the amount the flow has been turned through the passage and is directly related to the work done by the rotor on the fluid for a given axial velocity— see equations 9, and 10. In addition, the absolute flow angle represents a parameter that is calculated directly from the laser anemometer measurements of the axial and tangential velocity and therefore is subject to minimal uncertainties and assumptions.

Relative Mach Number Contours. In Figure 18 the cross-channel relative Mach number contour plots upstream (-5% rotor chord at station #1a) and downstream (station #3 of Figure 11) of the rotor operating at design speed for the low flow condition are presented. Note that the view shown in all cross-channel plots is that seen by an observer looking upstream and rotor rotation is counter-clockwise. These plots have been scaled such that 1) a unit measure in the radial direction is equal to a unit measure in the circumferential direction, and 2) a unit measure in Figure 18a is equal to a unit measure in Figure 18b. Therefore, the

reduction in size of the figures is directly attributed to the reduction in the flowpath area. The outline of the figure depicts the flow path annular section from hub to shroud in the radial direction and across two rotor pitches in the circumferential direction. Data were acquired from 15% to 95% span in Figure 18a and from 15% to 98% span in Figure 18b. Figure 18a shows the bow wave system immediately upstream of the blade where there is a compression wave just upstream of the blade pressure surface and an expansion wave just upstream of the blade suction surface. The strength of this wave system diminishes with distance upstream of the blade leading edge. The inlet Mach number is supersonic throughout the measurement range and decreases with radius as expected. Note there is very little tangential lean in the bow wave which indicates the shock surface is nearly normal in this cross-channel plane. Referring to the downstream plot, the flow is subsonic and the variation in the circumferential direction at a given radial location is primarily due to the rotor wake. If for sake of discussion the edge of the rotor wake is defined by the relative Mach number contour level of 0.65, then the rotor wake encompasses about one third of the pitch, and thins toward 40% span. Also, there is some influence of the outer endwall on the flow field as evidenced by the bending of the contours in the outer 10% of span. Since the wake region is a region of loss, the narrower wake at 40% span is consistent with the increase in the pressure rise at 40% span which was shown in curve 7 of Figure 15a. In

Figure 18 Contours of relative Mach number in a cross-channel plane, a) upstream (-5% chord) and b) downstream (station #3) of the rotor operating at design speed and low flow condition.



conclusion, these cross-channel plots of relative Mach number illustrate that the data is consistent in the radial-circumferential plane and that there are consistencies between the probe measurements and the LFA data.

Absolute Flow Angle Contours. Cross-channel plots of absolute flow angle downstream of the rotor at station #3 and station #4a of Figure 11 are presented in Figure 19. Since the inlet absolute flow angle is zero (axial inlet flow) the contours of the absolute flow angle upstream are not presented. Since the blade surface boundary layer fluid undergoes more turning than the freestream fluid, the regions of increased absolute flow angle depict the rotor wake region. Station #3 is near the rotor exit and data here depicts the variation of the wake width and depth with radius. In the outer 10% of span the wake fluid, endwall boundary layer fluid, and tip clearance fluid become indistinguishable and encompass the entire circumference. Near the inner wall the data does not extend below 15% of span, and there is no identifiable inner endwall influence at this point. Clearly, the outer endwall region is more complex than the midspan. Therefore, throughout the remainder of this document the flow field will be broken into 1) the outer endwall region or tip region encompassing the flow area from 80%-100% span, and 2) the core flow region which includes the flow area from 20% to 80% span.

While the wake is clearly identified by the absolute flow angle contours at station #3, by station #4a the wake has mixed out such that the pitchwise flow

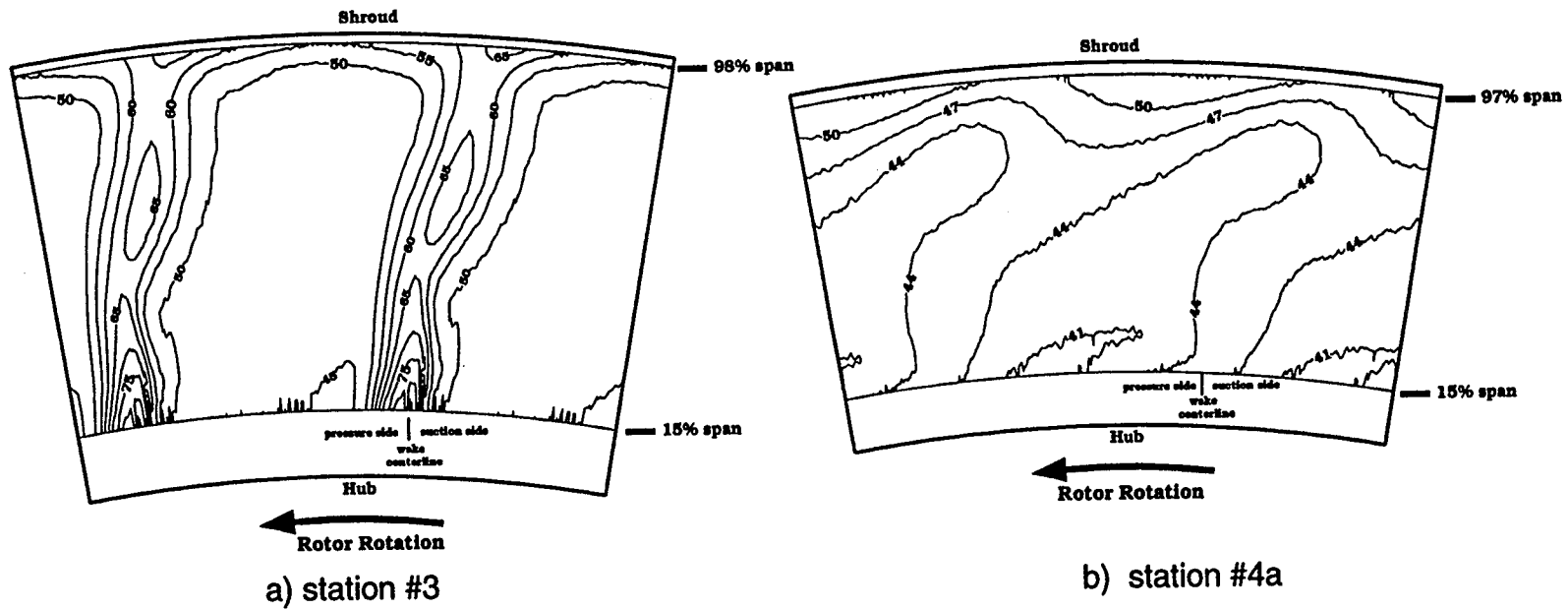


Figure 19 Contours of Absolute Flow Angle in a cross-channel plane, a) downstream (station #3) and b) downstream (station #4a) of the rotor operating at design speed and low flow condition.

angle variations are less than three degrees. Since station #4a is near station #4 where the probe surveys were acquired, the flow angle variations indicated by the cross-channel contour plot at station #4a are representative of the flow angle variations to which the probe measurements were subjected. In the following section discussing the 'Data Integrity' the axisymmetric average of the absolute flow angle at station #4a is compared to the survey probe data acquired at station #4 and the comparison will be shown to be within experimental uncertainty.

In summary, the cross channel plots of relative Mach number have demonstrated the diffusion that occurs across the blade passage and the plots of absolute flow angle have shown the amount the rotor turns the flow. The flow field can be divided into the core flow region and the endwall region. In the endwall region the flow is complex and contains wake fluid, endwall boundary layer fluid and tip clearance fluid. In the coreflow region the downstream flow consists of the freestream and the wake. The wake and freestream undergo significant mixing from the rotor exit to the far downstream measurement station. In the rotor frame of reference the inlet flow is supersonic and the exit flow is subsonic. The diffusion that occurs throughout the blade passage and the details of the rotor passage shock are not evident in these plots. Therefore, in the next section the flow field variations through the rotor along a blade-to-blade streamsurface will be presented.

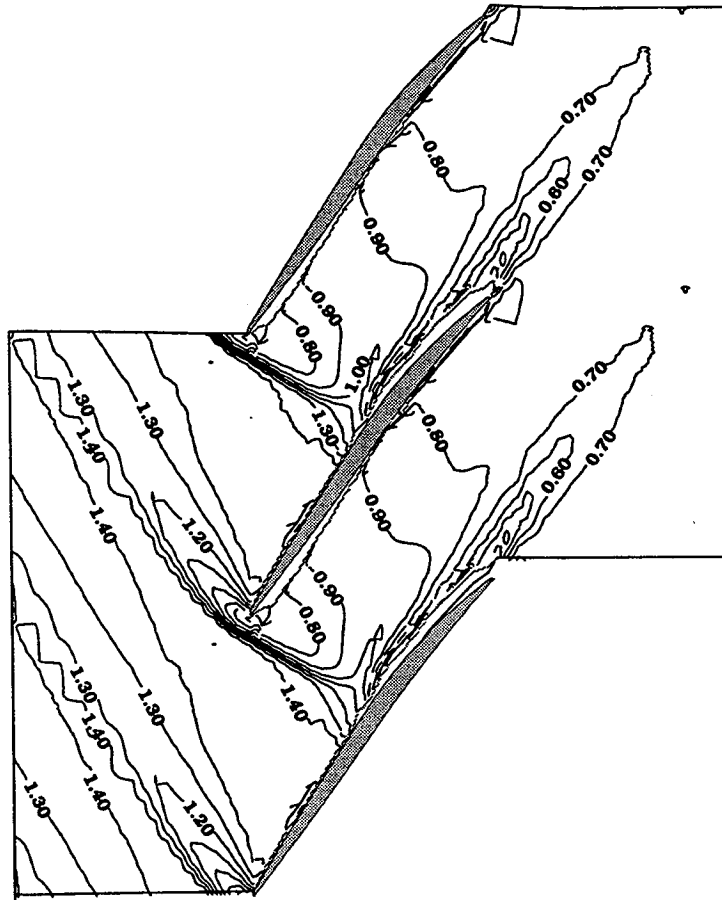


Figure 20 Contours of relative Mach number along the 70% streamsurface for the rotor operating at design speed and low flow condition.

4.2.2 Description of Blade-to-Blade Flow Field

The blade to blade flow field at 70% span for the rotor operating at design speed and low flow condition is presented in terms of relative Mach number contours in Figure 20. The white regions between the blade surfaces and the line where the contour lines end represent the region in which the measurements were difficult to obtain primarily because the beams and/or probe volume of the laser anemometer system were blocked by the rotor blades. In general this

blocked region will be on the pressure surface near the leading edge and on the suction surface near the trailing edge, due to the optics configuration and the blade geometry. The bow shock forms in the front of the blade and is detached. Downstream of the shock in front of the leading edge the flow is subsonic and there is a rapid acceleration around the leading edge of the blade on the suction surface. The flow continues to accelerate on the suction surface until it encounters the passage shock. Downstream of the shock the flow in the passage diffuses and the profile wake forms. Figure 21 features a blowup of the leading edge region of Figure 20 where the increment in the Mach number level has been decreased from 0.1 to 0.05 between contours. The shock strength is reasonable for a nearly normal shock as indicated by an upstream Mach number of 1.4–1.45 and a downstream Mach number of 0.7–0.8. (Note at an upstream Mach number of 1.4 a normal shock results in a post-shock Mach number of 0.74.) The spread in the contours across the shock is attributed primarily to the lag time associated with the seed particles not following the steep gradients through the shock. Also shown in Figure 21 is the interaction region between the rotor passage shock and the suction surface boundary layer. Since the boundary layer fluid cannot sustain the steep pressure gradient resulting from a nearly normal shock, the flow field adjusts and the shock becomes more oblique near the blade surface, thereby forming a lambda (λ) shock. Downstream of the lambda shock is evidence of a thickening of the blade suction

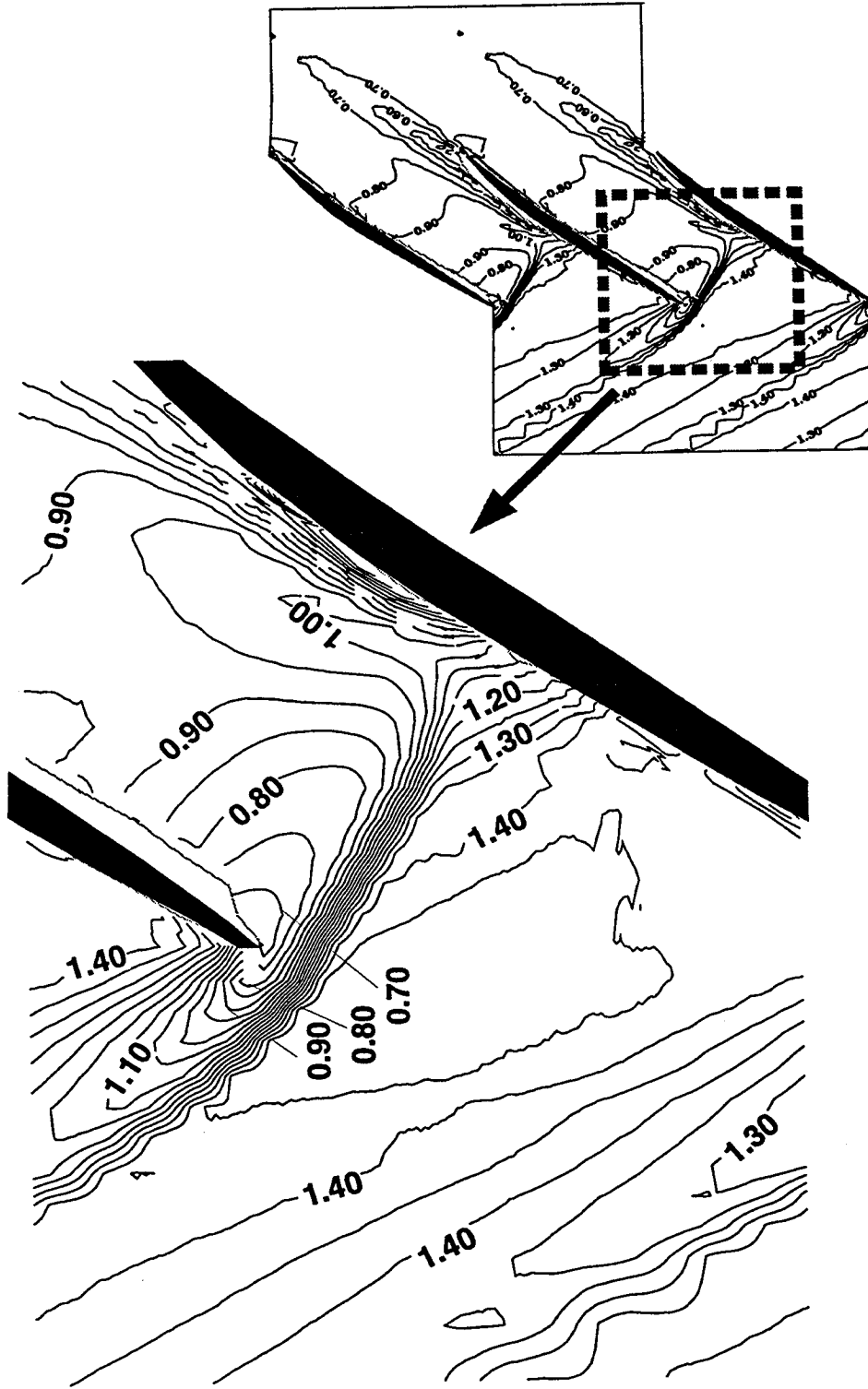


Figure 21 Zoom of Figure 20 depicting blade leading edge and shock boundary layer interaction region.

surface boundary layer (more clearly seen in Figure 20). Downstream of the shock and especially near the trailing edge it is evident that the suction surface boundary layer is considerably thicker than the pressure surface boundary layer. In summary, there is evidence of at least four loss mechanisms: 1) viscous drag on solid surfaces, i.e. blade boundary layers, 2) losses in total pressure associated with a shock system, 3) additional loss incurred by the thickening of the boundary layer resulting from the shock / boundary layer interaction, and 4) mixing losses inherent to the merging of the suction and pressure surface boundary layers to form the blade wake and subsequent downstream mixing.

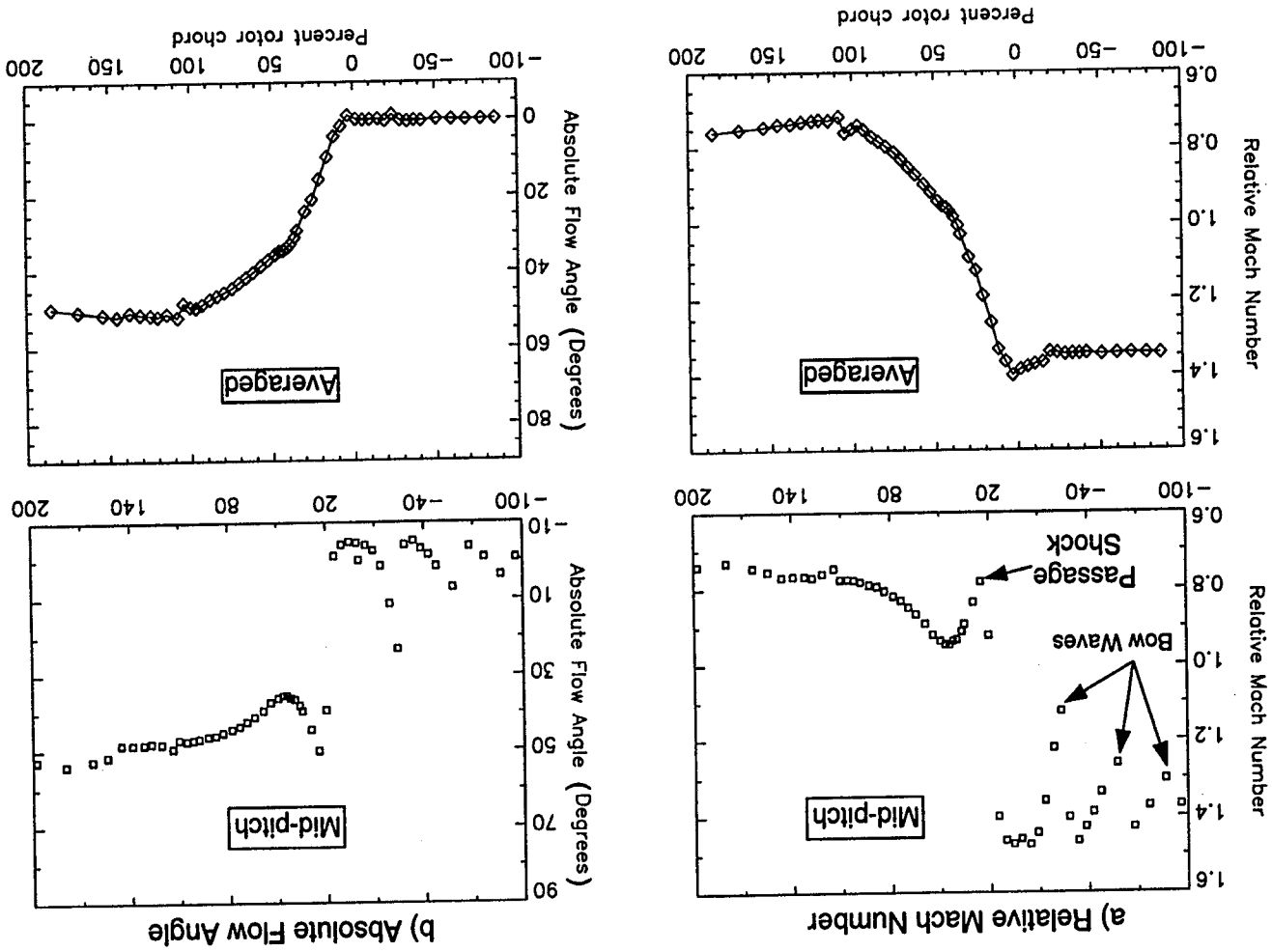
4.2.3 Comparison of the Axisymmetric Average Flow Field Versus the Flow Field at Mid-pitch.

A more quantitative view of the blade-to-blade flow field can be shown by plotting the data along the midpitch line through the compressor rotor and comparing it to the axisymmetric average of the flow field in the blade-to-blade plane. The axisymmetric average is calculated by forming an axial velocity weighted average (as opposed to a mass average) of the flow properties in the circumferential direction. Therefore the axisymmetric average results in a two-dimensional description of the flowfield in the axial/radial plane which is analogous to the results from through-flow CFD codes which are heavily used in the initial stages of the design process. The data along midpitch is representative

of the flow field in the 'inviscid freestream' while the axisymmetric average results include the viscous effects. A comparison between the data along mid-pitch and the axisymmetric average flowfield is presented to evaluate the diffusion and flow turning through the passage in an average sense and to assess the impact of the viscous effects on the flow behavior. The relative Mach number and absolute flow angle distributions along the midpitch line as well as the axisymmetric average of the 70% span streamsurface flow field for the rotor operating at design speed and low flow condition are presented in Figure 22.

Mach Number Distribution. The Mach number distribution along the midpitch line shows that the bow waves decrease in strength with increasing upstream distance. The passage shock accounts for the significant diffusion that takes place in the passage. Downstream of the shock there is a re-acceleration followed by a subsequent diffusion in the rear part of the passage to a level at the blade exit which is comparable to that observed immediately downstream of the shock. The axisymmetric average of the flow field indicates essentially a uniform inlet Mach number with continuous diffusion throughout the entire passage. The pre-shock and the exit relative Mach number from the midpitch line distribution is consistent with those from the axisymmetric average; however, the details in the diffusion through the passage are substantially different. The axisymmetric average relative Mach number indicates that the diffusion is attributed to the

Figure 22 Axisymmetric average and mid-pitchline relative Mach number and absolute flow angle distributions along the 70% streamsurface for the rotor operating at design speed and low flow condition.



passage shock and the diffusion in the rear of the blade passage. However, the mid-pitch line distribution indicates that there was no additional 'net' diffusion downstream of the shock because the diffusion in the rear of the passage merely offset the acceleration downstream of the shock. The re-acceleration at mid-pitch is driven by some non-axisymmetric influence such as a near wall viscous effect.

Absolute Flow Angle Distribution. In comparing the Mach number distribution to the flow angle distribution along mid-pitch it is evident that the flow turning occurs primarily across the passage shock. The axisymmetric average of the flow angle indicates that the average inlet flow angle is zero per the design and the axisymmetric averaged flow angle is comparable to the mid-pitch value at the rotor exit. Similar to the distributions of the relative Mach number, the flow turning through the rotor is substantially different for the axisymmetric results as compared to those at midpitch. The mid-pitch line distribution indicates that there was no additional 'net' turning downstream of the shock because the turning in the rear of the passage merely offset the decrease in the turning immediately downstream of the shock. Note, the absolute flow angle distribution (which for a constant chordwise axial velocity reflects the work input) is a mirror image of the relative Mach number distribution (which is indicative of the diffusion or pressure rise in the passage) in the sense that a decrease in relative Mach number coincides

with an increase in absolute flow angle and vice versa. Therefore, throughout the remainder of this chapter only the relative Mach number will be shown.

The rotor blade was designed with camber in the back half of the blade to increase the turning and therefore the diffusion in the aft part of the blade. However, it is clear from these figures that the flow angle and relative Mach number at the rotor exit are nearly equal to the values immediately downstream of the shock. The reacceleration and reduction in flow angle immediately downstream of the shock, as indicated in the midpitch line distributions, is clearly non-desirable and must be driven by some additional blockage to the flow. The hypothesis is that there is an increase in the boundary layer thickness downstream of the shock, resulting from the interaction between the passage shock and the suction surface boundary layer, which creates a blockage and induces an acceleration of the flow downstream of the shock, thereby reducing the flow turning in the passage. This additional blockage would also explain why measured values of the total temperature and total pressure rise at the outer spans of the rotor were lower than the design values (refer to the overall performance plots of Figure 13).

It is clear in a transonic compressor the shock system is a key player in determining the work input and the losses associated with compressor performance. In order to optimize blade performance it is exigent to 1) tailor the shock system to maximize pressure rise for the blade row and minimize shock loss, 2) better

understand the interaction between the passage shock and the blade surface boundary layer to reduce profile loss without sacrificing pressure rise capabilities. Therefore, it is imperative to fully understand and be able to predict the rotor shock structure and its interaction with the blade boundary layers. In the following sections, the characteristics of the rotor shock structure and the sensitivity of the rotor shock structure to the flow field will be addressed.

4.3 Data Integrity

Prior to further presentation of results, some checks on the integrity of the data will be discussed. Since the data were acquired over many months, issues such as the ability to reset the operating conditions and the repeatability of the data are critical. In addition, the CFD results are dependent on the blade geometry and therefore such issues as the geometry under load must be considered. Therefore, in Appendix A :‘Data Integrity,’ experimental documentation of the following are presented:

1. The data repeatability.
2. The particle lag associated with the LFA seed particles and its impact on the results.
3. The magnitude of passage-to-passage flow field variations and their impact on the results.
4. The level of agreement between the LFA and probe measurements.

5. The accuracy of the blade geometry.

A summary of the results presented in Appendix A is described below:

1. The data are repeatable within the experimental uncertainty of the measurements.
2. The particle lag distance across a normal shock with an inlet Mach number of 1.4 has been conservatively estimated to be 5–8% chord, and caution must be employed when evaluating the data immediately downstream of the shock. Since, in general the data are acquired every 5% chord this implies that the first measurement station downstream of the shock is subjected to particle lag effects. The particle lag distance is assumed negligible in all other regions of the flow field where the gradients are much less severe than those across a normal shock with an inlet Mach number of 1.4.
3. The variations in the rotor wake and shock characteristics among all of the rotor passages were evaluated at the high flow operating condition where the shock structure is sensitive to small changes in the backpressure and blade geometry. The results indicate that the effect of the passage to passage variations on the average passage results are 1) greatest on the location of the rotor shock, 2) much reduced at other regions in the flow field, and 3) small enough to warrant an average passage representation of the flow field.

4. Absolute flow angle, total temperature, and absolute velocity obtained from the aerodynamic probe measurements are compared to those obtained from the laser anemometer measurements. The results indicate the LFA measured velocities and the calculated flow angles and temperatures are within the stated uncertainty intervals. The procedure to calculate the temperature, and therefore the Mach number, with the LFA measured velocities has been validated to the extent that the results are in agreement with conventional thermocouple measurements. The comparisons of the laser anemometer results to 1) the conventional aerodynamic probe results and 2) to the CFD results of Wood [58] show that the LFA measurement system is working properly and it can be used to assess the velocity, flow angle, and temperature variations throughout the rotor flow field.
5. For a highly-loaded blade such as rotor 37 the geometry of the blade changes with operating condition due to the aerodynamic loading and rotational forces acting on the blade. The geometry is categorized as 'cold' geometry in reference to the geometry of the blade under no load at zero rotational speed (i.e. the manufacturing coordinates), and 'hot' geometry in reference to the geometry of the blade under load at the design rotational speed. The 'cold' geometry was inspected in the NASA Lewis Inspection Laboratory. Based on detailed inspections of the 'cold' blade geometry, which provided the

blade surface contour, the blade coordinates, and the blade surface angles, it was concluded that the blade was made to its specifications within the manufacturing tolerances. The 'hot' geometry under design speed conditions was determined by a NASTRAN analysis, which computes the stresses and deflections on the blade. The LFA system was used to determine the blade geometry of the blade tip section for the rotor running at base speed (2000 rpm) and design speed (17200 rpm). Based on the agreement of the blade geometry in the tip section between the NASTRAN analysis and the LFA measurements, the NASTRAN predicted geometry at design speed is believed to be the actual 'hot' geometry for the rotor operating at design speed, and it is the geometry that was provided to the CFD participants.

4.4 Sensitivity of Loss and Blockage Development in the 'Core Flow Region' to Changes in the Rotor Back Pressure at Design Speed.

Thus far the following loss mechanisms have been identified: 1) viscous loss due to the development of the blade boundary layers, 2) loss across the shock, 3) loss or blockage generated by the interaction between the passage shock and the boundary layer, and 4) loss associated with the wake including the mixing loss incurred from the merging of the pressure surface and suction surface boundary layers and that due to the mixing of the wake downstream of the blade. It was evident that the shock structure plays a significant role, both directly and indirectly,

in establishing these losses. In this section the variations in the blade-to-blade flow field with changes in the rotor back pressure will be discussed. In particular: How is the shock affected? How is the blade loading affected? How are the aforementioned loss mechanisms affected?

4.4.1 Impact on Measured Blade-to-Blade Flow Field

Relative Mach Number Contours. A description of the blade-to-blade flow field along the 70% streamsurface is depicted by contours of the relative Mach number for the rotor operating at design speed and the max flow, high flow, and low flow conditions in Figure 23. The slight variation in the inlet relative Mach number among these three operating conditions can be discerned by comparing the far upstream Mach contours. As the rotor back pressure is increased (from max flow to low flow condition), the passage shock is pushed further forward in the blade passage and the exit relative Mach number decreases. The differences between these contour plots are subtle in comparison to the differences in the overall performance between these three conditions as was shown in Figure 15, where max, high, and low flow correspond to curves labelled 1, 4, and 7 respectively. It is noteworthy that most comparisons between CFD and data are made with contour plots which generally do not provide sufficient detail to assess how well the data and CFD agree. The relative Mach number contours provide

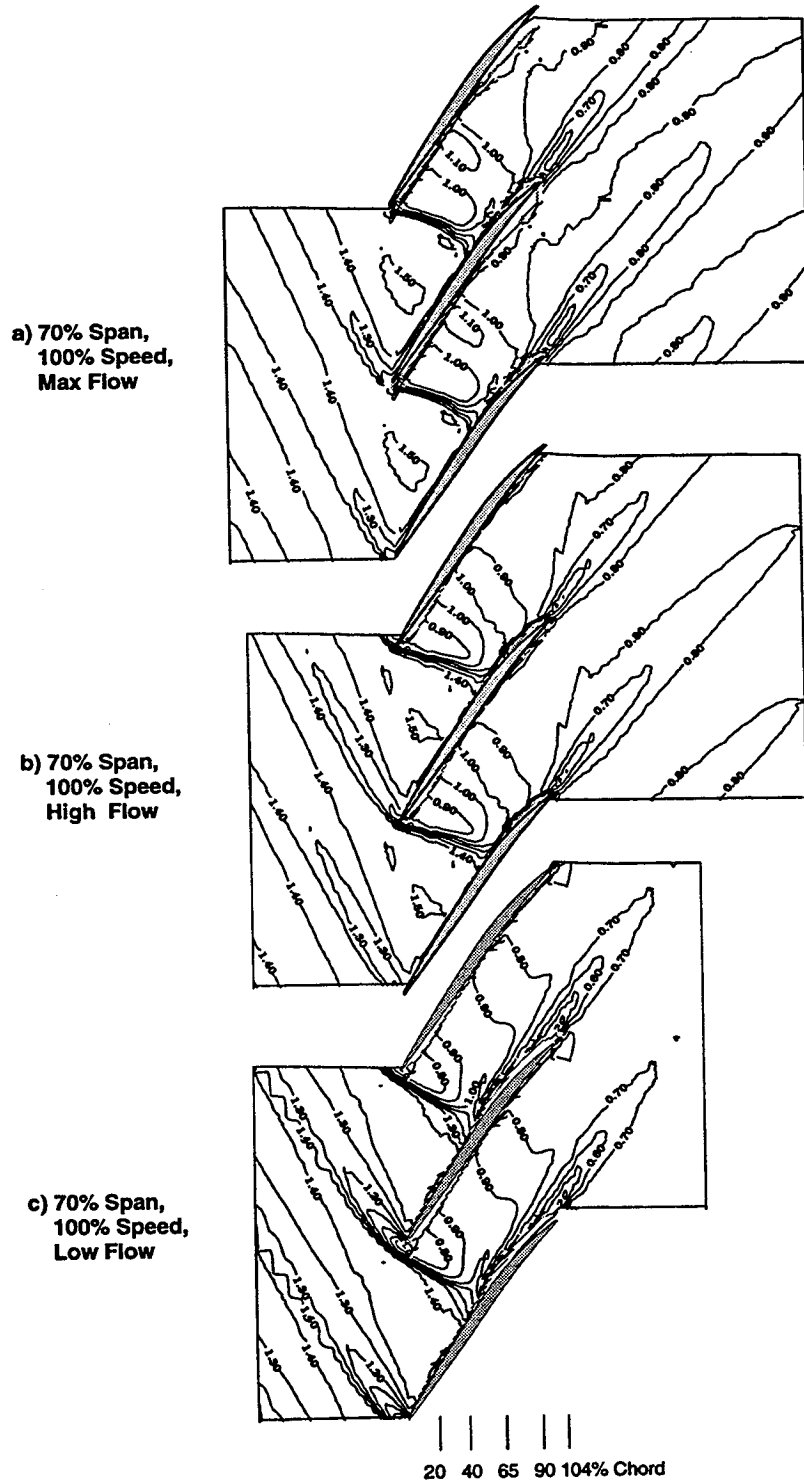


Figure 23 Contours of the relative Mach number in a blade-to-blade view along the 70% streamsurface for design speed and the a) max flow condition, b) high flow condition, and c) low flow condition.

a concise overview of the flow field, but in order to get a more quantitative description the data will be analyzed through the use of line plots.

Line Plots Indicating the Variation in the Pitchwise Direction. In Figure 24 the data are plotted in the pitchwise direction from the suction surface to the pressure surface for fixed axial locations corresponding to 20%, 40%, 65%, 90%, and 104% of rotor chord. These axial locations were selected to provide the details of the flowfield upstream and downstream of the shock impingement on the blade suction surface and near the blade trailing edge. For the plots at 20% to 90% of rotor chord the suction surface of one blade is on the left ordinate axis and the neighboring blade is shaded on the right side of each plot. The space between the last data point and the blade surface represents a region where no LFA data was acquired. For the plots at 104% rotor chord the data were shifted so that the profile wake, which results from the merging of the blade suction and pressure surface boundary layers, is centered in the middle of the plot. From the data at 20% chord in Figure 24 it is evident that 20% chord is upstream of the shock impingement on the blade suction surface. The shock is pushed forward in the passage with increasing rotor exit pressure as indicated by the shock being closer to the suction surface at the low flow condition in comparison to the max and high flow conditions. The Mach number change across the shock coupled with the measured relative flow angle can be used to assess the obliquity of the shock

relative to the oncoming flow. Applying this procedure to the data at 20% chord in Figure 24 indicates the shock is normal to the flow at low flow condition but is oblique for higher flow rates.

At 40% chord the data in Figure 24 indicate the shock has not impinged on the suction surface for the max flow and high flow conditions and is located at approximately the same location in the passage. However, for the low flow condition the data at 40% chord slices through the region where the shock impacts the blade suction surface. The flow at max and high flow conditions depicts an increase in the Mach number between the suction surface and the passage shock which would imply the flow is accelerating on the suction surface side of the passage near 40% chord. Similarly, there is an increase in the Mach number between the shock and pressure surface which implies the flow is accelerating on the pressure surface side of the passage near 40% chord. (Both of these regions of accelerating flow are also depicted in the contour plots in Figures 23a and 23b.) This acceleration downstream of the shock (in a region of Mach number less than one) on the pressure surface side of the passage implies that the effective flow area is decreasing which is believed to result from a blockage on the suction surface side of the passage which was generated from the shock boundary layer interaction.

In Figure 24 the data at 65% chord is downstream of the shock impingement point on the blade suction surface. There is evidence of a suction surface and

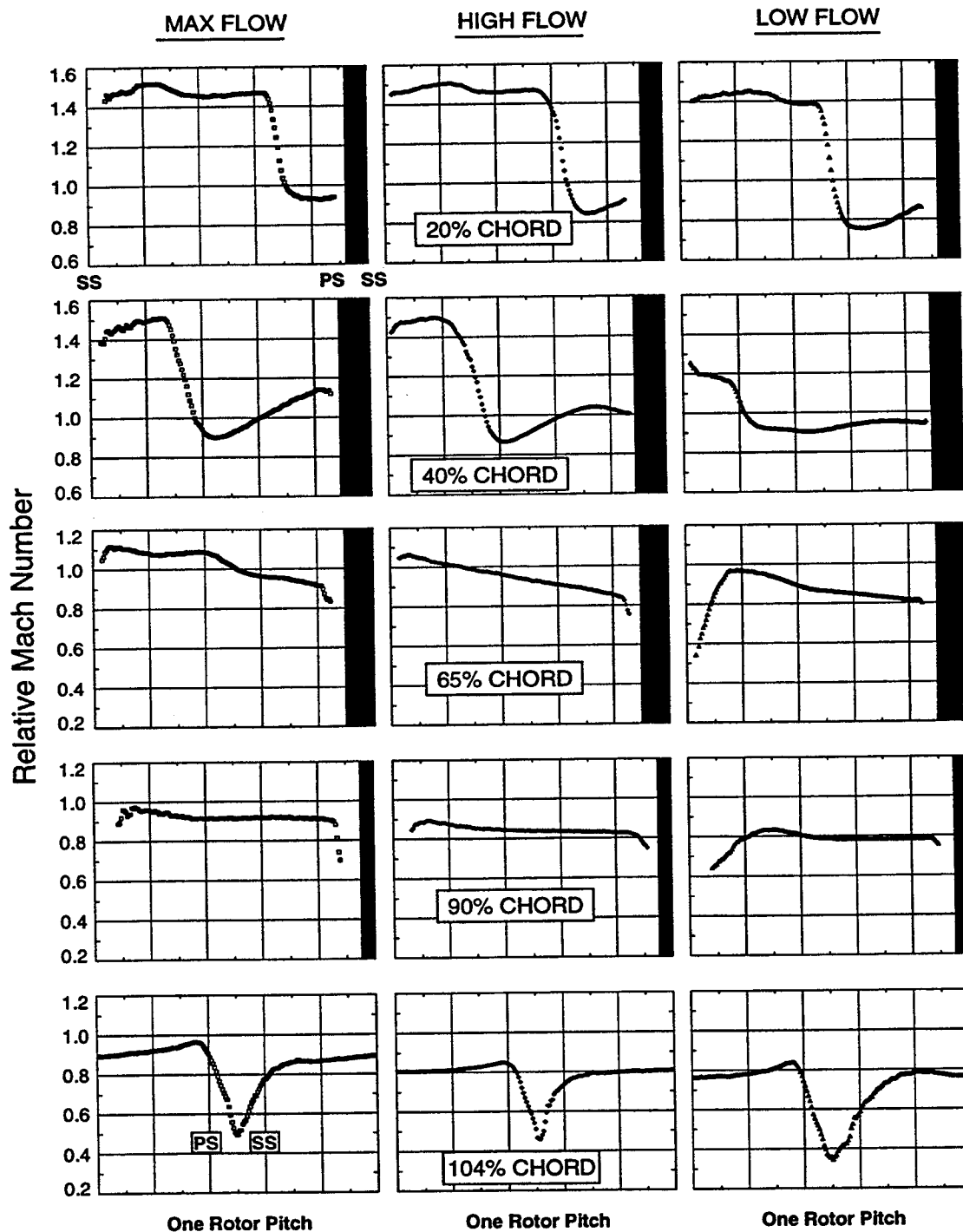


Figure 24 Pitchwise line plots of the relative Mach number at the 70% streamsurface for design speed and max flow, high flow, and low flow condition at 20% chord, 40% chord, 65% chord, 90% chord, and 104% chord.

pressure surface boundary layer for all three operating conditions. The differences in the thickness of the pressure surface boundary layer between operating conditions is indistinguishable. However, the suction surface boundary layer for the low flow condition is substantially thicker than that for the max flow and high flow conditions. The relative Mach number is greater than one across half of the pitch for the max flow condition and there is evidence of a weak passage shock. The relative Mach number remains greater on the suction surface than the pressure surface and these differences are indicative of the blade loading (difference in pressure on the blade pressure surface to the suction surface) at 65% chord.

In Figure 24 the data at 90% chord indicate that the relative Mach number is essentially constant across the pitch except near the blade surfaces, thereby indicating that the blade loading is very light at 90% chord. The 'freestream' level of the relative Mach number decreases with increasing rotor back pressure, indicating more diffusion since the inlet Mach number was nearly constant. In addition, the blade suction surface boundary layers have become noticeably thicker in going from 65% to 90% chord.

The data downstream of the blade trailing edge at 104% chord depict the width and depth of the rotor wake which is indicative of a region of loss and blockage. The width of the wake at 104% chord is comparable to the width determined by the sum of the blade thickness plus the thicknesses of the blade

pressure and suction surface boundary layers at 90% chord. Since the boundary layer did not grow appreciably from 90% chord to 104% chord, the characteristics of the wake can be directly traced back to the development of the blade pressure and suction surface boundary layers. For example, it is evident that the wake at 104% chord is much wider for the low flow condition in comparison to the max and high flow conditions. These differences in the wake width can be traced to the boundary layer development within the blade passage where the increased wake thickness at low flow condition is attributed to the increased thickness of the suction surface boundary layer.

In summary, the rotor shock is pushed further forward in the blade passage and becomes more normal (and therefore stronger) with increasing rotor back pressure. Therefore the shock loss increases with increasing rotor back pressure. The wake identifies another region of loss and blockage and its formation can be traced back the development of the blade boundary layers. The suction surface boundary layer appears to grow appreciably downstream of the shock impingement on the blade suction surface, while the pressure surface boundary layer does not grow appreciably. Factors affecting the boundary layer growth on the suction surface are 1) the strength of the shock (is it strong enough to separate the suction surface boundary layer?), 2) the condition of the boundary layer at the shock impingement point on the suction surface, and 3) the pressure gradient downstream of the

interaction between the shock and suction surface boundary layer. Therefore, in the next section the relative Mach number distributions along the suction and pressure surfaces will be presented because they provide an indicator of the blade loading, the location of where the shock hits the suction surface, and the pressure gradient downstream of the shock / boundary layer interaction.

4.4.2 Impact on Measured Blade Loading Distribution

The blade surface relative Mach number distribution provides a description of where the shock hits the blade suction surface in addition to indicating the rate of diffusion on the blade surface. The blade surface Mach number can be related to the pressure coefficient, C_p , by the following:

$$C_p = \frac{(p - p_1)}{0.5\rho_1 V_{rel,1}^2} = \frac{2}{(\gamma M_1^2)} \left\{ \left[\frac{2 + (\gamma - 1)M_1^2}{2 + (\gamma - 1)M^2} \right]^{\frac{\gamma}{\gamma-1}} * \frac{P'}{P_1} - 1 \right\} \quad (13)$$

and for isentropic flow the relation becomes:

$$C_p = \frac{(p - p_1)}{0.5\rho_1 V_{rel,1}^2} = \frac{2}{(\gamma M_1^2)} \left\{ \left[\frac{2 + (\gamma - 1)M_1^2}{2 + (\gamma - 1)M^2} \right]^{\frac{\gamma}{\gamma-1}} - 1 \right\} \quad (14)$$

Here M is the local relative Mach number at the edge of the boundary layer and M_1 is the reference relative Mach number which is taken as the Mach number at the edge of the suction surface boundary near the blade leading edge. Note that the Mach numbers used in this calculation are not based on isentropic flow assumptions and do include the temperature rise across the shock. The purpose of calculating the static pressure coefficient C_p is to cast the measured relative

Mach number distribution into its equivalent static pressure coefficient which then can be used to describe the blade loading (pressure difference between the blade surfaces) as well as the pressure gradient in the streamwise direction on each of the blade surfaces. Since the relative total pressure downstream of the shock is unknown and since the errors incurred by assuming isentropic flow to calculate the static pressure coefficient are small, equation 14 was used to evaluate the isentropic static pressure coefficient. Note the flow is nearly isentropic along the pressure surface and upstream of the shock on the suction surface, such that the errors in assuming isentropic flow to calculate C_p occur mainly on the suction surface downstream of the shock. The maximum error in assuming isentropic flow for this flowfield would result from the loss in total pressure across a normal shock at Mach number 1.5 which implies $1.0 \geq \frac{P'}{P_1} \geq 0.93$. Therefore the maximum error associated with assuming isentropic flow conditions to calculate C_p (i.e. the error in using equation 14 as opposed to equation 13) is about 12% and this error may occur only for the data located downstream of the shock on the blade suction surface. (Note that the calculated isentropic value of C_p is greater than the 'true' value by 0–12%.) This error is acceptable considering that the plots of static pressure coefficient are used only for qualitative discussions. Since the relative Mach number is obtained directly from the velocity measurements, the

wheel speed, and Euler's turbine equation, there is no such error associated with the measured relative Mach number distribution.

The plots of the measured relative Mach number distribution at the edge of the boundary layer and calculated isentropic static pressure coefficient at the 70% span streamsurface for the max flow, high flow and low flow conditions are presented in Figures 25 and 26, respectively. Note that the determination of the relative Mach number at the edge of the boundary layer for each chordwise point is evaluated independently of the others, yet the overall plot is consistent and therefore believed to be accurate. (The technique used to define the edge of the boundary layer will be addressed in the next chapter.) In addition, the values of static pressure coefficient at the blade trailing edge for the pressure and suction surfaces are nearly equal, and therefore using the isentropic static pressure coefficient is reasonable.

It is evident that the suction surface behaves much like a flat plate at zero pressure gradient (no acceleration or diffusion) prior to the passage shock. In general the relative Mach number distribution indicates a deceleration around the leading edge on the pressure surface side followed by an acceleration to a local maximum Mach number around 30–40% chord followed by a diffusion in the rear half of the blade. In contrast, the suction surface indicates a nearly uniform Mach number up to the shock impingement point, a rapid diffusion over the region of influence of the passage shock, followed by a more gradual diffusion over

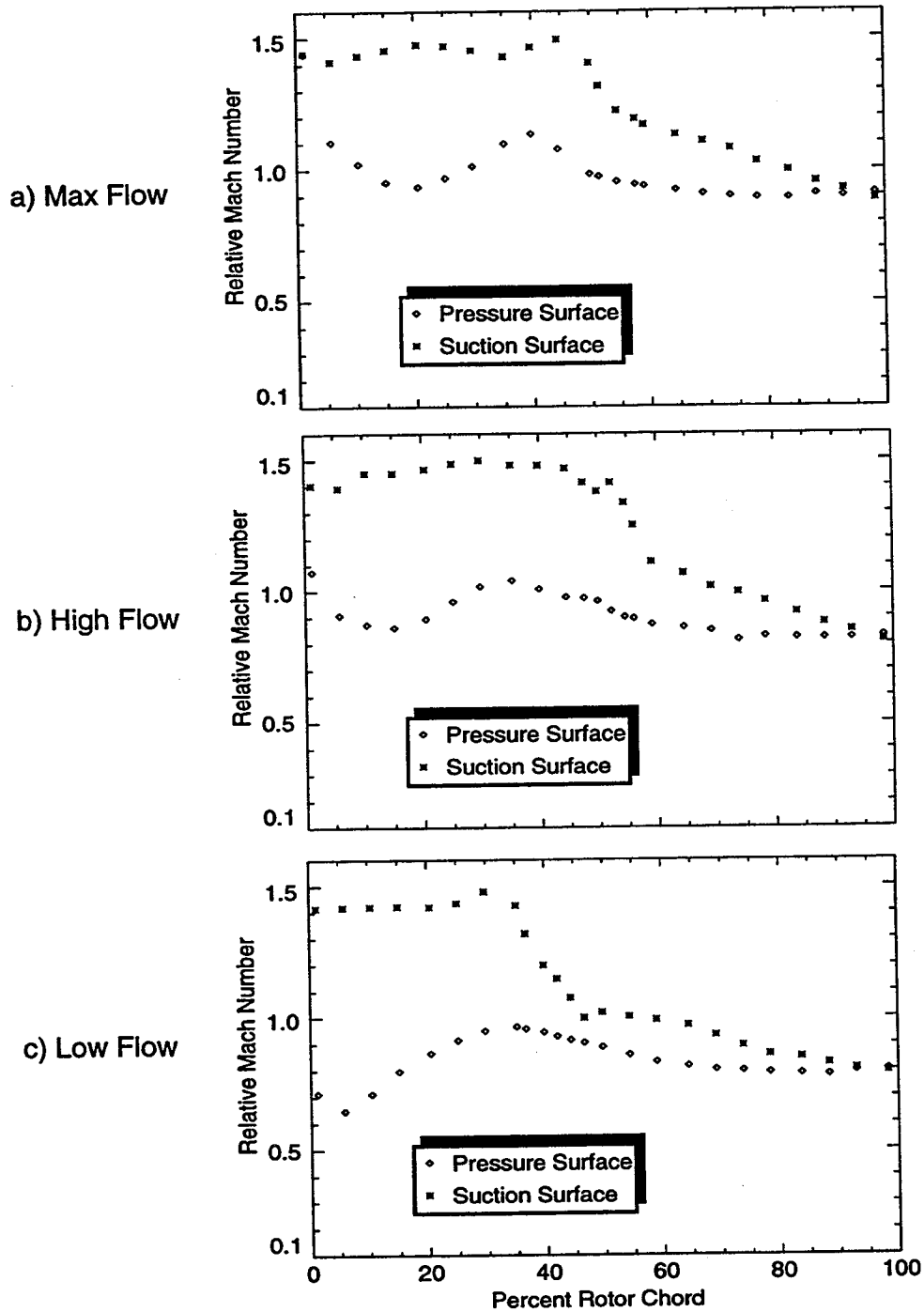


Figure 25 Distributions of the relative Mach number near the blade surfaces along the 70% streamsurface for design speed and the a) max flow condition, b) high flow condition, and c) low flow condition.

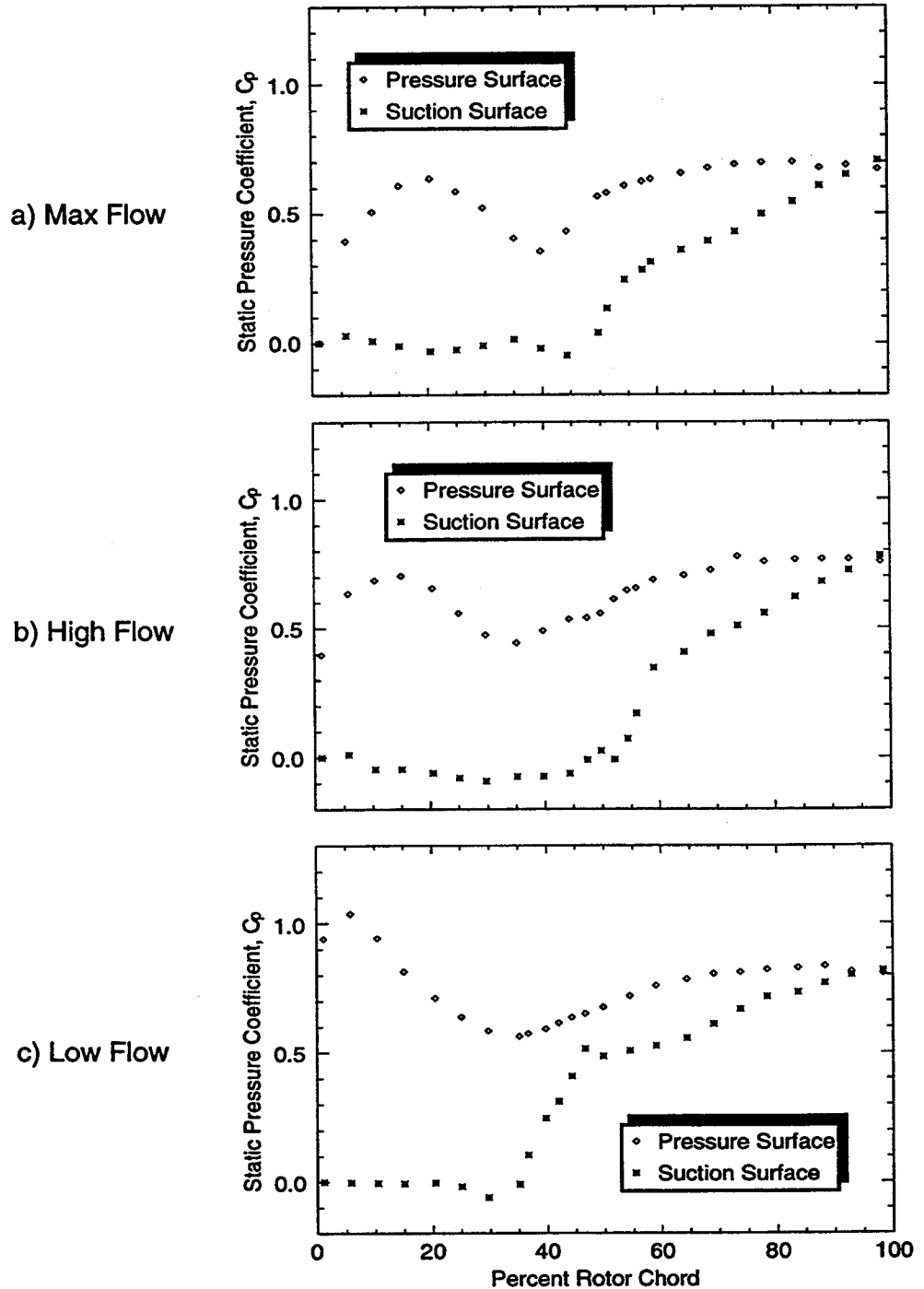


Figure 26 Distributions of the isentropic static pressure coefficient along the 70% streamsurface for design speed and the a) max flow condition, b) high flow condition, and c) low flow condition.

the rear half of the passage. It is evident that the shock impinges on the blade suction surface at 45–50% chord for the max flow and high flow conditions and at 30–35% chord for the low flow condition.

Note that the blade loading is indicated by the area between the pressure surface and suction surface curves of the static pressure coefficient. It is evident that the blade loading is greater in the front half of the passage as compared to the rear half of the passage. As the rotor back pressure is increased the blade loading in the front part of the passage increases as the shock is pushed forward in the passage. The region of influence of the shock /boundary layer interaction begins at the shock impingement point on the suction surface and is assumed to end where the slope of the static pressure coefficient changes abruptly to the slope corresponding to the pressure gradient in the rear part of the blade. Therefore the influence of the shock on the blade suction surface ends by 55% chord for the max flow, 60% chord for the high flow, and near 50% chord for the low flow. The pressure gradient in the rear part of the blade suction surface is nearly identical for the max and high flow conditions. The pressure gradient downstream of the shock / suction surface boundary layer interaction region for the low flow condition is much lower than that of the high and max flow conditions.

Recall, from Figure 24 the wake at low flow depicted the largest width despite the fact that the pressure gradient in the rear part of the passage is the lowest. It

is evident that the increased wake width at the low flow condition is due to the strength of the shock substantially thickening the suction surface boundary layer. However, at max flow the wake is wider than at high flow despite the fact that the shock is weaker and the pressure gradient in the rear part of the passage is nearly identical at max and high flow. It is unclear why the wake at max flow is wider than at high flow, but the following two reasons attribute to this fact: 1) Careful examination of the region of influence of the shock / boundary layer interaction on the suction surface indicates that the boundary layer downstream of the shock is influenced by the downstream pressure gradient from 55%—100% chord for the max flow condition in comparison to 60–100% chord for the high flow condition. Therefore, the suction surface boundary layer at max flow is slightly thicker than the boundary layer at high flow because the shock/boundary layer interaction ends earlier in the passage (probably due to the weaker shock strength) and the boundary layer is subjected to the pressure gradient in the rear part of the passage over a longer distance than the suction surface boundary layer at high flow condition.

2) The boundary layer at max flow conditions is thicker than that at high flow because at max flow the boundary layer is subjected to the primary passage shock and a secondary weaker shock in the rear portion of the blade.

4.4.3 Comparison to CFD Blade-to-Blade Flow Field

Recall that the intent of making these comparisons is to demonstrate the sensitivity of the rotor performance to small changes in blockage. Presented in Figure 27 is the blade to blade plot of the relative Mach number distribution along the 70% span streamsurface at design speed and high flow condition (which is the same operating condition at which the CFD and data were compared in the first section of this chapter dealing with the overall performance characteristics — refer to Figure 17) from the CFD solution #2 and the experimental measurements. Note the experimental results are identical to those presented in Figure 23b and are repeated here for comparison to the CFD results. The flow field upstream and downstream of the rotor blade are nearly identical for the CFD and data results. However within the blade passage the data indicates a relative Mach number of greater than 0.9 which reaches a value of 1.0 and greater downstream of the shock, whereas the CFD result indicates the relative Mach number downstream of the shock is primarily less than a value of 0.9. Therefore, the CFD is predicting more diffusion in the blade passage which is consistent with a higher work input which was expressed in terms of higher temperature rise at 70% span in Figure 17. Note the CFD does properly predict that the shock is detached from the blade leading edge and that the contours depicting the passage shock are spread further apart than those of the data. This smearing of the shock in the CFD results is due to

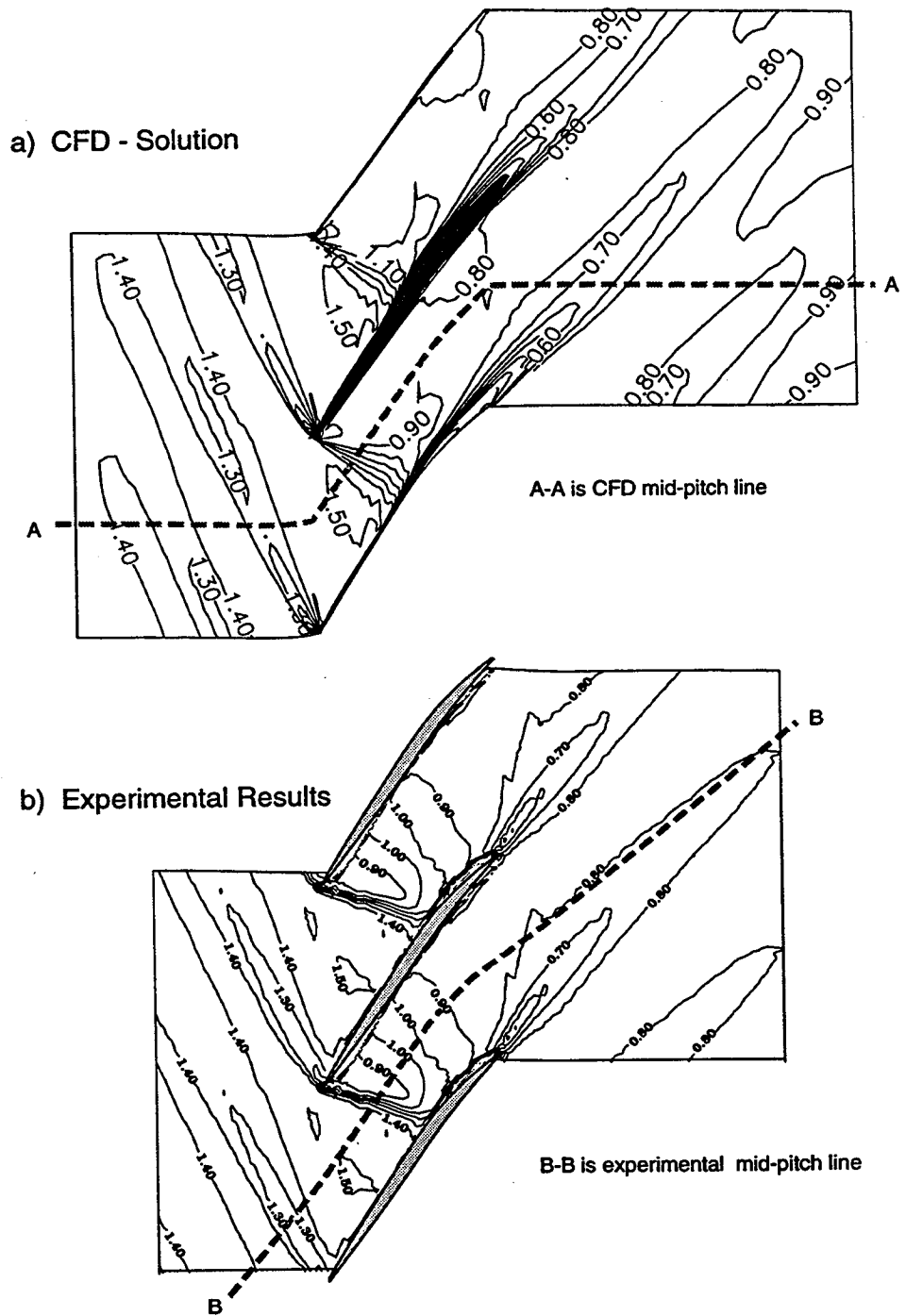


Figure 27 Contours of the relative Mach number in a blade-to-blade view along the 70% streamsurface for design speed and the high flow condition — a) based on the CFD solution and b) based on the experimental measurements.

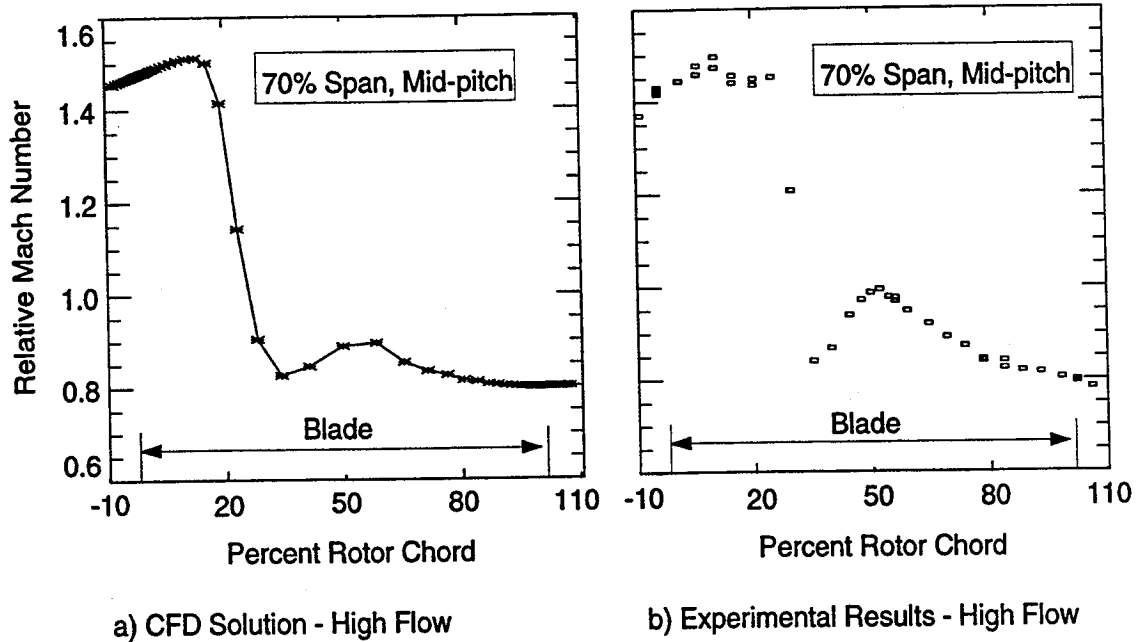


Figure 28 Comparison of the relative Mach number along the Midpitch line at 70% streamsurface for design speed and the high flow condition — a) based on the CFD solution and b) based on the experimental measurements.

the spacing of the computational grid which is clustered in the axial direction near the leading and trailing edges of the blade, but is stretched to an axial spacing of approximately 7% of axial chord by rotor mid-chord. Solutions have been performed where the grid was refined such that the axial spacing was limited to a maximum spacing of 1% chord. The results indicated a much sharper shock structure as expected but the flow field upstream and downstream of the shock was only mildly affected such that this CFD solution (#2) is still overpredicting the diffusion in the passage.

A more quantitative comparison between the CFD of solution #2 and the data is depicted in Figure 28 where the data along the midpitch line (identified in

Figure 27) from 0 to 100% chord is plotted for both the CFD and the data. The inlet Mach number, location of the passage shock (about 20% chord), post-shock Mach number (about 0.8) and blade row exit Mach number (about 0.8) are all within agreement. The primary difference occurs immediately downstream of the shock, where the data shows an acceleration from a relative Mach number of 0.8 to 1.0, whereas the CFD shows a much smaller acceleration from a relative Mach number of 0.8 to just less than 0.9. This discrepancy is believed to be due to the CFD underpredicting the blockage that results from the shock / boundary layer interaction. The distribution of blockage through the blade passage will be presented in the next chapter along with limited comparisons between the CFD and data. Note that the results presented above pertained only to CFD solution #2 in Figure 17, but are representative of the other solutions in the sense that the CFD solutions predict more diffusion within the rotor passage and underestimate the acceleration downstream of the shock /boundary layer interaction.

4.4.4 Summary of 'Core' Flow Field Results at Design Speed

This section focused on the flow physics associated with the blockage and loss development in the core flow region of the rotor operating at design speed and three different rotor exit pressures. The development of the blockage and loss in the core flow region have been traced to the shocks, wakes, and the interaction between the shock and the suction surface boundary layer. As the rotor back

pressure is increased the shock is pushed further upstream and becomes more normal to the flow field thus increasing the shock strength (and shock loss) and moving the position of the shock impingement on the blade suction surface further upstream which is accompanied by an increase in the blade loading in the front of the passage. The width of the rotor wake varied from the widest (most loss and blockage) at the low flow condition to the narrowest (least loss and blockage) at the high flow condition. These increases in the wake width were associated with the strength and location of the shock, the location of the shock /boundary layer interaction in relation to the blade loading, and the pressure gradient downstream of the shock / boundary layer interaction. The data was compared to CFD results which illustrated that the CFD was underpredicting the blockage associated with the shock / boundary layer interaction and therefore overpredicting the diffusion within the blade passage downstream of the shock. In the next section the discussion will focus on the outer endwall region.

4.5 Sensitivity of Loss and Blockage Development in the Outer 'Endwall Flow Region' to Changes in the Rotor Back Pressure at Design Speed.

In the discussion of the overall performance characteristics and the comparison with the CFD it was evident that the gradients of the pressure and temperature were largest near the endwall and the differences between the CFD and the data were significant in the outer endwall region, arbitrarily defined as the outer 15–20% of

span. Note in this context the term endwall region refers to the outer endwall region only, unless otherwise stated. In this section the details of the flow field in the endwall region and the sensitivity of this flowfield to the shock structure at design speed conditions are presented. In the endwall region the flow field is somewhat more complicated than in the core flow region due to the influences of the tip clearance flow. Therefore the objectives of this section are 1) to sort out the interplay between the flow phenomena in the endwall region, 2) to determine the impact on the development of blockage and loss in the rotor, and 3) to assess the sensitivity of the loss and blockage development as a function of rotor exit pressure at design speed.

4.5.1 Impact on Measured Blade-to-Blade Flow Field

Relative Mach Number Contours. A description of the blade-to-blade flow field along the 95% span streamsurface is depicted by contours of the relative Mach number for the rotor operating at design speed and the max flow, high flow, and low flow conditions in Figure 29. From computations performed on this same rotor and presented in Suder & Celestina [59], it was shown that the tip clearance fluid passing over the rotor tip from the pressure surface to the suction surface over the first 20% of rotor chord rolls into a vortex and the path of this leakage vortex coincides with the shock front distortion and the region of low dynamic head downstream of the shock. A comparison of the pathlines and Mach

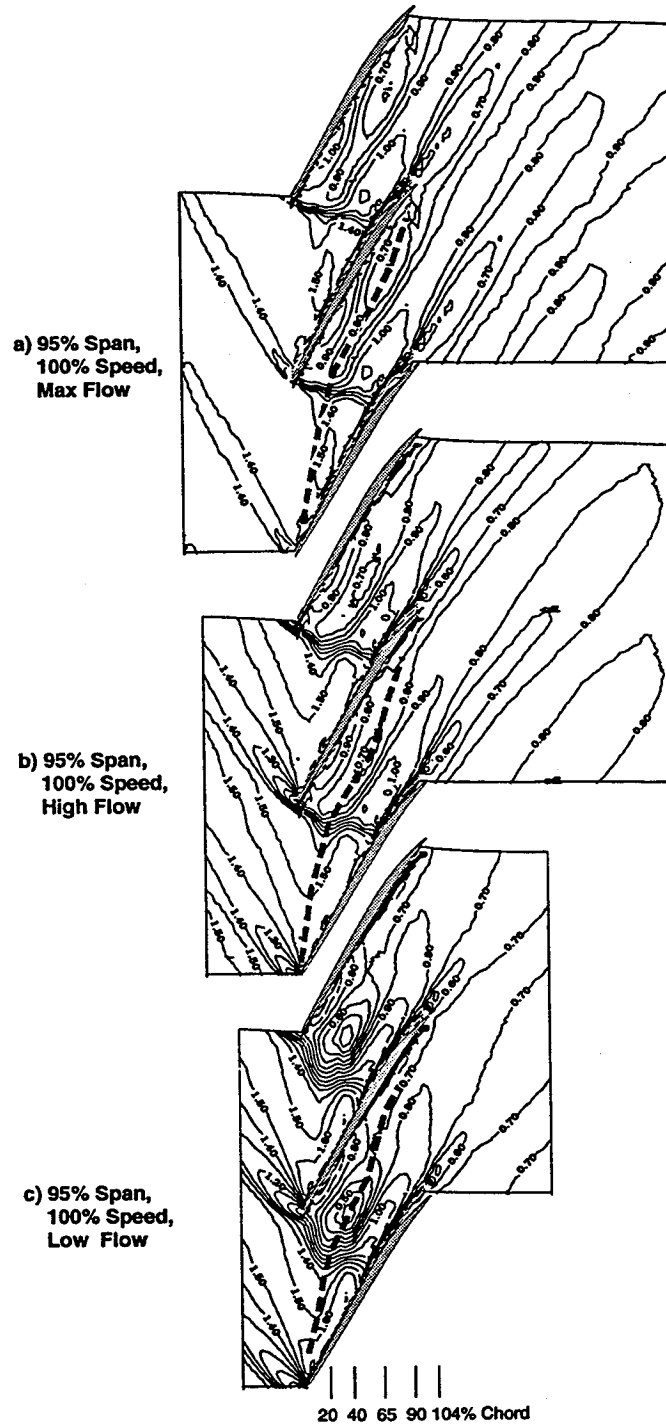


Figure 29 Contours of the relative Mach number in a blade-to-blade view along the 95% streamsurface for design speed and the a) max flow condition, b) high flow condition, and c) low flow condition where - - - indicates trajectory of tip leakage vortex.

number distributions further showed that the vortex path between the leading edge and the shock front can be inferred from the distortion of Mach contour lines in this region. The path of the tip clearance vortex was inferred using this method and is indicated by the dashed lines in this figure. The computed clearance flow path reported in [59] was in agreement with the path inferred from the data. In addition, calculations performed by Chima [60], who actually gridded the tip gap as opposed to modelling the gap as was done in Suder & Celestina [59], indicated good agreement between the computations, the data, and the model by Chen [39] in terms of the trajectory of the clearance vortex. Therefore, the inferred vortex trajectory shown in these figures is believed to be accurate. Note that the tip clearance height within which the clearance vortex originates is approximately 0.5% of span. Therefore, the Mach contours in Figure 29 at 95% span indicate the influence of the tip clearance flow which lies below the actual tip clearance region. As the rotor back pressure is increased (from max flow to low flow condition) the Mach contours at midpitch and 20% of rotor chord become more distorted due to a strengthening of the interaction between the clearance vortex and the passage shock. Downstream of the shock/vortex interaction, a region of low relative Mach number exists due to the blockage generated by the diffusion inherent to the vortex passing through the steep pressure gradient associated with the shock. The data indicate that the low Mach number fluid within the diffused vortex migrates toward

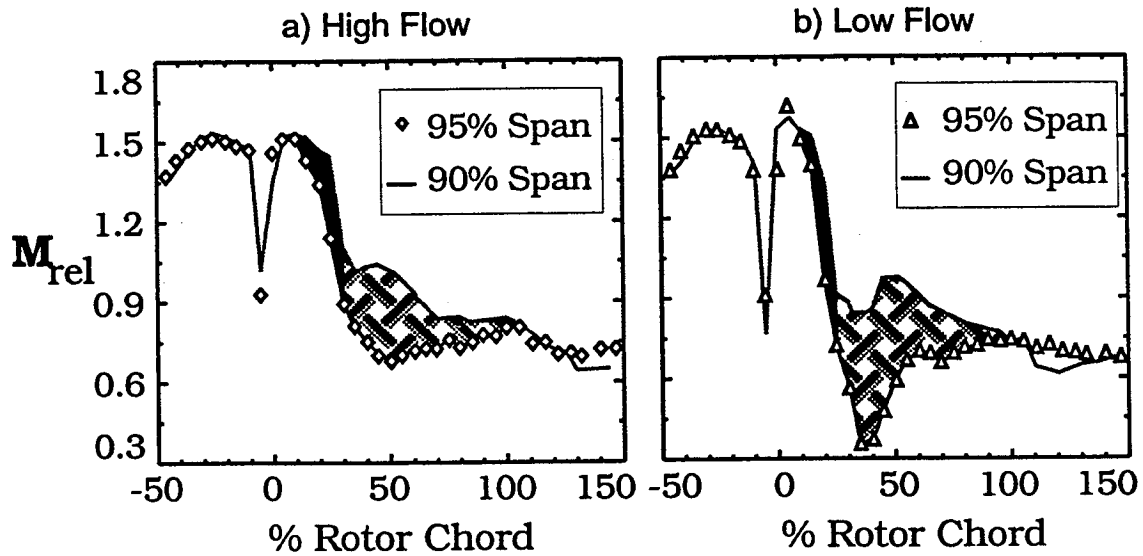


Figure 30 Relative Mach number distributions in the 95% streamsurface plotted along a line corresponding to the vortex trajectory at design speed and a) high flow condition, and b) low flow condition.

the pressure surface and merges with the rotor wake. Using the location of the lowest Mach number to indicate the 'heart' of the blockage region and the level to represent the severity, it is evident that the blockage becomes more severe and is located further upstream as the rotor backpressure is increased from the max flow to the low flow operating conditions.

Line Plots Indicating the Variation in the Streamwise Direction. To better quantify the blockage resulting from the interaction between the shock and the clearance vortex, the data at 90% and 95% span is plotted along a line corresponding to the inferred trajectory of the clearance vortex fluid. The results are shown in Figure 30. Comparisons of the blade-to-blade Mach number distributions at 95% span in Figure 29 to similar results obtained at 90% span

(which are not shown here) indicate that the upstream relative Mach number and blade incidence angle is virtually identical at 90% and 95% span. In addition, the blade geometry is nearly the same for these two sections. Therefore, the differences in the 90% and 95% span flow fields are primarily due to the influence of the tip clearance flow. In Figure 30 the symbols represent the data acquired at 95% span and the solid line represents the data acquired at 90% span (where data was acquired at the same spatial resolution as indicated by the symbols for the 95% span plot). The lightly shaded region represents the influence of the leakage vortex on the Mach number distributions upstream of the shock / vortex interaction and the darker shaded region represents the influence of the leakage vortex downstream of the shock / vortex interaction. The Mach number distributions are identical upstream of the leading edge and are nearly identical within the blade passage upstream of the shock / vortex interaction which occurs at approximately 20% rotor chord, indicating that the leakage vortex has very little influence at 95% span upstream of the shock. However, the most striking feature shown in Figure 30 is the difference in the Mach number in the region between the shock and the rotor trailing edge, which is evidence of the blockage generated when the leakage vortex crosses the shock.

Line Plots Indicating the Variation in the Pitchwise Direction. In order to further quantify the shock / clearance vortex interaction, the data at 95% span

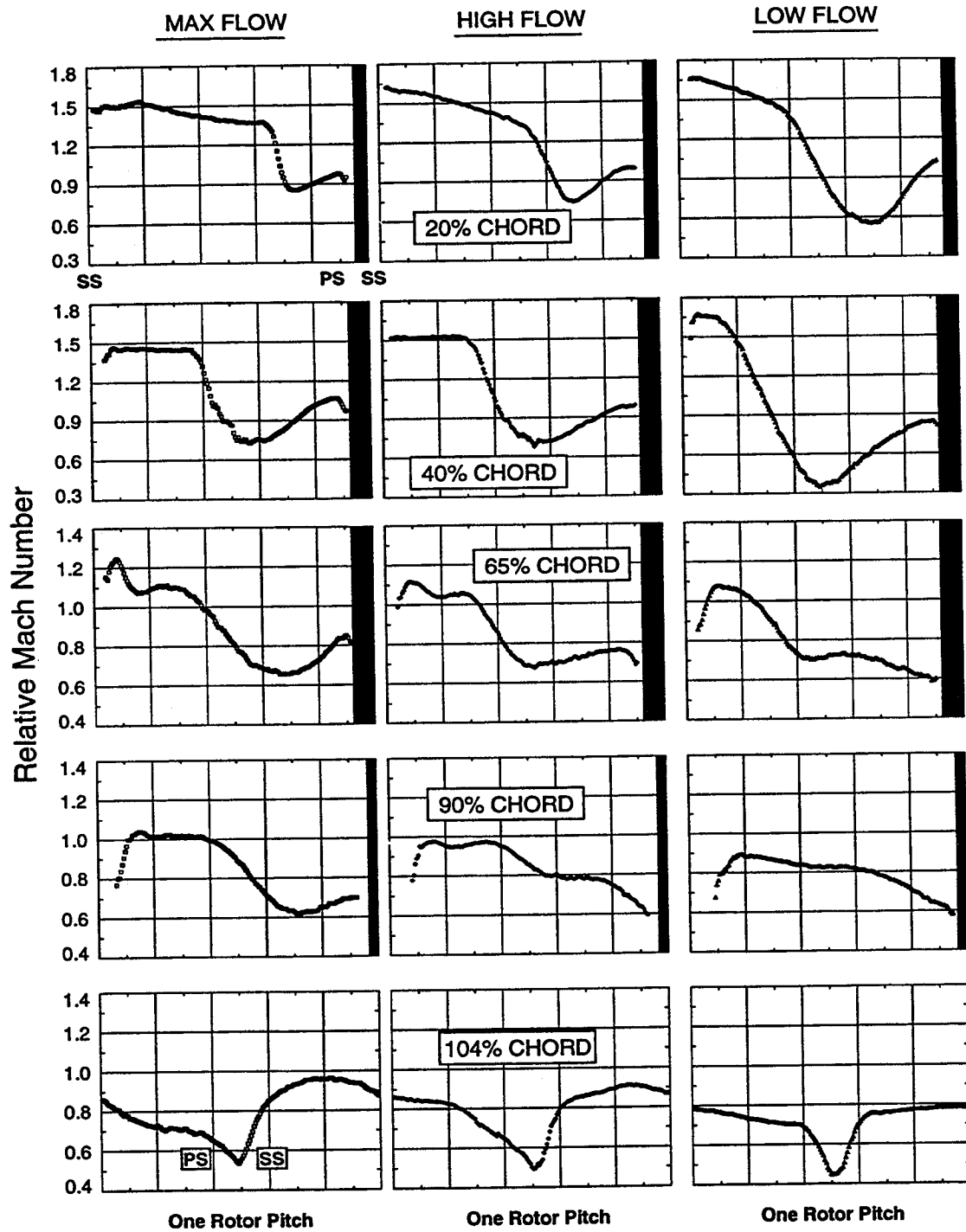


Figure 31 Pitchwise line plots of the relative Mach number at the 95% streamsurface for design speed and max flow, high flow, and low flow condition at 20% chord, 40% chord, 65% chord, 90% chord, and 104% chord.

are plotted in Figure 31 in the pitchwise direction from the suction surface to the pressure surface for fixed axial locations corresponding to 20%, 40%, 65%, 90%, and 104% of rotor chord. These axial locations were selected to provide the details of the flowfield near the shock/vortex interaction region, upstream and downstream of the shock impingement on the blade suction surface, and near the blade trailing edge. Throughout this discussion, the influence of the tip clearance flow on the 95% streamsurface will be emphasized by comparing this set of data at 95% span which is influenced by the tip clearance flow to data in the core flow at 70% span which was presented in Figures 23 and 24. Note that in Figure 31 the plots at 20% and 40% chord have a different scale and less sensitivity in the ordinate axis than the other plots in this figure to account for the large swings in the Mach number across the rotor pitch.

The influence of the tip leakage vortex on the flowfield at 20% chord is indicated by the drop-off in the relative Mach number from near the blade suction surface to the passage shock, and this influence is enhanced with increasing rotor back pressure. In addition, the increase in the relative Mach number near the blade suction surface from the max flow to low flow condition indicates an acceleration on the blade suction surface which is required to compensate for the blockage generated by the shock / vortex interaction. Analogous to the coreflow results, it is evident that the shock is pushed further upstream with the increase in rotor

backpressure from the max flow to low flow condition. These results are consistent with the Mach contours in Figure 29 that show the shock vortex interaction occurs at approximately 20% chord for the low flow and high flow conditions and slightly further downstream for the max flow condition.

The data at 40% chord, shown in Figure 31, is downstream of the shock vortex interaction and upstream of the shock impingement on the suction surface. The influence of the leakage flow on the flow field is evidenced by the change in relative Mach number across the shock. This influence becomes more prominent with increasing rotor back pressure. For example, the relative Mach number distribution for the low flow condition indicates a decrease in the relative Mach number from 1.65 near the suction surface to a value of 0.35 at midpitch. This amount of diffusion is not attainable across a normal shock (i.e., the post shock Mach number is 0.654 for a normal shock at Mach number of 1.65) and can only be the result of lower momentum fluid in the endwall region being displaced to the 95% streamsurface as a result of the interaction between the tip clearance flow, endwall boundary layer, and the rotor shock system. There is a loss associated with this low momentum fluid and a blockage which results in less work input (and therefore temperature rise) to the endwall fluid which is consistent with the reduced total temperature and pressure measured by the aerodynamic probes and presented in Figure 13.

The data at 65% chord, shown in Figure 31, lies downstream of the shock impingement on the blade suction surface. The drop in the Mach number near mid-pitch looks like a shock but it is not! The contour plot in Figure 29 shows the shock / boundary layer interaction is complete by 65% chord. Also from this contour plot note the flow has been divided into a region of high Mach number on the suction surface side of the passage and a low Mach number region on the pressure surface side of the passage. Therefore, the drop in Mach number near midpitch of the line plots at 65% chord indicates the separation of the passage into a high momentum and low momentum region. Analogous to the results at 70% span in Figure 24, the suction surface boundary layer is substantially thicker at low flow as opposed to the max flow and high flow conditions. Unlike the 70% span results, the low flow data at 65% chord and 95% span depicts a region of low Mach number from midpitch to the blade pressure surface. This region of low Mach number fluid becomes more substantial with downstream distance and its origin can be traced back to the low Mach number fluid downstream of the shock which resulted from the shock / vortex interaction — see the inferred vortex trajectory in Figure 29.

At 90% chord the Mach number is near one over nearly half of the pitch for the high and low flow conditions indicative of little diffusion in the flow (i.e. due to the blockage generated by the shock/vortex interaction). There is evidence of

thicker suction surface boundary layer for all three conditions and there is evidence of low Mach number fluid on the blade pressure surface over approximately one third of the pitch for the high and low flow conditions. This low momentum fluid on the pressure surface side of the passage is a result of the shock / clearance vortex interaction and the resulting blockage induces a higher momentum flow on the suction surface side of the passage.

At 104% chord the wakes at the max flow and high flow condition display a low Mach number region on the blade pressure surface side of the wake due to the accumulation of low momentum tip clearance flow on the pressure surface of the blade. However, the wake for the low flow condition appears narrower than the high and max flow wakes at the same location. For the low flow condition the shock / vortex interaction is sufficiently stronger to result in a larger blockage which encompasses the entire circumference. Therefore, the blockage and losses (as deduced from the wake width and depth) only appear to be smaller at the low flow condition when in reality they are much larger.

4.5.2 Comparison to CFD Blade-to-Blade Flow Field

The computational results presented by Chima [60], and Suder et al. [59] have demonstrated that the computations and the data are in agreement in terms of the general structure of the shock and the leakage vortex trajectory. In this

section it will be shown that the CFD underpredicts the blockage associated with the shock / tip clearance vortex interaction.

The relative Mach number contours along the 98% and 95% span streamsurface for the high flow operating condition resulting from CFD solution #2 are presented in Figure 32. The experimental results at 95% span and high flow condition were presented in Figure 29b. Recall that the influence of the shock vortex interaction is denoted by the distortion of the Mach lines depicting the shock front which is followed by a region of low Mach number fluid which migrates to the pressure surface and merges with the wake. The CFD results at 95% span (nor at 96% or 97% span, though not shown) do not indicate these flow phenomena. In fact the first detection of the distorted Mach lines at the shock front were not found in the CFD results until 98% span as shown in Figure 32. Therefore, the CFD is not only underpredicting the radial extent of influence of the shock / vortex interaction but also is underpredicting the blockage which results from the shock / vortex interaction. This underprediction of the blockage in the endwall region is consistent with the earlier results of Figure 17 which showed that the CFD was overpredicting the work input or temperature rise in the outer spans. In conclusion, the comparisons of the computations to the experiment, (more thoroughly presented in Suder & Celestina [59]), have revealed that the computations predict the correct

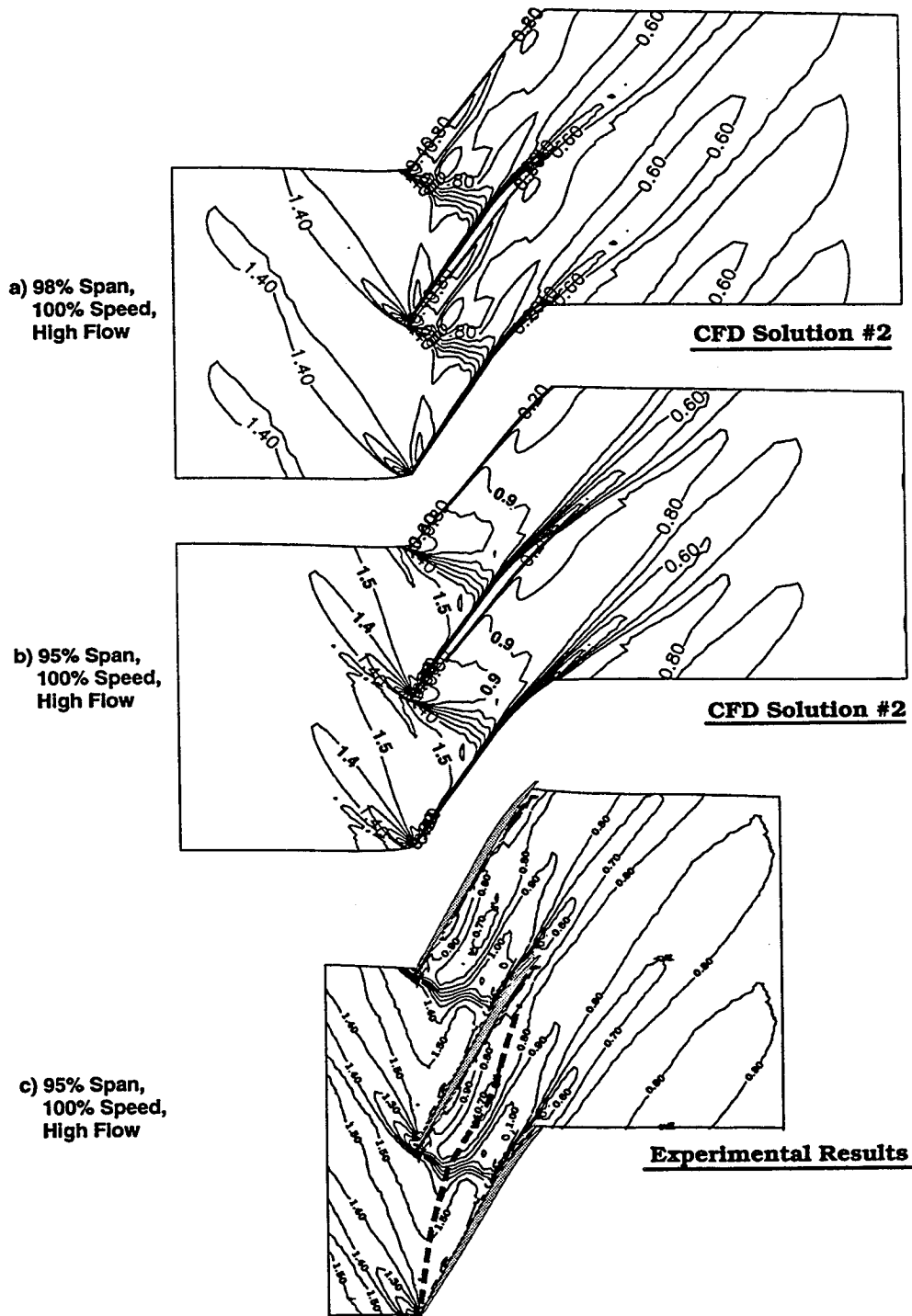


Figure 32 CFD relative Mach number distributions on the a) 95% span and b) 98% span streamsurface for the rotor operating at 100% speed and high flow.

structure of the leakage vortex, but underpredict the radial extent of influence of the tip leakage flow.

4.5.3 Summary of Endwall Flow Field Results at Design Speed

In summary, it has been shown that there is a strong interaction between the rotor passage shock and the tip leakage vortex which generates a high blockage in the passage which moves forward and becomes larger as the rotor loading is increased. The low momentum fluid resulting from the shock vortex interaction migrates to the pressure surface and merges with the wake. However, at the low flow condition the blockage generated by the shock / vortex interaction is so great that it encompasses the entire circumference. The low momentum fluid generated by the shock / vortex interaction mixes throughout the passage and in the case of the low flow condition is unidentifiable by the trailing edge of the rotor blade. Clearly, the development of loss and blockage is more complex in the endwall region than in the core flow region. In the endwall region not only does the blockage and loss develop from the shock, shock / boundary layer interactions, and ensuing wake, but there is the additional blockage and loss associated with the shock / vortex interaction.

4.6 Loss and Blockage Development in the Rotor at Part Speed Conditions.

Up to this point the discussion has focused on the development of loss and blockage in the endwall and core flow regions with changes in the rotor shock structure at essentially a constant inlet Mach number of about 1.4. In this section we will look at the impact of reducing the inlet Mach number on the loss and blockage development in the core flow and endwall regions. The loss and blockage development will be assessed at 80% and 60% speed where the nominal inlet Mach numbers at mid-span are 1.1 and 0.8, respectively.

4.6.1 Core Flow Field Results Measured at 80% Speed

Relative Mach Number Contours at 70% Span. In the core flow the losses at design speed were largely due to those associated with the blade boundary layers and the shock loss. The role of the shock was significant because the boundary layer thickened downstream of the shock due to the shock / boundary layer interaction. The blade to blade view of the relative Mach number distribution on the 70% span streamsurface for the rotor operating at 80% speed and high flow condition which is near peak efficiency is provided in Figure 33. The inlet relative Mach number has decreased from 1.4 at design speed (refer to Figure 23b) to 1.1 at 80% speed. At 80% speed the shock is pushed further out in front of the blade leading edge and hits the suction surface at approximately 35% rotor chord in

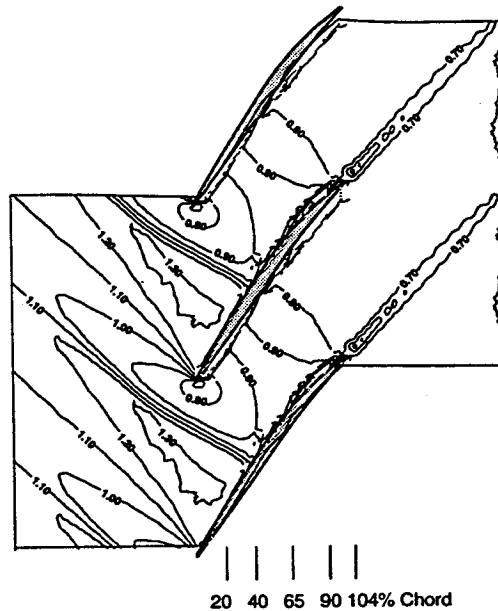


Figure 33 Relative Mach number distributions on the 70% span streamsurface for the rotor operating at 80% speed and near peak efficiency.

comparison to about 45% to 50% chord at high flow and design speed. Note that the foot of the shock, near the blade suction surface, does not exhibit the lambda (λ) shape as was evidenced in the design speed results and the wake appears to be narrower and less deep than the wake corresponding to the design speed flow.

Line Plots at 70% Span Indicating the Variation in the Pitchwise Direction.

A detailed comparison between the 80% speed and the design speed high flow condition of the 70% span streamsurface are presented in terms of pitchwise line plots at 20%, 40%, 65%, 90%, and 104% chord in Figure 34. The expansion around the leading edge on the blade suction surface results in a pre-shock relative Mach number of approximately 1.3 and 1.5 for the 80% speed and 100% speed high flow conditions, respectively. Based on the difference between the pre-shock

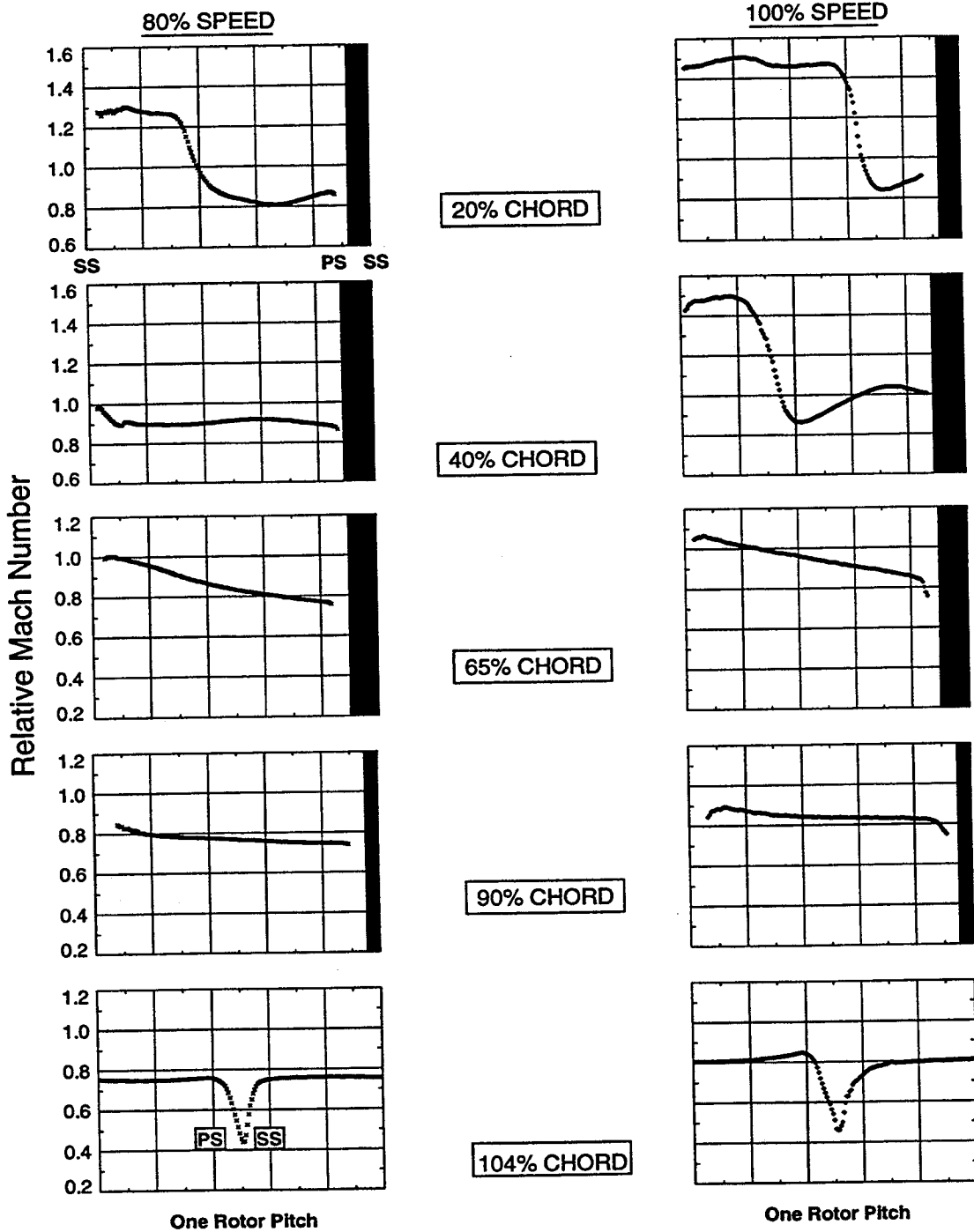


Figure 34 Pitchwise plots of relative Mach number distributions on the 70% span streamsurface at 20%, 40%, 65%, 90% and 104% chord for the rotor operating at 80% speed and 100% speed at high flow condition.

and post-shock Mach number observed at 20% chord in Figure 34a, it is evident that the shock is weaker and is located more forward in the passage than that corresponding to the design speed condition. For normal shocks of Mach number 1.3 and 1.5 the post-shock Mach numbers would be 0.79 and 0.70, respectively. The change in Mach number across the shock at 20% chord from 1.3 to 0.8 for 80% speed compared to the change from 1.5 to 0.85 for 100% speed indicates that the shock is more normal at 80% speed and this is also evident from the Mach number contour plots in Figures 33 and 23b.

By 40% chord it is evident that the shock has impinged on the blade suction surface for the 80% speed condition and not yet for the 100% speed condition. Therefore, if the boundary layer is separated or thickened by the shock, the boundary layer for the 80% speed case will have had more blade surface on which to grow in comparison to the design speed case. At 65% chord there is evidence of a thickened boundary layer on the blade suction and pressure surface for the design speed case. However at 80% speed the thickness of the boundary layer is indeterminate due to the lack of sufficient data close to the wall. The same is true at 90% chord. The change in Mach number from the suction to pressure surface at 65% chord and at 90% chord are nearly identical for the design speed and 80% speed cases which signify that the blade loading across the passage is nearly identical at these two locations. However, by 104% chord it is evident that

the wake is smaller at 80% speed than it is at design speed even though the shock hit the blade suction surface further upstream for the 80% speed condition.

It is evident that increasing the pre-shock Mach number from 1.3 (corresponding to the 80% speed at peak efficiency) to a value of 1.5 (corresponding to the design speed conditions) results in a significant change in the boundary layer development and the blockage associated with the rotor wake. Since the width and depth of the wake is an indicator of the loss and blockage associated with the blade boundary layers, the wake losses and blockages are reduced at part speed condition due to the change in the shock strength. In the next chapter the differences in the blockage between these two wakes will be quantified.

Impact on Blade Loading. To quantify the impact of the reduced inlet Mach number on the blade loading, comparisons of the relative Mach number and isentropic static pressure coefficient distributions along the blade surface at design speed and 80% speed case are presented for the 70% span streamsurface. The results at 80% speed are presented in Figure 35, while the corresponding results at design speed were presented in Figures 25b and 26b. A comparison of the relative Mach number distribution between the design speed and 80% speed case indicate that the shapes of the pressure surface distribution are similar and on the suction surface the shape of the Mach number distribution is nearly identical up to the location of the shock. The main difference between the design speed

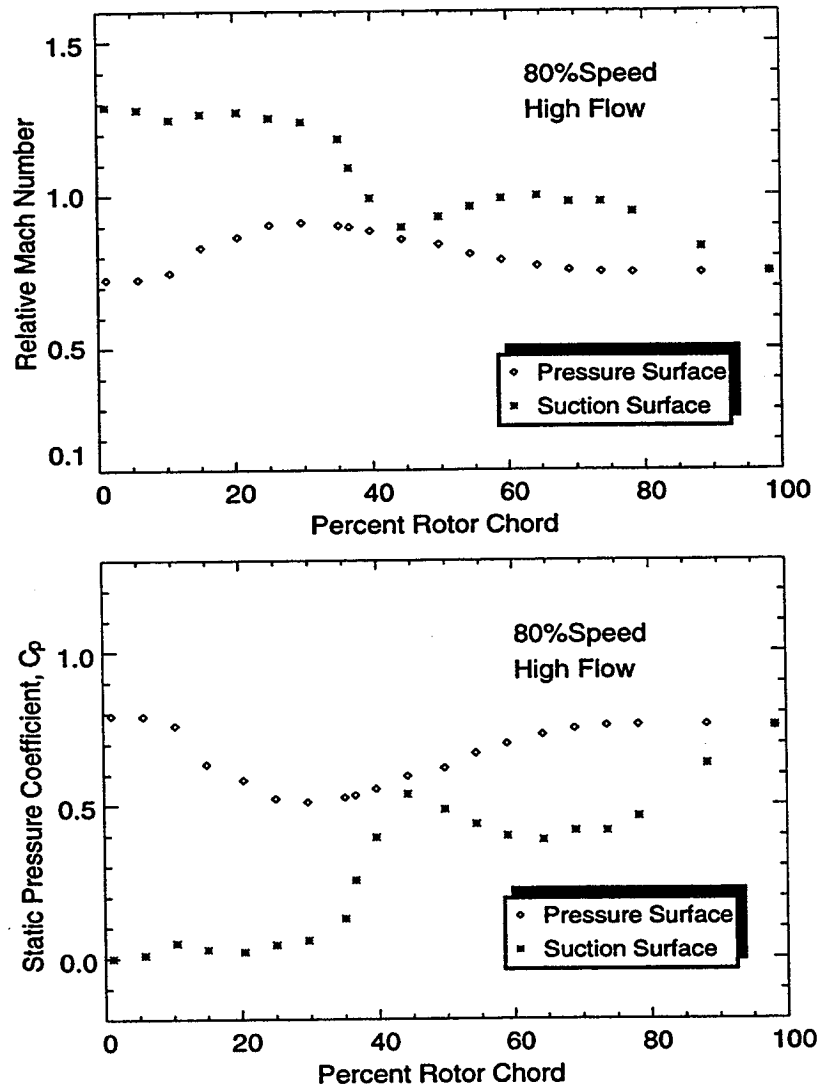


Figure 35 Blade surface relative Mach number distribution and static pressure coefficient on the 70% span streamsurface for the rotor operating at 80% speed and near peak efficiency.

and 80% speed Mach number distribution lies on the suction surface. At 80% speed the shock impinges on the blade suction surface between 30% to 35% rotor chord and the influence of the shock on the boundary layer extends to about 45% chord. Downstream of the shock there is an acceleration from 45% to 65% chord followed by a diffusion from 65% to 100% chord. In contrast, at design speed the

shock impingement point is at about 40–45% chord and the influence of the shock on the boundary layer extends from 40% to about 60% chord and downstream of the shock the flow merely diffuses. Similarly, in terms of the static pressure coefficient, it is evident that the difference in the loading between the part speed and the design speed case is due primarily to the shock location and strength. In addition, the loading at design speed is primarily in the front of the passage, whereas at 80% speed a considerable part of the overall loading is attributed to that in the back half of the passage. Also, for the 80% speed there is a region of favorable pressure gradient downstream of the shock which does not exist at design speed conditions. In summary, the loading level is decreased in going from design speed to part speed condition and this reduction is due to changes in the shock location and strength.

4.6.2 Core Flow Field Results Measured at 80% and 60% Speed

Streamsurface data at 60% speed were only acquired at 90% and 95% span. Suder & Celestina [59] showed that although the clearance flow influences the outer 10–15% span of the rotor flow field at design speed, the radial extent of the tip clearance flow at part speed conditions is only about 5–10% of span [59]. Therefore, the data acquired at 90% span for the rotor operating at 60% speed can be used to evaluate the influence of the inlet Mach number on the blockage and loss in the core flow field. To determine the impact of a reduction in the inlet

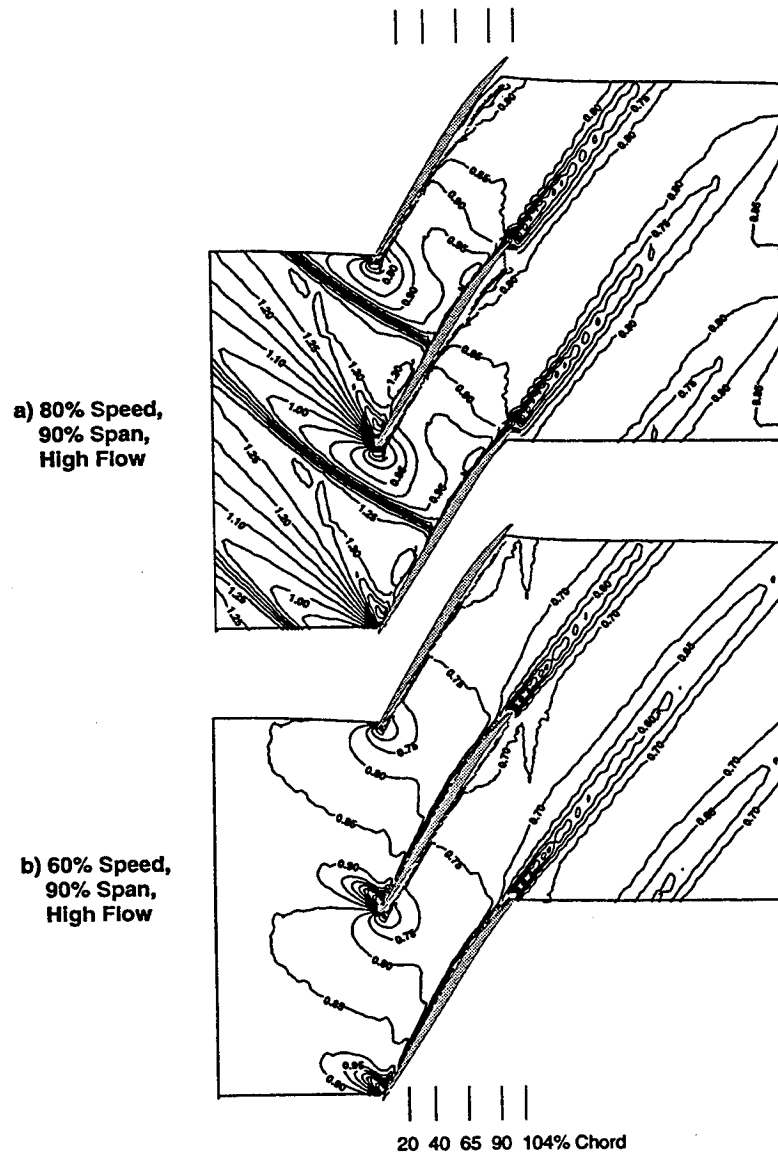


Figure 36 Relative Mach number distributions on the 90% span streamsurface for the rotor operating at 80% & 60% speed near peak efficiency.

Mach number below Mach one on blockage and loss development, comparisons are made between the 80% and 60% speed conditions.

Relative Mach Number Contours at 90% Span. The blade to blade view of the relative Mach number distribution on the 90% span streamsurface for the

rotor operating at 80% speed and 60% speed near peak efficiency is provided in Figure 36. Note that the increment in the contour lines has been reduced from 0.1 to 0.05 to better define the flow field at 60% speed where the variations are smaller in comparison to design speed and 80% speed. The inlet relative Mach number has decreased from 1.2 at 80% speed to 0.85 at 60% speed. For the 80% speed condition, the flowfield at 90% span has the same features as those observed at 70% span. For example, the shock is pushed out in front of the blade passage, the shock appears to be nearly normal to the blade in both cases, the shock impacts the suction surface near 35–40% chord, and there is no evidence of a lambda shaped shock foot near the blade suction surface. The flow field at 90% span for the 60% speed condition was expected to be subsonic throughout, however, there is evidence of a supersonic pocket on the blade suction surface near the leading edge of the blade. This supersonic region develops due to the high angle of attack resulting in an acceleration around the leading edge of the airfoil which is operating at positive incidence for this off-design condition. Note, for supersonic inlet conditions the flow is turned around the leading edge by a series of expansion waves located downstream of the bow shock and emanating from near blade the leading edge.

Line Plots at 90% Span Indicating the Variation in the Pitchwise Direction.

A detailed comparison of the 90% streamsurface between the 80% speed and 60%

speed near peak efficiency condition is presented in terms of pitchwise line plots at 20%, 40%, 65%, 90%, and 104% rotor chord in Figure 37. Note that the ordinate scale of these plots have the same sensitivity but the scale ranges are different. At 20% chord there is evidence of a thickened suction surface boundary layer at 60% speed which does not exist at 80% speed. At the downstream edge of the supersonic pocket that exists at 60% speed the flow encounters an adverse pressure gradient which results in a thicker and/or locally separated boundary layer. The data at 90% span for 80% speed is nearly identical to the earlier results at 70% span except the inlet Mach number is slightly higher and the location of the shock is slightly closer to the pressure surface. At 40% chord, the suction surface boundary layer has grown slightly for the 60% speed condition, and for the 80% speed case 40% chord represents the region of the shock / boundary layer interaction. By 65% chord there is evidence of a boundary layer on both the pressure and suction surfaces at 80% and 60% speed. At 90% chord the region of low Mach number fluid on the pressure surface has become larger, whereas the suction surface boundary layer thickness has remained nearly the same. The increased thickness on the pressure surface is due to the influence of the endwall flow and will be discussed in the next section. Note that for the 60% speed case the change in Mach number from the suction surface side to the pressure surface side of the passage is very small from 40% chord to the trailing edge which is

indicative of a very lightly loaded condition. At 104% chord a comparison of the rotor wakes indicates that the widths and depths of the wakes are similar. However, the wakes are not typical for the following reasons. The pressure surface side of the wake at 80% speed is influenced by the endwall flow and is wider than it would normally be in the core flow region. The development of the wakes at 60% speed are atypical in that the suction surface boundary layer is thicker than 'normal' due to the presence of an adverse pressure gradient at the downstream edge of the supersonic bubble which forms near the leading edge of the blade. Therefore, the flow at 60% speed is representative of operating a blade at subsonic conditions that was designed for supersonic conditions, but is not characteristic of a blade designed for subsonic inlet conditions.

4.6.3 Endwall Flow Field Results Measured at 60% and 80% Speed.

In this subsection the effect on the endwall flow of both reducing the shock strength and eliminating the shock will be investigated as the inlet Mach number is reduced at 80% speed and 60% speed. Note at 80% and 60% speed the centrifugal forces on the rotor blade are about 64% and 36% of that at design speed, resulting in a larger tip clearance and a reduction in the blade untwist. Since a NASTRAN analysis was only performed at design speed the 'hot' blade geometry is unknown at these operating conditions. However, the tip clearance was measured and the

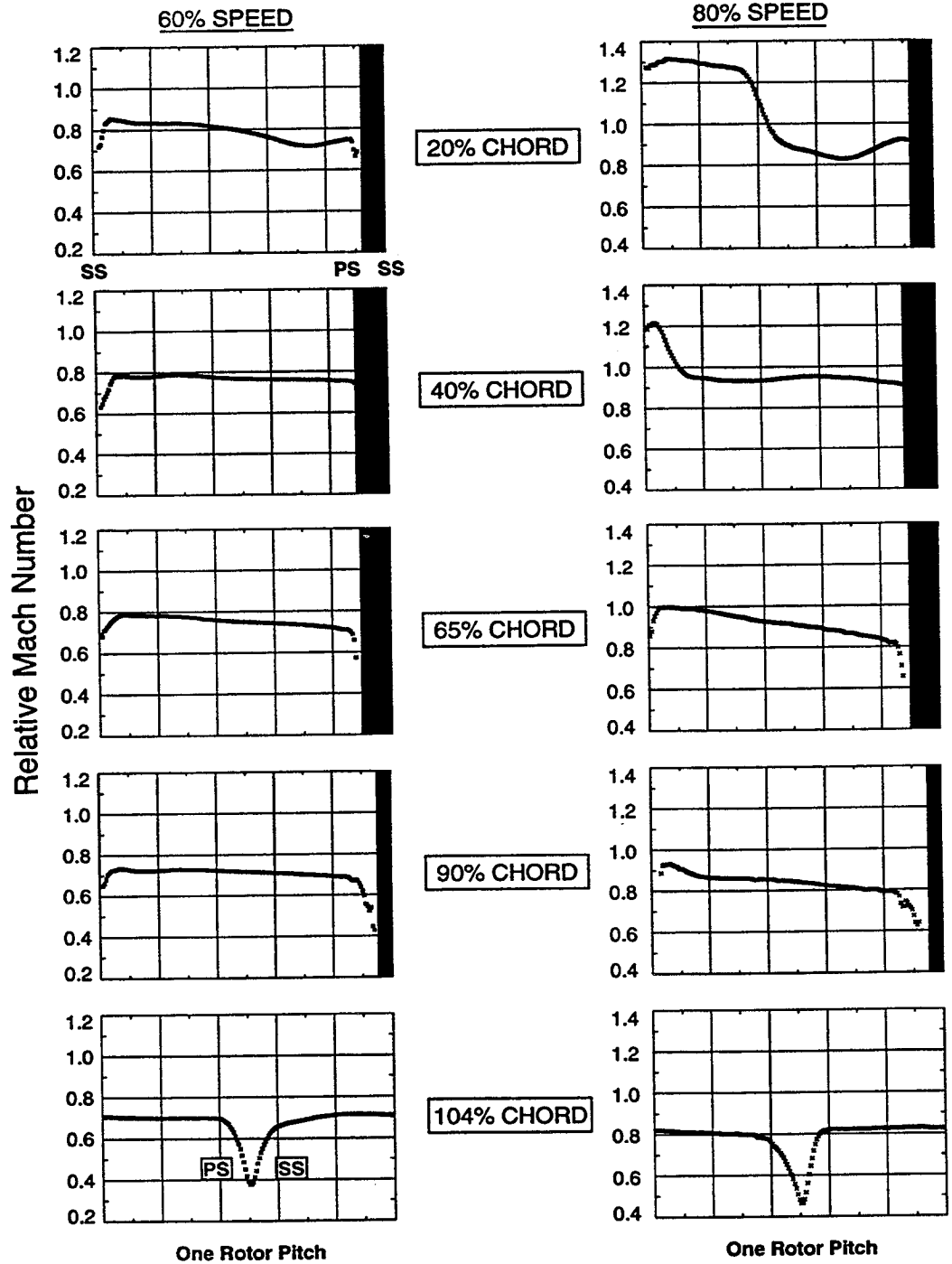


Figure 37 Pitchwise plots of relative Mach number distributions on the 90% span streamsurface at 20%, 40%, 65%, 90% and 104% chord for the rotor operating at 80% & 60% speed near peak efficiency.

resulting values are 0.500 mm (0.020 in.) at 80% speed and 0.580 mm (0.023 in.) at 60% speed, compared to 0.400 mm (0.016 in.) at design speed.

Relative Mach Number Contours. A description of the blade-to-blade flow field along the 95% streamsurface is depicted by contours of the relative Mach number for the rotor operating at 60% and 80% speed at near peak efficiency and an incidence comparable to the design speed high flow condition in Figure 38. These results can be compared to the design speed results in Figure 29 but note that for the 60% speed case the contour increment was decreased from 0.1 to 0.05 to enhance the variations in the relative Mach number. Analogous to the design speed results, the paths of the leakage vortex are inferred from the deflections of the Mach contours and are displayed on these figures by the dashed lines. Note there are two distinct vortex paths on the 60% speed plot. One vortex pathline emanates from near the leading edge and migrates to the pressure surface and this path is indicative of the tip clearance vortex. The other vortex trajectory, emanating from the suction surface and rear part of the blade, refers to the path of the 'second' vortex.

Computational results were used to determine the origin of this 'second' vortex and a discussion of the flow physics leading to the development of the 'second' vortex can be found in Suder & Celestina [59]. A summary of those results, which are primarily based on particle pathlines from the CFD and confirmed by the

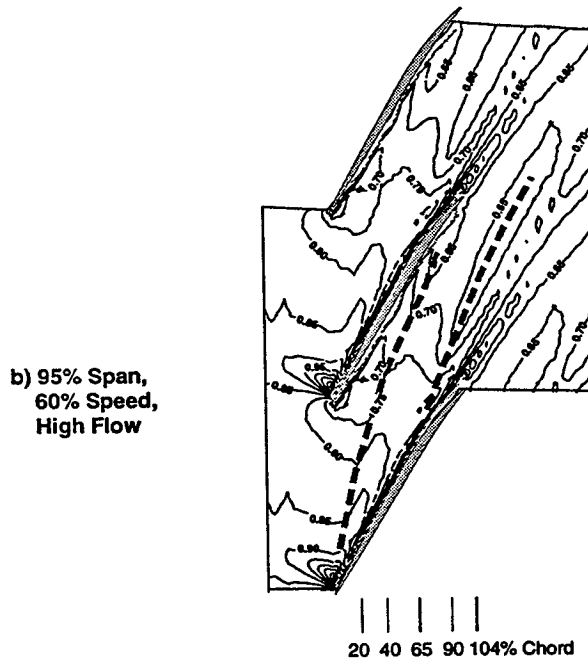
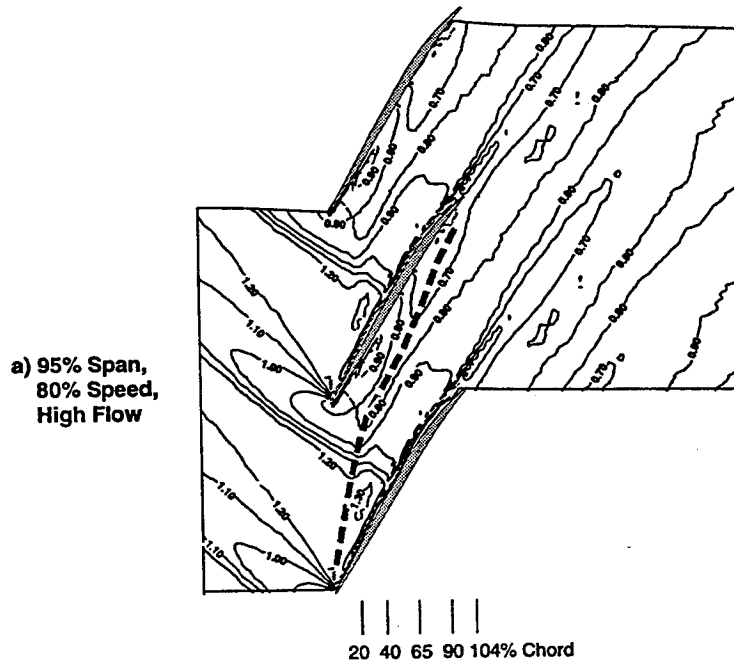


Figure 38 Relative Mach number distributions on the 95% span streamsurface for the rotor operating at 80% & 60% speed near peak efficiency where - - - - indicates trajectory of vortex.

agreement in the relative Mach number contours at 95% span between the CFD and the experimental data, will be discussed herein. The fluid forming the 'second' vortex does not pass through the rotor tip clearance gap. At the downstream edge of the supersonic region near the leading edge the flow encounters an adverse pressure gradient which results in a radial migration of fluid along the blade suction surface. (The CFD results indicate that the supersonic region near the leading edge exists over the outer 70% of blade span and the experimental data confirms its existence at 90% and 95% span.) The fluid climbing up the blade suction surface encounters the leakage fluid at the blade tip and rolls-up into a vortex. The 'second' vortex is constrained by the leakage fluid and therefore lies below the tip clearance region. The radial migration of fluid along the suction surface is the key to the formation of the 'second' vortex. At design speed the flow along the suction surface is expanding behind the shock in a favorable pressure gradient. Particle traces at design speed indicate virtually no radial migration upstream of the shock and downstream of the shock the migration is small. Therefore, the formation of the 'second' vortex is not related to the strength of the clearance flow but rather is due to the secondary flows along the blade suction surface that result from operating at an off-design condition.

A comparison of the shock vortex interaction at 80% speed to that at design speed indicates that the endwall flowfield at 80% speed is somewhat similar to

that at design speed. The leakage vortex influence on the 95% span streamsurface is indicated by the deflections in the Mach contours. The interaction between the clearance vortex and the shock occurs near 20% chord and midpitch. Downstream of the shock vortex interaction resides a region of low Mach number fluid which migrates towards the pressure surface and merges with the rotor wake. The path of the vortex trajectory is not very much different from the design speed results. A comparison of the results at 80% and 60% speed reveal the following: 1) the path of the tip clearance vortex is similar for both part speed conditions - the vortex moves across the passage and merges with the blade wakes, 2) at 60% speed there is the immergence of the 'second' vortex and 3) the 'second' vortex appears to extend far downstream.

Line Plots at 95% Span Indicating the Variation in the Pitchwise Direction.

A detailed comparison of the 95% streamsurface between the 80% speed and 60% speed near peak efficiency condition is presented in terms of pitchwise line plots at 20%, 40%, 65%, 90%, and 104% rotor chord in Figure 39. Note that the ordinate scale of these plots have the same sensitivity but the scale ranges are different. In order to illustrate the impact of the endwall flow field on these results the dashed line represents an overlay of the pitchwise distribution at 90% span (see Figure 37). For the 60% speed case, the plots at 20%, 40% and 65% chord are nearly identical at 90% and 95% span indicating there is very little influence of the tip

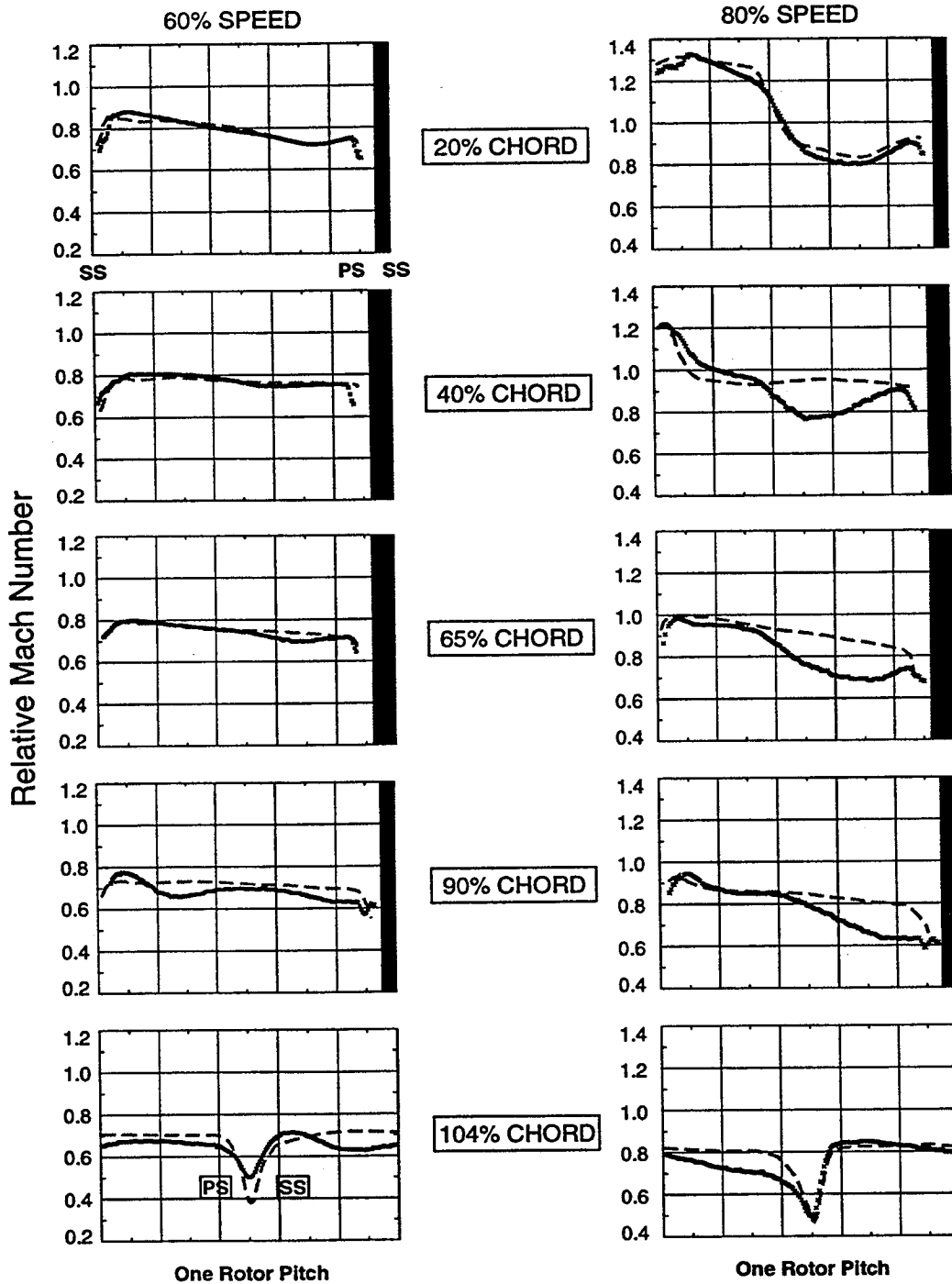


Figure 39 Pitchwise plots of relative Mach number distributions on the 95% span streamsurface at 20%, 40%, 65%, 90% and 104% chord for the rotor operating at 60% & 80% speed near peak efficiency. (--- indicates overlay of data at 90% span.)

clearance flow on the 95% span streamsurface over the front part of the rotor. In fact the supersonic bubble and its impact on the suction surface boundary layer is the dominant flow feature in the front part of the blade. However, at 90% chord there is evidence of the 'second' vortex located at approximately 30% pitch from the suction surface. In addition the region of low Mach number near the pressure surface represents the impact of the tip clearance vortex on the flow field at 95% span. Similarly at 104% chord the wake appears in the center of the plot and the low Mach number region near the suction side of the wake represents the 'second' vortex. The difference on the pressure side of the wake between the 90% span and the 95% span data is indicative of the deficit in Mach number attributed to the tip clearance vortex. At 80% speed there is little influence of the tip clearance flow prior to the shock vortex interaction as indicated by the similarity in the pitchwise distribution at 20% chord. However, at 40% chord, which is downstream of the shock / clearance flow interaction, the deficit in Mach number between the shock and the pressure surface is indicative of the additional blockage generated by the interaction between the clearance vortex and the shock. From 40% chord to 90% chord the low momentum fluid identified by the deficit in Mach number and resulting from the shock / clearance vortex interaction spreads across the passage to the pressure surface. At 104% chord the influence of this low Mach number fluid is evident on the pressure side of the wake.

In summary, at 60% speed operating condition the leakage flow over the front portion of the rotor rolls into a vortex which moves across the blade passage, impacts on the pressure surface before reaching the trailing edge, and merges with the rotor wake downstream of the blade. A 'second' vortex is formed by fluid which migrates radially outward along the suction surface and rolls up into a vortex when it encounters the tip leakage flow in the rear half of the blade. The 'second' vortex exits the blade passage at midpitch and persists for more than one rotor chord downstream. Downstream of the rotor the Mach number deficit of this 'second' vortex is comparable to that of the blade wake. At the 80% speed condition the leakage flow over the front portion of the rotor rolls into a vortex which moves across the blade passage and interacts with the rotor shock. The shock / vortex interaction generates a blockage in the passage which fills the pressure surface side of the passage and eventually merges with the rotor wake. The shock vortex interaction and ensuing blockage is consistent with that at design speed at a lower Mach number (i.e. weaker shock). In addition, there is no evidence of a 'second' vortex which is consistent with the results at design speed.

4.7 Summary of Flow Physics Regarding Blockage and Loss Development

The goal of this chapter was to discuss the flow physics relevant to the generation of loss and blockage in a transonic compressor rotor operating at design and part speed conditions. An overview of each section follows.

The first section discussed the overall performance characteristics and compared the measured result to the design intent and to the numerical simulations using state-of-the-art techniques employing three dimensional Navier-Stokes solvers. The experimental results did not agree with either the design intent nor the numerical simulations. The measured radial distributions of pressure and temperature indicated a change in shape from part speed to design speed which was attributed to the higher levels of Mach number at design speed.

The second section provided a general discussion of the flowfield of a transonic compressor rotor and the following loss mechanisms were identified: 1) viscous loss due to the development of the blade boundary layers, 2) loss across the shock, 3) loss or blockage generated by the interaction between the shock and the suction surface boundary layer, and 4) loss and blockage associated with the rotor wake. In addition, the core flow field and the endwall flowfield were defined and it was demonstrated that the shock structure played a significant role in the development of these losses.

The third section focused on the integrity of the data and a verification of the blade geometry which was deemed critical in lieu of the fact that the data did not agree with either the CFD results nor the design intent. In this section the repeatability, consistency, and validity of the data was demonstrated. The 'cold' geometry was verified with detailed inspections of the designed blade sections. The 'hot' geometry of the rotor as predicted with a NASTRAN analysis was verified with the LFA system at the rotor tip. The NASTRAN predicted blade geometry which accounts for the aerodynamic and mechanical loads on the blading was provided to the CFD participants.

The fourth section demonstrated the sensitivity of the loss and blockage development in the core flow field due to changes in the rotor back pressure at design speed. The blockage and loss that developed in the core flow field were directly related to the shock structure, the interaction between the shock and the suction surface boundary layer, and the wake structure. As the rotor backpressure increased the shock was pushed further upstream and became more normal to the flowfield, thereby increasing the shock strength (and therefore shock loss) and moving the location of the shock impingement on the blade suction surface upstream. The blockage and losses associated with the rotor wake width and depth were attributed to the strength of the shock, the state of the boundary layer at the shock impingement, and the pressure gradient downstream of the

shock / vortex interaction. In addition, comparison between the data and the CFD indicated that the CFD was overpredicting the diffusion in the passage due to an underprediction of the blockage generated by the shock boundary layer interaction all of which is consistent with the CFD overpredicting the temperature and pressure rise in this rotor.

The fifth section was an extension of the fourth section to the outer endwall region where the tip leakage flow, the shock, the shock / tip leakage vortex interaction, and the wake represented the key flow physics in generating the loss and blockage. The same features of the shock / boundary layer interaction that occurred in the core flow existed in the endwall with an additional source of blockage and loss being generated by the shock / vortex interaction. This additional blockage moved upstream in the passage and became more severe as the rotor backpressure was increased due to both 1) the strengthening of the shock and 2) the upstream movement of the shock and the shock/vortex interaction region. In addition, it was shown that the CFD underpredicted the radial extent of influence of the shock / boundary layer interaction as well as the level of blockage resulting from this interaction.

The sixth and final section investigated the sensitivity of the loss and blockage development in the core flowfield and the endwall region for changes in the inlet Mach number. The comparisons were made at 100%, 80%, and 60% of design

speed which corresponded to nominal inlet Mach numbers of 1.4, 1.1, and 0.8, respectively. In the core flow region and the endwall region the loss and blockage at 80% speed were analogous to those at design speed with a reduced influence on blockage and loss development consistent with a reduction in the rotor shock strength and resulting blade loading. At 60% speed, in the absence of the shock, the blockage and loss was identified by the rotor wake which was highly influenced by a local separation resulting from a supersonic pocket near the blade leading edge on the suction surface. In the endwall region the blockage and loss was identified with a tip clearance vortex, rotor wake, and a 'second' vortex. The 'second' vortex depicted a relative Mach number deficit comparable to the wake downstream of the rotor. The 'second' vortex resulted from secondary flows which were established by running a blade at subsonic conditions that was designed for supersonic flow. Therefore, the blockage and loss identified for the 60% speed case is not representative of blades designed for subsonic inlet conditions, but however are believed to be representative of a blade designed for supersonic inlet conditions operating at subsonic inlet conditions.

5 Quantification of Blockage and Loss Estimates

It has been established that there is a relationship between blockage and loss in a turbomachine [7, 6, 5]. However, it is important to realize that all losses are not a result of blockage and conversely all blockage does not imply a loss. For example, the loss across the shock does not impact the blockage. The increase in blockage attributed to the shock / boundary layer interaction results in an acceleration of the core flow downstream of the shock which results in less flow turning and therefore less work input. Therefore, it is important to realize that blockage leads to a reduction of the work input to the fluid and loss indicates how effectively the work input to the fluid results in a pressure rise.

In the previous chapter the flow mechanisms responsible for the development of loss and blockage in a transonic compressor rotor were identified. It was shown that the shock structure and the interaction of the shock with boundary layers and tip clearance flows plays a significant role in the development of loss and blockage. In this chapter the objective is to estimate the blockage and loss associated with the rotor wake and shock characteristics using the experimental data. The blockage and loss in the core flow region will be quantified both downstream and within the rotor blade row where the data is of sufficient detail. In the endwall region, where it has been shown that the flow gradients are large in the radial, circumferential,

and axial directions, there is not sufficient data in the radial direction to assess the loss and blockage within the blade row. Therefore, the endwall blockage will be quantified downstream of the rotor only.

5.1 Quantification of Blockage

Blockage was earlier defined as the effective reduction in flow area and is represented by:

$$B = \left[1 - \left(\frac{\text{effective flow area}}{\text{geometric flow area}} \right) \right] \quad (15)$$

which can be re-written as :

$$B = 1 - \frac{(A - \int \delta^* dr)}{A} \quad (16)$$

where A is the total area and δ^* is the integral of the velocity-density deficit across the rotor passage. The integral of the velocity-density deficit is defined at each radial measurement location by

$$\delta^*(r) = \int_{\theta=0}^{2\pi/NB} \left(1 - \frac{\rho u}{(\rho u)_{inviscid}} \right) r d\theta \quad (17)$$

and is analogous to the displacement thickness from boundary layer theory. (Note that δ^* will be referred to as the displacement thickness throughout the text.) The difficulty in evaluating δ^* arises in determining the inviscid velocity and density inside a compressor, in which the flow is compressible and not uniform across the passage. Since the density is not measured by the laser anemometer system, an

approximation of the displacement thickness inside the blade row is evaluated by neglecting the variation of density within the defect region , i.e. it is assumed that $\rho = \rho_{inviscid}$, and the displacement thickness is estimated by:

$$\delta^*(r) = \int_{\theta=0}^{2\pi/NB} \left(1 - \frac{u}{u_{inviscid}} \right) r d\theta \quad (18)$$

Downstream of the blade it is assumed that the static pressure is constant within the defect region and is equal to the value at the edge of the defect region.

Using this assumption of uniform static pressure and the ideal gas law, the ratio of density within the defect region to the inviscid density is evaluated by:

$\frac{\rho}{\rho_{inviscid}} = \frac{(T_s)_{inviscid}}{T_s}$ where T_s is the static temperature. Then the displacement thickness downstream of the blade is estimated by:

$$\delta_{downstream}^*(r) = \int_{\theta=0}^{2\pi/NB} \left(1 - \frac{T_{s,inviscid} u}{T_s u_{inviscid}} \right) r d\theta \quad (19)$$

The displacement thickness downstream of the blade has been evaluated using both equation 18 and equation 19. Comparing these calculations to those from CFD results indicate that using equation 19 is appropriate to account for the density variations in the defect region. The impact of density variations on the estimation of displacement thickness will be addressed later in this section.

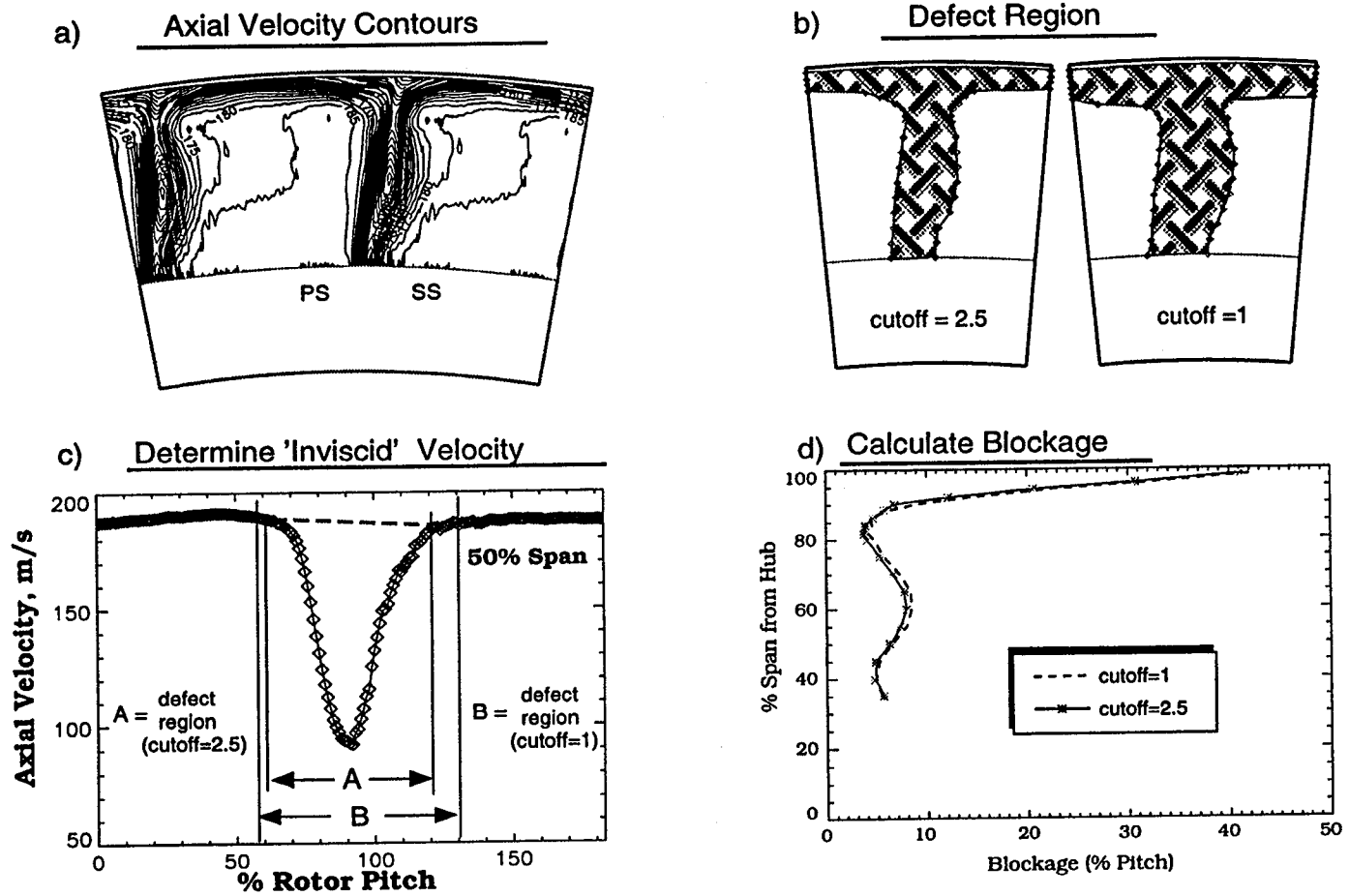


Figure 40 Procedure to calculate blockage downstream of the blade row.

1.1 Quantification of Blockage Downstream of the Rotor Blade Row

Downstream of the rotor blade row, data were acquired in a 'cross-channel plane' (circumferential direction versus the radial direction) at a given axial location. The blockage is evaluated by calculating the displacement thickness at each radial location where the data were measured using the axial velocity component. An example illustrating the method used is presented in Figure 40 and it shows the four main steps involved. Refer to Figure 40 for the discussion that follows:

- 1: *Identify the area at which to evaluate the blockage.*** Shown in Figure 40a is a cross-channel plane of the axial velocity contours at approximately 15% rotor chord downstream of the rotor trailing edge. The data were ensemble and passage averaged to represent the data in a representative rotor passage and were duplicated across two rotor pitches in the circumferential direction for clarity. The outlined region represents the annulus area from hub to tip across two rotor pitches. In this example the data were acquired from 35% to 98% of span from the rotor hub. The axial velocity contours are shown for increments of 5 m/s and the velocity deficit due to the rotor wake and endwall flow is clearly identifiable. Note that the left side of the wake is the pressure surface (PS) side and the right is the suction surface (SS) side of the wake.

2: Identify the velocity defect region. The defect region is determined by taking the gradient of the axial velocity in the radial and circumferential directions and applying a cutoff value:

$$\text{Defect Region : where } \left| \frac{\partial u}{\partial r} \right| + \left| \frac{\partial u}{\partial(r\theta)} \right| \geq (\text{cutoff}) \quad (20)$$

The cutoff value is influenced by the radial spacing of the measurements and the velocity gradients within the flowfield. In this investigation the radial spacing of the measurements was identical for each survey. However, the velocity gradients within the flowfield varied with operating condition and a different cutoff value was subjectively selected for each case. Note that the determination of this cutoff value is arbitrary but its choice is rather insensitive to the evaluation of the displacement thickness for two reasons. First, the velocity gradients decrease significantly with distance from the center of the defect region to the outer edges of the defect region. Second, outside of the defect region the velocity gradients are less than those within the defect region as is evident from the velocity contours in Figure 40a. To illustrate the sensitivity of the size of the defect region to the cutoff value, cutoff values of 2.5 sec^{-1} and 1.0 sec^{-1} were used. The resulting defect regions are plotted in Figure 40b. This cross-channel plot encompasses one rotor pitch and the defect region has been roughly centered on the plot. Note that near the shroud endwall the defect region encompasses the entire circumference

of the passage. A comparison of the axial velocity contours in Figure 40a to the defect region in Figure 40b illustrates that this method of determining the defect region is reasonable.

- 3: Determine the 'inviscid' velocity at each measurement location.** Outside of the defect region the 'inviscid' velocity is set equal to the local velocity. In the core flow region (the region in which the velocity defect no longer encompasses the entire circumference), the inviscid velocity across the defect region is linearly extrapolated from the velocity distribution in the circumferential direction outside of the defect region. This is shown schematically in Figure 40c, which depicts the circumferential distribution of the axial velocity at 50% span along with the location of the defect region. The dashed line indicates the estimated 'inviscid' velocity distribution which would be present if there were no viscous effects. Since the variation in the velocity between the pressure surface and the suction surface side of the wake is small in comparison to the velocity deficit within the wake, the calculation of the displacement thickness is insensitive to the estimation of the inviscid velocity. This process breaks down in the endwall region where the velocity defect encompasses the entire circumference. Therefore, in the endwall defect region the inviscid velocity is extrapolated in the radial direction from the velocity distribution outside of the defect region.

4: *Calculate the blockage at each radial measurement location.* Since the measurements do not span the entire annulus the blockage was calculated in a two-dimensional sense in that the displacement thickness is calculated at each radial measurement location and divided by the circumferential distance corresponding to the rotor pitch at that radial location.

$$B(r) = \frac{\delta_{downstream}^*(r)}{pitch(r)} \quad (21)$$

where the pitch is defined as $\frac{2\pi r}{NB}$ and NB is the number of rotor blades. To assess the sensitivity of the blockage to the cutoff value used, the blockage was evaluated for the two defect regions identified in Figure 40b. The results, presented in Figure 40d, indicate that the blockage is not a strong function of the cutoff value. The radial distribution of the blockage is identical in shape for both values of the cutoff and the maximum difference in the blocked area is about 0.8% of blade pitch. For all cases used in this investigation, the cutoff value ranged between 2 sec^{-1} and 3 sec^{-1} .

In order to assess the impact of the density variations in the defect region on the blockage calculations, CFD solution #2 was used to calculate the blockage using both the density-velocity defect (equation 17) and the velocity defect alone (equation 18). The results of these calculations are presented in Figure 41. The CFD results (though not shown herein) indicate the region of velocity defect is in

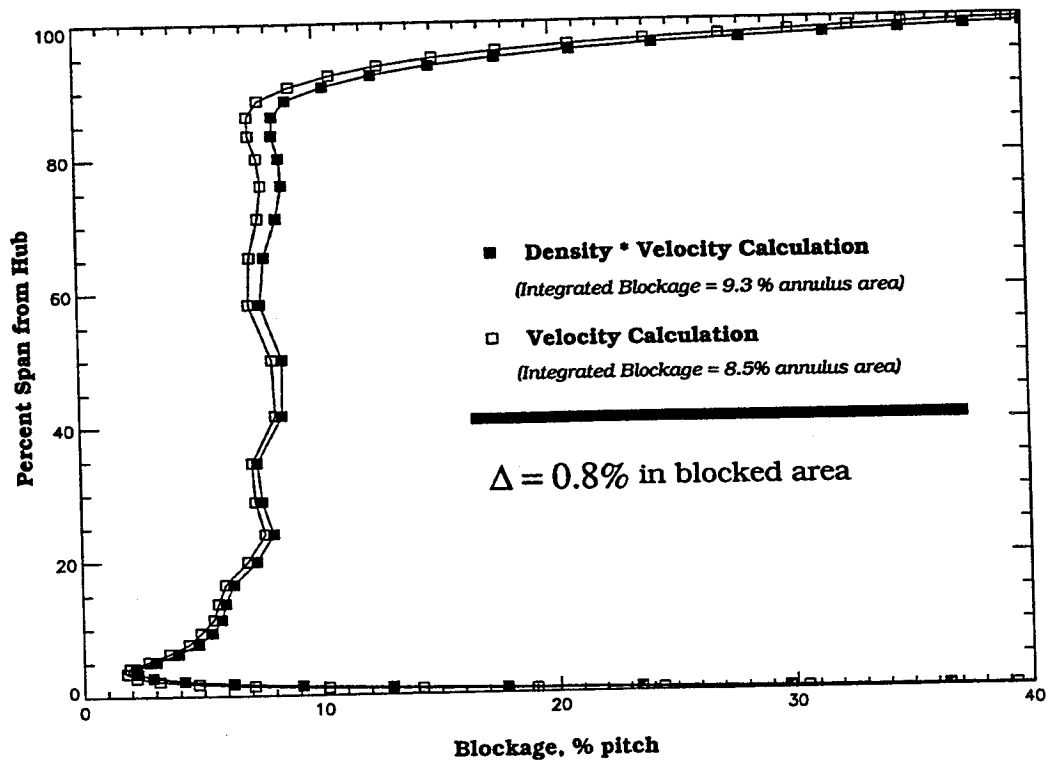


Figure 41 Impact of density on blockage calculation using CFD results.

phase with density defect, therefore neglecting density in the blockage calculation does not change the slope of the curve nor its magnitude by a significant amount. Also, since the variations in density and velocity are in phase, the trends of the blockage development are the same, i.e. the shape of the curve depicting the radial distribution of blockage is the same whether or not density is included in the calculation of displacement thickness. The inclusion of density variations in the blockage calculation does increase the overall level of blockage. However, in this example the difference in blockage is only 0.8% of the flow area. Also, note that CFD users can calculate the blockage using the same procedure used herein to compare their results to the data. In summary, the values of blockage calculated

downstream of the rotor using only the measured velocity distributions are within 10% of those calculated with density variations included, which is sufficient to establish trends and evaluate the regions of the flowfield which dominate the generation of blockage.

5.1.2 Quantification of Blockage within the Rotor

Within the blade row the evaluation of blockage becomes more difficult. In addition to the flow being more complex inside the blade-row, a further complication arises due to the fact that there are difficulties making measurements inside the blade boundary layer for the following reasons: 1) the curvature and radial twist of the blade make it impossible for the laser anemometer system to have an unobstructed view of the blade surfaces; 2) it is more difficult for the seed material to get into the boundary layer and therefore more difficult to make measurements; and 3) the reflections from the blade surface increase the noise level of the laser anemometer signal, and therefore data are rejected from the signal processor.

Upstream of the shock the boundary layer is very thin and there are very few measurements within the boundary layer. Fortunately, the data agrees very well with the CFD in the region ahead of the rotor passage shock where the blockage is minimal. The greatest discrepancies between the CFD and the data occur downstream of the shock where the blockage is sufficient to impact the flow.

Downstream of the shock the boundary layer is thick enough to enable acquisition of measurements within the outer region of the boundary layer. For example the relative velocity across a rotor pitch at approximately 85% rotor chord and 70% rotor span is plotted in Figure 42. The left hand side of the plot represents the suction surface of a rotor blade and the next blade is shaded on the right hand side of the plot. Note that there is no data within about 8% of pitch from the suction surface and about 5% of pitch from the pressure surface. In order to estimate the velocities within the inner region of the boundary layer where the data is missing the following steps were taken:

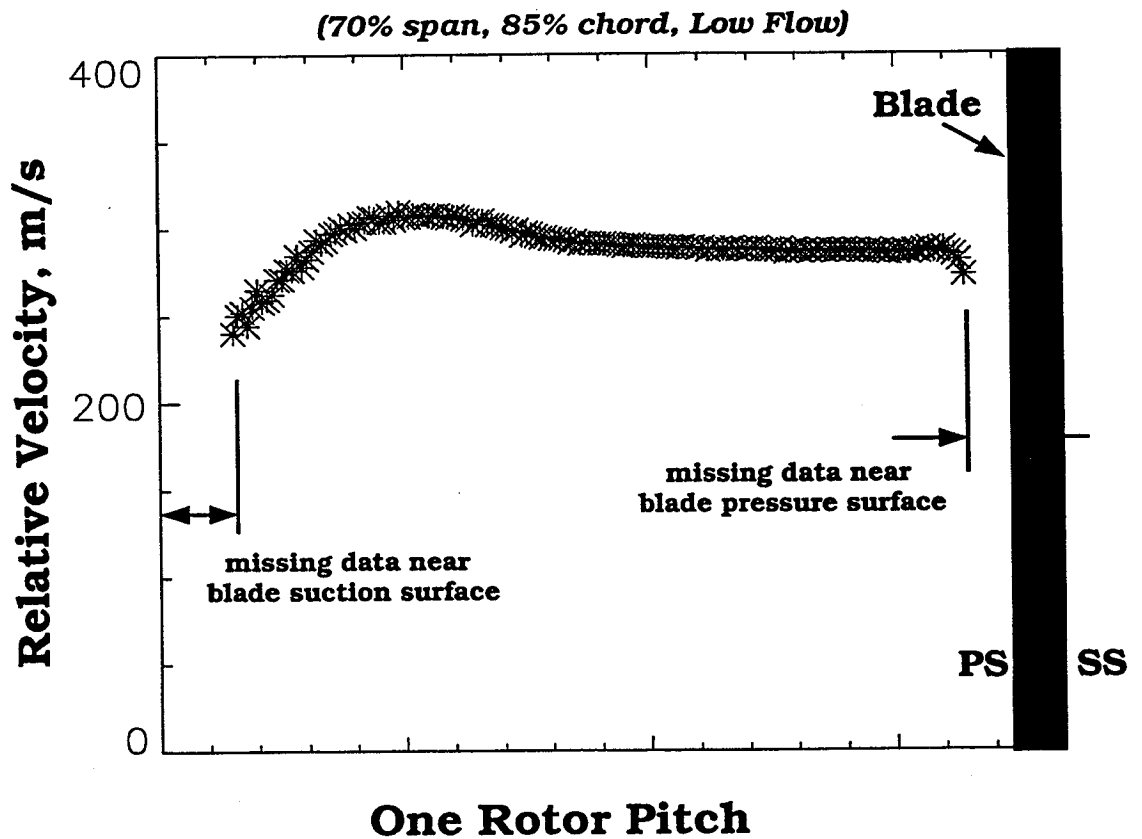


Figure 42 Example indicating that data is not acquired near the blade surfaces.

1. Identify the edge of the boundary layer in a manner similar to that described in the previous section for finding the edges of the wake.
2. Fit a power law velocity distribution to the data in the outer region of the boundary layer by determining the value of the exponent 'n' for:

$$\frac{u}{u_{inviscid}} = \left(\frac{y}{\delta}\right)^n \quad (22)$$

3. Use the power law fit to estimate the values of the velocity within the inner region of the boundary layer where no data was acquired.
4. Calculate the displacement and momentum thicknesses using the measured and estimated velocities within the boundary layer. The resulting shape factor is compared to the theoretical value of the shape factor H, where $H=2n+1$, to assess the 'goodness' of the power law fit described in item 2.
5. Calculate the blockage. To obtain a dimensionless blockage the displacement thickness is normalized by the rotor gap (the distance corresponding to one rotor pitch minus the blade thickness).

The blockage is calculated using the relative velocity component, which is approximately parallel to the blade surface. Figure 43 illustrates the estimation of the displacement thickness and blockage resulting from the suction surface boundary layer. By definition the displacement thickness is calculated in the

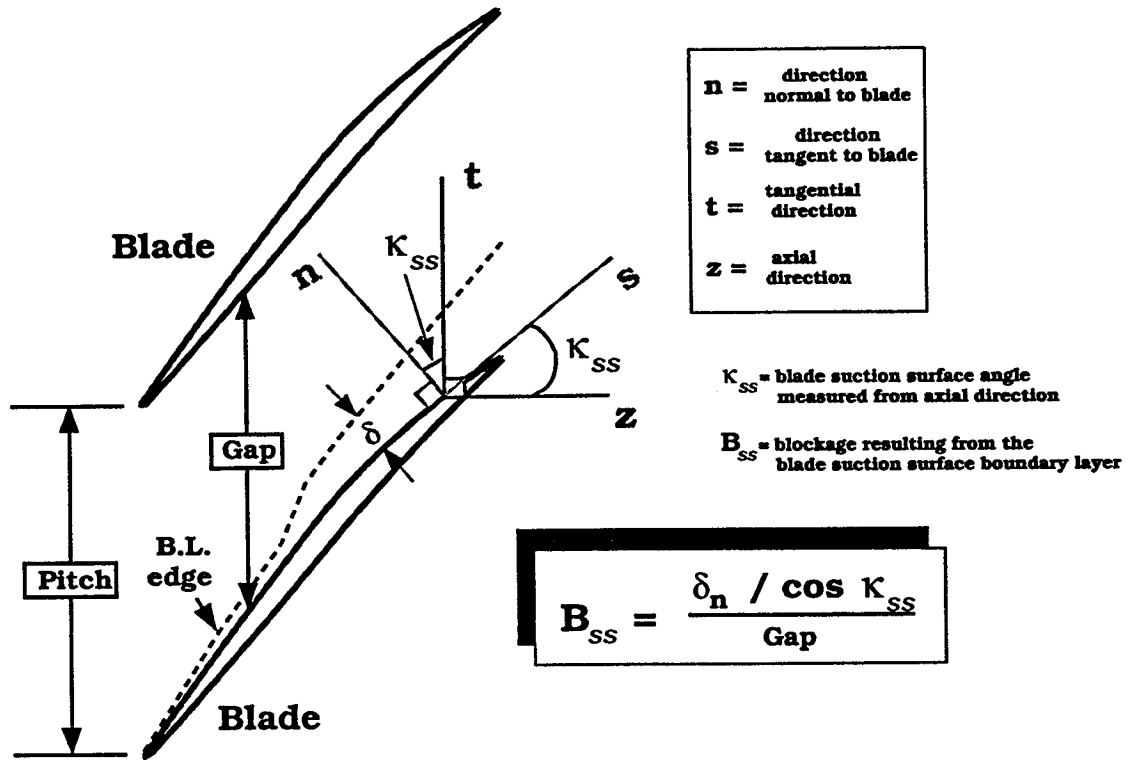


Figure 43 Blockage calculation inside the blade row.

direction normal to the wall or in this case the blade surface. However, the data were acquired along the 't' axis, while the velocity component is approximately normal to the 'n' axis. Therefore, the displacement thickness in the normal direction, 'n' is calculated as :

$$\delta_n^* = \int_{wall}^{\delta_n} \left(1 - \frac{u_s}{(u_s)_{inviscid}} \right) dn \tag{23}$$

where, $dn = dt * \cos \kappa$ and κ is the blade surface angle measured from the axial direction.

It is assumed that within the boundary layer the relative velocity measured along the 't' axis does not differ significantly from the relative velocity along the

'n' axis. Based on the small distances involved and the small streamwise gradients of the relative velocity and δ_n^* this is not a bad assumption. In order to calculate blockage, the boundary layer displacement thickness must be related to a reduction in effective flow area. Since the area of the flowpath normal to the axial direction was chosen as the reference geometric area, the blockage is evaluated by projecting the displacement thickness normal to the blade surface onto the tangential plane and normalizing by the rotor gap. Since the pressure surface and suction surface boundary layers are handled independently, the blockage is evaluated for each surface and summed to determine the total blockage at a given axial location:

$$B = \left[\frac{\delta_n^* / \cos \kappa_{ss}}{gap} \right]_{suction} + \left[\frac{\delta_n^* / \cos \kappa_{ps}}{gap} \right]_{pressure} \quad (24)$$

It may seem inconsistent that the blockage is calculated using the relative velocity component inside the blade row, whereas, downstream the axial velocity component is used. Actually, there is no discrepancy between these two methods because the relative velocity component multiplied by the cosine of the flow angle is the axial velocity component. Since the flow angle in the boundary layer is nearly the blade surface angle, κ , the blockage evaluated using the method described above with the relative velocity is equivalent to the method used downstream which uses the axial velocity component.

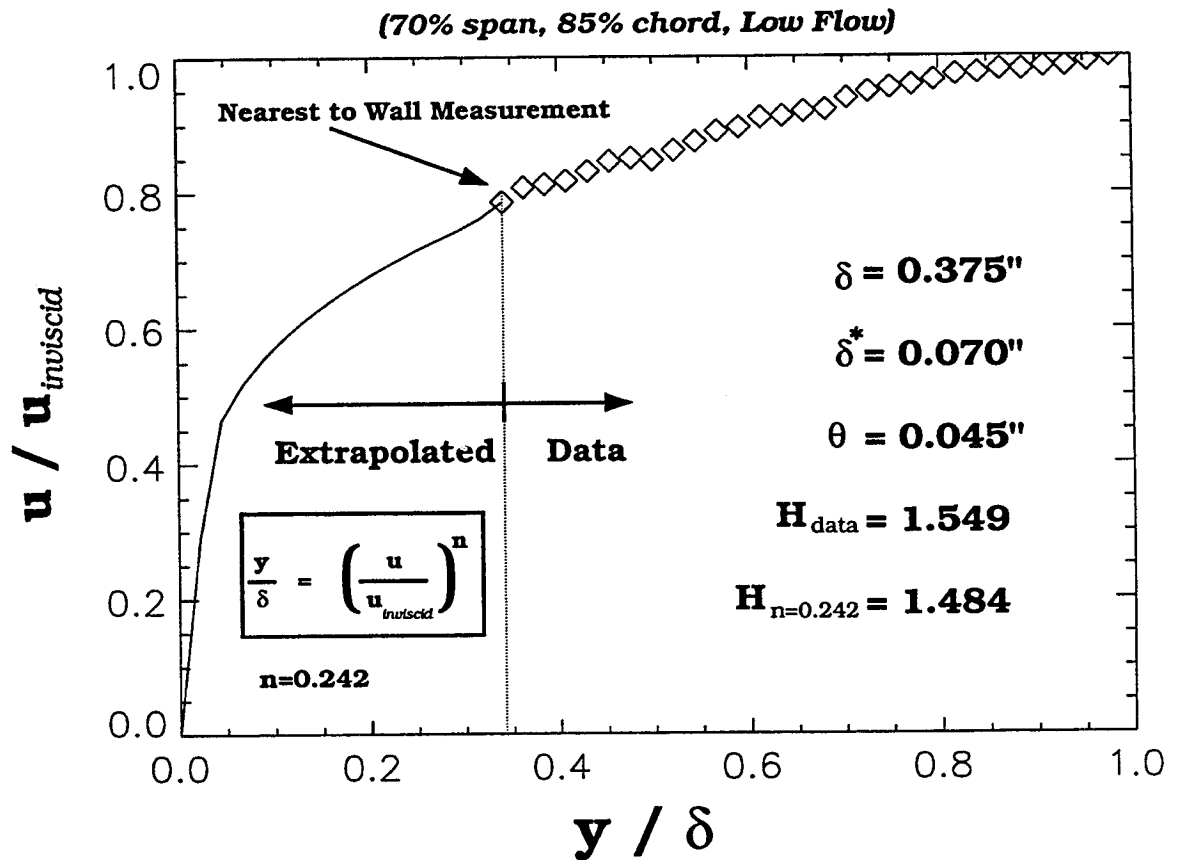


Figure 44 Sample calculation showing estimation of boundary layer parameters.

Sample Calculation. The result of this calculation procedure for the suction surface boundary layer shown in Figure 42 is presented in Figure 44. The shape factor calculated from the data is 1.55 versus the theoretical value of 1.48 which was based on the power law velocity distribution. The fact that the value for the shape factor is reasonable for a turbulent boundary layer in an adverse pressure gradient and that the shape factor from the idealized power law velocity distribution differs by about 5% from the measured data indicate that approximating the velocity

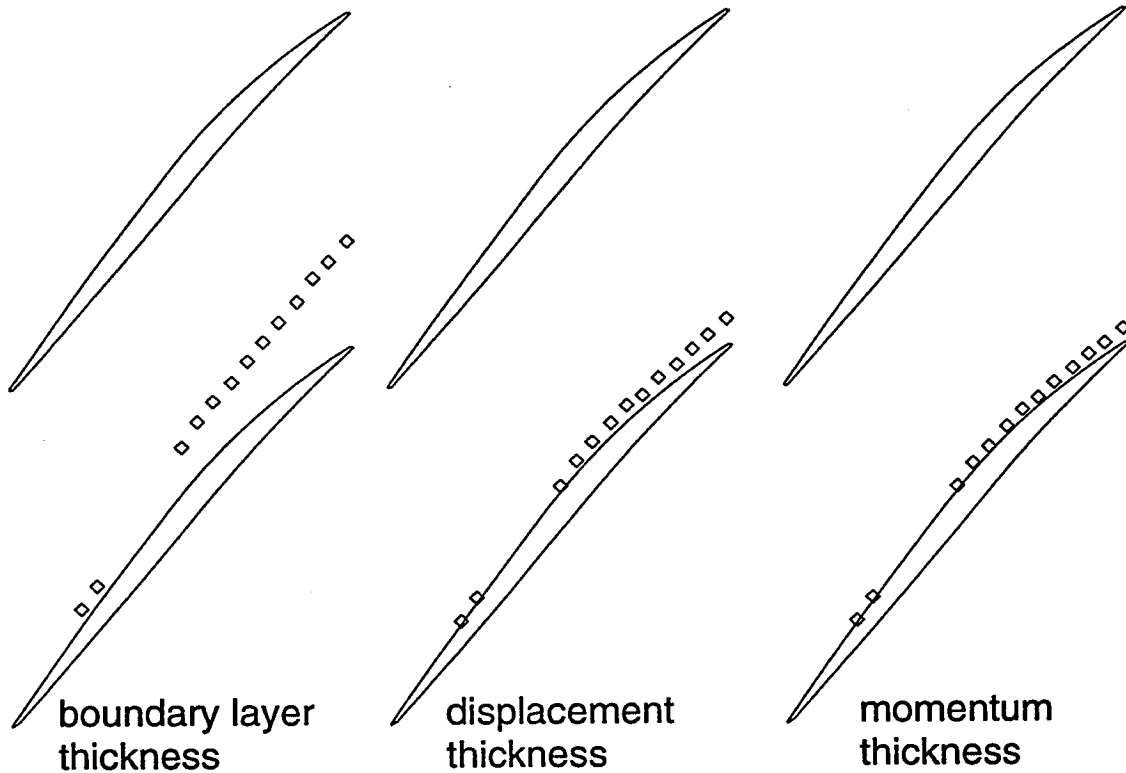


Figure 45 Development of the boundary layer thickness parameters, δ , δ^* , and θ for the low flow, design speed condition.

profile with a power law is a reasonable approach. In Figure 45, the calculations of the boundary layer parameters for the low flow design speed condition at 70% span are plotted in relation to the blade geometry. Note that at each axial measurement location the boundary layer parameters are calculated independently, yet as a group they appear well-behaved. In the following section these procedures will be used to calculate the blockage development within the blade row.

5.2 Calculation of Blockage

5.2.1 Downstream Blockage Calculations

At the trailing edge of the blade the boundary layers from the pressure and suction surface merge to form the rotor wake. In the region near the trailing edge, often referred to as the near wake region, there is significant momentum exchange and mixing between the two blade surface boundary layers. Once the rotor wake has formed it mixes more gradually with the freestream and decays in the core flow region analogous to the two-dimensional turbulent wake decay described in Schlichting [61]. For example, the change in the rotor wake structure with increasing distance from the blade trailing edge is plotted for the data at 70% span for high and low flow operating conditions in Figure 46. The wake has been centered in the plot for clarity. It is evident that the wake is nearly mixed-out by 152% rotor chord. To quantify the mixing of the wake with the freestream, the wake decay is defined as:

$$Wake\ Decay = \frac{(V_{rel})_{inviscid} - (V_{rel})_{min}}{(V_{rel})_{inviscid}} \quad (25)$$

The wake decay at 70% span for high and low flow condition is plotted in Figure 47. It is evident that the wake decays very rapidly in the first 20–30% chord downstream of the blade and by 150% rotor chord the mixing is nearly complete.

Since the blockage calculation essentially evaluates the wake displacement thickness, the blockage will vary with distance downstream of the blade trailing

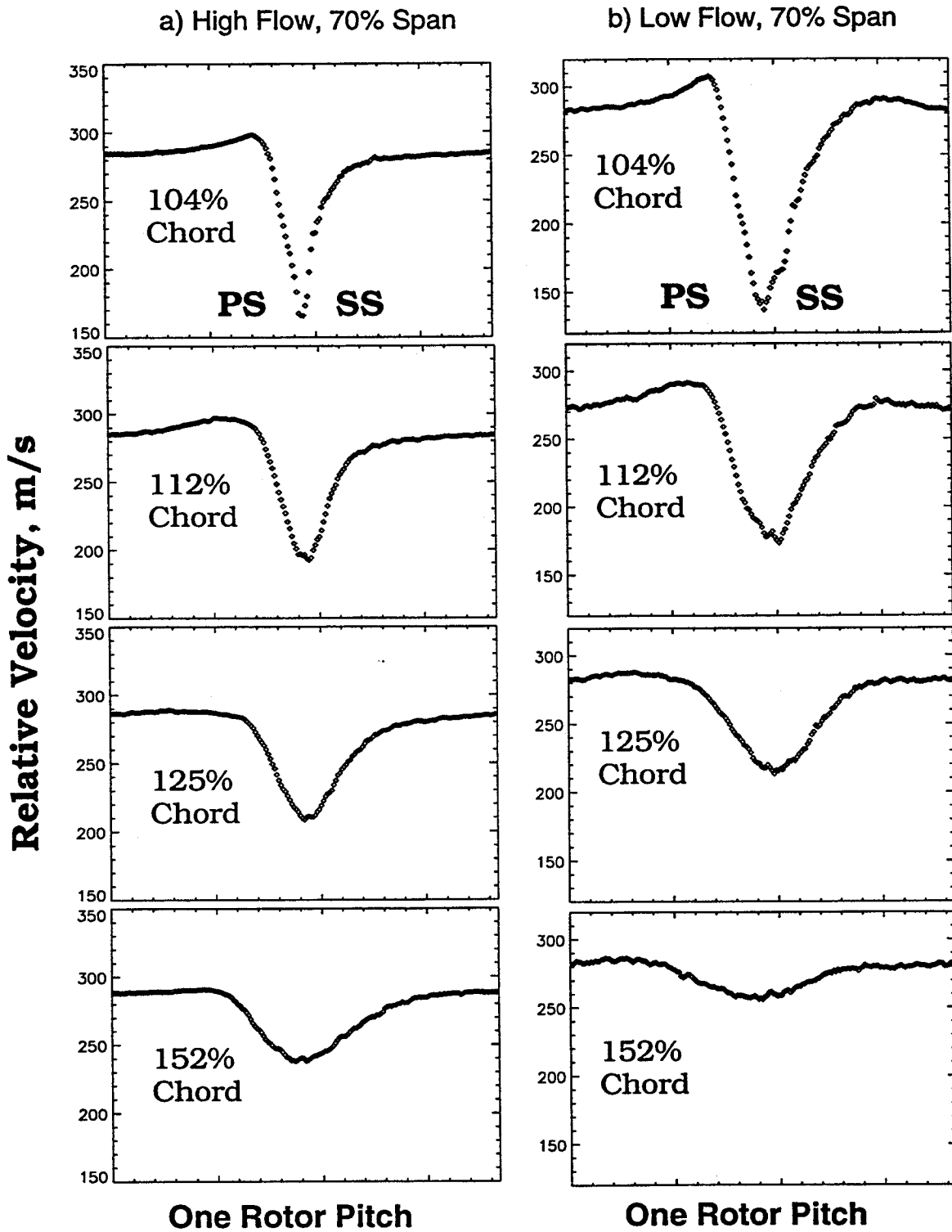


Figure 46 Wake profiles versus chord at 70% span for a) high flow and b) low flow operating condition at 100% speed.

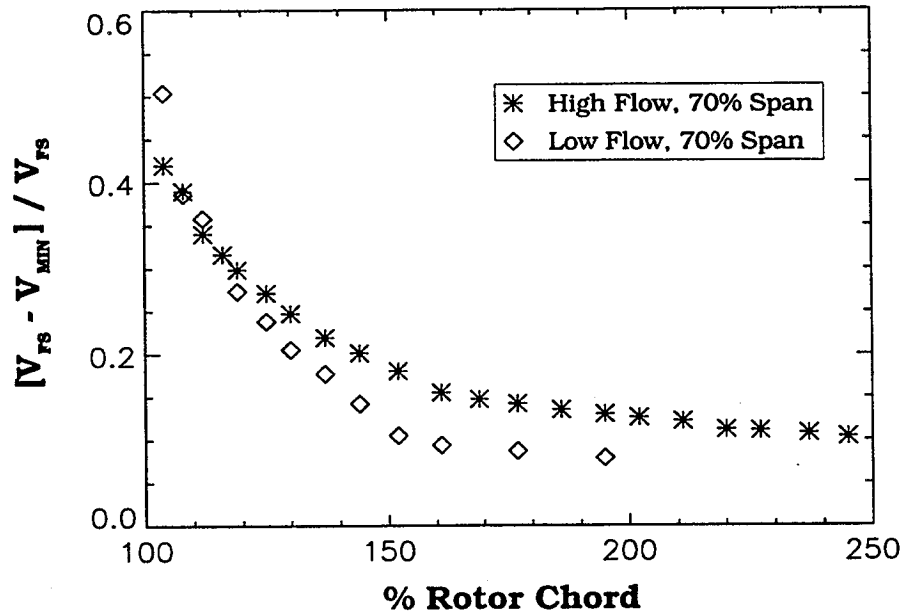


Figure 47 Wake decay versus percent of rotor chord at 70% span for high flow and low flow operating condition at 100% speed.

edge. It is clear that at an infinite distance from the blade trailing edge the blockage goes to zero. In order to determine the appropriate downstream location to assess the blockage, the distribution of the wake momentum thickness with distance downstream of the blade was calculated. The results at 70% span for the high flow, design speed condition are plotted in Figure 48. The momentum thickness increases during the first 15% chord downstream of the blade trailing edge which indicates the region of substantial mixing and momentum exchange, after which the momentum thickness is essentially constant, thereby indicating a two-dimensional wake decay behavior. These results are similar to those of McCormick et al. [62] who performed a detailed experimental investigation of the trailing edge flowfield on a large scale cascade which simulated compressor airfoils.

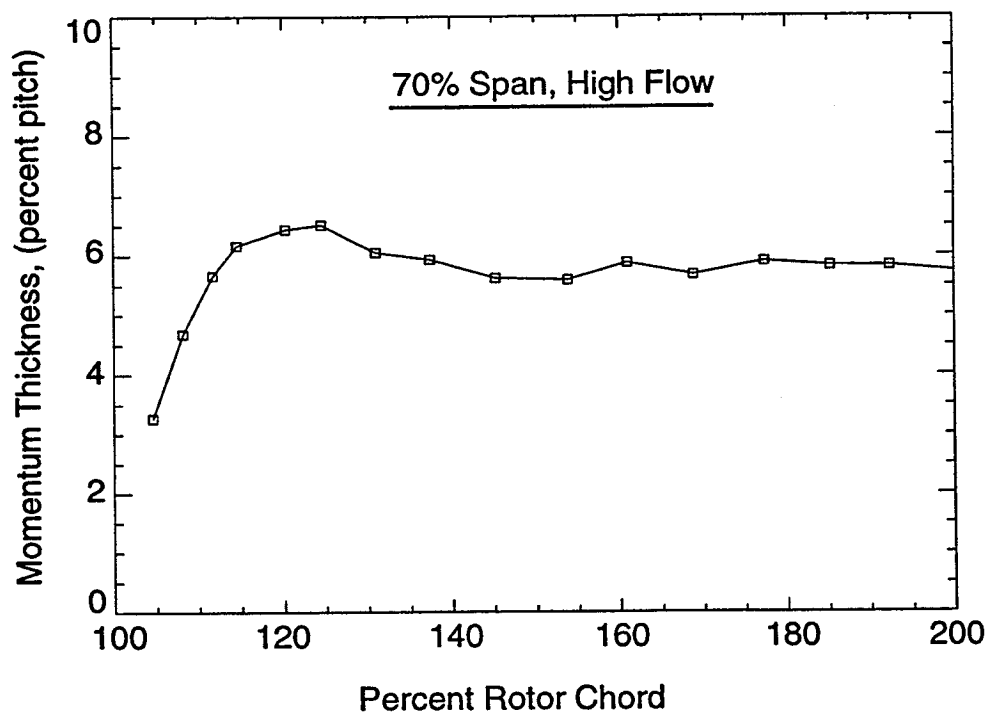


Figure 48 Wake momentum thickness versus chord at 70% span for high flow operating condition at 100% speed.

The results shown in Figures 47 and 48 suggest that streamwise gradients in blockage will be relatively small beyond 120%-130% chord, and that data acquired at 120% to 130% chord would be the most appropriate to use in the evaluation of blockage. Therefore, blockage will be evaluated at 130% chord for design speed operating conditions. At part speed conditions there is insufficient data at 130% chord and the blockage will be evaluated at 115% chord. To assess the variation in the blockage between 115% and 130% chord, the blockage distributions across the span for the high flow design speed condition are evaluated at both 115% and 130% chord and the results are presented in Figure 49. The differences are small across the span with the largest differences occurring in the endwall region

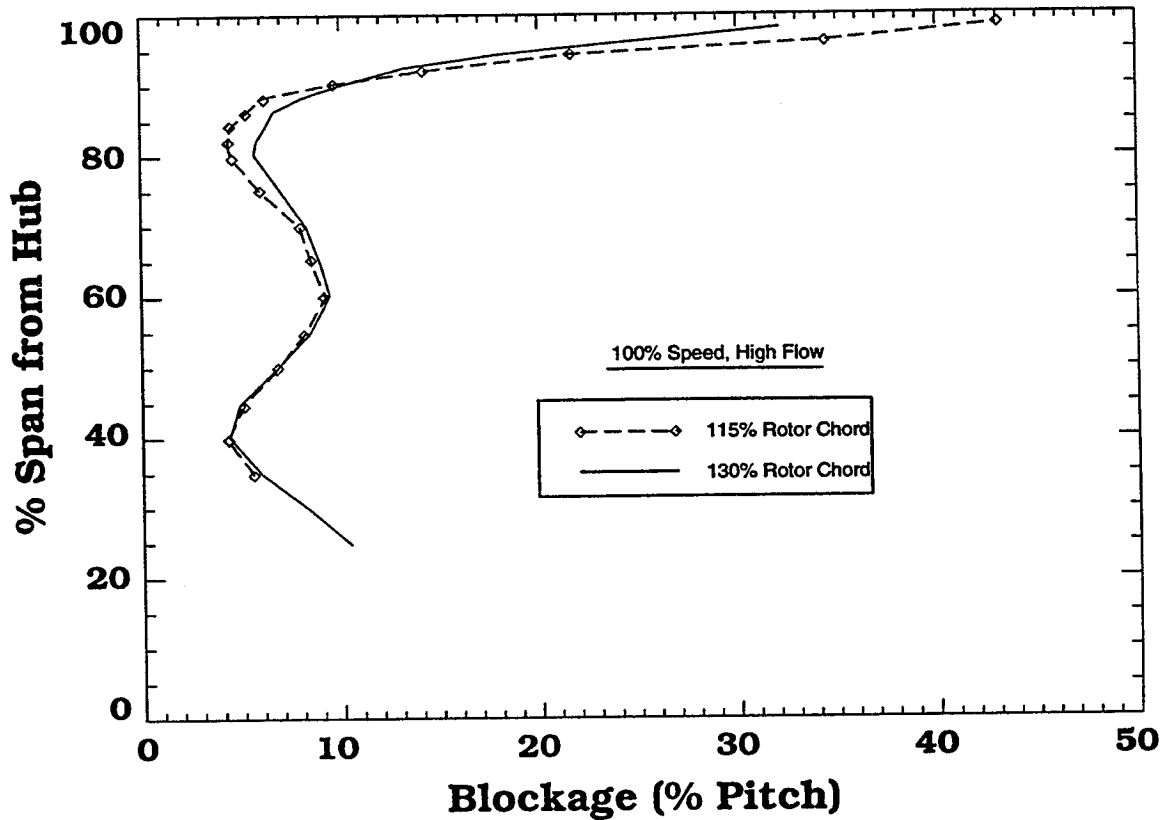


Figure 49 Radial distribution of blockage at 115% and 130% rotor chord for the 100% speed high flow operating condition.

where the gradient of the blockage distribution is greatest. There appears to be a redistribution of blockage from the endwall to the lower spans as evidenced by the decrease in blockage from 90–98% span and the increase in blockage from 70–90% span with increasing downstream distance, which merely emphasizes the point that the estimate of the blockage is sensitive to the location at which it is evaluated. However, the shape of the radial distribution of blockage is similar at these two locations and the blockage below 70% span is essentially constant. Since the conclusions drawn from the blockage distribution at 115%

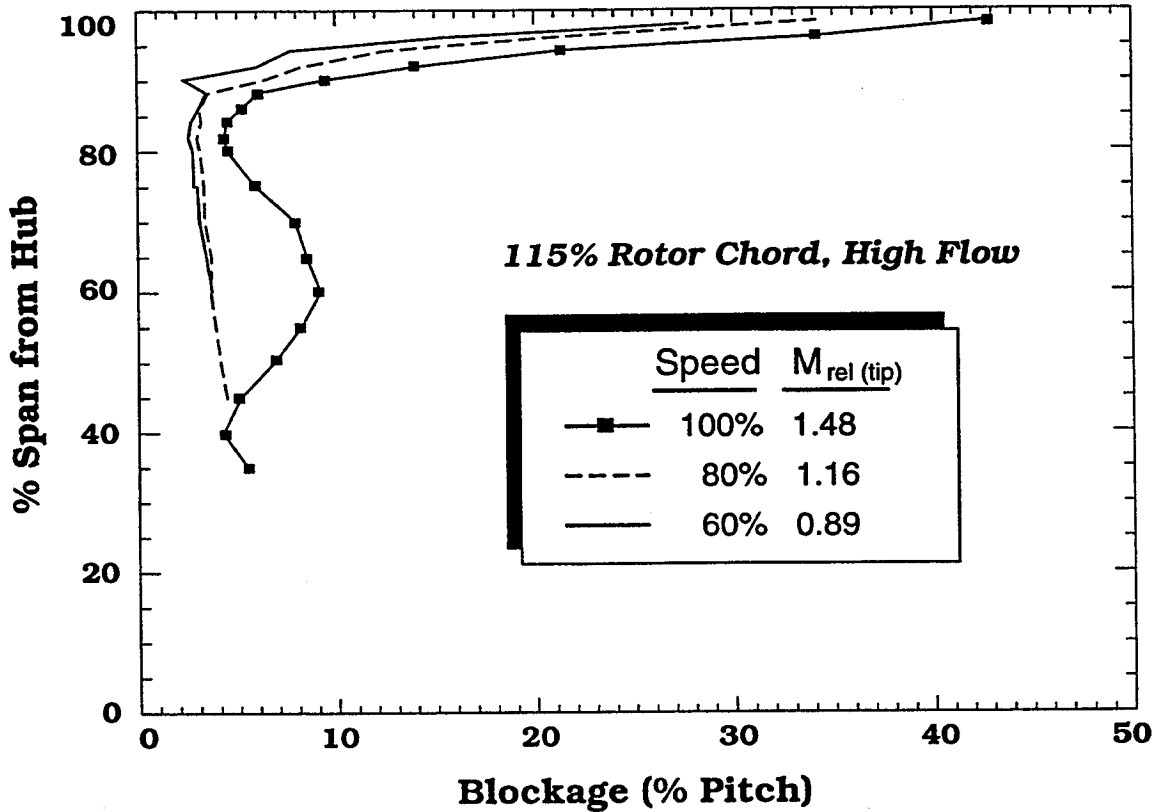


Figure 50 Radial distribution of Blockage at 60%, 80%, and 100% speed. chord would not differ from those at 130% chord, using either of these two locations is considered appropriate.

2.1.1 Comparison of Results at 100%, 80%, and 60% Rotor Speed. The radial distribution of blockage at 115% rotor chord for the rotor operating at a mass flow which maintains nearly the same flow incidence angle for 60%, 80%, and 100% of rotor design speed is plotted in Figure 50. This operating condition is near peak efficiency and corresponds to the circled conditions in Figure 12. The symbols for the design speed results indicate the measurement radii. These same measurement locations were used at 60% and 80% speed, but the symbols

were omitted for clarity. For part speed conditions the following observations are noteworthy:

1. Blockage in the endwall region is much larger than the core region.
2. Blockage in the endwall region is slightly higher for the 80% speed case as compared to the 60% speed case. Although the casing boundary layer is thicker and the tip clearance height is greater at 60% speed, the blockage generated by the tip clearance flow is larger at 80% speed due to 1) the higher blade loading which results in more flow through the tip clearance gap and 2) the interaction of the tip clearance vortex with the passage shock.
3. Blockage in the core region is nearly identical at 60% and 80% speed indicating the blockage due to the rotor wakes is nearly identical.
4. The radial distribution of blockage in the core region is nearly constant which indicates the blockage from each blade section is nearly identical.

Similarly, for the design speed data consider the following:

1. Blockage is significantly larger in the endwall region as compared to the core region much like that observed at part speed.
2. Blockage in the endwall region is much larger at design speed than part speed conditions. The increase in blockage from part speed to design speed conditions is attributed to the increase in rotor tip clearance flow and the

additional blockage resulting from the interaction between the shock (which is stronger at 100% speed in comparison to 80% speed) and the clearance flow.

3. The radial distribution of blockage in the core region is no longer constant with radius and the level is much larger than it was at part speed.

In the next subsection the increase in blockage at design speed will be shown to be due in part to the shock / boundary layer interaction thickening the blade suction surface boundary layer for the design speed data where the shock is strong enough to induce a small boundary layer separation. The variation of blockage with span is indicative of the sensitivity of the shock / boundary layer interaction to the blockage development. Note these results are consistent with the results presented in the earlier chapters which indicated a significantly larger rotor wake at design speed in comparison to the wakes at part speed conditions.

2.1.2 Comparisons of Design Speed Results at High and Low Flow.

The effect of blade loading on blockage development is illustrated in Figure 51 where the radial distribution of blockage at 130% chord for the rotor operating at design speed and the high and low flow conditions is plotted. The measurements at the high flow condition were acquired with the same resolution in the radial direction as that indicated by the symbols at the low flow condition but the symbols were omitted at high flow conditions for clarity. As the loading is increased from

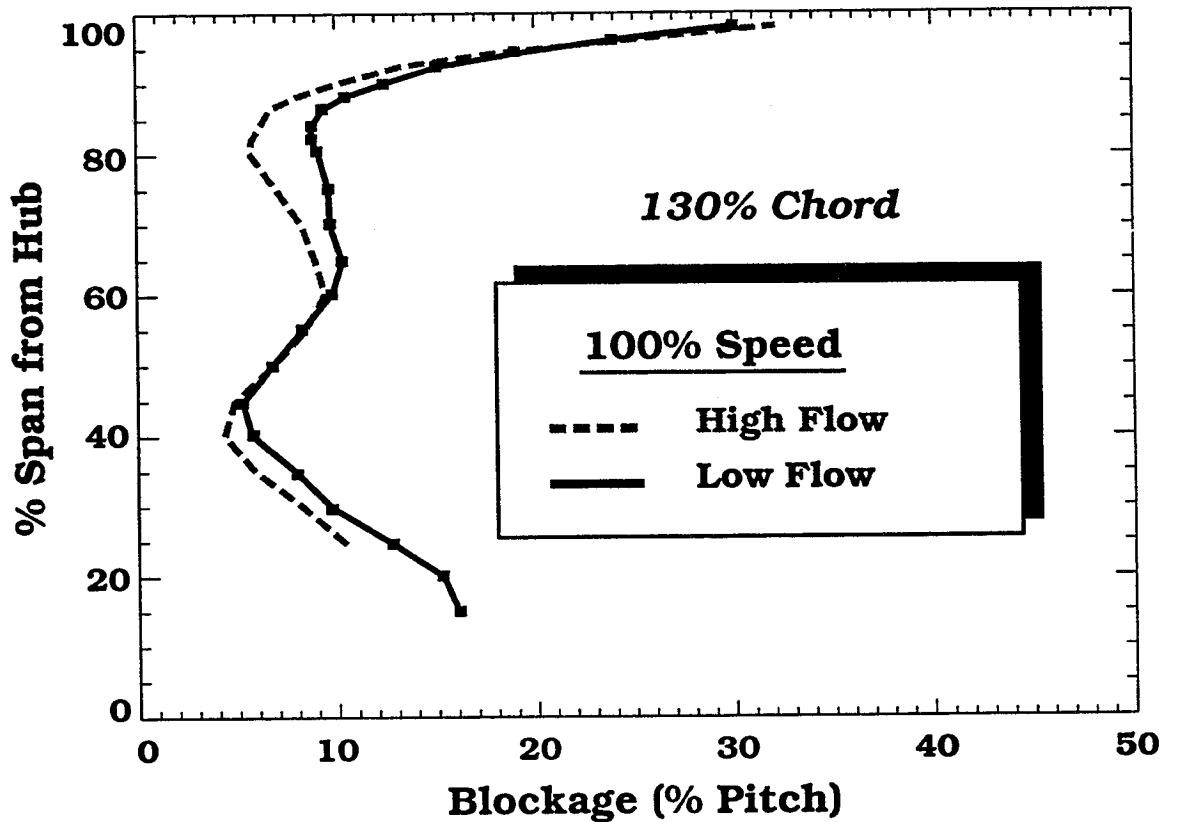


Figure 51 Radial distribution of Blockage at 130% chord and 100% speed for the low flow and high flow conditions.

the high flow to low flow condition the overall blockage increases as expected. However, the increase in blockage is not uniform across the span. From Figure 51 it is evident that the blockage increase primarily occurs from 60–90% span and below 40% span. It is also interesting to note that the shape of the curve representing the radial distribution of blockage is similar for the high and low flow conditions at design speed and very much different from that at part speed conditions. In addition, the blockage distribution is consistent with the radial distributions of pressure and temperature presented in Figure 15. For example, the blockage dips to a local minimum at 40% span which is consistent with a local

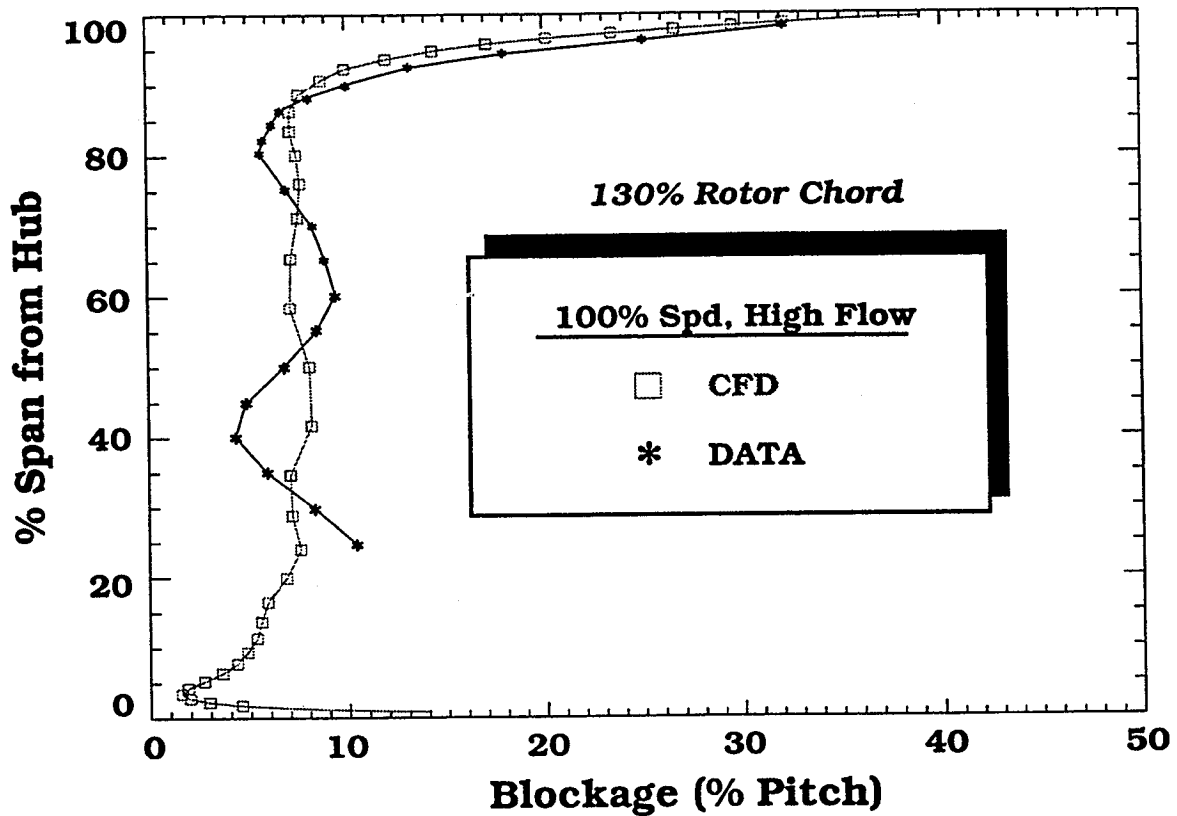


Figure 52 Radial distribution of Blockage at 130% chord and 100% speed for the high flow conditions — Comparison between CFD and Data.

increase in the total pressure and total temperature i.e. less blockage implies more work input and therefore more pressure rise.

2.1.3 Comparisons of Data to CFD Results. It has been shown that blockage is related to the performance and that the CFD does not accurately predict the performance at design speed. Therefore, it stands to reason that the CFD should not predict the blockage. The radial distribution of blockage was evaluated, using the same calculation procedure (see equations 19 and 21), from the CFD solution #2 and the data, and the results are presented in Figure 52. As expected the CFD

blockage calculation does not agree with the data. Not only are the differences in blockage of 3–4% indicated at 25%, 40%, and 60% span significant but the general shapes of the two curves are quite different and consistent with their respective radial distribution of pressure and temperature shown in Figure 17. It is evident that the CFD solution #2 is underpredicting the blockage in the outer endwall region which is consistent with the comparisons of the relative Mach number contours in the previous chapter which indicated the CFD solution #2 was underpredicting the radial extent of influence of the shock / leakage vortex interaction. Apparently, the CFD is missing some of the relevant flow physics associated with blockage development.

Comparison to Khalid's Model of the Endwall Blockage. Khalid [4] formulated a non-dimensional set of parameters which related the blockage generated in the endwall region by the leakage flow to the aerodynamic loading of the blade. A brief discussion on the development of Khalid's blockage and loading parameters follows. The blockage parameter can be summarized as:

$\frac{\text{blocked area in the endwall}}{\text{leakage flow area}} * \frac{\Delta P \text{ in through flow direction}}{\Delta P \text{ across blade tip}}$, where the second term is the ratio of the pressure difference which drives the mainflow through the passage to the pressure difference which drives the leakage flow through the clearance height. Note that blocked area in the endwall is denoted in Khalid's nomenclature by $A_b \cos(\beta_e)$ and the leakage flow area is denoted by τc where τ is the clearance

height and c is the aerodynamic blade chord. By performing a force balance in the axial direction, one obtains: $F_{lift} \sin \beta_{vm} = \Delta P_{in\ through\ flow\ direction} * s$, where F_{lift} is the mean lifting force and β_{vm} is the angle between the tangential direction and the mean lifting force. Therefore, the left hand side represents the lifting force in the axial direction and s is the blade spacing or pitch such that the force is evaluated for a unit length. The lifting force per unit length can also be written as $F_{lift} = \Delta P_{across\ blade\ tip} * c$. Therefore, the blockage parameter reduces to $\frac{A_b \cos \beta_e}{\tau c} * \frac{c F_{lift} \sin(\beta_{vm})}{s F_{lift}} = \frac{A_b \cos \beta_e}{\tau s / \sin \beta_{vm}}$. The loading parameter is the ratio of the difference in the static and relative total enthalpy (integrated over the defect region in the endwall) to the inlet relative dynamic head (evaluated at the radial reference location corresponding to two times the clearance height from the endwall) and is represented as: $\frac{\overline{\Delta H^a} - \overline{\Delta H_t^a}}{0.5 V_{2r}^2}$.

Khalid performed numerical simulations of a cantilevered stator, a low speed rotor (E3 rotor), and a transonic-fan (rotor 67) with various tip clearance heights from which he calculated the blockage and loading parameters. The results of Khalid's correlations are presented in Figure 53 where the ordinate represents the blockage parameter and the abscissa the loading parameter. There are four points plotted for each configuration tested corresponding to the blockage and loading at 25%, 50%, 75%, and 100% rotor chord. For example, the symbols with a solid border depict the blockage and loading at the blade trailing edge, while the

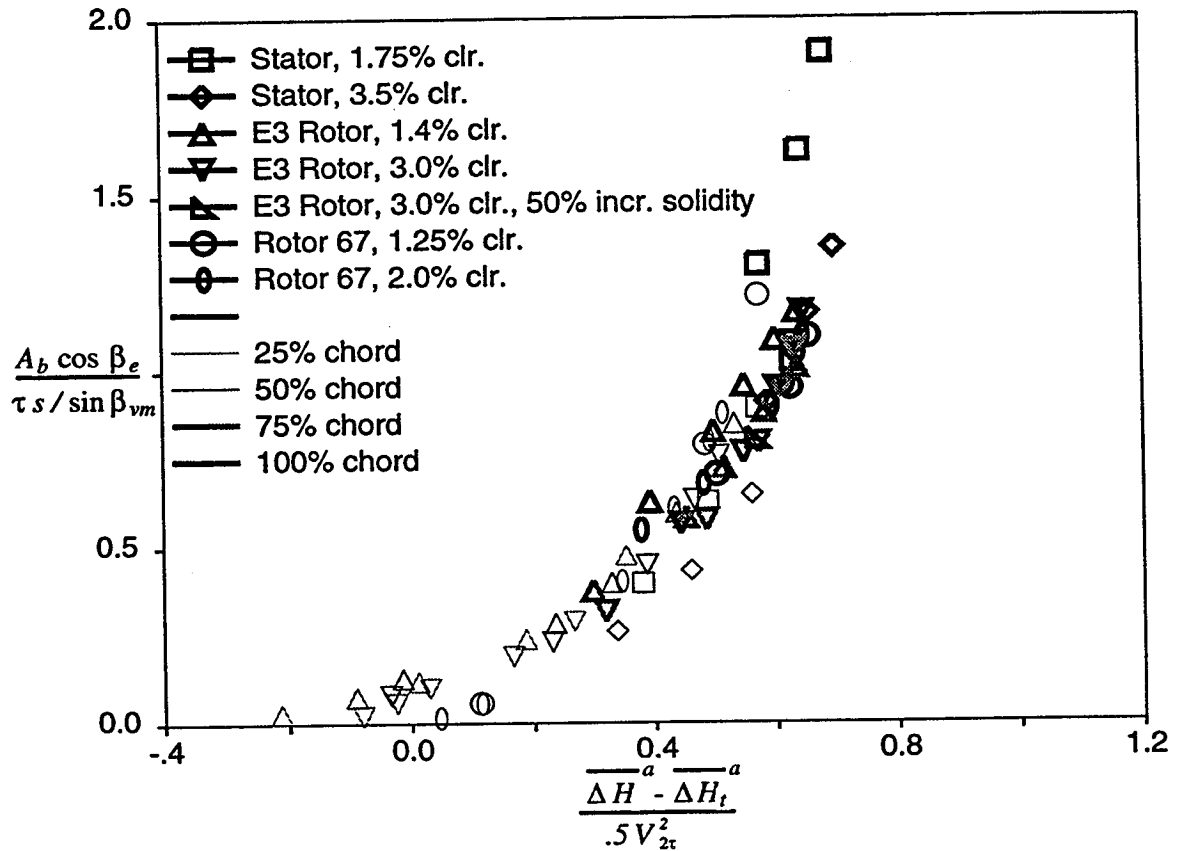


Figure 53 Khalid's [4] correlation of loading versus endwall blockage.

symbols outlined with the dashed line indicate the blockage and loading at 25% chord. These results illustrate the increase in the endwall blockage with increased loading and indicate that there is a limiting value of the loading parameter.

Khalid's development of blockage parameter versus loading parameter is based primarily on the blockage resulting from the leakage flow over the rotor tips and the mixing which takes place between the leakage vortex, leakage flow, and the main through-flow and therefore does not consider the blockage generated by the shock / vortex interaction. In addition, the correlation was based entirely on

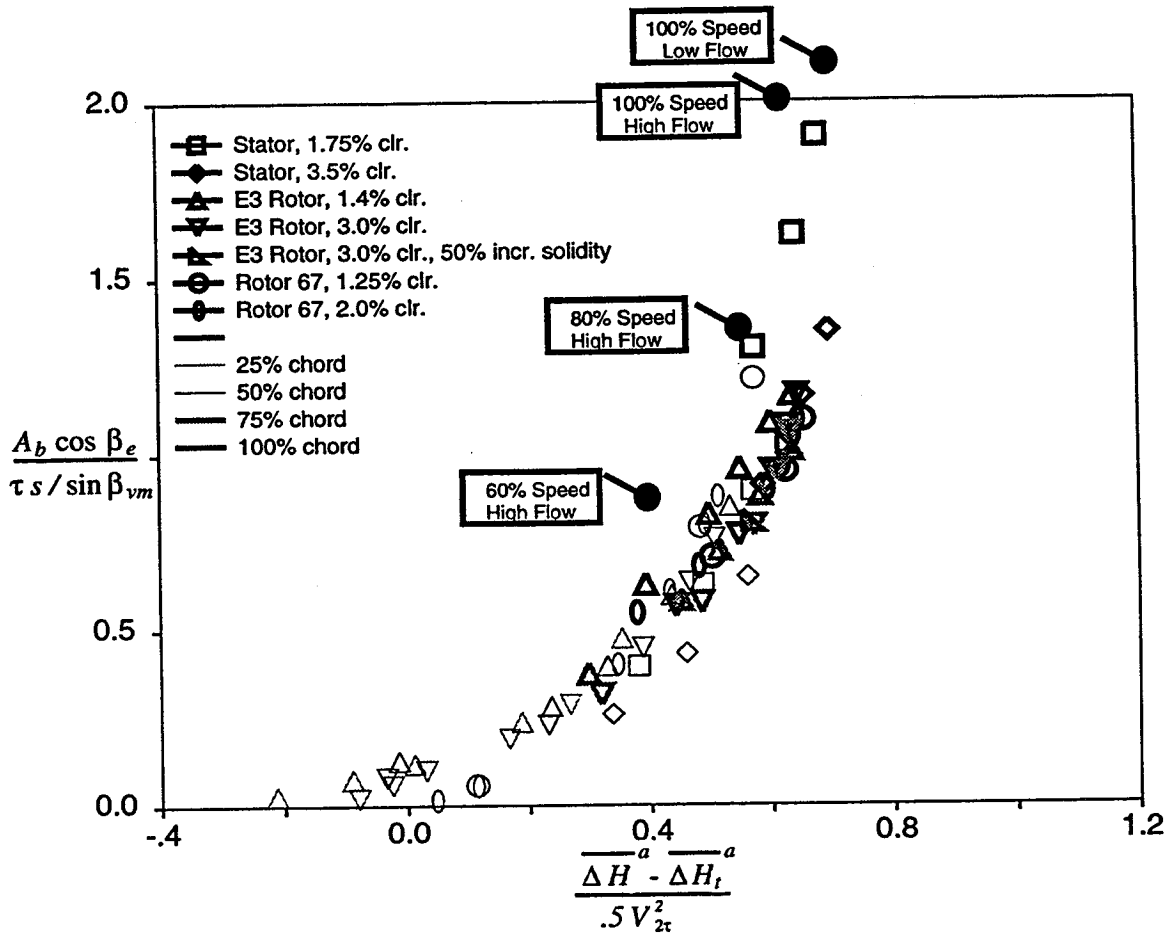


Figure 54 Comparison of NASA rotor 37 data to Khalid's [4] correlation of loading versus endwall blockage.

numerical simulations. Therefore, the data acquired in this investigation can be used to assess the correlation for a different blade row using experimental data rather than CFD simulation results. The data acquired in this investigation were normalized in a manner analogous to Khalid's blockage and loading parameters. However, the comparisons could only be made downstream of the blade row due to the insufficient spanwise resolution of the data inside the blade row. The results are presented in Figure 54 where the values for NASA rotor 37 are denoted by

the solid circles. The blockages are slightly higher for NASA rotor 37 than those of Khalid's analysis for the following reasons: 1) at design speed and 80% speed the blockage is increased due to the shock / clearance flow interaction and the shock / boundary layer interaction; 2) at 60% speed there is additional blockage in the endwall region which is attributed to the 'second' vortex, a flow feature which is not present at design speed conditions. However, the general trend of the correlation is preserved and the data exhibits the increase in endwall blockage with loading and is in agreement with the limiting value for the loading parameter. In conclusion, the data does confirm the analysis and parameterization developed by Khalid are appropriate for correlating endwall blockage.

Summary of Blockage Results Downstream of the Blade Row. Table 6 summarizes the blockage calculations downstream of the blade row. The blockage and loading parameters as defined in Khalid's analysis are included for completeness along with the identification of the endwall defect region. The last two columns of this table were generated by performing an integration of the radial distribution of the blockage in the core flow and endwall regions. For example the average blockage in the endwall region is evaluated by:

$$B|_{r_1-r_2} = \frac{\int_{r_1}^{r_2} \delta^*(r) dr}{\pi(r_2^2 - r_1^2)/NB} \quad (26)$$

Table 6 Summary of Integrated Blockage Results Downstream of the Rotor

% De-sign-Speed	Flow Rate	Endwall Defect Region (% span)	Khalid's Blockage Parameter	Khalid's Loading Parameter	Endwall Blockage (% area)	Core Flow Blockage (% area)
100	High	84 - 98	2.01	0.63	17	9
100	Low	84 - 98	2.11	0.69	18	10
80	High	86 - 98	1.32	0.55	14	4
60	High	86 - 98	0.86	0.40	10	4

where r_1 and r_2 indicate the radii over which the blockage is evaluated and in this case are representative of the endwall defect region. For example at design speed and high flow condition the average blockage in the endwall defect region (which is defined as from 84% to 98% span) is approximately 17%. In other words, between 84% to 98% of span the effective flow area is 83% of the geometric flow area. Similarly, the average blockage in the core flow region (radii outside of the endwall defect region) is 9% at high flow and design speed. From Table 6 it is evident that the integrated average of the blockage in the endwall defect region increases with rotational speed due to the increase in pressure difference across the blade tips and the influence of the shock / vortex interaction at higher speeds. Also, the blockage in the core flow region at design speed is approximately double that at part speed conditions due to the impact of the shock / boundary layer interaction on the blade suction surface.

5.2.2 Blockage Development within the Rotor Passage

The blockage on the blade suction surface was calculated at measurement locations upstream and downstream of the rotor shock on the 70% span streamsurface for the rotor operating at design speed and max flow, high flow, and low flow conditions and these results are presented in Figure 55. For each flow condition the region of the shock boundary layer interaction is identified by the region denoted 'lambda shock region'. In these regions there is strong evidence to suggest the presence of a lambda shock and it was quite difficult to define the edge of the boundary layer. It is evident that the blockage increases downstream of the shock due to the pressure rise across the shock and the blockage increase is more significant with increase in the rotor shock strength. This same development of blockage was evident in the high and low flow data at 50% span but at 30% span the data was not sufficient to estimate the blockage attributed to the suction surface boundary layer. A relevant question is whether the shock / boundary layer interaction is sufficient to separate the blade surface boundary layer.

Results from wind tunnel tests on flat plate turbulent boundary layers will be used to determine if the suction surface boundary layer is separated. Using separation criteria deduced from flat plate results is justified because the geometry and the flow over the first part of the blade suction surface of the airfoil section at 70% span resembles that of a flat plate geometry and flow structure. The suction

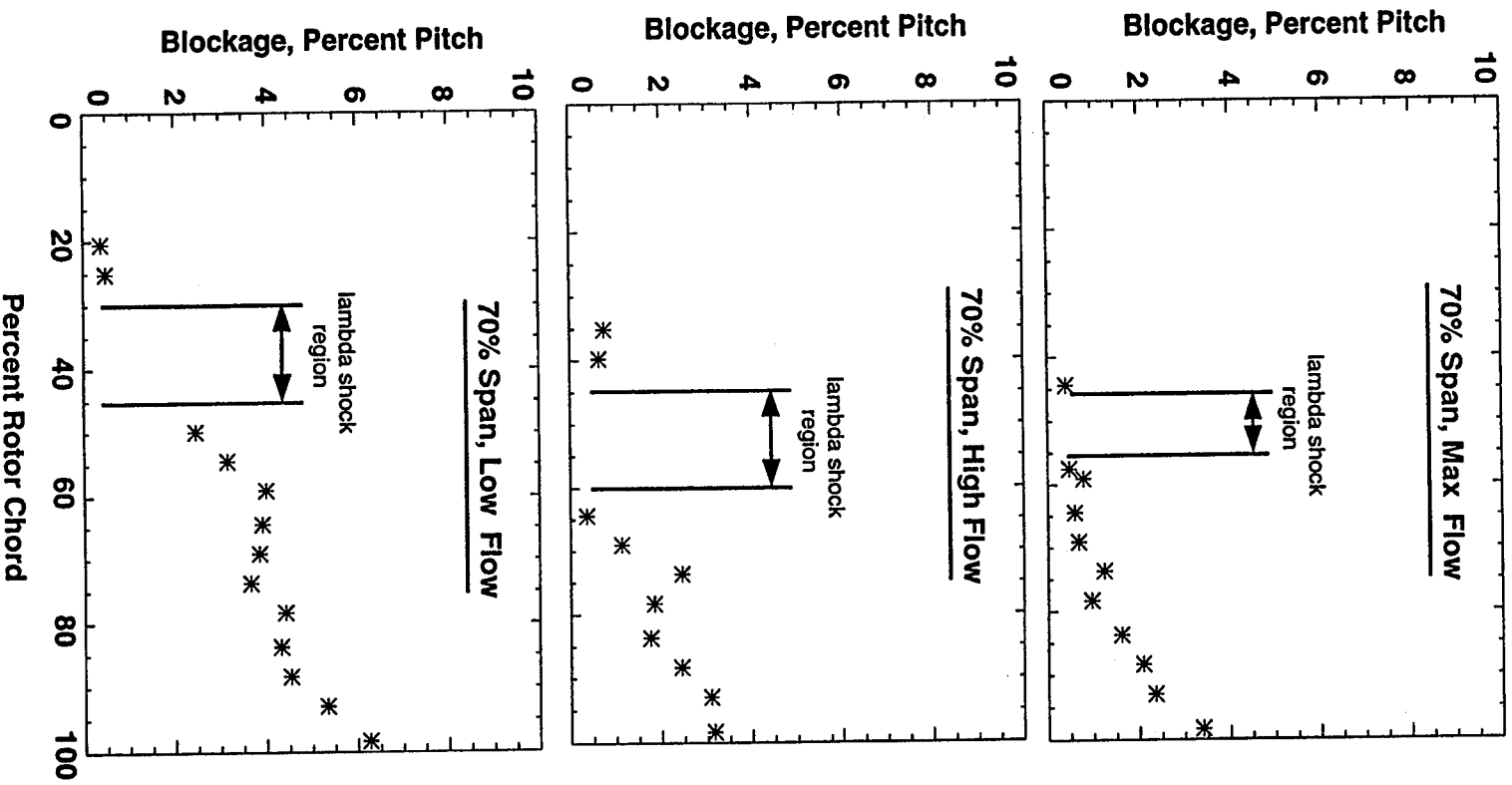


Figure 55 Blockage Development inside the blade passage at 70% span for max flow, high flow, and low flow conditions at design speed.

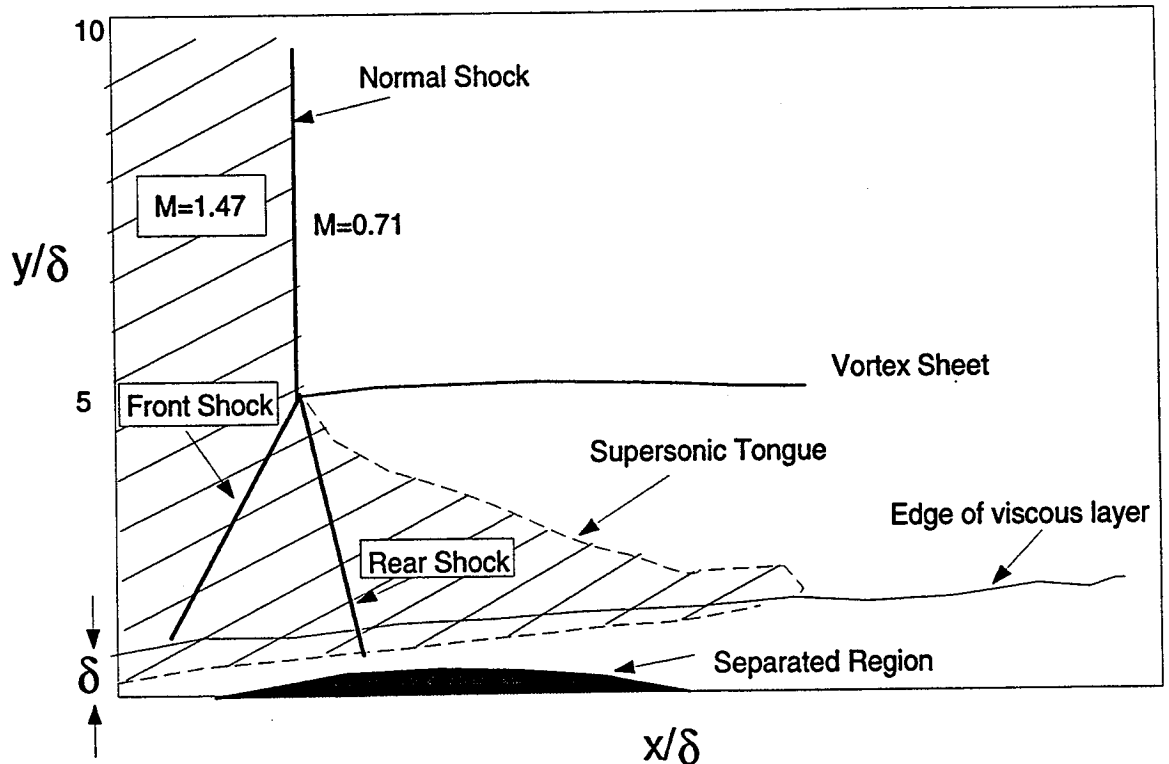


Figure 56 Seddon's model depicting the boundary layer separation due to a normal two-dimensional shock wave.

surface angles, shown in Figure 74, indicate very little turning over the front part of the airfoil prior to the shock impingement on the suction surface. In addition, the distribution of the relative Mach number near the blade surface (Figure 25) and the distribution of the isentropic static pressure coefficient (Figure 26) indicate the flow prior to the shock impingement on the suction surface is developing in a nearly zero pressure gradient.

Seddon's [20] model depicting the boundary layer separation due to a normal two-dimensional shock wave is presented in Figure 56. The normal shock is bifurcated into a classical lambda (λ) shape close to the surface. The front leg of

the lambda shock is formed in response to the separation bubble and directs the flow away from the surface. The rear leg of the lambda shock deflects the flow back into the mainflow direction. A vortex sheet is shed downstream of the bifurcation point due to the entropy differences of the flow region behind the normal shock and the two oblique shocks. For the rotor geometry in question the Reynolds number based on chord is about 1.8×10^6 and the boundary layer thickness ahead of the shock is approximately 4% of pitch. Therefore, it is anticipated that the separated region, if it exists, is much too small to measure. However, according to Seddon's model the lambda shock structure extends to a distance from the wall which is 5 times the boundary layer thickness and measurements were acquired in this region. In order to assess if the severity of the shock / boundary layer interaction is sufficient to cause a separation, the data was examined for features depicted in Seddon's model. For example, the turning of the flow inherent to a lambda shock where the front oblique shock turns the flow away from the surface and the second or rear oblique shock re-directs the flow in the mainflow direction. Alber [18] has shown that the boundary layer is separated if the flow undergoes a deflection angle greater than 6.6 degrees. Wind tunnel tests have shown that the pressure gradient required to separate a turbulent boundary layer on a flat plate is that corresponding to a normal Mach number of around 1.3 – 1.4 [17].

The flow deviation from the blade surface angle on the 70% span streamsurface is plotted for the max flow, high flow, and low flow conditions at design speed in Figure 57. The flow in general follows the pressure surface, whereas on the suction surface there are regions where the flow deviates from the blade surface angle. Near mid-chord there are regions of increasing and decreasing deviation which suggest flow turning through the front and rear legs of a lambda shock. For example, at the max flow and high flow conditions there is an increase in the suction surface deviation angle from 45% to 55% chord followed by a decrease in the deviation from 60% to 65% chord. This region from 45% to 65% chord corresponds to the region of the shock influence on the blade suction surface as depicted in the blade surface Mach number distributions in Figure 25. Similarly, at the low flow there is an increase in the deviation from 35% to 45% chord and a subsequent decrease in deviation from 45% to 50% chord. The change in the deflection is near the value of 6.6 degrees required for boundary layer separation. Unfortunately the data near the blade surface is not sufficient in detail to detect the size of the separation.

CFD Results for the Boundary Layer Characteristics.

CFD results were used to provide additional insight into the flow behavior near the blade surface by using lines of constant entropy to visualize the predicted boundary layer growth, as suggested by Chima [63, 41]. Entropy levels are highest

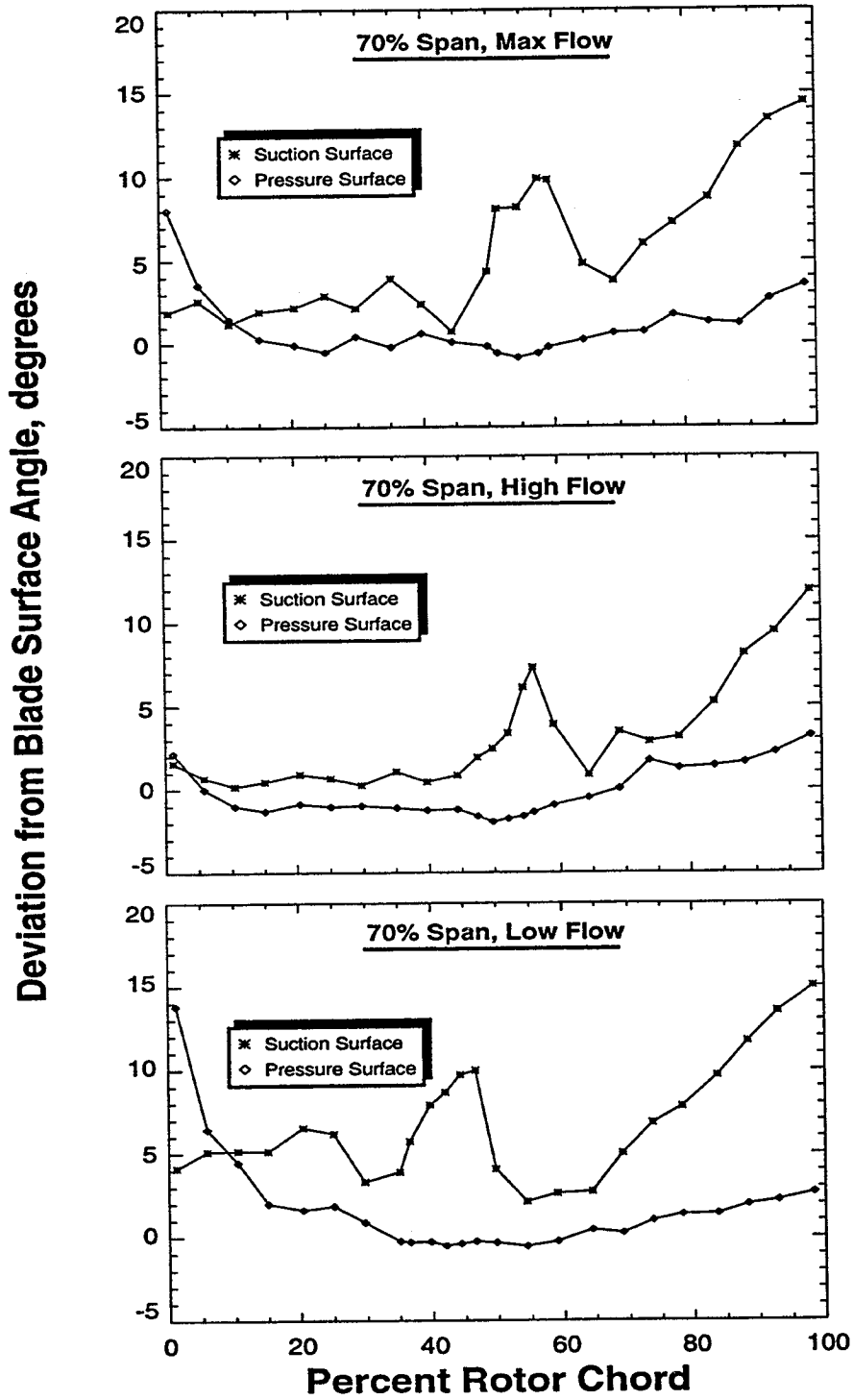


Figure 57 Deviation from blade surface angles on the 70% span streamsurface at max flow, high flow and low flow conditions at design speed.

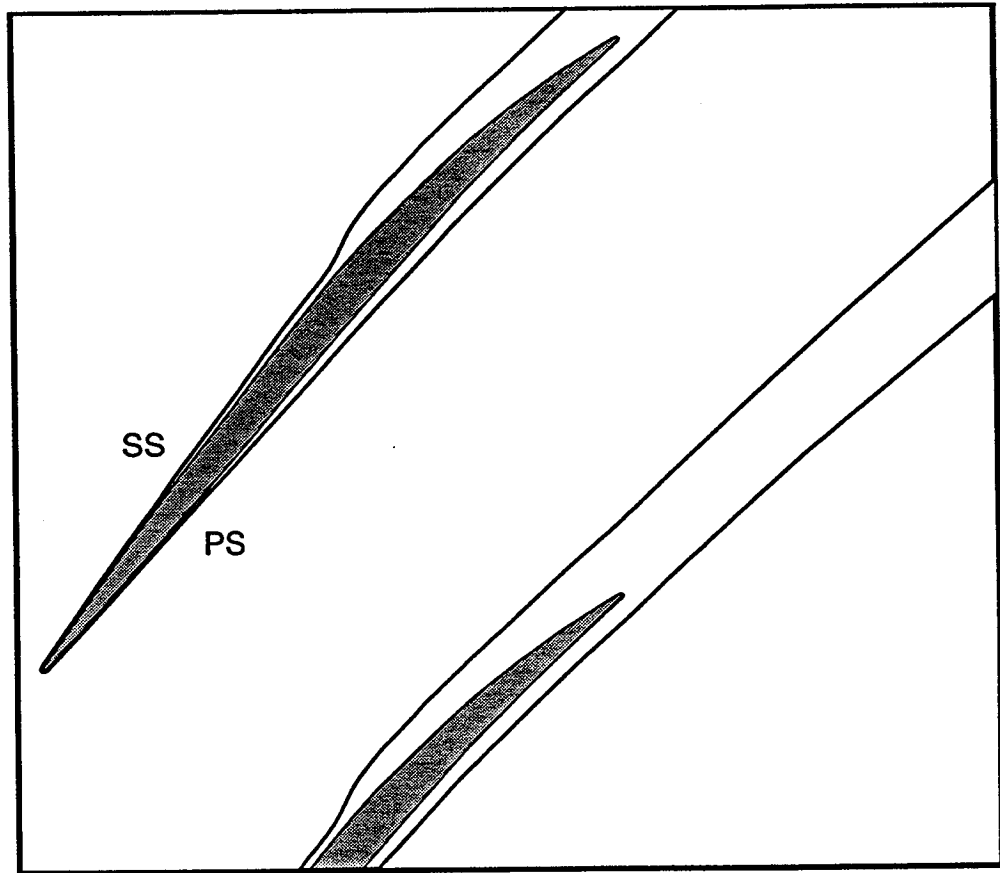


Figure 58 CFD results depicting the edge of the boundary layer on the 70% span streamsurface based on the entropy contour for the high flow design speed condition.

at the blade surface and decrease to their minimum values upstream of the blade passage. The entropy levels across the shock lie between the upstream and blade surface levels. The smallest entropy level which encompasses the blades but not the shock is therefore a reasonable representation of the boundary layer edge. The edge of the boundary layer on the 70% span streamsurface is depicted by the entropy contour in Figure 58. The results clearly indicate a thickening of the blade boundary layer near mid-chord where the passage shock impinges on the blade

suction surface. Also, the boundary layer is thicker on the suction surface than the pressure surface. These features are consistent with the experimental findings. The CFD results were examined to determine if the boundary layer was separated at or downstream of the shock / boundary layer interaction region. This exercise revealed a thin separated zone downstream of the shock which extended from the suction surface only about 1% of the boundary layer thickness at the blade trailing edge and this separated region was relatively independent of the backpressure. In conclusion, there is evidence to suggest the shock pressure rise is sufficient to induce a separation and based on the earlier comparisons with the CFD it is evident that the CFD is probably underpredicting the extent of the separation.

Results at Part Speed Conditions. Attempts to calculate the blockage development inside the blade for the data at part speed conditions were unsuccessful because the thickness of the boundary layer downstream of the shock was much reduced at part speed and the data was not of sufficient quality to evaluate the boundary layer displacement and momentum thicknesses. However, there was sufficient data to deduce the edge of the boundary layer and therefore the deviation from the blade surface angles were evaluated. The results for 85% speed and 80% speed conditions are presented in Figure 59. Except for the last 20% of blade chord on the suction surface it is evident that the flow follows the blade surfaces. At 85% speed there is evidence of an increase and decrease in deviation from 45%

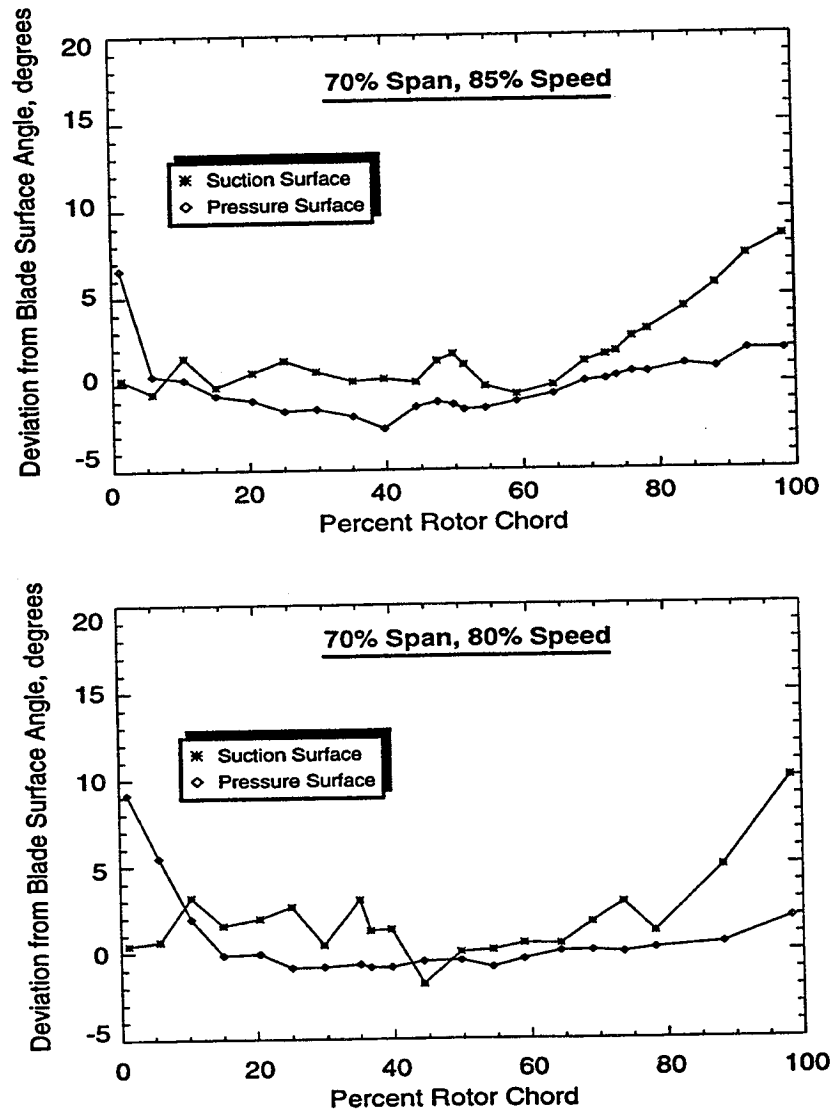


Figure 59 Deviation from blade surface angles on the 70% span streamsurface at 85% speed and 80% speed.

to 55% chord which corresponds to the location of the shock impingement and influence on the blade suction surface. However the flow deflection is less than three degrees and according to Alber [18] is not sufficient to indicate a separation. In contrast, at 80% speed there is no evidence of the increase and decrease in deviation due to a lambda shock as was evidenced in the design speed results

shown in Figure 57. Therefore, based on the distribution of the deviation from the blade surface angles, it is concluded that the shock is not of sufficient strength to separate the blade suction surface boundary layer at 80% and 85% speed. In the next section, the strength of the shock and the losses across the shock will be quantified at 80%, 85%, and 100% speed.

5.3 Quantification and Estimation of Losses

The total loss is determined from the aerodynamic probe measurements and is divided into two categories; 1) the loss in total pressure associated with the rotor shock which is referred to as the shock loss and 2) all other losses which are generally referred to as the profile loss. Note that all losses associated with the secondary flow structures and the mixing losses which occur downstream of the blade are lumped into the profile loss category. The total loss coefficient is defined as follows:

$$\omega_{total} = \frac{(P'_{ideal})_{te} - P'_{te}}{P'_{le} - p_{le}} \simeq \frac{P'_{le} - P'_{te}}{P'_{le} - p_{le}} \quad (27)$$

where the primes denote the relative frame of reference of the rotor, the subscripts 'le' and 'te' refer to the blade leading edge and trailing edge, and 'P' and 'p' refer to total and static pressure respectively. In making this calculation for the total loss coefficient, the total pressure and total temperature measured at station #4 were used in place of those at the trailing edge of the rotor.

The shock losses are estimated from the LFA measurements of the relative Mach number and flow angle upstream and downstream of the shock. Knowing the upstream and downstream relative Mach number in conjunction with the flow turning attributed to the shock, (θ), the inclination angle of the shock relative to the flow, (β), can be determined in an iterative process from the following:

$$M_2^2 \sin^2(\beta - \theta) = \frac{1 + \frac{\gamma-1}{2} M_1^2 \sin^2 \beta}{\gamma M_1^2 \sin^2 \beta - \frac{\gamma-1}{2}} \quad (28)$$

where the subscripts 1 and 2 refer to upstream and downstream of the shock, respectively. Since the shock structure varies across the passage and especially near the blade suction surface, it was decided to estimate the shock loss based on the shock structure at mid-pitch for each streamsurface survey. Then the total pressure loss across the shock was determined from:

$$\frac{P'_{t,2}}{P'_{t,1}} = \left[\frac{(\gamma + 1)M_n^2}{(\gamma - 1)M_n^2 + 2} \right]^{\frac{\gamma}{\gamma-1}} \left[\frac{\gamma + 1}{2\gamma M_n^2 - (\gamma - 1)} \right]^{\frac{1}{\gamma-1}} \quad (29)$$

where the normal Mach number is defined by $M_n = M_1 \sin \beta$. The shock loss coefficient is defined as:

$$\omega_{shock} = \frac{P'_{t,1} - P'_{t,2}}{P'_{le} - p_{le}} \quad (30)$$

The radial lean of the shock surface is neglected in this calculation of shock loss. However, since the shock crosses mid-pitch and impinges on the suction surface at nearly the same axial location for the radii corresponding to 30%, 50%, and 70%

Table 7 Estimation of Losses

% Design Speed	Flow	span	M_1	M_2	θ	β	M_n	ω_{total}	ω_{shock}	$\omega_{profile}$
100	low	30	1.395	0.821	6.5	75	1.347	0.125	0.079	0.046
"	"	50	1.436	0.777	4.5	77	1.400	0.173	0.106	0.067
"	"	70	1.396	0.735	4.5	90	1.396	0.196	0.088	0.108
100	high	30	1.461	0.949	6.7	63	1.302	0.097	0.057	0.039
"	"	50	1.477	0.877	5.4	66	1.349	0.127	0.078	0.049
"	"	70	1.494	0.846	6.8	68	1.385	0.136	0.098	0.038
100	max	70	1.506	0.907	6.0	63	1.341	0.120	0.073	0.048
85	max	70	1.318	0.850	4.4	75	1.273	0.059	0.046	0.013
80	high	70	1.258	0.868	0.4	75	1.215	0.049	0.026	0.023

span, the radial lean of the shock is considered negligible. Also, since particle lag effects are neglected, the shock loss estimate may be on the low side. However, based on the earlier discussion on particle lag it was shown that the post-shock Mach number for a nearly normal shock was within 0.02 of that corresponding to the normal shock relations. Lowering the post-shock Mach number by a value of 0.02 results in an increase in the shock loss coefficient of 0.01. Therefore, the estimates of the shock loss coefficient may be low by as much as 0.01 and the profile loss coefficient, which is calculated from the difference of the total loss coefficient and the shock loss coefficient, may be high by as much as 0.01. Table 7 summarizes the values used to estimate the shock loss and lists the loss distribution in terms of the total loss coefficient, shock loss coefficient, and the profile loss coefficient.

From Table 7 it is interesting to note that the normal Mach number is greater than 1.3 for the design speed cases at all spans. From wind tunnel tests [16, 17, 18, 19] it has been shown that the pressure rise associated with a normal shock Mach number of around 1.3 is required to separate the boundary layer. Therefore deducing from the plots of deviation from the blade suction surface (Figure 57) and the level of the estimated normal Mach number, there is evidence to suggest that the shock is sufficient to separate the boundary layer at design speed. However, at 85% and 80% speed the normal Mach number is less than 1.3 and based on the plots of deviation from the blade suction surface (Figure 59) in conjunction with the low values (relative to design speed) of the total loss coefficient and profile loss coefficient it is concluded that the shock strength is not sufficient to separate the boundary layer at the part speed conditions. As expected the shock loss increases with increasing values of the normal Mach number (normal shock loss is proportional to $(M-1)^3$ [64]). However, the profile loss varies randomly with increasing normal Mach number. This is attributed to the sensitivity of where the shock impinges on the blade suction surface and the curvature and pressure gradient at the location of the shock impingement point.

The adiabatic efficiency is another parameter which is used to represent the losses. Analogous to the breakdown of the loss coefficients, the decrement in the efficiency can be apportioned to that due to the shock losses and that due

to the profile losses. The efficiency, η , is defined in terms of the stagnation enthalpy, h , by:

$$\eta = \frac{(h_e)_{is} - h_1}{h_e - h_1} = \frac{h_2 - h_1}{h_e - h_1} + \frac{(h_e)_{is} - h_2}{h_e - h_1} \quad (31)$$

where the subscript 'is' refers to the isentropic or ideal condition and the subscripts 'e', '1', '2', refer to the axial locations of the rotor exit, the rotor inlet, and downstream of the shock, respectively. The first term on the right hand side represents the contribution of the shock losses and the second term represents the contribution of the profile losses in the efficiency calculation. Assuming the specific heat at constant pressure is constant throughout the flow, the stagnation enthalpies are defined in terms of the stagnation temperature such that

$$\eta = \frac{\frac{T_2}{T_1} - 1}{\frac{T_e}{T_1} - 1} + \frac{\left[\left(\frac{T_e}{T_1} \right)_{is} - \frac{T_2}{T_1} \right]}{\left(\frac{T_e}{T_1} - 1 \right)} \quad (32)$$

The conditions at rotor inlet and exit are known from the aerodynamic probe measurements and the isentropic or ideal enthalpy is calculated from the measured total pressure and represents the minimum work input required to achieve the measured pressure rise where:

$$\left(\frac{T_e}{T_1} \right)_{is} = \left(\frac{P_e}{P_1} \right)^{\frac{\gamma-1}{\gamma}} \quad (33)$$

Knowing the velocity throughout the flow field and estimating the static temperature from equation 12 which was based on Euler's equation and the conservation of

energy, the total temperature downstream of the shock is found from $T_2 = T_{s,2} + \frac{V_{abs}^2}{2c_p}$.

The distribution of the losses is plotted in terms of the decrement in the efficiency ($1-\eta$) and in terms of the loss coefficients in Figure 60 for the streamsurfaces in the core flow region. From Figure 60 note that the total losses increase with increasing rotor backpressure for all spans at design speed. Also, note that the earlier results at 70% span and design speed indicated an increase in the wake width and depth from high flow to max flow to low flow which is consistent with the increase in profile loss indicated in Figure 60. Perhaps the most striking feature found in both Table 7 and Figure 60 is the reduction in loss that occurs from 100% speed to 85% speed where the normal Mach number decreases from about 1.4 to 1.27 and the shock is no longer strong enough to induce a separation of the suction surface boundary layer.

5.3.1 Comparison of Profile Loss to Lieblein's Correlation

In this section the profile wake loss obtained from the experiment will be compared to Lieblein's correlation [15] of loading parameter versus loss parameter. It is standard practice to characterize the blade loading by Lieblein's diffusion factor, DF , [15] which is defined as:

$$DF = -\frac{\theta}{V} \frac{dV}{dx} \approx \left(1 - \frac{V_2}{V_1}\right) + \frac{\Delta V_\theta}{2\sigma V_1} \quad (34)$$

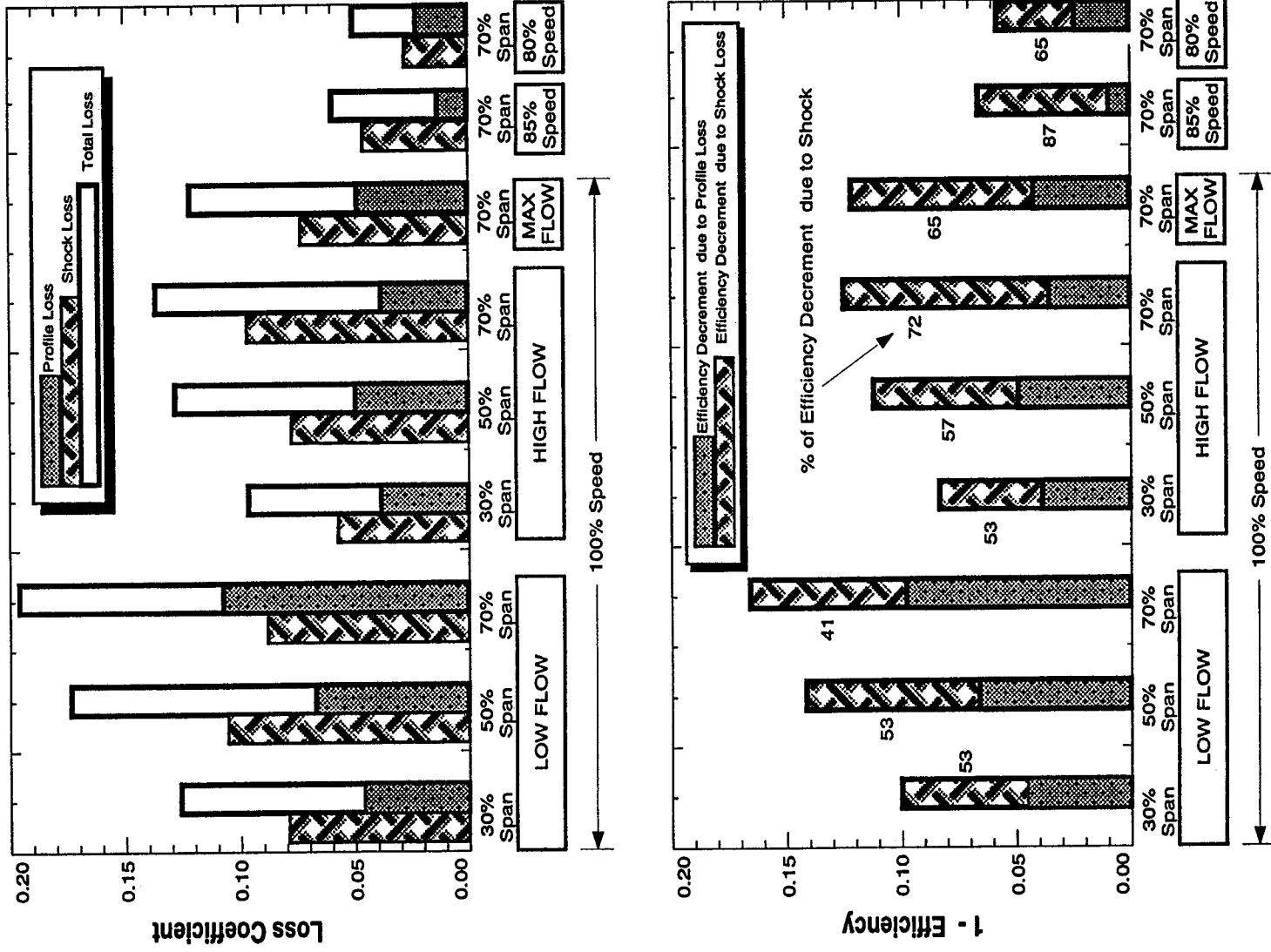


Figure 60 Distribution of Losses in the core flow region.

In fact blade designers typically use empirically developed loss tables and blockage estimates which are based on the distribution of the diffusion factor. In addition, the diffusion factor, DF, has been used as a parameter to characterize the possibility of separation of the blade boundary layers and is based on integral momentum boundary layer equation:

$$\frac{d\theta}{dx} = \frac{\tau}{\rho V^2} - (H + 2) \frac{\theta}{V} \frac{dV}{dx} \quad (35)$$

The shape factor, H, is set to a value of 2 and the shear stress, τ , is zero at separation. Therefore from equation 34 and equation 35 it can be shown that at separation $\frac{d\theta}{dx}|_{separation} \simeq constant \left(-\frac{\theta}{V} \frac{dV}{dx}\right) \propto DF$ [15]. For a conventional subsonic blade it is standard practice to limit the DF to below 0.6 because with $DF > 0.6$ the losses increase rapidly and it assumed the boundary layer has separated [15]. This rule of thumb is based on experimental data and experience but its derivation is directly related to how the shape of the blade surface velocity distribution is used to estimate the dV/dx term in equation 34. However, for a transonic blade where the shocks are responsible for most of the loading, the standard definition of diffusion factor is inappropriate because the dV/dx term of the diffusion factor definition cannot be approximated from the shape of the surface velocity distribution.

To illustrate the impact of using the subsonic correlation of diffusion factor versus loss for a supersonic blade, the data obtained at 70% span in this investigation

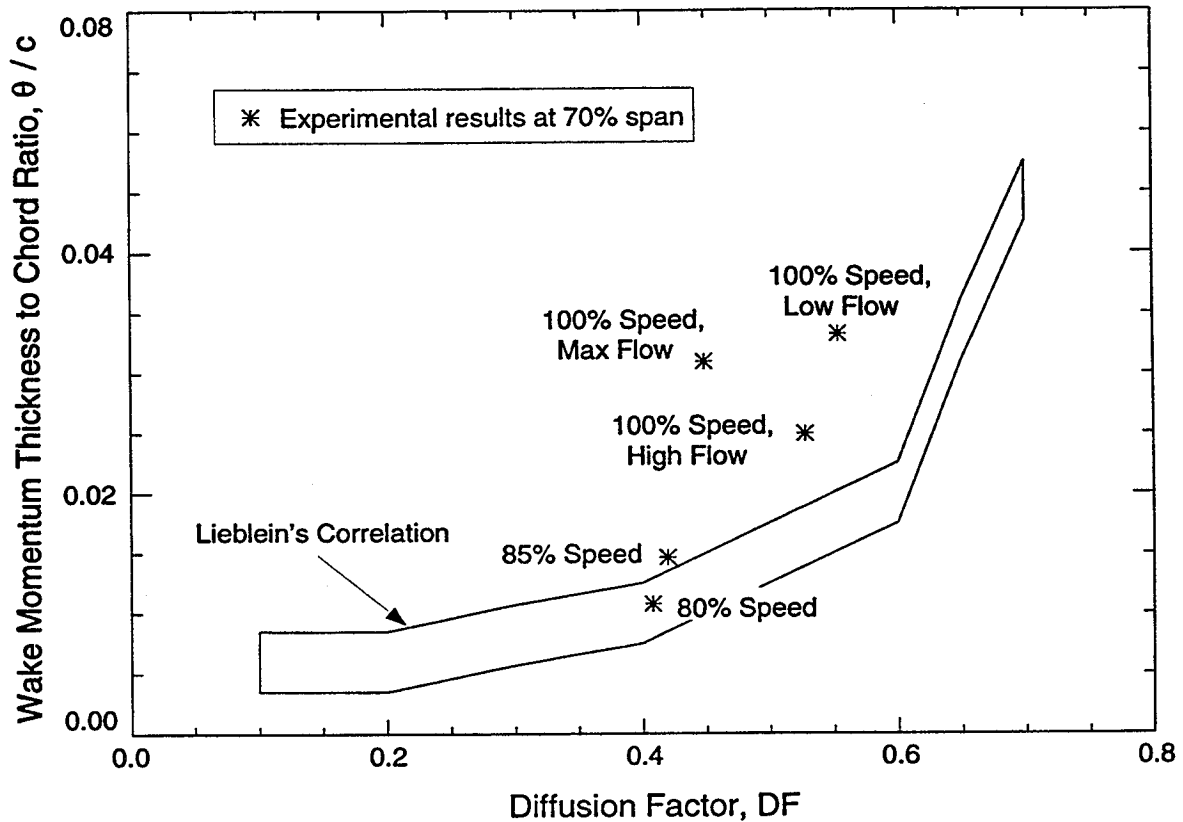


Figure 61 Comparison of measured wake profile loss at 70% span with Lieblein's [15] correlation of loading parameter versus loss parameter.

is compared to the correlation of loading versus loss found in [65] which was primarily based on the analysis of Lieblein et. al. [13, 12, 15]. The comparison is shown in Figure 61 where the loading parameter is Lieblein's diffusion factor, DF, and the loss parameter is represented by the ratio of the wake momentum thickness to aerodynamic blade chord, $\frac{\theta}{c}$. The outlined region represents the scatter of the data on which Lieblein's correlation was based. The results at 80% and 85% speed are in agreement with Lieblein's correlation indicating that for weak shocks Lieblein's correlation will still predict the wake profile loss. However at

design speed where it has been documented that the shock is of sufficient strength to separate the boundary layer, Lieblein's correlation underpredicts the loss, as expected. In addition, the limiting level of DF of 0.6 to predict separation is no longer appropriate for supersonic blading as evident by the data at design speed which separated at a lower level of diffusion factor. Therefore, caution must be employed when using Lieblein's correlation on supersonic blading. These results further illustrate the additional profile wake loss which occurs due to the shock / boundary layer interaction.

6 Concluding Remarks & Recommendations for Future Work

6.1 Concluding Remarks

A detailed experimental investigation to understand and quantify the development of loss and blockage in the flow field of a transonic axial flow compressor rotor has been undertaken. A two-color, fringe-type laser anemometer system was developed and configured to acquire detailed flow measurements upstream, within, and downstream of the transonic compressor rotor operating at design and off-design conditions. The rotor was operated at 100% speed, 85% speed, 80% speed, and 60% speed which provided inlet Mach numbers at the blade tip of 1.48, 1.26, 1.18, and 0.89 respectively. Comparisons of the blockage and loss development at 60%, 80% and 100% speed at a constant incidence angle provided a means to evaluate the effect of variations of the inlet Mach number on the development of loss and blockage development. Data acquired at design speed at varying rotor exit pressures provided a means to evaluate the sensitivity of loss and blockage to changes in shock structure at a nearly constant inlet Mach number. Data analysis was broken into two categories: 1) the flow physics associated with the development of loss and blockage and 2) the quantification of the loss and blockage.

The conclusions of this investigation regarding the flow physics associated with the development of loss and blockage in a transonic axial compressor are:

1. **Core Flow Region.** The blockage is primarily due to the blade surface boundary layers and wake development. The loss is attributed to the loss across the shock and the loss associated with the rotor wake and blade surface boundary layers. The development of the loss and blockage is sensitive to the shock structure and the interaction between the shock and the suction surface boundary layer. The strength of the shock and the location where the shock impinges on the suction surface as well as the pressure gradient on the blade surface were identified as parameters which affected the blockage. At 80% and 60% speed the width and depth of the rotor wake were nearly identical in character and much reduced in comparison to design speed which indicated that the shock / boundary layer interaction was sufficient to thicken the suction surface boundary layer at design speed but not at 80% speed.
2. **Endwall Flow Region.** The blockage is generated not only by the blade surface boundary layer and wake development but also by the tip leakage flow and the endwall flow. The losses were attributed to the blade surface boundary layers, rotor wake, the shock, and the interaction between the shock and tip leakage vortex. The development of the loss and blockage was not only sensitive to the shock / boundary layer interaction, but also to the interaction between

the shock and the tip leakage vortex which was sensitive to the clearance height, the loading across the blade and the shock structure. At design speed the interaction between the rotor passage shock and the tip leakage vortex generated a region of high blockage in the passage which moved forward and became larger in both the circumferential and radial directions as the rotor loading was increased. The low momentum fluid resulting from the shock / vortex interaction merged with the rotor wake and became indistinguishable from the wake fluid. At 80% speed the blockage generated by the shock / vortex interaction was consistent with the design speed results at a reduced level of shock strength. At 60% speed, in the absence of the shock, a 'second' vortex forms along the blade suction surface near the blade trailing edge as fluid within the suction surface boundary layer migrates outward radially and encounters the tip clearance flow over the rear half of the blade. The 'second' vortex forms as a result of operating at an off-design condition and provides additional blockage and loss in the endwall region at 60% speed which does not exist at either 80% or 100% of design speed.

3. **Comparisons to CFD.** Comparisons were made between several CFD solutions, aerodynamic probe survey data, and laser anemometer data. The CFD results predicted a higher total pressure rise and total temperature rise across the rotor as compared to the aerodynamic probe surveys. In addition, the

radial distributions of the total pressure ratio and total temperature ratio were much different from the probe surveys. Additional comparisons with the laser anemometer results indicated that the CFD was overpredicting the diffusion in the passage which is consistent with overpredicting the pressure and temperature rise. The CFD was in qualitative agreement with the experimental data in terms of the shock structure and shock stand-off from the rotor leading edge, and the CFD qualitatively captured the features of the shock / vortex interaction in the endwall region and shock / boundary layer interaction in the core flow region. In the core flow region, the discrepancies in the quantitative comparisons between the CFD and the data occurred downstream of the rotor shock and were attributed to the CFD not accurately predicting the strength of the interaction between the shock and the suction surface boundary layer. In the endwall region, the radial extent of influence of the shock / leakage vortex interaction and therefore the blockage resulting from this interaction was underpredicted by the CFD. The variation among the different CFD results further demonstrated the sensitivity of the rotor performance to small changes in blockage.

The conclusions of this investigation regarding the quantification of blockage and loss in a transonic axial compressor are:

1. The radial distribution of the blockage was consistent with the radial distribution of the pressure and temperature rise across the rotor such that a local increase in blockage coincided with a local decrease in the temperature and pressure rise and conversely, a region of reduced blockage coincided with a region of increased pressure and temperature rise.
2. Blockage in the endwall region was 2–3 times greater than that in the core flow region.
3. In the core flow region at design speed conditions the blockage is more than double that at part speed conditions for the same incidence. This increase in blockage is due to the interaction of the shock with the suction surface boundary layer.
4. Blockage in the endwall region increases with loading in agreement with Khalid's [4] correlation of endwall blockage versus aerodynamic blade loading.
5. Comparisons of the blockage calculated from the CFD results using the same procedure as that used to calculate blockage from the data indicated that the CFD is not predicting the correct radial distribution of the blockage and this was attributed to the inability of the CFD to accurately model the interaction

between the shock and the suction surface boundary layer and the interaction between the shock and the leakage flow.

6. A shock strength corresponding to a normal shock Mach number of 1.27 (85% speed) was not sufficient to separate the suction surface boundary layer, but at design speed where the normal shock Mach number reached 1.39 the shock did induce a separation of the blade suction surface boundary layer. These findings are consistent with wind tunnel investigations of the shock / boundary layer interaction which concluded a normal shock Mach number of between 1.3 and 1.4 was required to induce separation on a turbulent flat plate boundary layer.
7. Losses increased with increased rotor back pressure.
8. Losses increased substantially with Mach number not only due to the loss across the shock but the increase in profile loss resulting from the shock / boundary layer interaction at normal Mach numbers greater than 1.3.
9. The profile losses varied randomly with increased normal shock Mach number above that required to induce boundary layer separation ($M_n > 1.3$) and this is attributed to the sensitivity of where the shock impinges on the blade suction surface and the curvature and pressure gradient to which the boundary layer is subjected.

6.2 Recommendations for Future Work.

There are many features of the flow at design speed, where the shock is sufficient in strength to impact the suction surface boundary layer and the leakage flow, that are not well understood. The capabilities of the CFD need to be improved to accurately model these flow phenomena. The results presented herein illustrate the effect of the rotor shock structure, the shock / leakage vortex interaction, and the shock / boundary layer interaction on the performance characteristics of this compressor rotor. The data were lacking in many areas and the CFD was incapable of accurately predicting all of the flow features. Therefore the following are recommendations for future work:

1. Experimental, analytical, and computational efforts must be made to improve the turbulence and mixing models employed in CFD codes.
2. Improvements in the laser anemometer measurement technique must be made to provide measurements closer to the blade surfaces such that the characteristics of the boundary layer are known upstream and downstream of the shock impingement on the blade surface. In addition, if a separated region exists the size and location of the separated region must be defined.
3. Improvements in the laser anemometer measurement technique must be made to provide measurements closer to the endwall region. In the endwall region the flow gradients are severe and the flowfield is complex. In addition, the

discrepancies between the CFD and the data were greatest in the endwall region.

4. Improvements in the laser anemometer measurement technique must be made to provide measurements in the radial direction so that radial migration that occurs downstream of the shock, along the blade surfaces, and in the rotor wakes can be quantified. The radial velocity component is essential to assess the secondary flows and formation of vortex structures. In this investigation the CFD was used to estimate the impact of the radial velocities and in general the impact was considered negligible. However, the radial flows are likely to be large in areas of separation which are regions where the CFD is most likely to be in error.
5. In addition to the laser anemometer measurements, measurements of thermodynamic properties such as density and pressure need to be made so that the entropy (loss) can be accurately measured and the effects of the density variations can be included in the results. Currently, an optical measurement system that combines the techniques of laser induced fluorescence and Raman scattering to measure the density and temperature in the rotor frame of reference is in development. These techniques are generally used in environments where the variations of density and temperature are large, for example in a combustion process. Theoretically these techniques should

be applicable for the variations of density and temperature observed in turbomachinery, but the system is in the initial development stages and there are several issues that need to be addressed prior to fully implementing the system.

6. Since it is evident that the losses and blockages are more substantial in the outer endwall region, experiments need to be defined to assess the ability to control or reduce the losses and blockage associated with the tip leakage flow. Casing treatment studies in the past have basically been limited to adding circumferential grooves or axial skewed slots in the casing and the result has been to extend the stall margin with reductions in efficiency. As our understanding of the endwall flow physics improve, there may be an opportunity to improve the performance in the endwall flowfield either by reducing the impact of the shock / leakage vortex interaction or by re-directing or energizing the low momentum flow in the endwall. Clearly, the endwall represents a region where there is potential for improvement.

Bibliography

- [1] Cumpsty, N., *Compressor Aerodynamics*, Longman Scientific & Technical and co-published with John Wiley & Sons, 1989.
- [2] Crouse, J. and Gorell, W., "Computer Program for Aerodynamic and Blading Design of Multistage Axial-Flow Compressors.," *NASA TP 1946*, 1981.
- [3] Law, H. and Puterbaugh, S., "A Computer Program for Axial Compressor Design (UDO300M)," *Air Force Wright Aeronautical Laboratories Publication AFWAL-TR-82-2074*, 1982.
- [4] Khalid, S., *The Effects of Tip Clearance on Axial Compressor Pressure Rise*, Ph.D. Dissertation, Massachusetts Institute of Technology, 1994.
- [5] Koch, C., "Stalling Pressure Rise Capability of Axial Flow Compressor Stages," *ASME Journal of Engineering for Power*, Vol. 103, 1981, pp. 645-656.
- [6] Koch, C. and Smith, L., "Loss Sources and Magnitudes in Axial-Flow Compressors," *ASME Journal of Engineering for Power*, Vol. 98, 1976, pp. 411-424.
- [7] Smith, J. L.H., "Casing Boundary Layers in Multistage Axial-Flow Compressors," *Flow Research on Blading*, edited by A. L. S. Dzung, Elsevier. , 1970, pp. 275-304.
- [8] McNally, W., "Calculation of Losses in Turbomachines," Lecture notes for Compressor Aerodynamics Course at NASA Lewis Research Center.
- [9] Howell, A., "Fluid Dynamics of Axial Compressors," *Proc. Instn. Mech. Engrs., Lond.* 153, 1945.
- [10] Jennions, I. and Shin, C., "An Exhaustive Study of the Flow in a Transonic Rotor," *International Symposium on Experimental and Computational Aerothermodynamics of Internal Flows*, 1993.
- [11] Denton, J., "Loss Mechanisms in Turbomachines," *ASME 93-GT-435*, 1993.

- [12] Lieblein, S. and Roudebush, W., "Theoretical Loss Relations for Low Speed Two-Dimensional Cascade Flow," *NACA TN 3662*, 1956.
- [13] Lieblein, S., "Diffusion Factor for Estimating Losses and Limiting Blade Loadings in Axial Flow Compressor Blade Elements," *NACA RM E53D01*, 1953.
- [14] Stewart, W., "Analysis of Two-Dimensional Compressible Flow Characteristics Downstream of Turbomachine Blade Rows in Terms of Basic Boundary Layer Characteristics," *NACA TN 3515*, 1955.
- [15] Lieblein, S., Schwenk, F., and Broderick, R., "Diffusion Factor for Estimating Losses and Limiting Blade Loadings in Axial-Flow-Compressor Blade Elements," *NACA RM E53D01*, 1953.
- [16] Nussdorfer, T., "Some Observations of Shock-induced Turbulent Separation on Supersonic Diffusers," *NACA RM E51 L26*, 1956.
- [17] Atkin, C. and Squire, L., "A Study of the Interaction of a Normal Shock Wave with a Turbulent Boundary Layer at Mach Numbers between 1.3 and 1.5," *European Journal Mechanics B/Fluids*, Vol. 11, no. 1, 1992.
- [18] Alber, I., Bacon, J., Masson, B., and D.J., C., "An Experimental Investigation of Turbulent Transonic Viscous-Inviscid Interactions," *AIAA Journal*, Vol. 11, no. 5, 1973, pp. 620-627.
- [19] Chriss, R., Keith, T., Hingst, W., Strazisar, A., and Porro, A., "An LDA Investigation of Three-Dimensional Normal Shock-Boundary Layer Interactions in a Corner," *AIAA-87-1369*, 1987.
- [20] Seddon, J., "Flow Produced by Interaction of a Turbulent Boundary Layer with a Normal Shock Wave of Strength Sufficient to Cause Separation," *Brit. Aero. Res. Council Report and Memo No. 3502*, March, 1960.
- [21] Schreiber, H., "Shock-Wave Turbulent Boundary Layer Interaction in a Highly Loaded Transonic Fan Blade Cascade," *85th AGARD PEP Symposium*, 1995, pp. 17-1 to 17-12.
- [22] Schultz, K., Bolcs, A., and Dalbert, P., "Experimental Investigation in Annular Compressor Cascades at Transonic Flow Conditions," Submitted for 41st ASME Gas Turbine and Aeroengine Congress, in Birmingham, U.K., 1996.

- [23] Griepentrog, H., "Shock Wave Boundary Layer Interaction in Cascades," *Agardograph No. 164 on Boundary Layer Effects in Turbomachines*, edited by J. Surugue, North Atlantic Treaty Organization (NATO), Advisory Group for Research & Development (AGARD), 1972, pp. 443-456.
- [24] Ackeret, J., Feldmann, F., and Rott, N., "Investigation of Compression Shocks and Boundary Layers in Gases Moving at High Speed," *NACA TM 1113*, 1947.
- [25] Liepmann, H., "The Interaction between Boundary Layer and Shock Waves in Transonic Flow," *Journal of Aeron. Sciences*, Vol. 13, no. 12, 1946.
- [26] Pearcey, H., "Some Effects of Shock Induced Separation of Turbulent Boundary Layers in Transonic Flow Past Aerofoils," *A.R.C. R&M*, no. 3108, 1959.
- [27] Bell, R. and Fottner, L., "Investigations of Shock/Boundary Layer Interaction in a Highly Loaded Compressor Cascade," *ASME Paper 95-GT-84*, 1995.
- [28] Miller, G., Lewis, G., and Hartmann, M., "Shock Losses in Transonic Rotor Flows," *Transactions of the ASME Journal of Engineering for Power*, Vol. 83, 1961, pp. 235-242.
- [29] Freeman, C. and Cumpsty, N., "A Method for the Prediction of Supersonic Compressor Blade Performance," *ASME paper 89-GT-326*, 1989.
- [30] Strazisar, A., "Investigation of Flow Phenomena in a Transonic Fan Rotor using Laser Anemometry," *Journal of Engineering for Gas Turbines and Power*, Vol. 107, 1985, pp. 427-435.
- [31] Wood, J., Strazisar, A., and Simonyi, P., "Shock Structure Measured in a Transonic Fan using Laser Anemometry," *AGARD CP-401: Transonic and Supersonic Phenomena in Turbomachines*, AGARD (Advisory Group for Aerospace Research and Development) of the North Atlantic Treaty Organization, 1986.
- [32] Wisler, D., "Loss Reduction in Axial-Flow Compressors Through Low-Speed Model Testing," *ASME Journal of Turbomachinery*, Vol. 107, 1985, pp. 354-363.

- [33] Inoue, M., Kuroumaru, M., and Fukuhara, M., "Behavior of Tip Leakage Flow Behind an Axial Compressor Rotor," *ASME Journal of Engineering for Gas Turbines and Power*, Vol. 108, 1986, pp. 7-13.
- [34] Inoue, M. and Kuroumaru, M., "Structure of Tip Clearance Flow in an Isolated Axial Compressor Rotor," *ASME Journal of Turbomachinery*, Vol. 111, 1989, pp. 250-256.
- [35] McDougall, N., "A Comparison Between the Design Point and Near Stall Performance of an Axial Compressor," *ASME Journal of Turbomachinery*, Vol. 112, 1990, pp. 109-115.
- [36] Stauter, R., "Measurement of the Three-Dimensional Tip Region Flowfield in an Axial Compressor," *ASME 92-GT-211*, 1992.
- [37] Copenhaver, W., Hah, C., and Puterbaugh, S., "Three-Dimensional Flow Phenomena in a Transonic High-Through-Flow Axial-Flow Compressor Stage," *ASME Paper No. 92-GT-169*, 1992.
- [38] Storer, J. and Cumpsty, N., "An Approximate Analysis and Prediction Method for Tip Clearance Loss in Axial Compressors," *ASME 93-GT-140*, 1993.
- [39] Chen, G., Greitzer, E., Tan, C., and Marble, F., "Similarity Analysis of Tip Clearance Flow Structure," *ASME Journal of Turbomachinery*, Vol. 113, 1991, pp. 260-271.
- [40] Adamczyk, J., Celestina, M., and Greitzer, E., "The Role of Tip Clearance in High-Speed Fan Stall," *ASME Journal of Turbomachinery*, Vol. 115, 1993, pp. 28-38.
- [41] Suder, K., Chima, R., Strazisar, A., and Roberts, W., "The Effects of Adding Roughness and Thickness to a Transonic Axial Compressor Rotor," *Journal of Turbomachinery*, Vol. 117, no. 4, 1994, pp. 491-505.
- [42] Urasek, D. and Janetzke, D., "Performance of Tandem-Bladed Transonic Compressor Rotor with Rotor Tip Speed of 1375 Feet per Second," *NASA TM X-2484*, 1972.
- [43] Bruckner, R., Brokopp, R., and Gronski, R., "NASA Lewis High-Speed Single Stage Axial Flow Compressor Facility," to be published as a NASA Technical Memorandum.

- [44] Reid, L. and Moore, R., "Design and Overall Performance of Four Highly Loaded, High-Speed Inlet Stages for an Advanced High-Pressure Ratio Core Compressor," *NASA TP 1337*, 1978.
- [45] Moore, R. and Reid, L., "Performance of Single-Stage Axial-Flow Transonic Compressor with Rotor and Stator Aspect Ratios of 1.19 and 1.26, Respectively, and with Design Pressure Ratio of 2.05," *NASA TP 1659*, 1980.
- [46] Strazisar, A., "Application of Laser Anemometry to Turbomachinery Flowfield Applications," *Measurement Techniques in Turbomachines, von Karman Institute for Fluid Dynamics Lecture Series 1985-03*, 1985.
- [47] Strazisar, A., "Laser Fringe Anemometry for Aero Engine Components," *Advanced Instrumentation for Aero Engine Components, AGARD CP-399*, 1986.
- [48] Verhoff, V., "Three-Dimensional Laser Window Formation," *NASA Reference Publication 1280*, 1992.
- [49] Strazisar, A., Wood, J., Hathaway, M., and Suder, K., "Laser Anemometer Measurements in a Transonic Axial-Flow Fan Rotor," *NASA TP 2879*, 1989.
- [50] Pierzga, M. and Wood, J., "Investigation of the Three-Dimensional Flow Field Within a Transonic Fan Rotor: Experiment and Analysis," *Journal of Engineering Gas Turbines Power*, Vol. 107, no. 2, 1985, pp. 436-449.
- [51] Hathaway, M., Gertz, J., Epstein, A., and Strazisar, A., "Rotor Wake Characteristics of a Transonic Axial-Flow Fan," *AIAA Journal*, Vol. 24, no. 11, 1986, pp. 1802-1810.
- [52] Hathaway, M., Chriss, R., Wood, J., and Strazisar, A., "Experimental and Computational Investigation of the NASA Low-Speed Centrifugal Compressor Flow Field," *ASME Journal of Turbomachinery*, Vol. 115, 1993, pp. 527-542.
- [53] Nichols, J. C.E., "Preparation of Polystyrene Microspheres for Laser Velocimetry in Wind Tunnels," *NASA TM 89163*, 1987.
- [54] Adamczyk, J., Celestina, M., Beach, T., and Barnett, M., "Simulation of Three-Dimensional Viscous Flow Within a Multi-Stage Turbine," *ASME Journal of Turbomachinery*, Vol. 112, no. 3, 1989, pp. 370-376.

- [55] Kirtley, K., Beach, T., and Adamczyk, J., "Numerical Analysis of Secondary Flow in a Two-Stage Turbine," *AIAA-90-2356*, 1990.
- [56] Crook, A., "Numerical Investigation of Endwall/Casing Treatment Flow Phenomena," M.S. Thesis, Massachusetts Institute of Technology, 1989.
- [57] Kline, S. and McClintock, F., "Describing Uncertainties in Single Sample Experiments," *Mechanical Engineering*, Vol. 75, 1953, pp. 3-8.
- [58] Wood, J., "personnel communication," Unpublished CFD Calculations and results provided by Mr. Jerry Wood.
- [59] Suder, K. and Celestina, M., "Experimental and Computational Investigation of the Tip Clearance Flow in a Transonic Axial Compressor Rotor," *Journal of Turbomachinery*, Vol. 118, no. 2, 1996, pp. 218-229.
- [60] Chima, R., "Calculation of Tip Clearance Effects in a Transonic Compressor Rotor," Submitted for 41st ASME Gas Turbine and Aeroengine Congress, in Birmingham, U.K., 1996.
- [61] Schlichting, H., *Boundary-Layer Theory*, Seventhth ed., McGraw-Hill, 1979.
- [62] McCormick, D., Paterson, R., and Weingold, H., "Experimental Investigation of Loading Effects on Simulated Compressor Trailing Edge Flowfields," UTRC Report 87-14 also Navy Contract Report N00014-83-C-0434 tech. rep., 1987.
- [63] Chima, R., "personnel communication,".
- [64] Liepmann, H. and Roshko, A., *Elements of Gasdynamics*, Wiley, New York, 1967.
- [65] Staff of Lewis Research Center, I. edited by Johnsen and Bullock, R., "NASA SP-36 : Aerodynamic Design of Axial-Flow Compressors," National Aeronautics and Space Administration, Lewis Research Center, Cleveland, Ohio tech. rep., 1965.

Appendix A Data Integrity

Since the data were acquired over many months, issues such as how well can the operating conditions of the test facility be reset and how repeatable are the data are critical. In addition, the CFD results are dependent on the blade geometry and therefore such issues as how well do we know the geometry must be considered. Therefore, in this appendix the objectives are to determine the following:

1. The data repeatability.
2. The particle lag associated with the LFA seed particles and its impact on the results.
3. The magnitude of passage-to-passage flow field variations and their impact on the results.
4. The level of agreement between the LFA and probe measurements.
5. The accuracy of the blade geometry.

A.1 Repeatability of the Data

The repeatability of the data is not only a function of the quality of the measurement process and instrumentation used but also depends on the ability to reset the operating conditions of the facility on a day-to-day basis. In order to assess how well the operating conditions could be reset, the radial distribution of the flow angle, pressure, and temperature measured downstream of the rotor

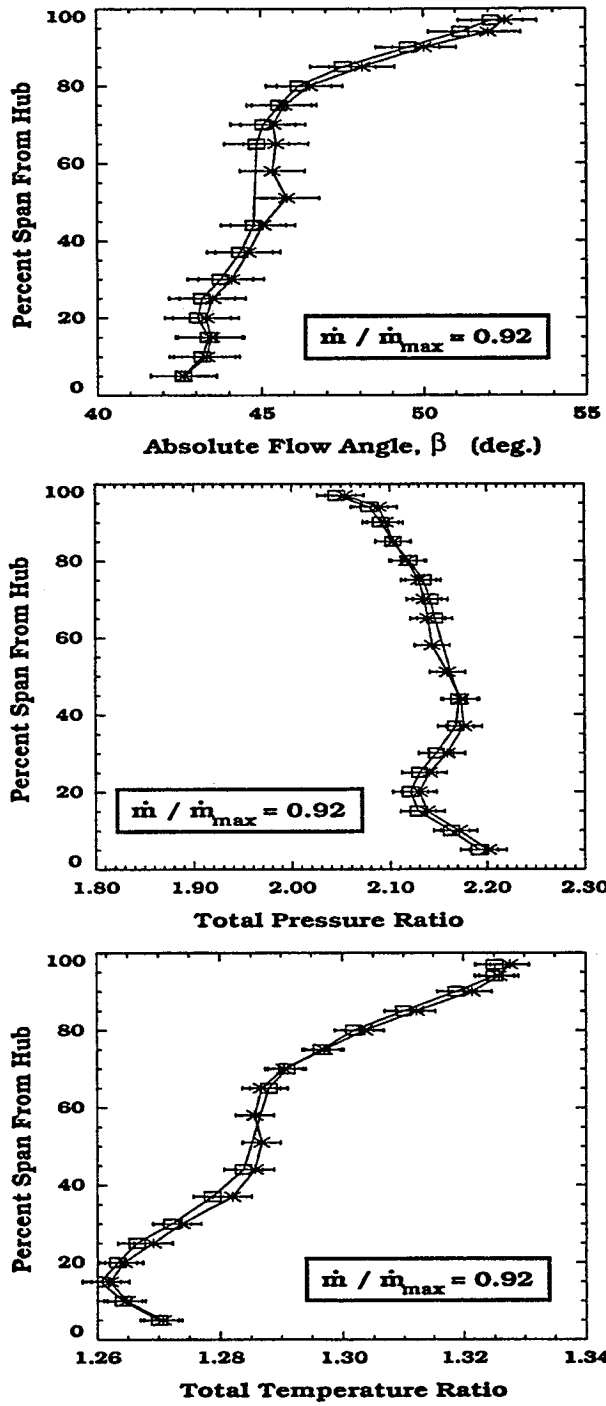


Figure 62 Repeatability of Aerodynamic Probe Data.

at the beginning and end of a test period which spanned over one year in length are compared in Figure 62. The differences in the flow angle measurements are less than one degree, the pressure differences are about 0.011 N/cm^2 (0.015 psia), and the temperature differences are 0.8K (1.5°R). As can be seen by the overlapping of the uncertainty intervals plotted in Figure 62, these differences are better than or approaching the experimental uncertainty of the measurement (flow angle, $\pm 1^\circ$, total pressure, $\pm 0.01 \text{ N/cm}^2$ and total temperature, $\pm 0.6\text{K}$). In Figure 15 it was shown that the variations of the flow angle, pressure, and temperature over the operating range of the compressor are approximately 10° in flow angle, 1.5 N/cm^2 (2.2 psia) in pressure and 12K (22°R) in temperature. Based on these results, the ability to reset rig conditions is within the measurement uncertainty and therefore does not adversely affect the results presented herein.

A.2 Evaluation of Particle Lag

Recall that in the discussion of the laser anemometer system a compromise had to be made in the choice of seed particle size. The seed particles have to be large enough for the LFA to make measurements but not so large that they do not follow the gradients of the flow field. The steepest gradient in the flow field results from the formation of the rotor passage shock. Therefore, to assess how well the particles follow the flow, the measured Mach number change across the shock is compared to the ideal value of that across a normal shock. In order for

this comparison to be a valid assessment of the seed particle lag, the shock must in reality be normal to the measured flow field. In this three-dimensional flow field the shock in all likelihood is rarely normal to the oncoming flow. However, we can make a conservative estimate of the particle lag distance by comparing the measured Mach number change across a nearly normal shock and comparing that to the ideal change in Mach number across a normal shock.

For a shock detached from the leading edge of the blade, the shock is normal over a small region just in front of the leading edge of the blade and becomes more oblique with increasing distance from the blade surface. The assessment of particle lag will be evaluated for the rotor operating at design speed and low flow condition because at this operating condition the shock is detached and nearly normal to the entire flow passage (experimental evidence of this fact will be shown later). A plot of the relative Mach number along a line (line A-A) which is nearly normal to this detached shock is shown in Figure 63. Since the shock standoff distance from the blade leading edge is less than the spatial resolution of the measurement locations (5% chord), it is difficult to evaluate the particle lag in a direction along the centerline of the blade section (i.e. the direction normal to the detached shock). Measurement line A-A is located along the 70% span streamsurface at 90% pitch from the blade suction surface. (Note that 0% pitch refers to the blade suction surface and 100% pitch corresponds to the suction surface of the

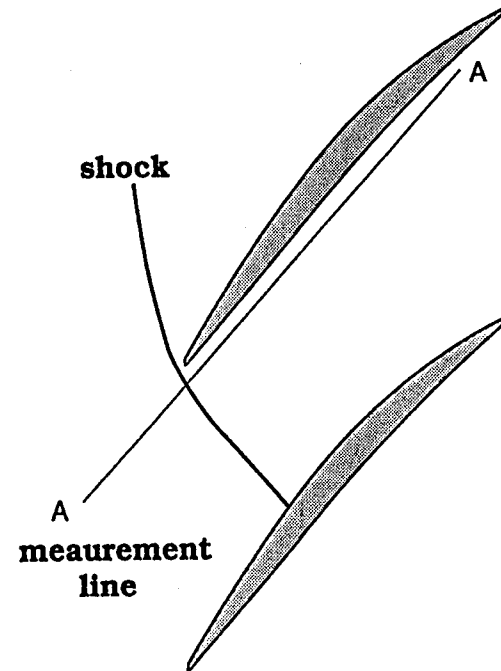
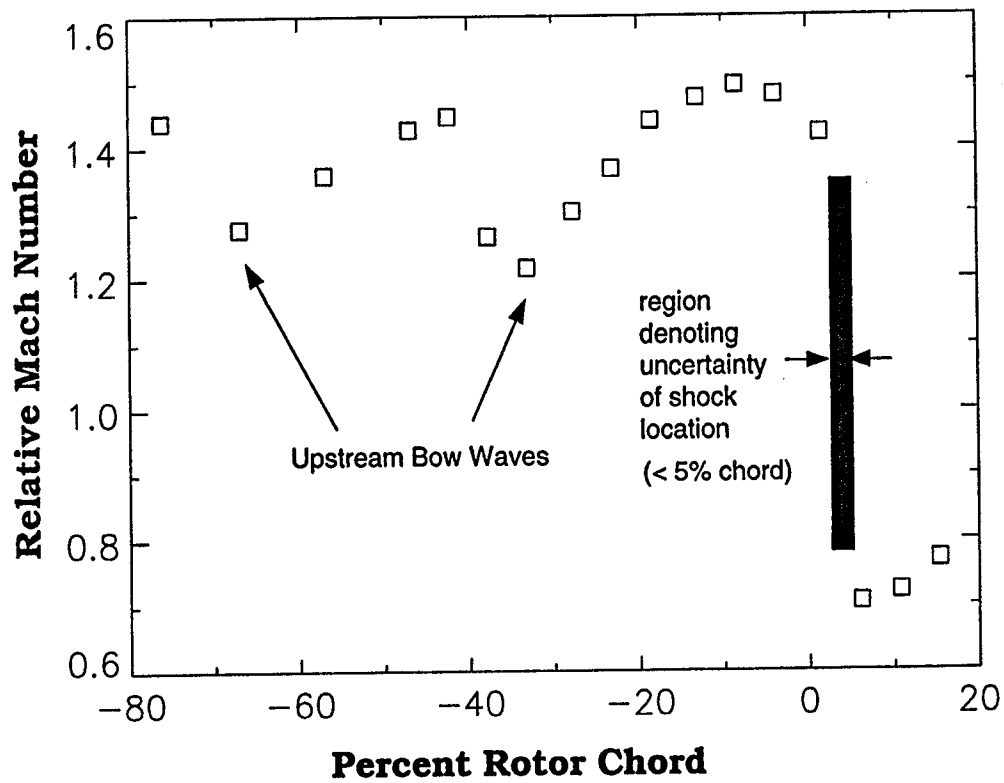


Figure 63 Particle lag evaluated in the streamwise direction (along line A-A at 70% span and 90% pitch from blade suction surface) across a nearly normal shock at design speed high flow condition.

succeeding blade.) This plot indicates that the particle lag is equal to or less than 5% of rotor chord which corresponds to the spatial resolution of the data.

To better define the particle lag, the data was evaluated in the circumferential direction where there is a finer spatial resolution of the measurements. For example, at the radius corresponding to 70% span, the spatial resolution of the measurements in the pitchwise direction is roughly 0.2 mm compared to a 1.5 mm spacing in the axial direction. Figure 64 shows the relative Mach number distribution across the rotor pitch at 20% chord, for the same span and rotor operating condition as Figure 63. For the measured shock face Mach number of 1.425 the ideal post-shock Mach number for a normal shock is 0.729. The gas velocity changes instantaneously across the shock, as shown by the broken line in Figure 64. However, due to their finite inertia, the seed particles require a finite distance to relax to the post shock gas velocity. The particles do decelerate to nearly the post shock Mach number of the idealized normal shock. However, the particle lag distance is approximately 15% pitch for the case shown here. For the blade geometry at 70% span, shown schematically in the right half of the figure, this distance corresponds to 8% of blade chord. Investigations of the rotor flow field throughout the passage indicate that the flow field downstream of the shock is accelerating and therefore the particle lag is being evaluated in a region of rapid deceleration across the shock and gradual acceleration in the flow

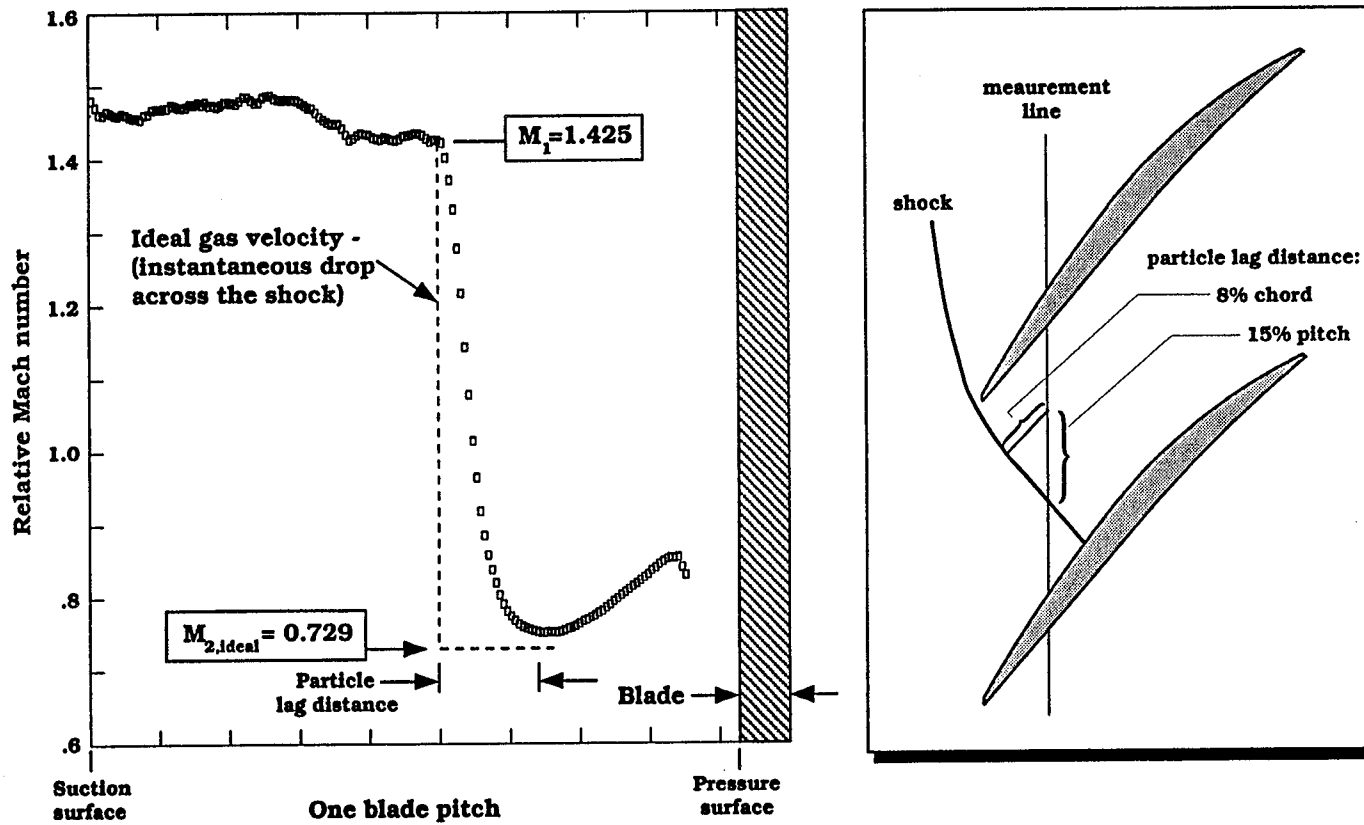


Figure 64 Particle lag evaluated in the pitchwise direction across a nearly normal shock.

field downstream of the shock. Therefore, this estimate for the particle lag is conservative. Evaluating the particle lag across the rotor passage shock at different spanwise and chordwise locations and making the same normal shock assumptions has resulted in particle lag estimates of 5–8% chord.

In summary, the particle lag distance across a normal shock with an inlet Mach number of 1.4 has been conservatively estimated to be 5–8% chord, and caution must be employed when evaluating the data immediately downstream of the shock. Since, in general the data is acquired every 5% chord this implies that the first measurement station downstream of the shock is subjected to particle lag effects. The particle lag distance is assumed negligible in all other regions of the flow field where the gradients are much less severe than that across a normal shock with an inlet Mach number of 1.4.

A.3 LFA Passage-to-Passage Flow Field Variations

In the section describing the data reduction procedure it was stated that the results are presented in an averaged rotor passage. In this section the variation between the flow field of one rotor passage and the remaining passages will be illustrated, and it will be shown that an average passage is representative of the flow field in the individual passages. In a transonic rotor the operating characteristics are dictated by the change in the structure of the rotor passage shock. In order to make a conservative assessment of the passage to passage flow

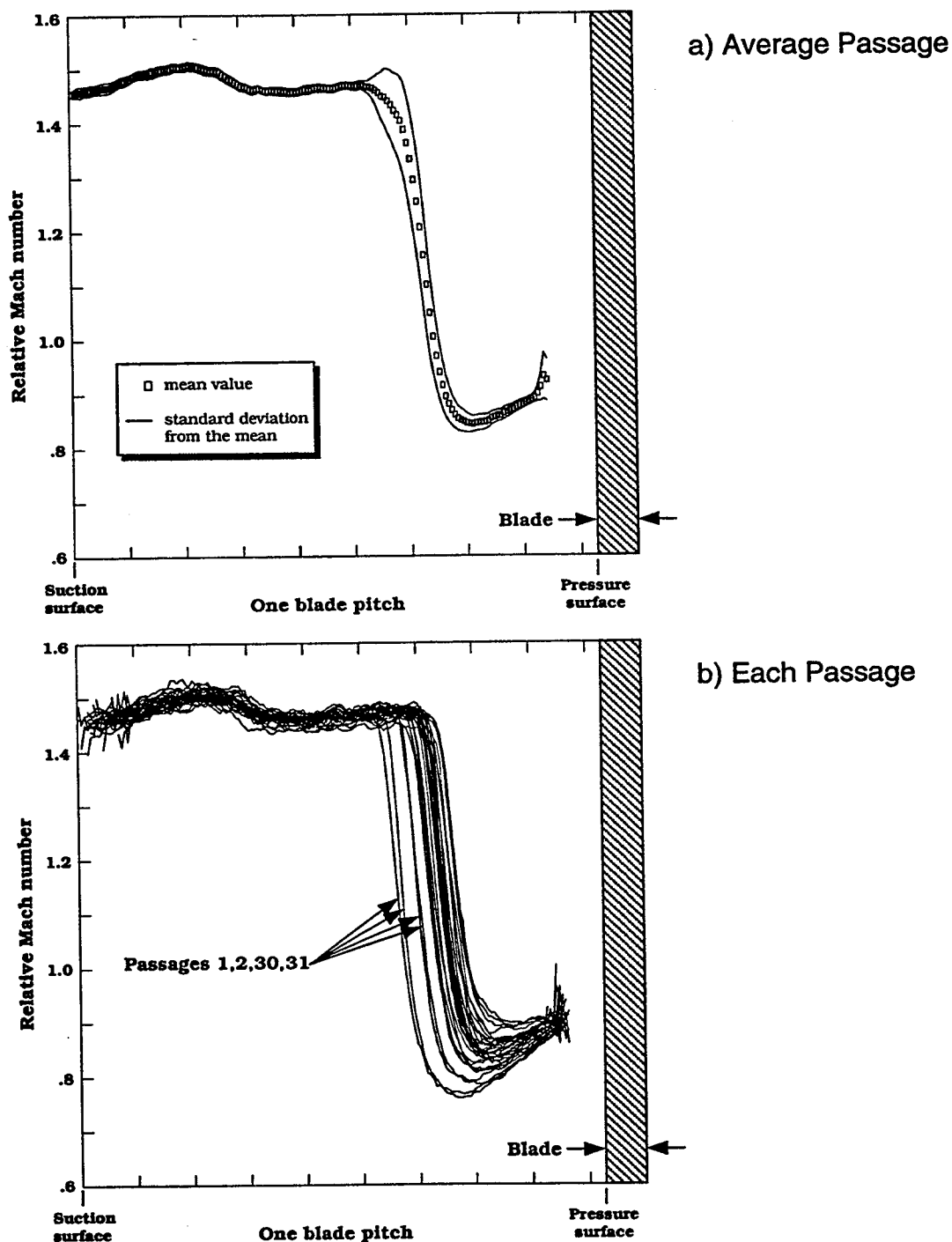


Figure 65 Pitchwise distribution of relative Mach number for each of the 36 blade passages at 20% chord, 70% span for the rotor operating at design speed and high flow conditions.

field variations, the variations in the rotor shock strength and location between passages will be evaluated at the high flow operating condition where the shock structure is sensitive to small changes in the backpressure and blade geometry.

In Figure 65, the pitchwise distribution of the relative Mach number measured at 20% chord and 70% span from the rotor operating at the high flow condition is plotted. In Figure 65a, the symbols represent the average Mach number at each pitchwise measurement location and the lines represent the standard deviation between the average value and the values in each of the 36 blade passages around the rotor wheel. In general, the standard deviation of the data corresponds to the outer edge of the symbols and therefore, will be omitted throughout this document for clarity. As Figure 65a indicates the scatter in the data is largest through the shock. However based on the discussion of seed particle lag, it is clear that caution must be taken when interpreting the data within 5% chord downstream of the rotor shock. The relative Mach number distribution in each of the 36 individual passages is plotted in Figure 65b. Note that the shock location and strength are slightly different in each passage and that 4 passages in particular have shock locations which are noticeably different than that of the remaining 32 blade passages. Since the leading edge on each blade is hand-finished and therefore slightly different, accompanied by the fact that inspection of the rotor wheel has indicated that there are very slight differences in the axial alignment of the blade leading edges and

differences in the circumferential blade spacing, these passage to passage variations are believed to be due to differences in blade geometry. To determine the impact of these "outlier" passages on the average passage result, 21 of the 36 passages which are nearly identical are averaged and compared to the average of all 36 passages. These results are presented in Figure 66 where the line represents the average of all blade passages and the symbols represent an average of the nearly identical 21 passages. The shock is more clearly defined by a sharper drop-off in relative Mach number for the average of the 21 nearly identical passages, but the shock location and strength do not change appreciably when compared to the average of all 36 passages. Due to the difficulty in removing selected blade passages to form the average passage for the many different measurement locations, the average passage results reported herein are computed using all 36 blade passages.

The effect of the passage to passage variations on the average passage results are much reduced at other regions in the flow field. For example, a comparison of the passage to passage variations downstream of the blade are presented in Figure 67. The data in Figure 67 were acquired at axial station #3 of Figure 11 and at the same operating condition used to acquire the data in Figure 66. The line represents the average of all blade passages and the symbols represent an average of the nearly identical 21 passages. Note that even though the sensitivity of the ordinate scale is twice as fine as that shown in Figure 66 (increment in relative

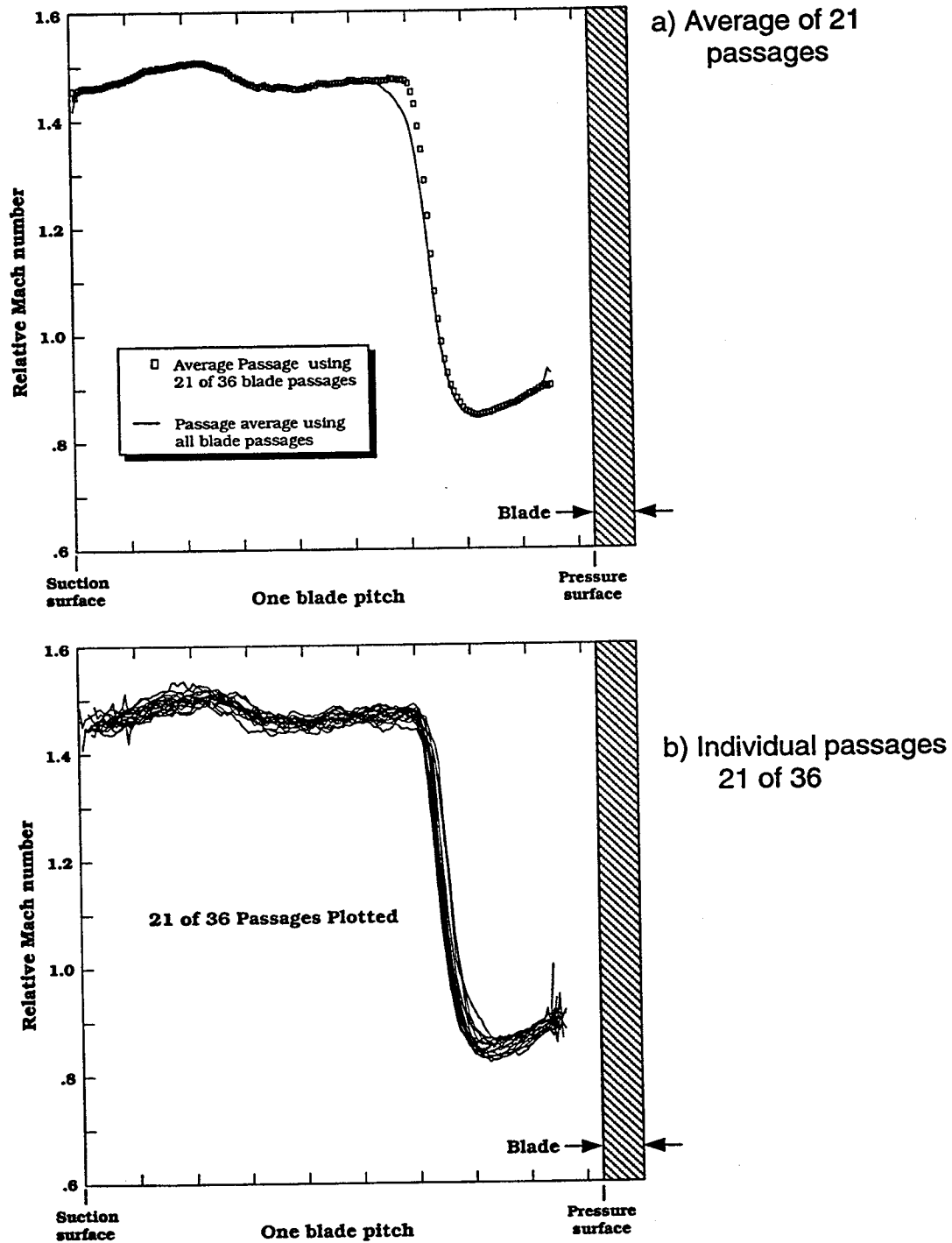


Figure 66 Pitchwise distribution of relative Mach number comparing the ensemble average of the nearly identical 21 passages to the ensemble average of all 36 blade passages at 20% chord, 70% span for the rotor operating at design speed and high flow conditions.

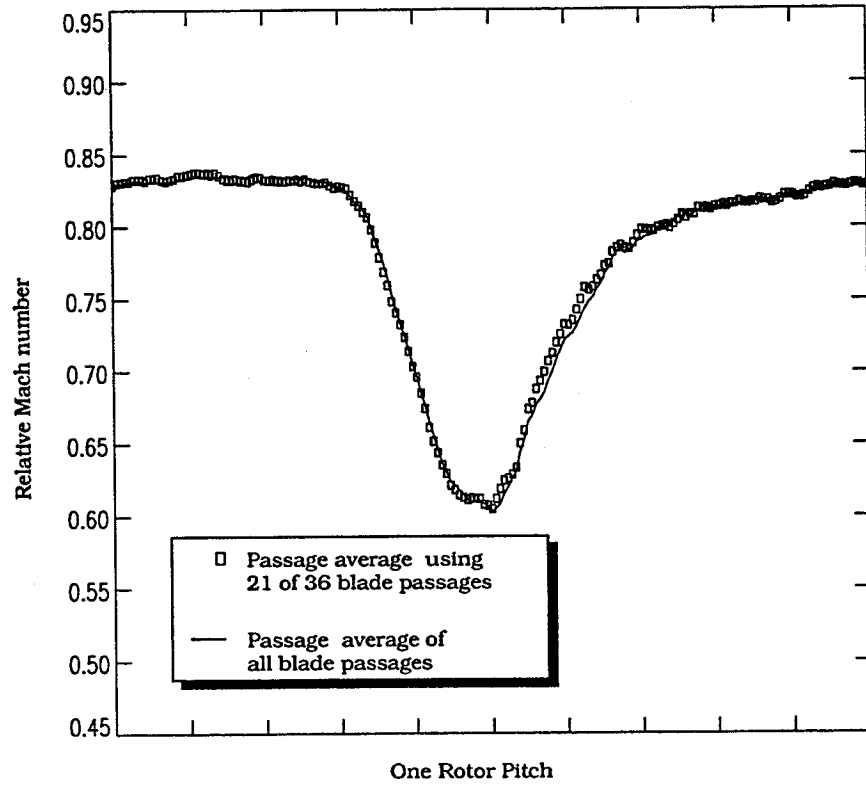


Figure 67 Pitchwise distribution of relative Mach number for all 36 passages at station #3, 70% span for the rotor operating at design speed and high flow conditions.

Mach number of 0.05 compared to 0.1), the removal of blade passages from the passage average does not significantly affect the passage averaged Mach number distribution across the rotor wake. Therefore, the variation in the blade passages is small enough to warrant an average passage representation of the flow field.

A.4 Comparison of LFA and Aerodynamic Probe Measurements

The aerodynamic probe measurements of total pressure, total temperature, static pressure, and flow angle are independent of one another. Similarly, the

measurements from each of the laser anemometer channels are independent of each other. However, to resolve velocity components from the aerodynamic probe data requires use of the total temperature, total pressure, static pressure, and flow angle — see equation 2. Similarly, to calculate the Mach number or temperature from the laser data requires a calculation using both LFA measured velocity components, the plenum temperature, and the wheel speed — see equations 8 and 12. The point is that there is no way to make a direct one-to-one comparison between the laser anemometer and probe measurements. Therefore, the following comparisons will be made: 1) comparison of the probe measured flow angle to the flow angle calculated from the laser anemometer measurements, 2) total temperature measured directly by the probes to the temperature calculated from laser anemometer measurements using Euler's turbomachinery equation and the energy equation, and 3) a comparison of the absolute velocity calculated from the probe measurements to the velocity computed by combining the velocity components measured with the LFA system. Also, note that the probe measurements and LFA measurements were not made simultaneously. Therefore, the differences due to day-to-day repeatability and resetting rig operating conditions are also affecting these comparisons. The comparisons are made between probe measurements at station #4 and LFA measurements at station #4a (refer to Figure 11). Since the flowpath is a constant area duct between these stations and they are located far

downstream of the rotor, the differences in the flow field at these two survey stations is considered negligible and should not affect the comparisons.

A comparison of the probe measured flow angle to the flow angle calculated from the axial and tangential velocity components measured by the LFA system is presented in Figure 68. The error bars on each of the symbols represent the uncertainty band for a 95% confidence interval. The solid lines in Figure 68b represent the minimum and maximum value in the pitchwise direction which went into the average value plotted for each radial measurement location, whereas the dashed line is an overlay of the probe data in Figure 68a where the error bars have been omitted for clarity. A closer examination of the pitchwise distribution of the LFA measurements (not shown) indicates that the variation in flow angle is sinusoidal with a period equal to a rotor pitch. The rotor blade passing frequency is approximately 10Khz and the survey probe cannot respond to these fluctuations. However, the comparison of flow angle measurements in Figure 68 indicates that there is a difference in the mean flow angle of only 1–1.5° between the probe and the LFA measurements which is within the uncertainty of the measurements themselves.

The comparison of the total temperature measurements is shown in Figure 69. The minimum and maximum temperature values, derived from the LFA measurements, are presented along with the mean values and their corresponding

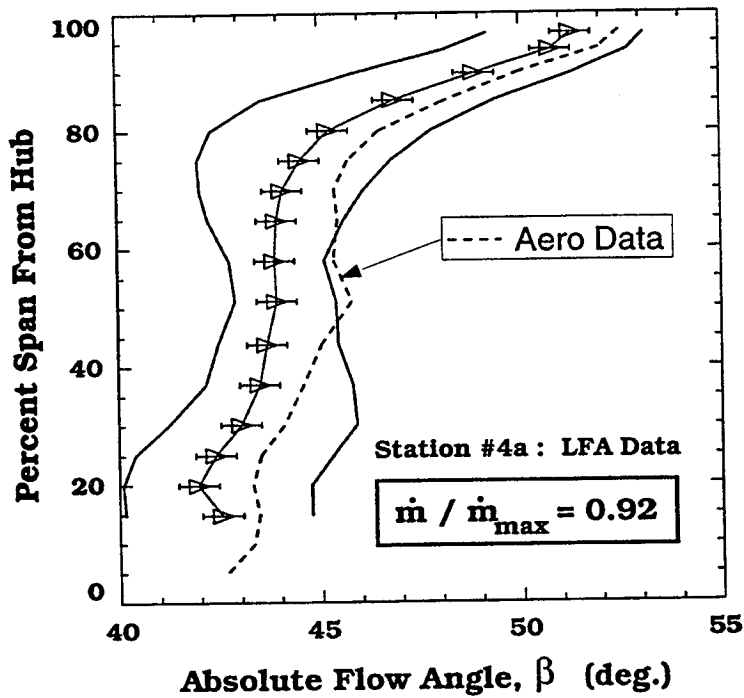
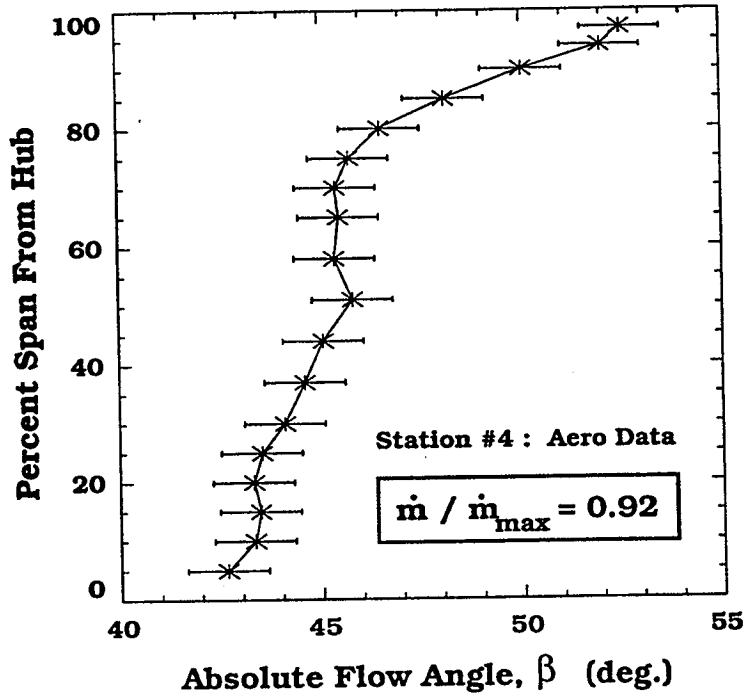


Figure 68 A comparison of the probe measured flow angle at station #4 to the LFA measured flow angle at station #4a for the rotor operating at design speed and low flow conditions.

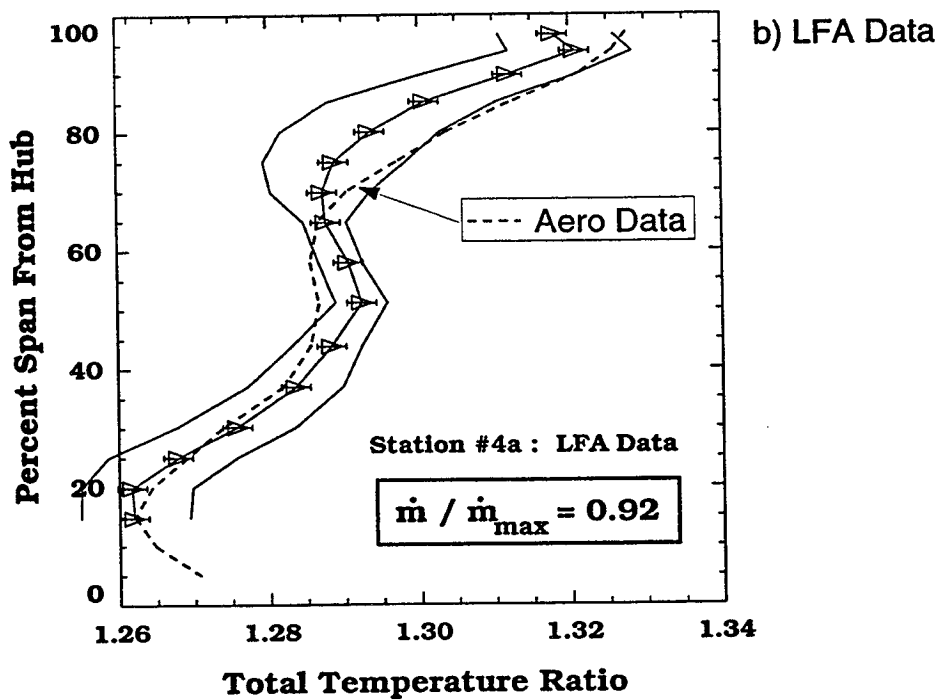
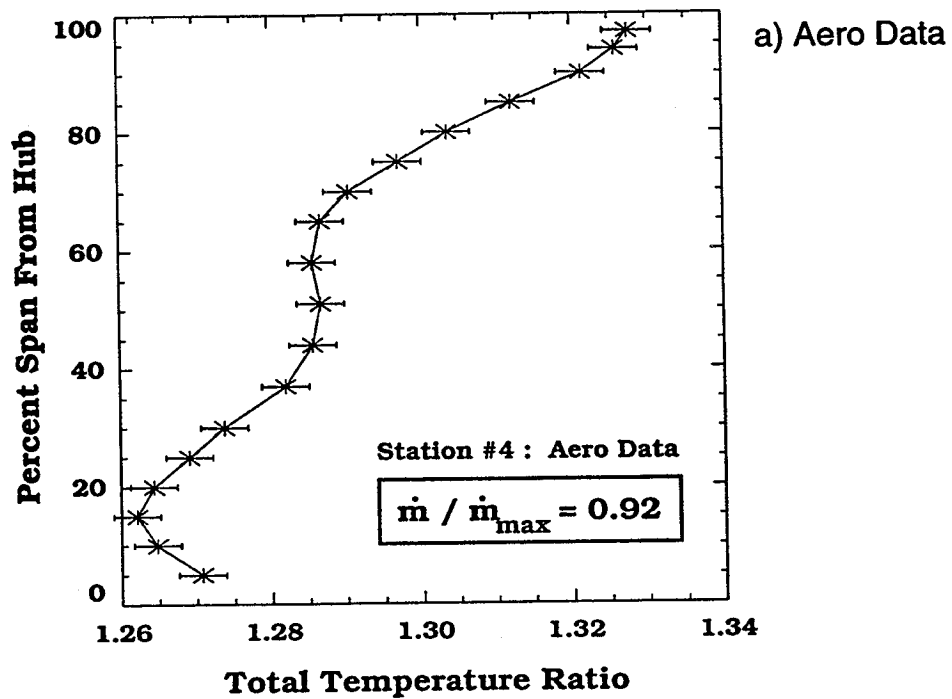


Figure 69 A comparison of the probe measured total temperature at station #4 to the LFA inferred total temperature at station #4a for the rotor operating at design speed and low flow conditions.

error bars in Figure 69b. From 70% span and below the data agree within the uncertainty of the values. However in the outer 30% span, where the gradient in temperature is most severe, there is a discrepancy of about 3°R between the probe measurements and the LFA calculated values of the mean total temperature. This difference lies just outside of the estimated uncertainty levels but still lies within minimum and maximum values in the unsteady flow field. Note also that the two measurement systems indicate the same shape in the radial profile of the temperature. A close examination of the aerodynamic probe data indicates the mass flow through the machine decreases by about 0.04 lbm/s as the probes are immersed into the flow stream. Therefore, the rotor is operating at a slightly different operating condition for each radial measurement. When looking at the variation of the temperature profile (refer to Figure 15) with operating condition it is apparent that only a small change in the operating condition could account for this difference in the LFA and probe determined values of the total temperature. Since the discrepancy in the LFA calculated and probe measured temperature is within the temperature fluctuations measured by the LFA system, and since the reasons given to explain this discrepancy do not fault the LFA method of calculating the temperature rise of the rotor, the LFA determined values of temperature are considered to be accurate.

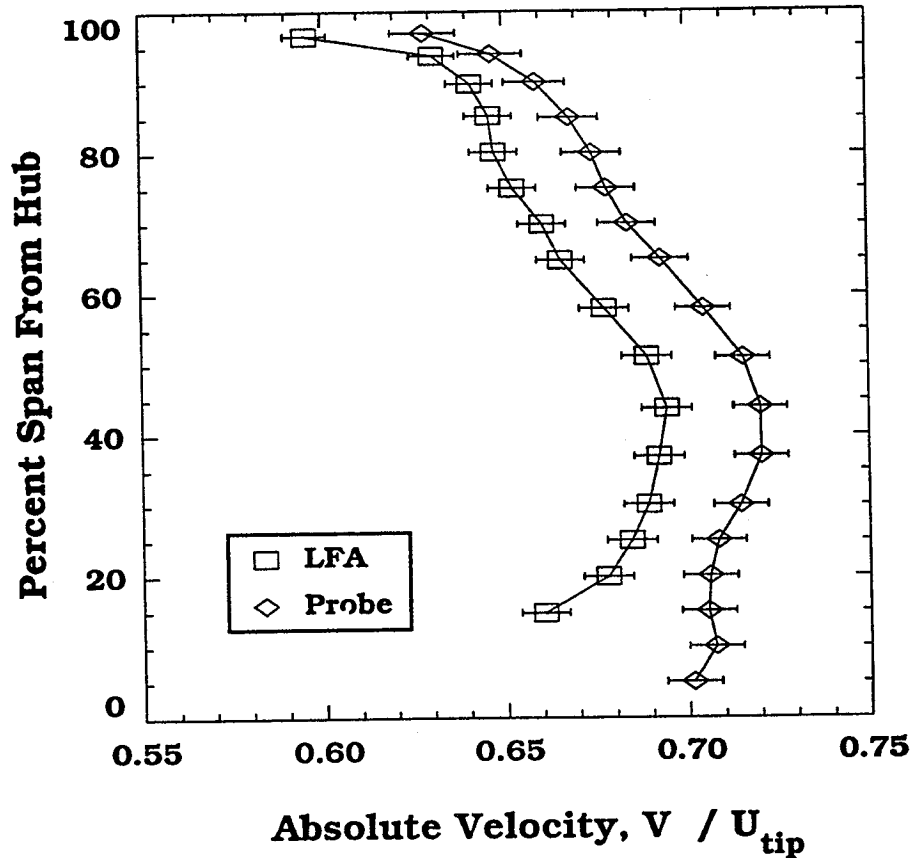


Figure 70 A comparison of the probe inferred absolute velocity at station #4 to the LFA inferred absolute velocity at station #4a for the rotor operating at design speed and low flow conditions.

Comparison of the total velocity components is shown in Figure 70. The difference in the mean values is about 4% but the separation between the error bars is only about 1% and is believed to be due to errors in the measurement of static pressure by the wedge probe. To insure that the reason for this discrepancy is in the probe measurement of static pressure and not the LFA measurement, the velocity of the LFA is compared to the computational results at the rotor inlet where the CFD is assumed to be very reliable. This comparison is illustrated in

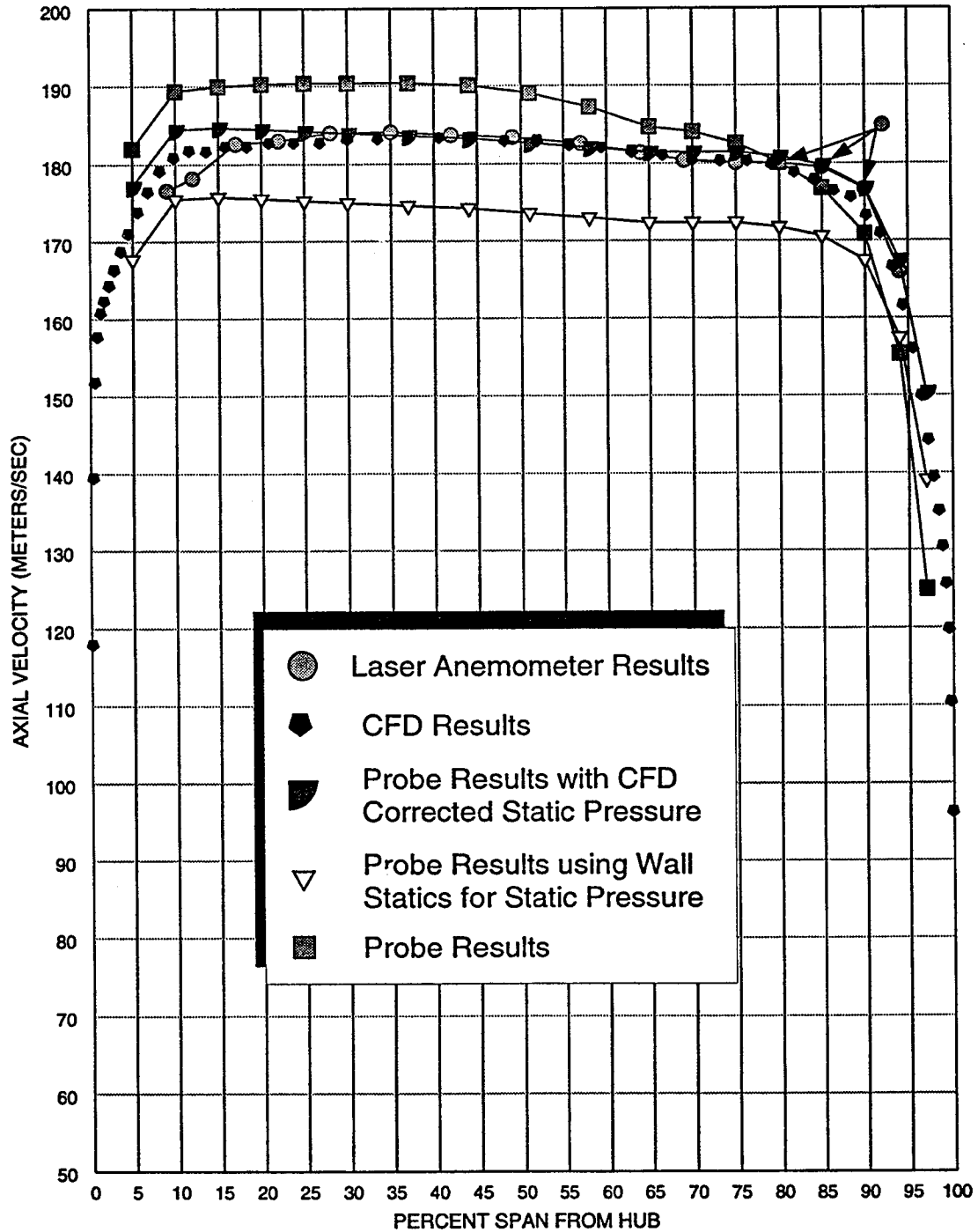


Figure 71 A comparison of the CFD absolute velocity at station #1 to the LFA inferred absolute velocity at station #1 for the rotor operating at design speed and high flow conditions.

Figure 71 where the circles denote the LFA measured velocities and the pentagon symbols represent the velocities from the CFD. This agreement is considered quite good. Also, if the static pressure calculated from the CFD is used in combination with the probe measured total pressure and total temperature the resulting velocity (denoted by the quarter circle symbol) is in agreement with both the CFD and LFA velocity (denoted by the pentagon and circle symbols respectively). In contrast, the probe-measured velocity determined using either the radial static pressure distribution measured with a wedge static probe (denoted by the square) or the wall static pressure (denoted by the upside-down triangle) do not agree with the LFA result. Therefore, the discrepancy between the probe-determined and LFA-determined velocity shown in Figure 70 is believed to be largely due to the difficulties in obtaining an accurate value of the static pressure.

In summary, the LFA and probe data have been shown to be reliable and repeatable. The probe measurements of the flow angle, total temperature, and total pressure are believed to be accurate within the calculated uncertainties. However, due to the difficulty in making measurements of the static pressure, the values of velocity obtained from the aerodynamic probe measurements are only accurate to within about 2–4%. The LFA measured velocities and the calculated flow angles and temperatures are also believed to be within the stated uncertainty intervals. The procedure to calculate the temperature and therefore the Mach number from

the LFA measured velocities has been validated to the extent that the results are in agreement with conventional thermocouple type measurements. The comparisons of the laser anemometer results to 1) the conventional aerodynamic probe results and 2) to the CFD results show that the LFA measurement system is working properly and it can be used to assess the velocity, flow angle, and temperature variations throughout the rotor flow field.

A.5 Geometry Considerations

The blade geometry is designed on two-dimensional blade sections and stacked radially to form the three-dimensional blade shape. For a highly-loaded blade such as rotor 37 the geometry of the blade changes with operating condition due to the aerodynamic loading and rotational forces acting on the blade. The geometry is categorized as 'cold' geometry in reference to the geometry of the blade under no load (i.e. the manufacturing coordinates) , and 'hot' geometry in reference to the geometry of the blade under load. In order to get the desired 'hot' blade geometry not only does the manufacturer have to make the blade to the specifications of the 'cold' geometry, but the transformation in the design process from the 'hot' geometry to the 'cold' geometry must be done correctly. The 'cold' geometry was inspected in the NASA Lewis Inspection Laboratory. The LFA system in

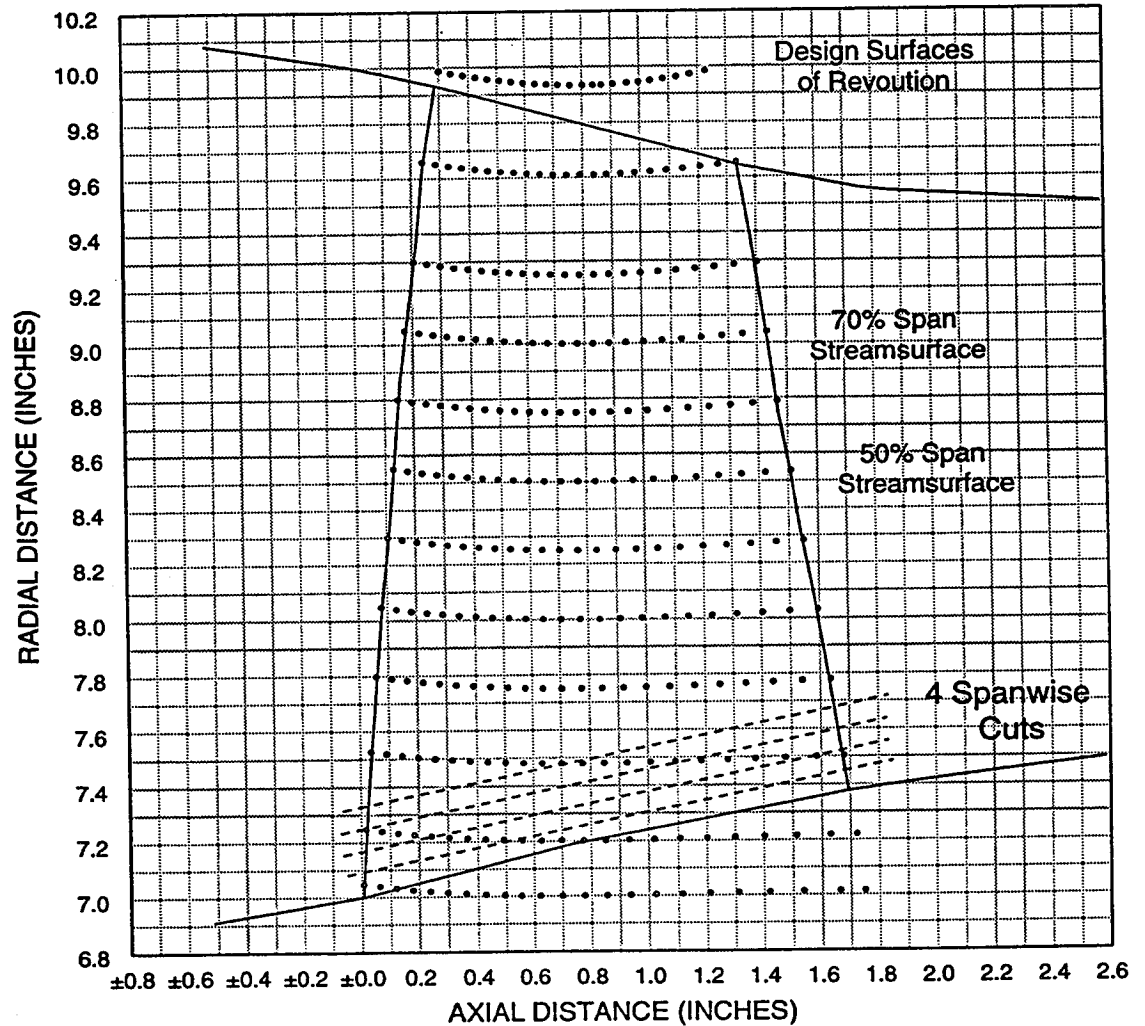


Figure 72 Design blade sections and location of inspection plane.

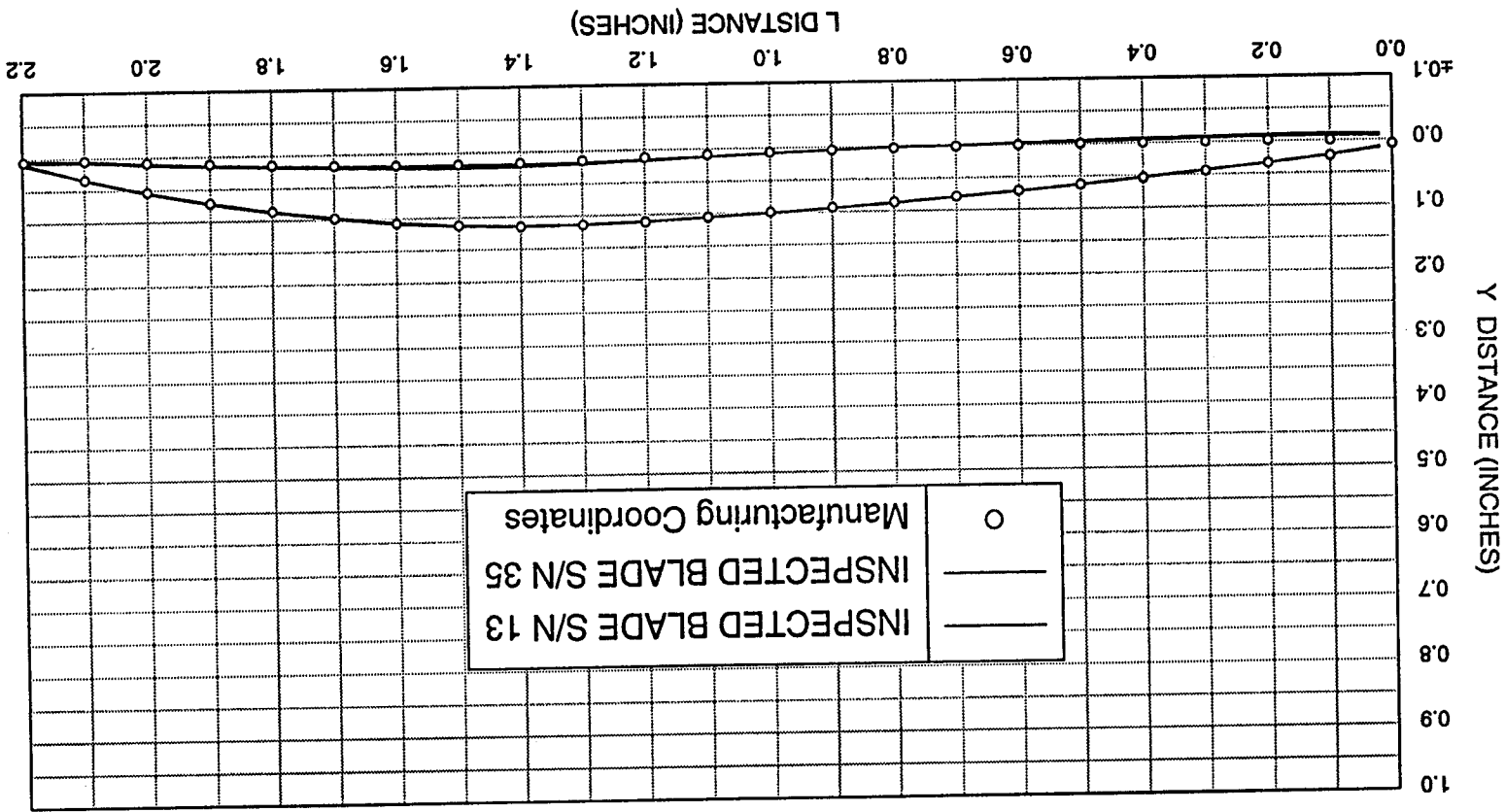
conjunction with a NASTRAN analysis was used to assess the 'hot' geometry under design speed conditions.

Inspection of the 'cold' geometry. Blades were inspected at most of the two-dimensional design blade sections shown in Figure 72 and were compared with the 'cold' blade geometry. Several rotor blades were inspected along several of the design geometry planar surfaces using an eyelash machine which traces the

contour of the blade surface. The accuracy of an eyelash machine is ± 0.025 mm (± 0.001 in.). The design specifications call for the blade surface to fall within ± 0.127 mm (± 0.005 in.) of the design blade contour with a maximum deviation in the total blade thickness of ± 0.127 mm (± 0.005 in.). Note that the original inspections are performed at a scale ten times the actual size so that discrepancies from the design intent can be more accurately measured, and in general the blades were within design tolerances. A CORDAX machine was used to evaluate the blade coordinates at several of these inspected planes. An example comparing the CORDAX inspection of the blade shape to the manufacturing coordinates ('cold' geometry) for the blade section near 70% span is presented in Figure 73. In addition, the blade surface angles were calculated from the measurements of the blade shape obtained with the CORDAX machine and compared to the manufacturer's coordinates. The results for the 70% span blade section are presented in Figure 74. There are subtle differences between the different blades and the desired 'cold' geometry, but in general the inspection results indicate that the blade was made to the specifications within the manufacturing tolerances. All other inspection surfaces show comparable agreement.

In addition to the design planar surfaces indicated on Figure 72, there are four spanwise cuts located near the hub. At these locations additional eyelash inspections were performed to insure that the blade thickness and setting angle

Figure 73 Comparison between the manufacturing coordinates and the inspected blade section near 70% span.



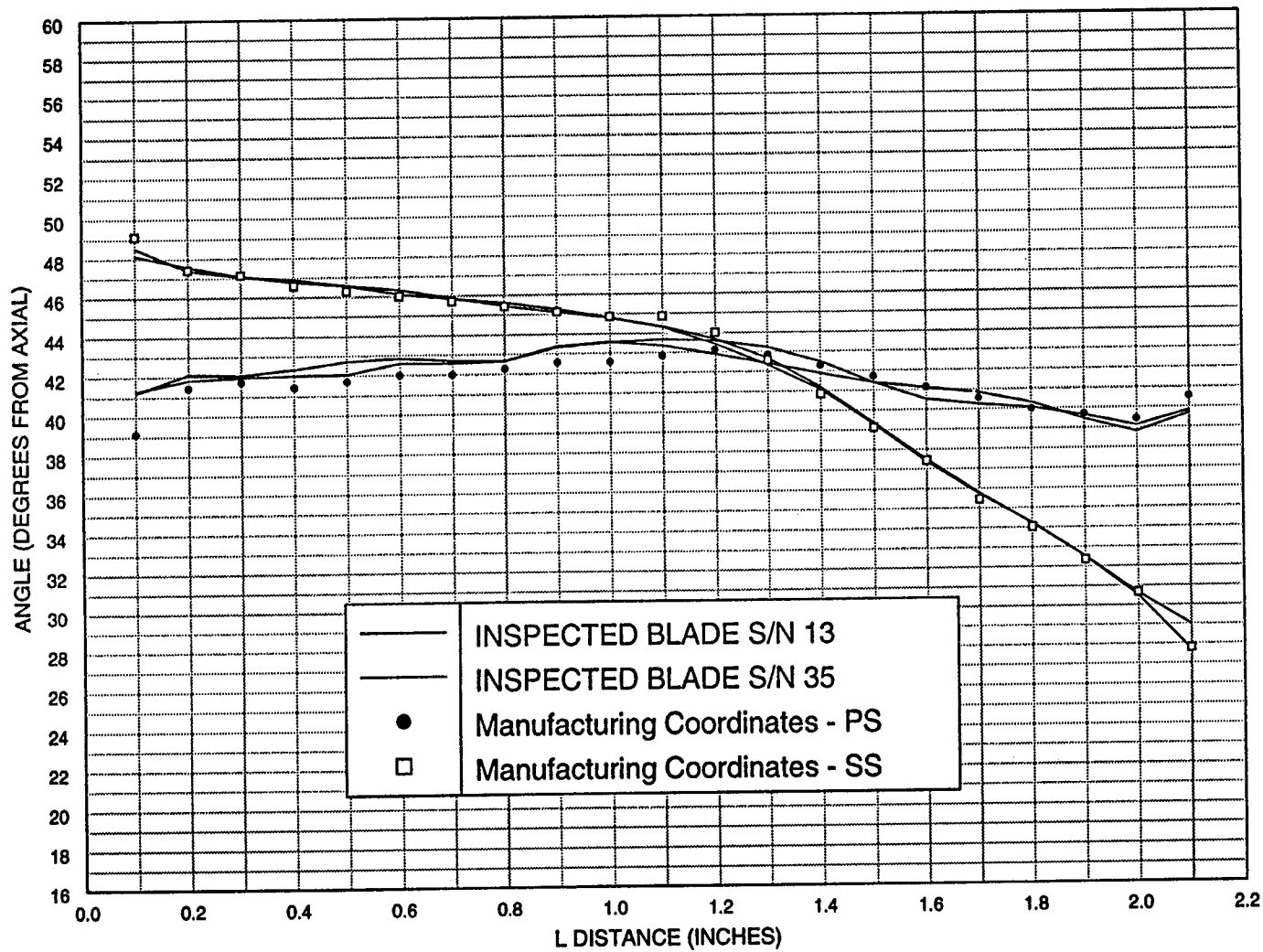


Figure 74 Comparison between the designed blade surface angles and the inspected blade surface angles for the blade section near 70% span.

were in agreement with the desired 'cold' geometry. Though these inspections are still underway, the preliminary indication is that the blade is within specifications in this hub region.

The tips of the rotor blades were also inspected to determine if the blade tips were rounded or if they formed a sharp edge. This detail becomes significant in the modelling of the flow over the rotor tip. For example, if the edges are sharp, general practice during CFD analysis is to reduce the physical clearance height to simulate a discharge coefficient to account for the vena-contracta effect for the flow over the rotor tips. On the other hand, if the edges are rounded the model would be applied with a discharge coefficient of one, thereby modelling the flow over the full clearance height. The inspection results indicated the blade tips were rounded. Although these inspection results were supplied to the CFD testcase participants, all participants chose to treat the rotor blade tip as having a sharp edge.

Verification of the 'hot' geometry. The LFA system was used to determine the blade geometry of the blade tip section for the rotor running at base speed (2000 rpm) and design speed (17200 rpm). The probe volume of the LFA system was focused on the blade tip with the laser at low power levels and essentially recorded a measurement using the blade tip as the 'seed' particle. In order to make these measurements the rotor had to be rotating through the LFA probe volume. The results at idle condition are assumed to be representative of the 'cold'

geometry and the design speed results depict the 'hot' geometry. Unfortunately this measurement technique could only be applied at the tip section of the rotor because at lower blade spans the part of the blade above the blade section of interest interferes with the laser beams. Therefore, to determine the blade shape at all spans with the rotor under load, a NASTRAN analysis was performed on the blade. The NASTRAN results are compared with the LFA measurements of the rotor tip section at design speed in Figure 75. In addition, the LFA measurements at idle or no load condition are compared to the manufacturing coordinates ('cold' geometry). The agreement between the LFA and the NASTRAN analysis validated the deflections predicted by the NASTRAN analysis. It is evident from Figure 75 that the rotor tip section untwists by approximately 2 degrees in going from the no load condition at idle to the loads encountered at design speed. Another comparison between the NASTRAN analysis and the LFA measurement indicate that the rotor wheel assembly moved outward radially approximately 0.305 mm (0.012 in.) under the centrifugal loads at design speed. In addition, CFD simulations indicated the choke flow changed from 20.54 kg/s (45.6 lbm/s) using the cold geometry to 20.91 kg/s (46.0 lbm/s) using the NASTRAN 'hot' geometry. Thus the choke flow calculated with the NASTRAN predicted 'hot' geometry was in agreement with the choke flow measured in the stage configuration. Based on these comparisons between the NASTRAN analysis and the LFA measurements, and the accurate

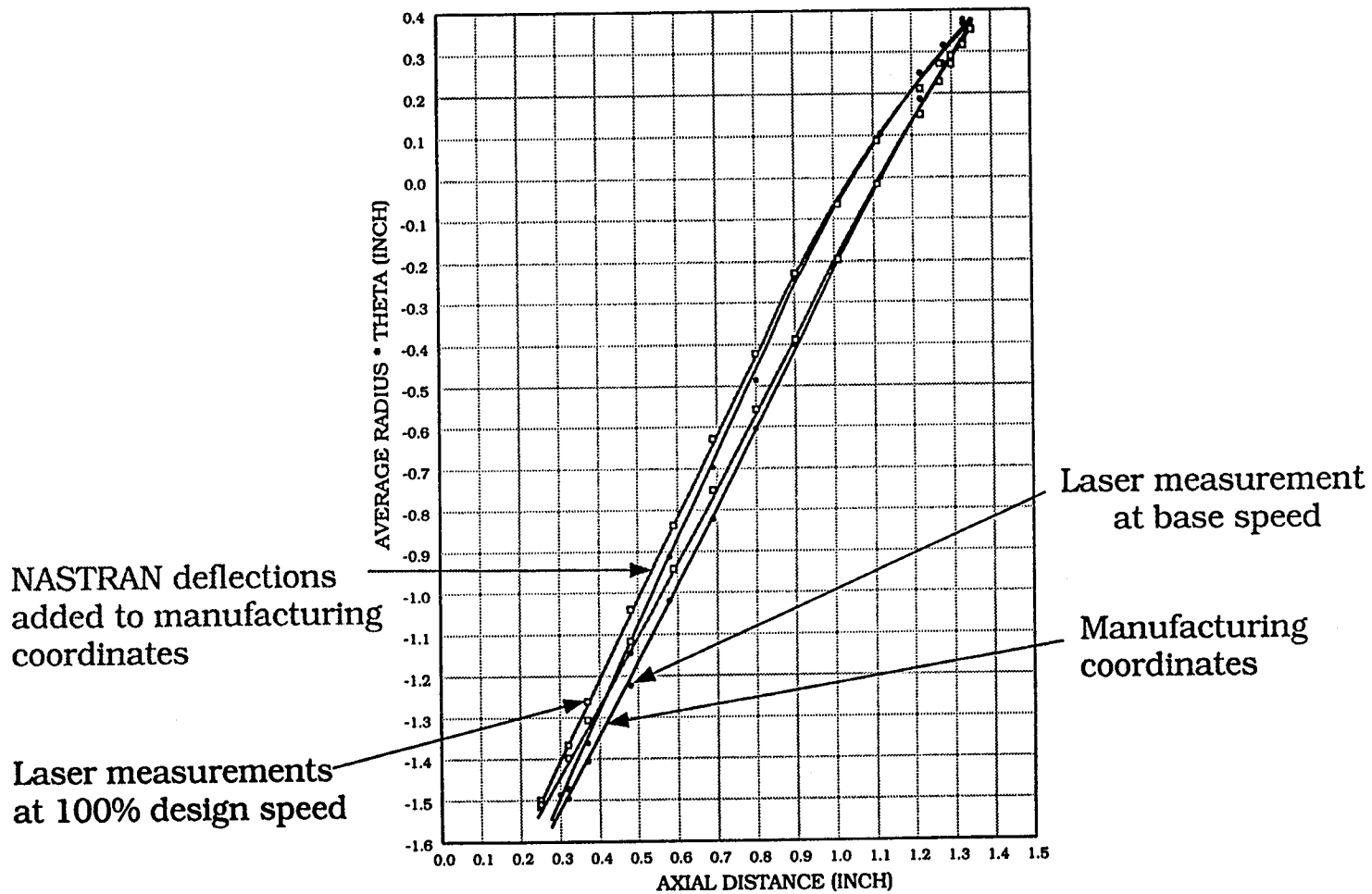


Figure 75 Comparison of the tip geometry measured with the LFA to that predicted by NASTRAN at design speed and to the 'cold' geometry at base speed.

CFD prediction of the choke flow when using the NASTRAN 'hot' geometry, the NASTRAN predicted geometry at design speed is believed to be the actual 'hot' geometry for the rotor operating at design speed, and it was the geometry provided to the CFD participants in the ASME testcase.

Comparison of 'hot' geometry to design intent. The 'hot' geometry at design speed as determined by the NASTRAN analysis and as verified by the LFA measurements did not agree with the original design intent. The original mechanical design did not properly account for the untwist in the blade under load, resulting in a discrepancy of about 1–2 degrees such that the actual 'hot' blade is untwisted more than the design intent. Note that these blades were originally designed in the mid 1970's and during this time sophisticated analysis tools such as NASTRAN to evaluate the blade deflections were just becoming available. Therefore, it is not surprising that the original design did not account for the 1–2 degrees of blade untwist under load at design speed.

REPORT DOCUMENTATION PAGE

Form Approved
OMB No. 0704-0188

Public reporting burden for this collection of information is estimated to average 1 hour per response, including the time for reviewing instructions, searching existing data sources, gathering and maintaining the data needed, and completing and reviewing the collection of information. Send comments regarding this burden estimate or any other aspect of this collection of information, including suggestions for reducing this burden, to Washington Headquarters Services, Directorate for Information Operations and Reports, 1215 Jefferson Davis Highway, Suite 1204, Arlington, VA 22202-4302, and to the Office of Management and Budget, Paperwork Reduction Project (0704-0188), Washington, DC 20503.

1. AGENCY USE ONLY (Leave blank)	2. REPORT DATE October 1996	3. REPORT TYPE AND DATES COVERED Technical Memorandum	
4. TITLE AND SUBTITLE Experimental Investigation of the Flow Field in a Transonic, Axial Flow Compressor With Respect to the Development of Blockage and Loss		5. FUNDING NUMBERS WU-505-62-52	
6. AUTHOR(S) Kenneth L. Suder		8. PERFORMING ORGANIZATION REPORT NUMBER E-10403	
7. PERFORMING ORGANIZATION NAME(S) AND ADDRESS(ES) National Aeronautics and Space Administration Lewis Research Center Cleveland, Ohio 44135-3191		10. SPONSORING/MONITORING AGENCY REPORT NUMBER NASA TM-107310	
9. SPONSORING/MONITORING AGENCY NAME(S) AND ADDRESS(ES) National Aeronautics and Space Administration Washington, D.C. 20546-0001		11. SUPPLEMENTARY NOTES This report was submitted as a thesis in partial fulfillment of the requirements for the degree Doctor of Philosophy to Case Western Reserve University, Cleveland, Ohio, August 1996. Responsible person, Kenneth L. Suder, organization code 2640, (216) 433-5899.	
12a. DISTRIBUTION/AVAILABILITY STATEMENT Unclassified - Unlimited Subject Category 02 This publication is available from the NASA Center for AeroSpace Information, (301) 621-0390.		12b. DISTRIBUTION CODE	
13. ABSTRACT (Maximum 200 words) A detailed experimental investigation to understand and quantify the development of loss and blockage in the flow field of a transonic, axial flow compressor rotor has been undertaken. Detailed laser anemometer measurements were acquired upstream, within, and downstream of a transonic, axial compressor rotor operating at design and off-design conditions. The rotor was operated at 100%, 85%, 80%, and 60% of design speed which provided inlet relative Mach numbers at the blade tip of 1.48, 1.26, 1.18, and 0.89 respectively. At design speed the blockage is evaluated ahead of the rotor passage shock, downstream of the rotor passage shock, and near the trailing edge of the blade row. The blockage is evaluated in the core flow area as well as in the casing endwall region. Similarly at part speed conditions for the cases of 1) where the rotor passage shock is much weaker than that at design speed and 2) where there is no rotor passage shock, the blockage and loss are evaluated and compared to the results at design speed. Specifically, the impact of the rotor passage shock on the blockage and loss development, pertaining to both the shock/boundary layer interactions and the shock/tip clearance flow interactions, is discussed. In addition, the blockage evaluated from the experimental data is compared to 1) an existing correlation of blockage development which was based on computational results, and 2) computational results on a limited basis. The results indicate that for this rotor the blockage in the endwall region is 2-3 times that of the core flow region and the blockage in the core flow region more than doubles when the shock strength is sufficient to separate the suction surface boundary layer. The distribution of losses in the core flow region indicate that the total loss is primarily comprised of the shock loss when the shock strength is not sufficient to separate the suction surface boundary layer. However, when the shock strength is sufficient to separate the suction surface boundary layer, the profile loss is comparable to the shock loss and can exceed the shock loss.			
14. SUBJECT TERMS Supersonic; Compressor; Rotor; Laser; Anemometer system; Shock/boundary layer interaction; Blockage; Tip clearance flows		15. NUMBER OF PAGES 269	16. PRICE CODE A12
17. SECURITY CLASSIFICATION OF REPORT Unclassified	18. SECURITY CLASSIFICATION OF THIS PAGE Unclassified	19. SECURITY CLASSIFICATION OF ABSTRACT Unclassified	20. LIMITATION OF ABSTRACT